THE UNIVERSITY OF CHICAGO

PRODUCT BRANCHING IN THE PHOTODISSOCIATION OF CHLOROACETALDEHYDE AND THE INCORPORATION OF ANGULAR MOMENTUM IN STATISTICAL PREDICTIONS OF PRODUCT BRANCHING

A DISSERTATION SUBMITTED TO
THE FACULTY OF THE DIVISION OF THE PHYSICAL SCIENCES
IN CANDIDACY FOR THE DEGREE OF
DOCTOR OF PHILOSOPHY

DEPARTMENT OF CHEMISTRY

BY
JONATHAN DAVID ADAMS

CHICAGO, ILLINOIS
MARCH 2017

TABLE OF CONTENTS

LIST OF FIGURES vi

LIST OF TABLES xi

ACKNOWLEDGMENTS xii

ABSTRACT xiii

CHAPTER

1. INTRODUCTION 1
  - 1.1 Motivation 1
  - 1.2 Chemical System Studied 3
  - 1.3 Experimental Methods 5
    - 1.3.1 Velocity Map Imaging 6
    - 1.3.2 Crossed Laser-Molecular Beam Scattering 8
    - 1.3.3 Comparison 10
  - 1.4 References 11

2. IMAGING LAB STUDY OF THE PHOTODISSOCIATION OF CHLOROACETALDEHYDE AT 157 nm: DETECTION OF UNIMOLECULAR DISSOCIATION PRODUCTS OF VINOXY 14
  - 2.1 Introduction 14
  - 2.2 Experimental Details 17
    - 2.2.1 Velocity Map Imaging 17
    - 2.2.2 Computational Methods 19
  - 2.3 Results 20
    - 2.3.1 Electronic Structure Calculations 20
    - 2.3.2 Primary C−Cl Bond Photofission Channel 23

2.3.3 Detection of Ketene, CH_2CO 31

2.3.4 Detection of Methyl Radicals, CH_3 35

2.4 Discussion 38

2.5 References 43

3. INCORPORATING ANGULAR MOMENTUM IN STATISTICAL PREDICTIONS OF PRODUCT BRANCHING: REASSESSING THE BARRIER FOR THE UNIMOLECULAR DISSOCIATION OF VINOXY TO H + KETENE 48

3.1 Introduction 48

3.2 Development of Model 51

3.2.1 Rotational Model 51

3.2.2 Branching Model 53

3.3 Model Predictions for Photodissociation of Chloroacetaldehyde at 157 nm and the Branching of Vinoxy 61

3.3.1 Considerations for the Branching Model 62

3.3.2 Results 66

3.4 Discussion 81

3.5 References 86

4. CHARACTERIZATION OF PRIMARY PRODUCT BRANCHING IN THE PHOTODISSOCIATION OF CHLOROACETALDEHYDE AT 157 nm 88

4.1 Introduction 88

4.2 Experimental Details 93

4.2.1 NSRRC Scattering Apparatus 93

4.2.2 Computational Methods 95

4.3 Results 96

4.3.1 Overview of Primary Photodissociation Channels of Chloroacetaldehyde 97

4.3.2 Primary Photodissociation Channels: C−Cl Bond Fission and HCl Photoelimination 98

4.3.3 Primary Photodissociation Channels: C−C Bond Fission 108

4.3.4 Branching Ratios for Primary Photodissociation Channels 113

4.3.5 Unimolecular Dissociation of Vibrationally Excited Vinoxy Radicals Resulting From Primary C−Cl Bond Fission 114

4.3.6 Unimolecular Dissociation of Vibrationally Excited Ketene Resulting From HCl Photoelimination..130

4.3.7 Unimolecular Dissociation of Vibrationally Excited Formyl Radicals Resulting From Primary C−C Bond Fission 136

4.3.8 Partial Photoionization Cross Section for Vinoxy to CH_3^+ + CO 138

4.4 Discussion 140

4.5 References 148

5. CONCLUSIONS...155

5.1 References 157

APPENDIX

A. SUPPLEMENTAL INFORMATION FOR CHAPTER 2 159

A.1 Geometries of the Conformers of Chloroacetaldehyde 159

A.2 EOM-CCSD Calculations of Excited States of Chloroacetaldehyde Along the C−Cl Coordinate 161

A.3 Rough Division of the C−Cl Bond Fission P(E_T) to Assess the Cl($^2P_{1/2}$)/Cl($^2P_{3/2}$) Branching Ratio in the Fast Component and the Portion of the Slow Component that Can Produce $\tilde{B}$ State Vinoxy 163

A.4 Speed Dependence of the Anisotropy Parameter $\beta_2(v)$ for Cl($^2P_{1/2}$) and Cl($^2P_{3/2}$) 166

A.5 Gaussian Convolution of the Predicted P(v_{net}) for the Methyl Signal from the Dissoicative Ionization of Vinoxy to CH_3^+ + CO 168

B. SUPPLEMENTAL INFORMATION FOR CHAPTER 3...169

B.1 Correction to the Effective Barrier Height Caused by the Shift of the Minimum or Saddle Point to a Nearby Geometry Along the IRC 169

B.2 Description of the Permutation Vectors Used in the Rotational Model 171

B.3 Smoothed and Interpolated P(E_T)s for Cl($^2P_{3/2}$) and Cl($^2P_{1/2}$) Used in the Branching Calculations 176

B.4 Estimate of the P(E_T) for a Minor HCl Photoelimination Channel Derived from the Difference Between the Predicted and Experimental P(v_{net}) for Ketene.................................177

C. SUPPLEMENTAL INFORMATION FOR CHAPTER 4 179

C.1 Molecular Beam Speed Distribution 179

C.2 Alternative Fits to the *m/z* = 35 and *m/z* = 36 TOF Spectra Using the C−Cl Bond Fission P(E_T) Derived in the Velocity Map Imaging Study 180

C.3 Potential Energy Surface of HCCHO Radical..184

C.4 Calculation of Branching Ratios Between Primary Photodissociation Channels Using the C−Cl Bond Fission P(E_T) From the Velocity Map Imaging Study...185

C.5 Results of Our Branching Calculations Using the G4 Barrier Height for the H + Ketene Channel and Subsequent Fits to the *m/z* = 42 TOF Data 186

C.6 Cationic Potential Energy Surface of HCCHO Vinoxy 189

C.7 Comparison of the Contribution to the *m/z* = 15 TOF Data From Dissociative Ionization of Stable Vinoxy Radicals to CH3+ Using the Stable Portion of the C−Cl Bond Fission P(E_T) From Both Studies..190

C.8 Alternative Fits to the m/z = 42 TOF Data Using an Anisotropic Angular Distribution ..192

LIST OF FIGURES

2.1 Stationary points on the potential energy surface of the vinoxy radical 22

2.2 Cl ion images obtained on velocity map imaging apparatus and corresponding speed distributions..24

2.3 Photofragment recoil kinetic energy distribution for C−Cl bond fission events derived on velocity map imaging apparatus 27

2.4 Smoothed and interpolated photofragment recoil kinetic energy distribution for C−Cl bond fission events showing onsets of excited state vinoxy..28

2.5 Speed distribution for $m/z = 42$ (CH_2CO^+) derived on velocity map imaging apparatus 32

2.6 Experimentally determine portion of total primary C−Cl bond fission P(E_T) that produced vinoxy that dissociates to H + ketene products...34

2.7 Speed distribution for $m/z = 15$ (CH_3^+) derived on velocity map imaging apparatus.............37

3.1 Diagram of the energetics involved in a general unimolecular reaction 55

3.2 Example of the rotationally corrected IRCs for the unimolecular dissociation of the vinoxy radical...58

3.3 Geometries of the transition states used in our branching calculations..................................65

3.4 Plots of the E_T dependence on the effective barrier height calculated from the rotational model..68

3.5 E_T dependence of the branching fraction for the unimolecular dissociation channels of vinoxy from our branching calculations using the G4 barrier height for the H loss channel and the anti conformer of chloroacetaldehyde 70

3.6 E_T dependence of the branching fraction for the unimolecular dissociation channels of vinoxy from our branching calculations using the G4 barrier height for the H loss channel and the syn conformer of chloroacetaldehyde 71

3.7 Results of our branching calculations using the calculated G4 barrier height for the H loss channel 74

3.8 Results of our branching calculations using a barrier height of 44.6 kcal/mol for the H loss channel 77

3.9 E_T dependence of the branching fraction for the unimolecular dissociation channels of vinoxy from our branching calculations using a barrier height of 44.6 kcal/mol for the H loss channel and the anti conformer of chloroacetaldehyde 79

3.10 E_T dependence of the branching fraction for the unimolecular dissociation channels of vinoxy from our branching calculations using a barrier height of 44.6 kcal/mol for the H loss channel and the syn conformer of chloroacetaldehyde 80

4.1 Time-of-flight spectrum taken at $m/z = 38$ ($H^{37}Cl^+$) 101

4.2 Photofragment recoil kinetic energy distribution for HCl elimination events, including those that produce stable and unstable ketene 102

4.3 Time-of-flight spectrum taken at $m/z = 35$ (Cl^+) with a source angle of 20° 103

4.4 Photofragment recoil kinetic energy distribution for C−Cl bond fission events 104

4.5 Time-of-flight spectrum taken at $m/z = 35$ (Cl^+) with a source angle of 10° 105

4.6 Time-of-flight spectrum taken at $m/z = 36$ ($H^{35}Cl^+$) 107

4.7 Time-of-flight spectrum taken at $m/z = 49$ (CH_2Cl^+) 110

4.8 Photofragment recoil kinetic energy distribution for C−C bond fission events 111

4.9 Time-of-flight spectrum taken at $m/z = 29$ (HCO) 112

4.10 Results of our branching calculations using the C−Cl bond fission $P(E_T)$ derived on the scattering apparatus and a barrier height of 44.6 kcal/mol for the H loss channel 117

4.11 Time-of-flight spectrum taken at $m/z = 42$ (CH_2CO^+) 120

4.12 Product recoil kinetic energy distribution for the unimolecular dissociation of vibrationally hot vinoxy to H + ketene 121

4.13 Time-of-flight spectrum taken at $m/z = 15$ (CH_3^+) 124

4.14 Product recoil kinetic energy distribution for the dissociation of vinoxy to CH_3 + CO induced by absorption of another 157 nm 125

4.15 Product recoil kinetic energy distribution for the unimolecular dissociation of vibrationally hot vinoxy to CH_3 + CO 127

4.16 Time-of-flight spectrum taken at $m/z = 28$ (CO^+)....129

4.17 Time-of-flight spectrum taken at $m/z = 14$ (CH_2^+) 133

4.18 Product recoil kinetic energy distribution for the unimolecular dissociation of vibrationally hot ketene products from HCl photoelimination to CH_2 + CO....134

4.19 Product recoil kinetic energy distribution for the dissociation of CH_2Cl to CH_2 + Cl induced by absorption of another 157 photon 135

4.20 Product recoil kinetic energy distribution for the unimolecular dissociation of vibrationally hot HCO products from C−C bond fission to H + CO 137

4.21 Speed distribution for $m/z = 42$ (CH_2CO^+) from the velocity map imaging apparatus fit using the P(E_T,2°) and isotropic angular distribution derived from the scattering data 147

A.1 Geometries of the conformers of the chloroacetaldehyde 159

A.2 Singlet excited states of chloroacetaldehyde along the C−Cl bond coordinate....161

A.3 Triplet excited states of chloroacetaldehyde along the C−Cl bond coordinate....162

A.4 First option for division of the C−Cl bond fission P(E_T) into three components 164

A.5 Second option for division of the C−Cl bond fission P(E_T) into three components....165

A.6 Speed dependence of the anisotropy parameter $\beta_2(v)$ for Cl($^2P_{3/2}$)....166

A.6 Speed dependence of the anisotropy parameter $\beta_2(v)$ for Cl($^2P_{1/2}$)....167

A.8 Gaussian convolution of the predicted P(v_{net}) from CH_3^+ from dissociative ionization of vinoxy 168

B.1 Diagram of the energetics involved in a unimolecular reaction in which the minimum and saddle point geometries of the rotationally correct IRC differ from that of the IRC with $\vec{J}_{rot} = 0$ 170

B.2 Depiction of the effects of the permutation vector on the rotational energy of a stationary point 172

B.3 Permutations of the terminal H atoms used to get from the moiety of the 1a conformer of chloroacetaldehyde to the vinoxy radical and then to a given transition state............................173

B.4 Permutations of the terminal H atoms used to get from the moiety of the 1b conformer of chloroacetaldehyde to the vinoxy radical and then to a given transition state............................174

B.5 Permutations of the terminal H atoms used to get from the moiety of the 2 conformer of chloroacetaldehyde to the vinoxy radical and then to a given transition state............................175

B.6 Weighted photofragment translational energy distributions for photodissociation events producing vinoxy + Cl($^2P_{3/2}$) and vinoxy + Cl($^2P_{1/2}$) used in our branching calculations...........176

B.7 Determination of the speed distribution for ketene produced by HCl photoelimination from the experimental and predicted speed distribution at $m/z = 42$ (CH_2CO^+) 177

B.8 Predicted photofragment recoil translational energy distribution for HCl photoelimination events producing stable ketene 178

C.1 Molecular beam speed distribution 179

C.2 Alternative fits to the $m/z = 35$ (Cl^+) TOF spectrum taken at a source angle of 20° using the C−Cl bond fission P(E_T) derived on the velocity map imaging apparatus 180

C.3 Photofragment recoil kinetic energy distribution for C−Cl bond fission events in the dimer hydrate of chloroacetaldehyde 181

C.4 Alternative fits to the $m/z = 35$ (Cl^+) TOF spectrum taken at a source angle of 10° using the C−Cl bond fission P(E_T) derived on the velocity map imaging apparatus 182

C.5 Alternative fits to the $m/z = 36$ ($H^{35}Cl^+$) TOF spectrum using the C−Cl bond fission P(E_T) derived on the velocity map imaging apparatus as the contribution for bleed in from $m/z = 37$ (Cl^+)..183

C.6 Stationary points on the potential energy surface of the HCCHO radical 184

C.7 Results of our branching calculations using the C−Cl bond fission P(E_T) derived on the scattering apparatus and using the G4 barrier height for the H loss channel..............................186

C.8 Alternative fit to the $m/z = 42$ (CH_2CO^+) TOF spectrum using the results from our branching calculations with the G4 barrier height for the H loss channel and an isotropic angular distribution..187

C.9 Product recoil kinetic energy distribution for the unimolecular dissociation of vibrationally hot vinoxy to H + ketene using the results from our branching calculations with the G4 barrier height for the H loss channel and an isotropic angular distribution 188

C.10 Stationary points on the cationic surface of the vinoxy radical 189

C.11 Comparison of the portion of the C−Cl bond fission P(E_T) producing stable vinoxy predicted by our branching calculations in both the scattering lab study and the velocity map imaging study...190

C.12 Comparison of the contributions from dissociative ionization of stable vinoxy to CH_3^+ derived from the stable portion of the C−Cl bond fission P(E_T) determined in this study and in the velocity map imaging study 191

C.13 Alternative fit to the $m/z = 42$ (CH_2CO^+) TOF spectrum using the results from our branching calculations with a barrier height of 44.6 kcal/mol for the H loss channel and an anisotropic angular distribution 192

C.14 Product recoil kinetic energy distribution for the unimolecular dissociation of vibrationally hot vinoxy to H + ketene using the results from our branching calculations with a barrier height of 44.6 kcal/mol for the H loss channel and an anisotropic angular distribution 193

C.15 Alternative fit to the $m/z = 42$ (CH_2CO^+) TOF spectrum using the results from our branching calculations with the G4 barrier height for the H loss channel and an anisotropic angular distribution...194

C.16 Product recoil kinetic energy distribution for the unimolecular dissociation of vibrationally hot vinoxy to H + ketene using the results from our branching calculations with the G4 barrier height for the H loss channel and an anisotropic angular distribution.......................................195

LIST OF TABLES

2.1 Relative energy, percent composition in the molecular beam, C−Cl bond dissociation energy, and average internal energy of the conformers of chloroacetaldehyde at 25°C 21

A.1 Cartesian coordinates for the conformers of chloroacetaldehyde..160

A.2 Ratios of the signal intensity between the P(E_T)s for each spin-orbit state and Cl($^2P_{1/2}$)/Cl($^2P_{3/2}$) branching ratios for each component of the C−Cl bond fission P(E_T) following the first option...164

A.3 Ratios of the signal intensity between the P(E_T)s for each spin-orbit state and Cl($^2P_{1/2}$)/Cl($^2P_{3/2}$) branching ratios for each component of the C−Cl bond fission P(E_T) following the second option 165

ACKNOWLEDGMENTS

First and foremost, I would like to thank my advisor Professor Laurie Butler who let me join her group even though she said that she was not accepting any more students when I first asked. She has always been supportive and, not-to-mention, patient in spite of my overly complicated sentence wording and goof-ups in the first set of my rotational calculations. I also want to thank her for all of her help and support in finding teaching positions for me and for letting me TA for another whole year which I greatly enjoyed. I am forever grateful that I got to be one of the last members of the Butler Group at the University of Chicago and I wish her all of the best in the future. I would like to thank the other group members who I had the pleasure of working with in my time at the University of Chicago: Preston Scrape, Trevor Roberts, Matt Brynteson, Lei Wang, Chow-Shing (Martin) Lam, and Ryan Booth. I would like to extend a special thanks to Chow-Shing (Martin) who trained me on the imaging apparatus and was instrumental (pun intended) in setting up the 157 nm excimer in the imaging lab. I would like to extend another special thanks to Preston for putting up with me and my bad pun for four years. He has also always been there for support and for bouncing questions off of.

I would also like to my undergraduate advisor at Gettysburg College (and former Butler Group member), Professor Michael Wedlock, for being a mentor and getting me interested in physical chemistry. I extend a special thanks to the members of my entering class at the University of Chicago for helping me get through the first year. Of course, I would like to thank my family for their love and support over the years. They always believed in me and I know they are proud of me. Lastly, I would also like to thank the Chicago Gay Men’s Chorus for not only providing me with a break from science every now and again, but also for being like a family to me during my time in Chicago.

ABSTRACT

These studies combine velocity map imaging and crossed laser-molecular beam scattering to study the primary photodissociation channels of chloroacetaldehyde and the unimolecular dissociation channels of the vinoxy radical, CH_2CHO. In our velocity map imaging study, we investigate the unimolecular dissociation of vinoxy radicals prepared with high internal energy imparted by photodissociation of chloroacetaldehyde, CH_2ClCHO, at 157 nm. We measured the speed distribution of the recoiling chlorine atoms, Cl($^2P_{3/2}$) and Cl($^2P_{1/2}$), and derived from this the resulting distribution of kinetic energy imparted to the Cl + vinoxy fragments upon dissociation. The recoil translational energy distributions, P(E_T)s, derived for the C−Cl bond fission presented in this work suggest the vinoxy radicals are formed in the $\tilde{A}$ and $\tilde{B}$ state. We also took ion images at *m/z* = 15 and *m/z* = 42 to characterize the branching between the unimolecular dissociation channels of the vinoxy radical to H + ketene and methyl + CO products. In our scattering experiments, we further characterized the primary photodissociation pathways of chloroacetaldehyde and found evidence of HCl photoelimination and C−C bond fission in addition to C−Cl bond fission. This is the first direct evidence of the C-C bond fission channel in chloroacetaldehyde and we found that it significantly competes with the C−Cl bond fission channel. The branching between these channels suggests the presence of interesting excited state dynamics in chloroacetaldehyde following excitation. We also found evidence of secondary dissociation of the vibrationally excited products formed from these primary photodissociation channels. While we detected methyl and ketene products from the unimolecular dissociation of vinoxy in both studies, we were unable to determine the branching ratio between these product channels. However, we observed that the production of ketene is favored over the production of methyl for the high internal energy vinoxy radicals produced at

157 nm; prior work which formed lower internal energy vinoxy radicals found the CH_3 + CO product channel was dominant.

In addition to the experimental studies, we developed a model for the branching between unimolecular dissociation channels that takes into account how the change in rotational energy en route to the products affects the vibrational energy available to surmount the barriers to the channels. The model predicts the portion of the C-Cl bond fission $P(E_T)$ that produces dissociative vinoxy radicals, then predicts the branching ratio between the H + ketene and CH_3 + CO product channels at each E_T. The model uses RRKM rate constants at the correct sums and densities of vibrational states while accounting for angular momentum conservation. We find that the predicted portion of the $P(E_T)$ that produces vinoxy that dissociates to H + ketene products best fits the experimental portion of the ketene speed distribution from the velocity map imaging study (that we derive by taking advantage of conservation of momentum) if we use a barrier height for the H + ketene channel that is 4.0 ± 0.5 kcal/mol higher than the isomerization barrier en route to CH_3 + CO products. Using the G4 computed isomerization barrier of 40.6 kcal/mol, this gives an experimentally determined barrier to the H + ketene channel of 44.6 kcal/mol. From these calculations, we also predict the branching ratio between the H + ketene and methyl + CO channels to be approx. 2.1:1.

CHAPTER 1

INTRODUCTION

1.1 Motivation

Bimolecular reactions underlie virtually all of chemistry and, in particular, their study in the gas phase allows us to assess the detailed dynamics of such reactions. This provides critical benchmarks of electronic structure theories that can then be used in condensed phase systems. Reviews of gas phase studies of bimolecular reactions, both experimental[1,2] and theoretical,[3,4] describe the progress made in discovering the full quantum dynamics of such reactions. The applications of such results include reactions in combustion and atmospheric chemistry, but these reactions often involve radical intermediates that are difficult to probe experimentally. Such radical intermediates control the product branching in, for example, the reaction between radicals and unsaturated hydrocarbons.[5] An in-depth knowledge of the chemical transformations involved could help to characterize and even help to control combustion reactions, which is especially useful if the products are pollutants or other radicals which can react further. However, the dynamics of bimolecular reactions involving polyatomic molecules and radicals are often complex, consisting of possibly many product channels.[6,7] In order to understand the dynamics of such complex reactions, a methodology must be implemented to selectively probe the dynamics through each channel.

The most common methods for studying bimolecular reactions involving radicals are crossed molecular beam scattering[5-7], shock tube studies[8-10], and laser photolysis/laser-induced fluorescence.[11-13] Such methods start from the entrance channel of the reaction and track the presence of reactants, products, or radical intermediates as a function of time. Typically, the internal energies of the reactants are difficult to characterize in these methods, which makes it difficult to assess the total energy of the reactants. Even then, the energy available to the reactants allows the reaction to sample a large number of reaction pathways along the potential energy surface. This paints a broad picture of the reaction dynamics allowing for the identification of the primary product channels, measurements of branching fractions, and ideas regarding the reaction mechanisms. However, it is difficult to pick out details about a specific pathway with these methods. To get a more detailed view of the reaction dynamics, one must probe only one pathway at a time or focus in on a specific region of the potential energy surface.

In recent years, the Butler group has developed an experimental method for studying the dynamics of bimolecular reactions that proceed through radical intermediates.[14] This method involves initiating the reaction from a radical intermediate along the reaction pathway, which is done by photodissocating an appropriate halogenated precursor to produce the radical intermediate of interest. These radical intermediates are generated with a range of internal energies thereby allowing some of them to overcome energetic barriers along the potential energy surface (PES) and undergo unimolecular dissociation. By determining the internal energy distribution of the radicals and observing how their subsequent unimolecular dissociation product depends on internal energy, the dynamics of the radical intermediate can be investigated. The benefit of this method is that it allows for the isolation of particular pathways within the whole PES so that its specific attributes, like barrier heights and rate constants, can be investigated.

This dissertation details our work to further characterize the unimolecular dissociation pathways of a common radical intermediate in atmospheric and combustion chemistry, the vinoxy radical. We generated this radical via the photodissociation of chloroacetaldehyde at 157 nm and measured the kinetic energy imparted to the photofragments to derive the internal energy of the radicals. We also probed the products of the unimolecular dissociation of vinoxy radicals to determine a potential cause for the observed suppression of one set of products in prior experiments done at 193 nm.[15] While photodissociation of a halogenated precursor is an extremely useful method for generating radicals with well-characterized internal energy distributions, the energy partitioning between rotation and vibration in the radical is often non-statistical. This partitioning may have a substantial effect on the dynamics of the nascent radical. This dissertation also details our efforts to develop a model that uses Rice-Ramsperger-Kassel-Marcus (RRKM) calculations[16] to predict the product branching in the nascent radical from the distribution of kinetic energy imparted from photodissociation. Previously, our group developed a model to approximate the rotational energy imparted to a radical during carbon-halogen bond cleavage.[17,18] Our branching model builds upon the rotational model as it incorporates the rotational energy imparted to the radical and predicts the effect of the rotational energy on the subsequent dynamics of the radical.

1.2 Chemical System Studied

Vinoxy is one of the most frequently studied radicals due to its importance as an intermediate in combustion; it is a product in the reaction of O(^{3}P) with ethene[19] and propene,[20] and of OH with ethyne.[21] These reactions are commonly present in combustion of larger aliphatic[22] or aromatic[23] compounds. The vinoxy radical is also known to undergo a fast reaction with NO_2 in the atmosphere and could possibly contribute to the photochemical production of smog.[24] Another atmospheric process involving vinoxy is the ozonolysis of propene, which generates a Criegee intermediate, CH_3CHOO, that can subsequently decompose to vinoxy + OH.[25] Such reactions serve as a low-light source of OH in the atmosphere.

The unimolecular dissociation of the vinoxy radical has two major channels. One is the fission of the C−H bond to produce H + ketene (channel 1), and the other yields CH_3 + CO via an isomerization to the acetyl radical (channel 2).

$CH_2CHO \rightarrow H_2C{=}C{=}O$ (ketene) + H (1)

$CH_2CHO \rightarrow CH_3CO$ (acetyl radical) $\rightarrow CH_3 + CO$ (2)

In 2004, Miller et al.[15] published a study characterizing the internal energy of vinoxy radical following photodissociation of chloroacetaldehyde at 193 nm and detecting the products from unimolecular dissociation of the nascent radicals. The photodissociation generated radicals with a range of internal energies spanning the barriers to both channels; however, a negligible amount of ketene from secondary dissociation of vinoxy was detected. This result contrasts with prior experiments done by Osborn et al.[26] and Morton et al.[27] who characterized the branching between the two channels and found the H + ketene channel to dominate. Although these studies produced vinoxy radicals in electronically excited states, it has been shown that there is an effective mechanism for internal conversion of the vinoxy to its ground state potential energy surface and so the dynamics is expected to occur on this surface.

While the barrier height for the H + ketene channel is higher than that for the isomerization barrier to acetyl, the two barriers heights differ by approx. 2 kcal/mol and the H + ketene channel is expected to have a looser transition state. Based on RRKM calculations, the H + ketene channel should effectively compete with the CH_3 + CO channel at vibrational energies close to the barrier heights. Miller et al. concluded that the H + ketene channel was being suppressed and suggested this could be a result of nonadiabatic effects from a conical intersection en route to the H + ketene products. However, more recent computational studies of the conical intersections[28] and barrier heights[29] along the potential energy surface point to insignificant nonadiabatic effects. Therefore, there still exists a large discrepancy between the experimental branching and RRKM predictions that has not been explained.

Chapter 2 describes our first study done on the vinoxy radical, which we produced using the same method as Miller et al., but using 157 nm light instead for the photodissociation of chloroacetaldehyde. In this study, we characterized the internal energy distribution of the vinoxy radicals from photodissociation at 157 nm and detected methyl and ketene products from secondary dissociation. This shorter wavelength produces vinoxy radicals with a higher internal energy distribution allowing a larger fraction of the radicals to dissociate to H + ketene. Chapter 3 details our model for properly including angular momentum conservation when one uses statistical theories to predict the product branching in the unimolecular dissociation of radicals formed from photolytic carbon-halogen bond cleavage. To complement the analysis of the data described in Chapter 2, we applied the model to the vinoxy data and present those results in this chapter as well. Chapter 4 describes a further study done on the same system in which we characterized the other primary photodissociation channels of chloroacetaldehyde at 157 nm and calculated the branching ratios between the major primary and secondary dissociation channels. This study provides a more complete picture of the photodissociation processes of chloroacetaldehyde at 157 nm and the subsequent dynamics of the system.

1.3 Experimental Methods

The experimental studies presented herein were performed on two apparatuses: a velocity map imaging apparatus here at the University of Chicago and a crossed laser-molecular beam scattering apparatus at the National Synchrotron Radiation Research Center (NSRRC) in Hsinchu, Taiwan. Both machines are designed to produce radical intermediates of interest under collision-free conditions by photodissociation of a halogenated precursor and then measure the kinetic energy of the photofragments. Because the two fragments produced from carbon-halogen bond cleavage are momentum-matched under these conditions, the kinetic energy imparted during the photodissociation can be determined by detecting either fragment. Since the radical fragment can undergo subsequent dissociation, detecting the halogen atom allows us to characterize all of the C−Cl photofission events and thus is used to get a distribution of kinetic energies imparted during the photodissociation. From conservation of energy, the internal energy of the radical fragments can be determined from the kinetic energy distribution using

$$h\nu + E_{\mathrm{int}}(\mathrm{precursor}) = D_o(\mathrm{C-X}) + E_{\mathrm{T}} + E_{\mathrm{int}}(\mathrm{X}) + E_{\mathrm{int}}(\mathrm{radical}), \quad (3)$$

where $h\nu$ is the energy of the incident photon, E_{int}(precursor) is the internal energy of the halogenated precursor, D_{o}(C−X) is the carbon-halogen bond dissociation energy, E_T is the center-of-mass total recoil kinetic energy, E_{int}(X) is the internal energy of the halogen atom co-fragment, and E_{int}(radical) is the internal energy of the radical co-fragment. In general, the photodissociation imparts a large range of kinetic energies which gives the radicals a large range of internal energies. A portion of the radicals will then have enough energy to overcome the energetic barriers along the potential energy surface and undergo secondary dissociation.

1.3.1 Velocity Map Imaging

The velocity map imaging apparatus at the University of Chicago is based on the design of Eppink and Parker.[30-31] A molecular beam is prepared by bubbling a light carrier gas through a liquid sample of the halogenated precursor. The beam is then supersonically expanded through a pulsed nozzle into a vacuum chamber and passes through a skimmer before entering the main chamber. The supersonic expansion of the molecular beam cools the rotational degrees of freedom of the precursor, but not the vibrational degrees of freedom.[32] Once in the interaction region, the precursor is then photodissociated using an excimer laser beam which travels perpendicular to the molecular beam. Following a short delay (~40 ns), the recoiling fragments are photoionized by a photoionization beam in the interaction region. The ionized photofragments are then accelerated down a time-of-flight (TOF) tube towards the detector by an electrostatic ion lens assembly. The lens assembly consists of a repeller and extractor plate, maintained at a voltage ratio of 1.4:1, and also a grounded plate. The benefit of the assembly is that it maps all ions with the same initial velocity vector to the same location on the detector.

The detector consists of a Chevron microchannel plate (MCP) and a P-20 phosphor screen. Ions colliding with the MCP produce an electron cascade, which induces phosphorescence on the phosphor screen in the position the ion struck the MCP. Ions with different mass-to-charge ratios will have different arrival times at the detector. To detect ions with a particular mass-to-charge ratio, the front plate of the MCP is held at a large positive voltage and then pulsed at -750 V for 80 ns at the arrival time for the mass-to-charge ratio of interest. The illuminated areas are imaged and recorded by a cooled charge-coupled device (CCD) camera. The images are then analyzed using the ion counting method of Houston[33] and an inverse Abel transformation[34] is used to reconstruct the three-dimensional ion image. The image is integrated over all solid angles to yield a speed distribution of fragments.

The photolysis beam is vertically polarized, which provides the recoiling fragments with a cylindrical symmetry allowing us to utilize the inverse Abel transformation to reproduce the ion sphere and simultaneously measure the angular distribution of the photofragments. Characterizing the angular distribution of the recoiling fragments is useful because it gives us information about the precursor's transition moment dipole.[35] The angular distribution at each speed is fit to the function

$$I(\theta) \propto 1 + \beta_2 P_2(cos\theta) + \beta_4 P_4(cos\theta) \qquad (4)$$

where θ is the angle between the recoil velocity vector and the electric vector of the photolysis laser, P_n is the nth order Legendre polynomial, and β_2 is the anisotropy parameter, hereafter denoted β.

This apparatus allows for the use of two different ionization schemes: single photon ionization, typically at 10.5 eV,[36] or resonance enhanced multiphoton ionization (REMPI). Single photon ionization is not state-selective and can be used to detect the radical cofragment or products from secondary dissociation, while REMPI is state-selective and can be used to detect halogen atoms. Considering equation 3, state-selective detection of the ground and excited spin-orbit states of the halogen atoms is important as a radical produced from the photodissociation of a precursor that results in excited spin-orbit halogen will have less internal energy. However, the effect that this will have on the dynamics depends on the magnitude of the spin-orbit splitting in the halogen being studied. In either case, it is important that the spin-orbit states can be detected separately.

1.3.2 Crossed Laser-Molecular Beam Scattering

The crossed laser-molecular beam apparatus at the NSRRC in Taiwan is based on the design of Lee[37] and utilizes tunable VUV photoionization obtained by tuning the U9 undulator gap of a synchrotron. Much like in the velocity map imaging apparatus, a liquid sample of the precursor is seeded in light carrier gas and the gaseous mixture is supersonically expanded through a pulsed valve into a vacuum chamber. The molecular beam may be rotated off of the detector axis. After passing through two skimmers, the molecular beam enters the interaction region where it intersects an excimer laser beam oriented perpendicular to the plane created by the molecular beam and the detector axis. Fragments scatter in all directions with a range of recoil velocities but only those with a net velocity vector pointing into the 1.5° acceptance angle of the detector enter the ionizer region. The fragments are photoionized using synchrotron radiation.

The ions are then accelerated toward the detector by ion lenses and filtered by mass using a quadrupole. The ions with the selected mass are strike a Daly detector[38] maintained at −30 kV and a multi-channel scaler (MCS) records the time-of-flight (TOF) spectrum which is the ion count as a function of arrival time. The arrival time represents the total flight time, which is the sum of the neutral flight time of the fragment from the interaction region to the ionizer and the ion flight time of the nascent ions to detector. The ion flight time is proportional to the product of the square root of the mass-to-charge ratio of the ionized fragment and the ion flight constant, which depends on the apparatus. The neutral flight time is calculated by subtracting the total flight time by the ion flight time. The velocity of the neutral fragments can be calculated using the neutral flight time and the distance between the interaction region and the ionizer. However, this velocity is the vector sum of the molecular beam velocity and the recoil velocity imparted during the photodissociation. The molecular beam velocity is measured frequently using photodepletion and then subtracting this velocity from the velocity of the neutral fragments yields information about the photodissociation.

The TOF spectra are analyzed using a forward-convolution method. This method takes an initial guess for the recoil translational energy distribution, P(E_T), and convolves it over all velocities of the molecular beam, kinematic scattering factors, acceptance angle of the detector, and transit times through the ionizer to yield a theoretical TOF spectra. We fit these theoretical TOF spectra to the experimental data by iteratively adjusting the P(E_T) until the two match.

1.3.3 Comparison

Overall, both apparatuses can measure the speed and angular distribution of photofragments produced from photodissociation of a halogenated precursor. However, velocity map imaging allows us to measure both distributions simultaneously whereas the crossed laser-molecular beam apparatus requires a series of measurements to obtain an angular distribution. Both apparatuses also use “soft ionization” techniques, which minimize contributions from dissociative ionization in which a neutral fragment is ionized and then dissociates along the cationic potential energy surface. The tunable VUV photoionization on the crossed laser-molecular beam apparatus in Taiwan allows us to minimize the signal from dissociative ionization even more as we can tune the photoionization energy to just above the threshold for the fragment we wish to detect. While the velocity map imaging experiments in this thesis use only a photoionization energy of 10.5 eV to detect most species, they do use state-selective detection of halogen atoms using REMPI.

While there are differences between the two apparatuses, they are complimentary to one another For instance, it is hard to discern contributions from dissociative ionization in the velocity map imaging apparatus because the recoil imparted from dissociative ionization of the neutral parent to the cation daughter smears out the velocity distribution coming from the neutral fragment. However, the TOF spectrum of the cation daughter from dissociative ionization in a scattering apparatus is simply the TOF spectrum of the neutral parent shifted in time due to a different ion flight time; it is not broadened by the velocity imparted during dissociative ionization. This allows one to detect neutral recoil velocities with the smearing from dissociative ionization on the crossed laser-molecular beam apparatus. Using the velocity map imaging apparatus and crossed-molecular beam apparatus together can thus provide a great deal of information about the chemical dynamics of photolytically-produced radical intermediates.

1.4 References

(1) Alagia, M.; Balucani, N.; Casavecchia, P.; Stranges, D.; Volpi, G. G. *J. Chem. Soc. Faraday Trans.* **1995**, *91*, 575-96.

(2) Yang, X. *Annu. Rev. Phys. Chem.* **2007**, *.58*, 433-59.

(3) Bowman, J. M.; Schatz, G. C.; *Annu. Rev. Phys. Chem.* **1995**, *46*, 169-95.

(4) Althorpe, S. C.; Clary, D. C. *Annu. Rev. Phys. Chem.* **2003**, *54*, 493-529.

(5) Balucani, N.; Leonori, F.; Casavecchia, P. *Energy* **2012**, *43*, 47-54.

(6) Albert, D. R.; Davis, H. F. *Phys. Chem. Chem. Phys*. **2013**, *15*, 14566-80.

(7) Liu, K. *J. Chem. Phys.* **2006**, *125*, 132307.

(8) Bott, J. F.; Cohen, N. *Int. J. Chem. Kinet.* **1991**, *23*, 1075-94.

(9) Bradley, J. N.; Capey, W. D.; Fair, R. W.; Pritchard, D. K. *Int J. Chem. Kinet.* **1976**, *8*, 549-61.

(10) Chuong, B.; Stevens, P. S. *J. Phys. Chem. A* **200**, *204*, 5230-7.

(11) Tully, F. P *Chem. Phys. Lett.* **1983**, *96*, 148-53.

(12) Tully, F. P *Chem. Phys. Lett.* **1988**, *143*, 510-4.

(13) Zellner, R.; Lorenz, K. *J. Phys. Chem.* **1984**, *88*, 984-9.

(14) Mueller, J. A.; Miller, J. L.; Butler, L. J.; Qi, F.; Sorkhabi, O.; Suits, A. G. *J. Phys. Chem.* **2000**, *104*, 11261-4

(15) Miller, J. L.; McCunn, L. R.; Krisch, M. J.; Butler, L. J. *J. Chem. Phys.* **2004**, *121*, 1830-38.

(16) Klippenstein, S. J. *Comprehensive Chemical Kinetics.* **2003**, *39*, 55-103.

(17) McKown, B. G.; Ceriotti, M.; Womack, C. C.; Kamarchik, E.; Butler, L. J.; Bowman, J. M. *J. Phys. Chem. A* **2013**, *117*, 10951-63.

(18) Brynteson, M. D.; Womack, C. C.; Booth, R. S.; Lee, S.–H.; Lin, J. J.; Butler, L. J. *J. Phys. Chem. A* **2014**, *118*, 3211-29.

(19) Balucani, N.; Leonori, F.; Casavecchia, P.; Fu, B.; Bowman, J. M. *J. Phys. Chem. A.* **2015**, *119*, 12498-12511.

(20) Leonori, F.; Balucani, N; Nevrly, V.; Bergeat, A.; Falcinelli, S.; Vanuzzo, G.; Casavecchia, P. *J. Phys. Chem. C* **2015**, *119*, 14632-52.

(21) McKee, K. W.; Blitz, M. A.; Cleary, P. A.; Glowacki, D. R.; Pilling, M. J.; Seakins, P. W., Wang, L. *J. Phys. Chem. A* **2007**, *111*, 4043-55.

(22) Westbrook, C. K.; Dryer, F. L. *Symp. Int. Combust. Proc.* **1981**, *18*, 749-67.

(23) Brezinsky, K. *Prog. Energy Combust. Sci.* **1986**, *12*, 1-24.

(24) Bernhard, K. I.; Santiago, A.; He, H.; Asmar, F.; Weiner, B. R. *Chem. Phys. Lett.* **1991**, *178*, 150-6.

(25) Liu, F.; Beames, J. M.; Petit, A. S.; McCoy, A. B.; Lester, M. I. *Science* **2014**, *345*, 1596-98.

(26) Osborn, D. L.; Choi, H.; Mordaunt, D. H.; Bise, R. T.; Neumark, D. M.; Rohlfing, C. *J. Chem. Phys.* **1997**, *106*, 3049-66.

(27) Morton, M. L.; Szpunar, D. E.; Butler, L. J. *J. Chem. Phys.* **2001**, *115*, 204-16

(28) Piechowska-Strumik, K.; Bacchus-Montabonel, M.-C.; Tergiman, Y. S.; Sienkiewicz, J. E. *Chem. Phys. Lett.* **2006**, *425*, 16-21.

(29) Bennett, D. I. G.; Butler, L. J.; Werner, H.-J. *J. Chem. Phys.* **2007**, *127*, 094309.

(30) Eppink, A. T. J. B.; Parker, D. H.; *Rev. Sci. Instrum*. **1997**, *68*, 3477-84.

(31) Parker, D. H.; Eppink, A. T. J. B. *J. Chem. Phys.* **1997**, *107*, 2357-62.

(32) Levy, D. H.; *Ann. Rev. Phys. Chem*. **1980**, *31*, 197-225.

(33) Chang, B.-Y.; Hoetzlein, R. C.; Mueller, J. A.; Geiser, J. D.; Houston, P. L.; *Rev. Sci. Instrum*. (1998), *69*, 1665-70.

(34) Dribinski, A.; Ossadtchi, V. A.; Mandelshtam; Reisler, H. *Rev. Sci. Instrum*. **2002**, *73*, 2634-42.

(35) Zare, R. N. *Mol. Photochem*. **1972**, *4*,1-37.

(36) Ratliff, B. J.; Tang, X.; Butler, L. J.; Szpunar, D. E.; Lau, K. *J. Chem. Phys.* **2009**, *131*, 044304.

(37) Lee, Y. T.; McDonald, J. D.; LeBreton, P. R., Herschbach, D. R. *Rev. Sci. Instrum.* **1969**, *40*, 1402-8.

(38) Daly, N. R.; *Rev. Sci. Instrum.* **1960**, *31*, 264-7.

CHAPTER 2

IMAGING LAB STUDY OF THE PHOTODISSOCIATION OF CHLOROACETALDEHYDE AT 157 nm: DETECTION OF UNIMOLECULAR DISSOCIATION PRODUCTS OF VINOXY

The data presented in this chapter was previously published in the Journal of Physical Chemistry A. The following content was reprinted with permission from [C. - S. Lam., J. D. Adams, and L. J. Butler, "The Onset of H + Ketene Products from Vinoxy Radicals Prepared by Photodissociation of Chloroacetaldehyde at 157 nm" J. Chem. Phys. A, DOI 10.1021/acs.jpca.6b01256 (2016)], Copyright 2016, American Chemical Society.

2.1 Introduction

Vinoxy is one of the most frequently studied radicals and has been shown to play a role in a number of atmospheric processes. First and foremost, it is a common intermediate in the combustion of larger aliphatic[1] or aromatic[2] compounds and is produced from the reaction of O(^{3}P) with ethene[3] and propene,[4] and OH with ethyne.[5] The vinoxy radical is also known to react rapidly with NO_2, which can contribute to the production of smog.[6] The ozonolysis of propene can also produce vinoxy via the generation and decomposition of a Criegee intermediate, CH_3CHOO.[7] Therefore, the unimolecular dissociation of the vinoxy radical has been of interest for decades since it provides information on the lifetime of the radical.

There are two viable dissociation pathways of vinoxy: the fission of the C−H bond to produce H + ketene (channel 1), and isomerization to the acetyl radical followed by C-C bond fission to produce CH_3 + CO (channel 2).

$CH_2CHO \rightarrow H_2C{=}C{=}O$ (ketene) + H (1)

$CH_2CHO \rightarrow CH_3CO$ (acetyl radical) $\rightarrow CH_3 + CO$ (2)

To study the branching, Osborn et al.[8] prepared the radical primarily in the $\tilde{B}$ state (3.569 eV above ground state) by photodetachment of the vinoxide ion, CH_2CHO^-, generated by a discharge source. The branching between the two channels was found to be 4:1, in agreement with their RRKM predictions assuming internal conversion to the ground electronic state. Previous work in our group[9] on the photodissociation of methyl vinyl ether generated vinoxy radicals primarily in the $\tilde{A}$ state (0.99 eV above ground state). That study found that the branching to the CH_3 + CO products was not discernible underneath the other source of methyl radicals from the photodissociation of methyl vinyl ether. In a following study[10], we prepared the vinoxy radical in the ground electronic state, $\tilde{X}$, by photodissociation of the precursor chloroacetaldehyde at 193 nm. The nascent vinoxy was produced with a distribution of internal energies peaked at 40 kcal/mol, which is much lower than that in the work of Osborn et al. The results showed negligible (< 2%) dissociation to H + ketene in contrast to the RRKM predicted branching based on the barrier heights calculated at the G3//6-31G+(d)/B3LYP level of theory. In that paper, we suggested that nonadiabatic recrossing might be inhibiting the H + ketene product channel.

To understand the experimental results, several groups pursued theoretical calculations. Early studies focused on the mechanism for internal conversion from $\tilde{B} \rightarrow \tilde{A} \rightarrow \tilde{X}$. Matsika and Yarkony[11] applied a multi-reference configuration interaction (MRCI) method to locate accessible avoided crossings and conical intersections. They suggested that a radiationless transition between the $\tilde{B}$ and $\tilde{A}$ states occurs via a local minimum resulting from an avoided crossing and then conversion from the $\tilde{A}$ state to the ground state occurs via a conical intersection. This mechanism provides computational support for the observations of Osborn et al., elucidating a mechanism that converts radicals in the $\tilde{B}$ state to the ground state. Following this conversion, the dissociation dynamics is then governed by the ground state potential energy surface (PES). Their work also provides a mechanism for the formation of products in the photodissociation of methyl vinyl ether as the radicals produced in the $\tilde{A}$ state can convert to the ground state via the conical intersection and then evolve further on the ground state PES. Since the lowest energy conical intersection is approx. 3000 cm^{-1} above the $\tilde{A}$ state minimum, the internal energy imparted to the radical should be enough to access this point. The evolution of the excited states is further supported by the quantum dynamic study done by Piechowska-Strumik et al.; however, they could not conclude that all relaxation from the $\tilde{B}$ state to the $\tilde{A}$ state happens via the avoided crossing.[12]

There is not yet an adequate theoretical explanation for the results of the study on the photodissociation of chloroacetaldehyde at 193 nm. In particular, that study found that the H + ketene product channel of the vinoxy radical is so suppressed that a negligible amount of ketene was formed, even though the calculated barriers to both channels do not differ by more than 2 kcal/mol. Later Young and Yarkony[13] investigated the topography of the conical intersections in proximity to the transition states (TSs) en route to the H + ketene products. They concluded that the conical intersection would not facilitate any nonadiabatic recrossing to suppress the H + ketene channel. Effort has also been put into refining the quality of the calculated barriers,[14] however modelling the branching with these refined barriers still could not accurately explain the experimental result. So, a large discrepancy with the experimentally observed branching still remains.

In order to resolve this, we were motivated to generate vinoxy radicals by a method that would allow us to characterize the portioning of the internal energy of the nascent radical between rotation and vibration. To do this, we photodissociated chloroacetaldehyde as in the previous study, but used 157 nm light instead. After absorbing a 157 nm photon, the molecule is promoted to an excited state that is nearly directly repulsive in the C−Cl bond. Once that bond breaks, the vinoxy radical is produced in a collision-free environment with a range of rotational and vibrational energies. Since we expect the photodissociation of chloroacetaldehyde to evolve on a repulsive PES, the angular momentum of the nascent vinoxy radicals should be well-predicted by our rotational model described in McKown et al.[15] and Brynteson et al.[16] We can thus characterize the rotational energy imparted to the radical at equilibrium geometry and, using conservation of angular momentum, to any geometry along the reaction coordinate. The higher internal energy of the radicals in this study should give more unstable vinoxy that can undergo subsequent unimolecular dissociation to form H + ketene.

2.2 Experimental Details

2.2.1 Velocity Map Imaging

The 2-D velocity map imaging experimental setup used in this work has been described elsewhere,[17,18] so we provide a summary here. A 3% beam of chloroacetaldehyde (50% solution in water from Sigma-Aldrich, without further purification) was created by bubbling helium gas through the liquid sample to a total backing pressure of ~600 torr. The beam was supersonically expanded at room temperature through a General Valve Iota One pulsed valve with an orifice diameter of 0.8 mm. After passing through a skimmer, the molecules were photodissociated using vertically polarized 157 nm light from a GAM (EX350F) F_2 excimer laser. Since atmospheric O_2 strongly absorbs 157 nm light, the excimer was fitted with a line leading up to the main vacuum chamber that was constantly purged with N_2 gas. Along this line, the beam passed through a CaF_2 thin film polarizer to obtain the desired polarization and a MgF_2 lens that focused it to approximately a 2 mm × 1 mm spot in the interaction region. The MgF_2 lens also served as the barrier between the purging line and the main vacuum chamber. Typical pulse energies were around 0.6 mJ/pulse. Approximately 40 ns after photodissociation, the products were ionized using one of two schemes discussed below.

For the detection of the Cl atom, we used 2 + 1 resonance enhanced multiphoton ionization (REMPI) to selectively ionize the $Cl(^2P_{3/2})$ and $Cl(^2P_{1/2})$ photofragments with 235.34 nm ($4p\ ^2D_{3/2} \leftarrow 3p\ ^2P_{3/2}$) and 235.20 nm ($4p\ ^2P_{1/2} \leftarrow 3p\ ^2P_{1/2}$) photons, respectively. These wavelengths were generated by tripling the output of a Lambda Physik Fl 3002 dye laser (LDS 698 dye) that was pumped by a pulsed Continuum Powerlite Precision 9020 Nd:YAG laser. The ~706 nm dye output passed through a potassium dihydrogen phosphate (KDP) crystal, which doubled the frequency, and then the second harmonic was mixed with the fundamental in a β-barium borate (BBO) crystal to produce vertically polarized photons at the REMPI wavelength. This light was separated from the other frequencies using a Pellin-Broca prism and was focused using a 25.4 cm focusing lens into the chamber, where it crossed the molecular beam at a right angle. The accumulated signal was obtained by then scanning over a Doppler profile of +/- 0.008 nm from the line center.

For the detection of ketene and methyl radical products, we used 10.5 eV photoionization generated by tripling the 355 nm output of a pulsed Continuum Surelite I-20 Nd:YAG laser. The 355 nm beam passed through a beam expander (focal length = -150 mm and focal length = 300 mm at 588 nm) and then through two lenses that focused the light into a 21 cm low-pressure gas cell filled with 24 torr of high purity Xe (>99.995%). The gas cell was mounted onto the main vacuum chamber with a MgF_2 lens (focal length = 120.3 mm at 193 nm) that served as the barrier between the cell and the chamber. The lens recollimated the 355 nm light while focusing the 118 nm light.

Following photodissociation and photoionization, the electrostatic lens optics with repeller and extractor voltages in a 1.404:1 ratio (3932 V and 2800 V, respectively) accelerated the spherically expanding ions down a ~557 mm grounded time-of-flight tube toward the detector. The Burle3040FM detector is comprised of a position-sensitive Chevron microchannel plate (MCP) assembly coupled to a P-20 phosphor screen. The front plate of the MCP was pulsed at -750 V for 80 ns to selectively detect ions based on their arrival time. The voltage of the phosphor screen was maintained at 3.3 kV above the potential at the rear plate of the MCP. Ions colliding with the MCP produce an electron cascade, which induces phosphorescence on the screen in the position the ion struck. A cooled charged-coupled device (CCD) camera (La Vision Imager 3QE) with a standard 35 mm lens was used to take images. The images were then processed using Houston's ion counting[19] method; speed distributions, along with angular distributions, were obtained using the BASEX code of Dribinski et al.[20] The timing for the opening of the pulsed valve, firing the lasers, pulsing the MCP, and capturing the ion images was controlled by a digital delay generator (Stanford Research DG535) with a repetition rate of 20 Hz.

2.2.2 Computational Methods

We calculated minima and transition states relevant to the dissociation of ground state vinoxy radicals, updating our previous calculations at the G3//B3LYP level of theory with the more recent G4 protocol. Optimized molecular geometries and vibrational frequencies were found using the B3LYP density functional and the 6-311++G(3df,2p) basis set. The geometries converged to a root-mean-square (rms) force below 1×10^{-5} and an rms displacement below 4×10^{-5}, where both values are in atomic units. Wave functions for doublet species were spin-unrestricted, and wave functions for singlet species were spin-restricted. The computation of the zero-point vibrational energies used the B3LYP/6-311++G(3df,2p) vibrational frequencies scaled by 0.9854[21] as the G4 method required.[22] The G4 method is the latest in the series of Gn theories, which are composite methods based on a sequence of single-point energy calculations. To confirm the calculated transition states lead to the desired products, we also ran an intrinsic reaction coordinate (IRC) calculation at the B3LYP/6-311++G(3df,2p) level. The calculations use the GAUSSIAN09 program, version A.02.[23]

2.3 Results

In the following sections, we present the velocity map imaging data for the photodissociation of chloroacetaldehyde and the subsequent unimoleuclar dissociation of the vinoxy radical. We begin with a brief review of the PES for the unimolecular dissociation channels of the vinoxy radical. Section 2.3.2 details the center-of-mass translational energy distributions obtained from the detection of the chlorine atom co-fragment of vinoxy from the primary photodissociation. Section 2.3.3 describes the detection of ketene and identifies its source by examining its kinetic energy distribution. In section 2.3.4, we present the data recorded at m/z =15; the contributions to this signal include the dissociation of vinoxy to CH_3 + CO and the dissociative ionization of stable vinoxy radicals to CH_3^+ + CO.

2.3.1 Electronic Structure Calculations

To characterize the rotational and vibrational energy distribution of the vinoxy radicals formed by photolysis, the molecular conformers of the precursor chloroacetdaldehyde have to be considered. Based on our calculations, there are three conformers of chloroacetdaldehyde: one syn conformer and two anti conformers, which differ in their respective Cl-C-C-O dihedral angles (see Appendix A). The zero-point level of the syn conformer in the gas phase is slightly higher than the anti conformers due to the unfavorable interaction between the Cl atom and the O atom. Their single-point energies were calculated at 0K and 298K, the nozzle temperature. Accounting for the degeneracy of the anti structures, the relative populations are summarized in Table 2.1.

Table 2.1: Relative Energy, Percent Composition in the Molecular Beam, C−Cl Bond Dissociation Energy, and Average Internal Energy of the Conformers of Chloroacetaldehyde at 25°C

Conformer	Relative Energy[a] (kcal/mol)	Percentage in Molecular Beam	D_o(C−Cl)[b] (kcal/mol)	Average Internal Energy (kcal/mol)
Anti	0	92.68%	73.4	1.20
Syn	1.09	7.32%	72.3	1.08

[a] The relative energies are with respect to the anti conformer.

[b] The bond dissociation is obtained by subtracting the sum of the G4 energy of the radical and Cl($^2P_{3/2}$) from the G4 energy of each conformer.

The PES for the unimolecular dissociation of vinoxy radical has been revisited at the G4//B3LYP/6-311++G(3df,2p) level of theory. Based on the optimized structures, we report the recalculated energy barriers along each secondary dissociation pathway. Unsurprisingly, the difference between these results and our previous G3//B3LYP is very small. The computational studies by Bennett et al. and the Yarkony group have shown that the barrier heights of channel (1) and (2) should be within 2-3 kcal/mol. Nevertheless, for clarity we depict all the stationary points and transition states identified and their zero point-corrected G4 energies relative to ground state vinoxy in Figure 2.1.

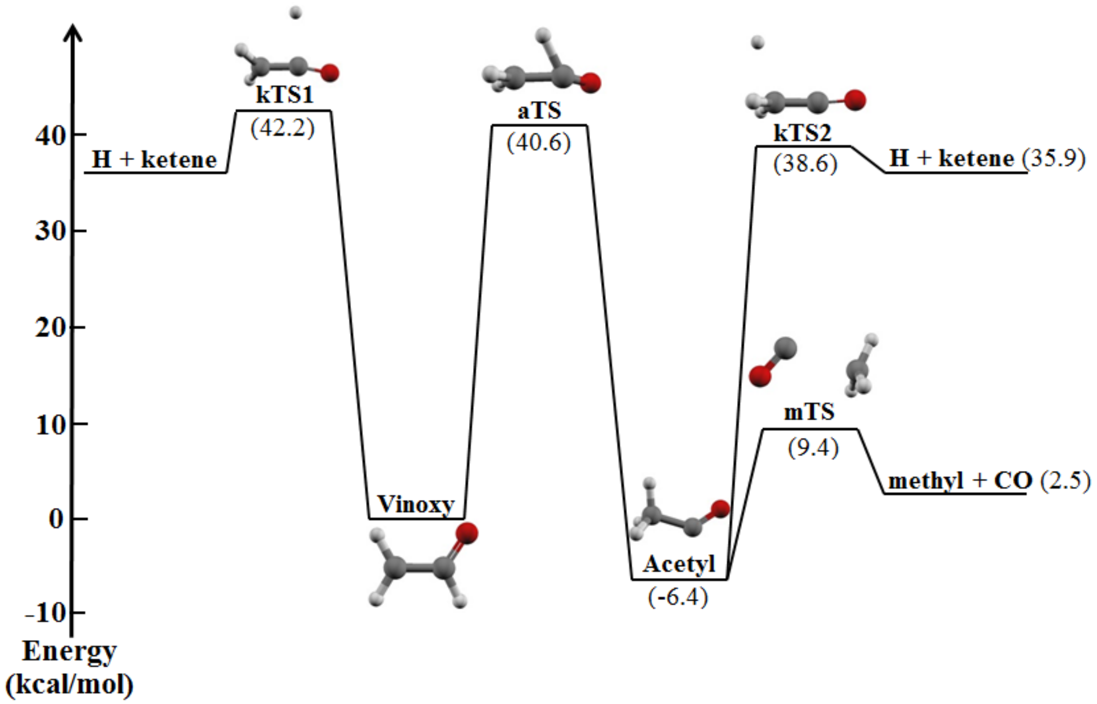

Figure 2.1: Selected minima and transition states on the potential energy surface for unimolecular dissociation of the vinoxy radical. The energies of the stationary points relative to the zero-point level of ground state vinoxy are given in parentheses. They are calculated at the G4//B3LYP/6-311G++(3df,2p) level of theory and include harmonic zero-point energy corrections.

2.3.2 Primary C−Cl Bond Photofission Channel

The goal of the study is to prepare vinoxy radicals with a vibrational energy distribution spanning the barriers en route to both dissociation channels. Our velocity map imaging apparatus enables us to characterize the speed and angular distributions of the fragments resulting from photodissociation of the halogenated precursor. Here, we report the measured speed of the recoiling chlorine atoms and derive from this the resulting distribution of kinetic energy imparted to the Cl + vinoxy fragments upon dissociation. The recoiling chlorine atoms from the photolytic cleavage of C−Cl bond in the precursor may be formed in either of two spin−orbit states, $^2P_{3/2}$ or $^2P_{1/2}$. Using resonance-enhanced multiphoton ionization (REMPI), we selectively ionize and detect the recoiling chlorine atoms in their respective spin−orbit states. This C−Cl photofission translational energy distribution, $P(E_T)$, is then used to determine the internal energy distribution of the nascent vinoxy radicals.

Figures 2.2a and 2.2b show the ion images of $Cl(^2P_{1/2})$ and $Cl(^2P_{3/2})$, respectively. These images are background subtracted and thus show the signal from the photodissociation at 157 nm and REMPI photoionization. The arrow indicates the direction of the polarization of the photolysis laser. Comparatively, the image of $Cl(^2P_{1/2})$ has more counts at the outer rim. Nevertheless, both images do not give a sharp ring structure at their edges as typically observed when detecting the halogen atoms from photolysis of alkyl halides. Neither of the images display a distinctive anisotropy. Though both images are two-dimensional, by using the inverse Abel transformation in the BASEX program, they are readily reconstructed as three-dimensional scattering distributions. By integrating all solid angles at each speed, the speed distribution $P(v)$ for Cl atoms produced in each spin−orbit state can be obtained; they are shown in Figure 2.2c ($Cl(^2P_{1/2})$ in red and $Cl(^2P_{3/2})$ in blue).

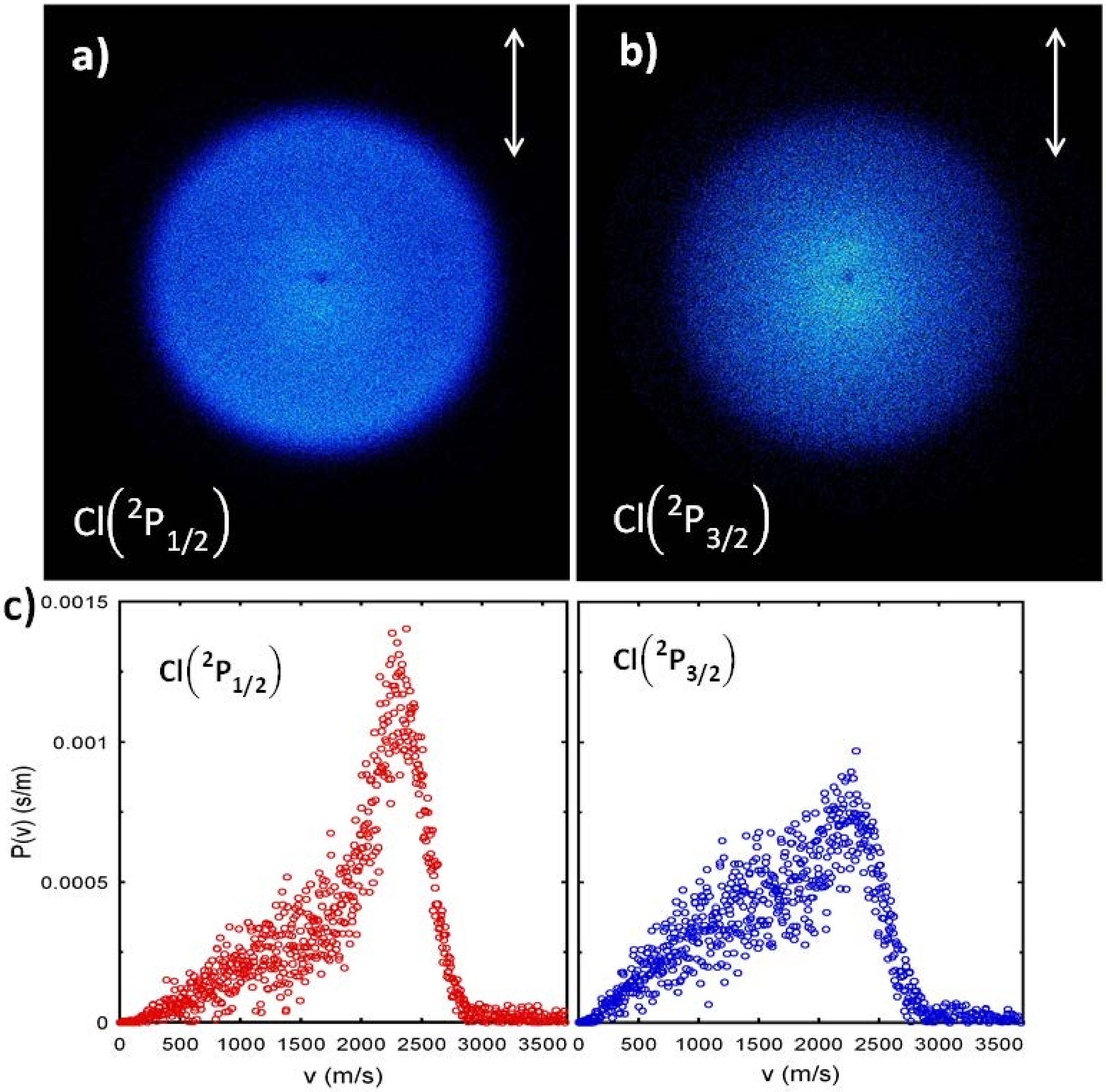

Figure 2.2. Background-subtracted images for (a) Cl($^2P_{1/2}$) and (b) Cl($^2P_{3/2}$). The dimensions of the images shown are 928 pixels × 1040 pixels. The direction of photodissociation laser polarization is shown by the arrow in the upper right of each image. The lower frame (c) shows the corresponding speed distributions for Cl($^2P_{1/2}$) (in red) and Cl($^2P_{3/2}$) (in blue) normalized to unit area.

The speed-dependent anisotropy parameter $\beta(v)$ is shown in Appendix A; it is obtained by fitting the angular distributions to $I(\theta) \propto 1 + \beta_2 P_2(\cos\theta) + \beta_4 P_4(\cos\theta)$, where P_n is the nth order Legendre polynomial and θ is the angle between the recoil velocity vector and the electric vector of the photolysis laser. The β_4 parameter is found to be negligible for Cl atoms in each spin−orbit state; we therefore approximate the angular distribution to be $I(\theta) \propto 1 + \beta P_2(\cos\theta)$, where the anisotropy parameter, β, ranges from −1 to 2 (with $\beta = -1$ corresponding to a perpendicular transition and $\beta = 2$ corresponding to a parallel transition). The resulting values of β show that both images are not entirely isotropic. For both spin−orbit states of Cl, the value of β gradually increases from zero to ~0.5 as the recoil speed ranges from 2000 m/s to 2500 m/s.

Relative translational energy distributions, P(E_T), for Cl($^2P_{3/2}$) + vinoxy and Cl($^2P_{1/2}$) + vinoxy were calculated from the measured Cl speed distributions using momentum conservation and applying Jacobian corrections. The C−Cl fission P(E_T)s to form Cl($^2P_{3/2}$) and Cl($^2P_{1/2}$) are weighted by the spin-orbit branching ratio and summed together to yield the total P(E_T) for all dissociation events. We determine the spin-orbit branching ratio using the expression shown in Equation (3) below.

$$\frac{N[\mathrm{Cl}(^2\mathrm{P}_{1/2})]}{N[\mathrm{Cl}(^2\mathrm{P}_{3/2})]} = k\frac{S[\mathrm{Cl}(^2\mathrm{P}_{1/2})]}{S[\mathrm{Cl}(^2\mathrm{P}_{3/2})]} \tag{3}$$

Here, $S[\mathrm{Cl}(^2P_{1/2})]/S[\mathrm{Cl}(^2P_{3/2})]$ is the ratio of the integrated signal intensity of the spin-orbit states, determined by accumulating chlorine signal while scanning over the Doppler profile of each states. By scaling with the REMPI line strength, $k = 0.85 \pm 0.10$,[24] the resulting branching ratio $N[\mathrm{Cl}(^2P_{1/2})]/N[\mathrm{Cl}(^2P_{3/2})]$ is calculated to be 0.82 ± 0.16. If we divide up the C−Cl P(E_T) into a fast component peaking near 40 kcal/mol and a broad slow component, we calculate the Cl($^2P_{1/2}$)/Cl($^2P_{3/2}$) ratio to be near unity for the fast component, and near a statistical ratio of 1:2 for the portion of the slow component with E_T less than 20 kcal/mol. The weighted P(E_T)s for photodissociation events leading to Cl($^2P_{3/2}$) and Cl($^2P_{1/2}$) are shown in blue and red line, respectively, in Figure 2.3. Both distributions peak at 40 kcal/mol although the distribution for Cl($^2P_{1/2}$) shows a sharper peak at this translational energy. Our total translational distribution, shown in black line in Figure 3, also peaks at about 40 kcal/mol and has an average translational energy, $\langle E_T \rangle$, of 28.5 kcal/mol. Figure 2.4 shows an smoothed C−Cl bond fission P(E_T) generated from the P(E_T) in Figure 2.3 by averaging the P(E_T) values in each E_T range of 2.5 kcal/mol, putting the average value in the weighted center of the range. These P(E_T) values are then interpolated to an even spacing in E_T.

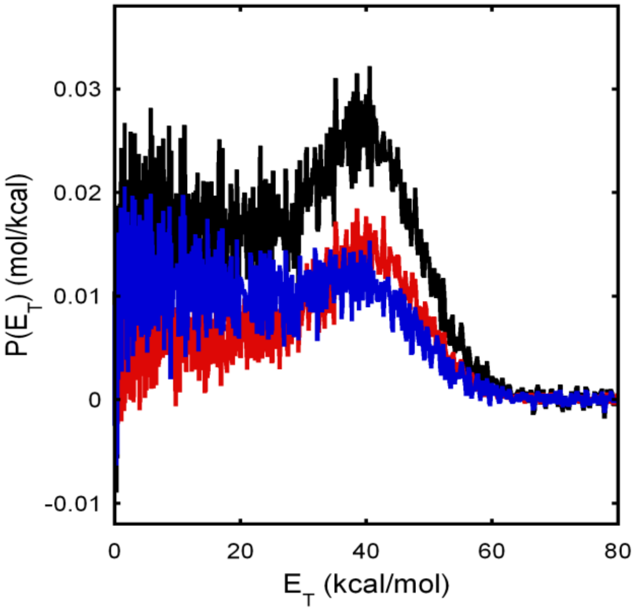

Figure 2.3: The total relative translational energy distribution, P(E_T), for all C−Cl photofission events. The figure shows the total relative translational energy distribution (black), which is the sum of the contributions of the vinoxy + Cl($^2P_{3/2}$) P(E_T) (blue) and the vinoxy + Cl($^2P_{1/2}$) P(E_T) (red) derived from the imaging data in Figure 2.2 by applying conservation of momentum and Jacobian corrections.

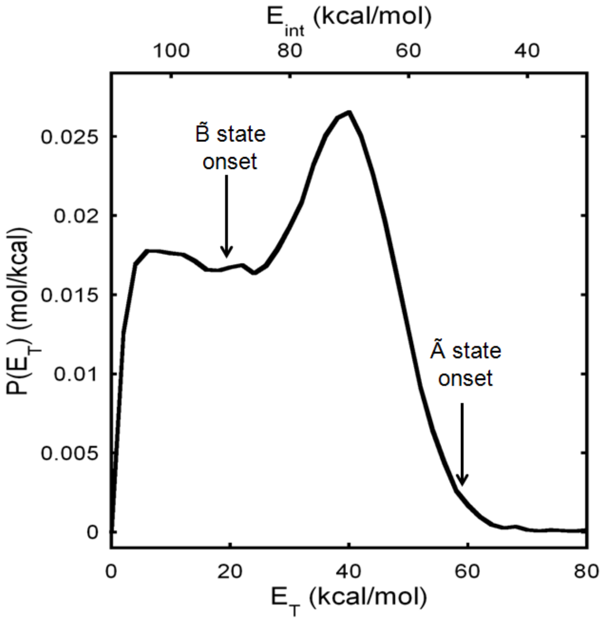

Figure 2.4: The total P(E_T) for all C−Cl photodissociation events smoothed and interpolated from the black curve in Figure 2.3. The lower axis, E_T, is the translational energy imparted to the vinoxy and Cl products of the dissociation of chloroacetaldehyde; the upper axis, E_{int} is the internal energy of the vinoxy radicals assuming they are formed in the ground electronic state and the Cl atoms are formed in the ground spin-orbit state ($^2P_{3/2}$). The labels on the plot indicate the onsets of Ã state and B̃ state vinoxy calculated by determining the maximum E_T value that would allow for either state to be formed from C−Cl photodissociation by conservation of energy. The rotational energy used in calculating the onsets was approximated using our model with the geometry of the anti conformer of the precursor and equilibrium geometry of each excited state.

The P(E_T) derived from the detection of Cl also allows us to determine the internal energy distribution of all the nascent vinoxy radicals. Conservation of energy requires that the sum of the energy of the photon, $h\nu$, and the internal energy of the parent molecule prior to dissociation, $E_{\text{int}}(\text{precursor})$, must be equal to the energy partitioned into the product fragments. Some of this energy is consumed in breaking the C−Cl bond, $D_o(\text{C-Cl})$, and the remaining energy is distributed among recoil translational energy in the center-of-mass reference frame, E_{T}, and internal energy of the fragments, $E_{\text{int}}(\text{Cl})$ and $E_{\text{int}}(\text{radical})$

$$h\nu + E_{\text{int}}(\text{precursor}) = D_o(\text{C}-\text{Cl}) + E_{\text{T}} + E_{\text{int}}(\text{Cl}) + E_{\text{int}}(\text{radical}) \qquad (4)$$

Using this equation, the total primary P(E_{T}) can be used to derive the distribution of internal energy in the vinoxy radical, P(E_{int}). The internal energy scale depicted by the upper axis in Figure 4 was calculated for C−Cl photodissociation events that produce Cl($^2P_{3/2}$). Any events producing Cl($^2P_{1/2}$) would produce vinoxy radicals with 2.5 kcal/mol less in internal energy. (In our later calculations, we explicitly determine the internal energy distribution of vinoxy radicals produced in coincidence with both Cl($^2P_{3/2}$) and Cl($^2P_{1/2}$) as we measured the P(E_{T})s individually.) The internal energy of the vinoxy radicals ranges from 40 to 110 kcal/mol and peaks at about 70 kcal/mol. Since the previous study at 193 nm had a smaller range of internal energies in the radical and peaked at 40 kcal/mol, the vinoxy radicals produced in this study have more energy at their disposal for subsequent dissociation. However, we must now account for conservation of angular momentum; energy in vibrations is responsible for traversing barriers along the PES and the internal energy in the radical is comprised of vibrational and rotational energy.

It is also worth investigating the possibility that C−Cl photodissociation produces vinoxy in an excited state as opposed to the ground electronic state. Using Equation (4), we can calculate the relative translational energy that would correspond to the production of vinoxy radicals in either the Ã or B̃ state with zero vibrational energy (while conserving angular momentum) and Cl($^2P_{3/2}$) as the cofragment. We used our rotational model to approximate the rotational energy in terms of E_T for the vinoxy radical at its equilibrium geometry for either the Ã or B̃ state and subtract this from E_{int} of the radical. These “onsets” of excited state vinoxy are shown in Figure 4 by arrows pointing to the E_T values with labels above describing the excited state to which they refer. The onset of the Ã state is E_T = 58.5 kcal/mol and the onset of the B̃ state is E_T = 19.0 kcal/mol, which seem to fit well with the features of the distribution. Since the model requires a precursor geometry to calculate an angular momentum vector, the choice of the precursor to be used is important and it should be noted that the anti conformer of chloroacetaldehyde was used in the calculated onsets in Figure 2.4. The onsets calculated using the less probable syn conformer are 54.4 kcal/mol for the Ã state and 18.1 kcal/mol for the B̃ state. One can see that C−Cl photofission at 157 nm may produce vinoxy radicals in the Ã and B̃ states; almost the entire primary P(E_T) can be attributed to vinoxy radicals in excited states based on these calculations. The rotational model is described in greater detail in Chapter 3 of this dissertation.

Ideally, we would also detect stable vinoxy radicals at *m/z* = 43 to further characterize the primary C−Cl bond fission channel as enough energy is portioned to rotational energy to form some vinoxy radicals stable to subsequent dissociation. While the ionization energy of vinoxy is calculated to be approximately 9.13 eV,[25] the significant difference in equilibrium geometry between the radical and its cation allows for little Franck-Condon overlap in the vertical region on the cation’s PES. This makes detecting vinoxy at its cation mass following photoionization difficult; no photoionization spectrum for vinoxy radical at *m/z* = 43 has been reported in the literature. Thus, we did not attempt to accumulate data at *m/z* = 43. However, vinoxy radicals are found to give signal at *m/z* = 15 from dissociative ionization when the photon energy is above 10.3 eV.[26,27] When analyzing the signal detected at *m/z* = 15 in section 3.3.4, we will consider possible contribution from stable vinoxy to the signal at *m/z* = 15.

Another primary photodissociation channel of chloroacetaldehyde is HCl elimination, which produces ketene and can thus contribute signal to the *m/z* = 42 data. Ideally, we would also characterize this primary channel and subtract its contribution to the *m/z* = 42 data leaving us with the ketene produced solely from secondary dissociation of vinoxy. However based on the data taken at *m/z* = 42 and the subsequent branching calculations discussed in Chapter 3, the primary HCl photoelimination channel appears to be relatively insignificant. We also further investigate the contribution of this channel in the study described in Chapter 4.

2.3.3 Detection of Ketene, CH_2CO

We detected the ketene product from the unimolecular dissociation of vinoxy to characterize the branching to this product channel as a function of internal energy in the vinoxy radical. On the same apparatus, instead of the REMPI detection scheme used to detect Cl fragments, we employ photoionization at 10.5 eV to detect ketene. With the photon energy substantially higher than the photoionization threshold (9.62 eV[28]) but yet below the first appearance energy yielding daughter ions, (11.75 eV[28]), neutral ketene products with various recoil kinetic energies should be detected without bias. The net speed distribution derived from the ion image recorded at *m/z* = 42 is shown in Figure 2.5. The net speed, v_{net}, is the magnitude of the net velocity vector, which is the vector sum of the velocity of the vinoxy co-fragment imparted during C−Cl bond fission and the velocity imparted during secondary dissociation.

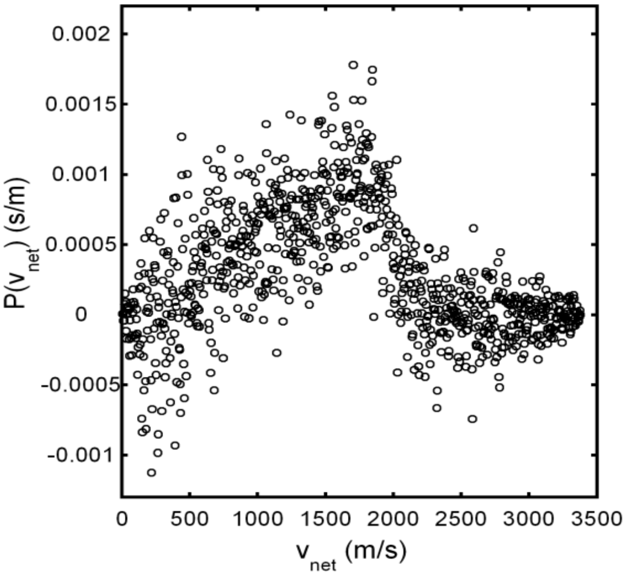

Figure 2.5: Speed distribution for *m/z* = 42 (CH_2CO^+) fragments derived from the ion image.

The measured net speed distribution of the ketene products allows us to determine the speed distribution of the nascent vinoxy radicals that dissociate to H + ketene. Due to the overwhelming mass difference between the H + ketene cofragments, the H atom is imparted with the majority of the relative velocity vector by conservation of momentum. In other words, regardless of the amount of secondary recoil kinetic energy imparted, the resultant net velocity of ketene is nearly identical to the velocity of the vinoxy radical that dissociates to H + ketene. Consequently, we used the measured net speed distribution of ketene to approximate the $P(v)$ of all vinoxy radicals that dissociated to H + ketene products. The resultant $P(E_T)$ calculated from this speed distribution is depicted in green trace in Figure 2.6. We can thus compare the total Cl + vinoxy $P(E_T)$ to the portion that produces vinoxy radicals that dissociated to H + ketene products. We have assumed all of the ketene is from vinoxy generated from C−Cl photofission, so the $P(E_T)$ in green shows the portion of the C−Cl photofission events that gives vinoxy radicals which dissociate to H + ketene products. The total primary $P(E_T)$ is shown in black trace in Figure 2.6 for comparison. The "ketene" portion was scaled to the same height as that predicted by the ratio calculated in Chapter 3. In this way, we account for the fact that vinoxy can also dissociate via channel (2). Comparing the two traces in the figure, their shapes are fairly similar in the region between 10 and 25 kcal/mol and appear relatively flat. This suggests that the branching fraction to the H + ketene channel is roughly constant for vinoxy radicals produced from events within this range of relative translational energy (where C−Cl fission produced internally hot vinoxy radicals). In the higher kinetic energy portion of the $P(E_T)$ where vinoxy is produced with lower vibrational energies, the dissociation to H + ketene drops off.

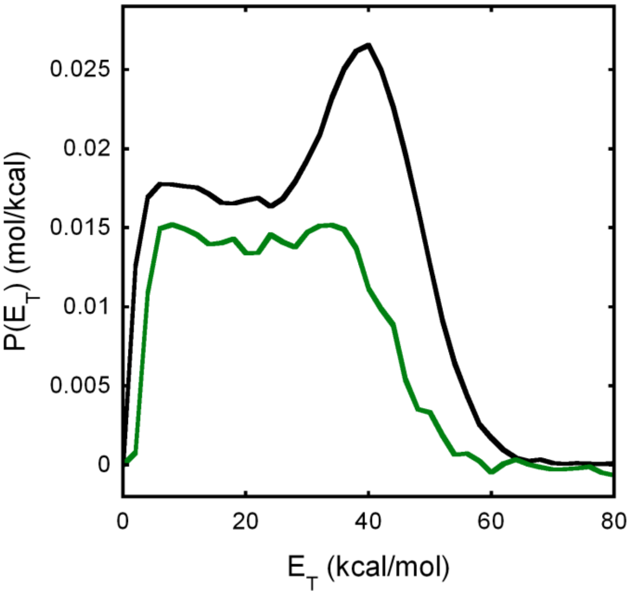

Figure 2.6: The green trace is the portion of the total primary P(E_T) that leads to H + ketene products upon secondary dissociation derived from the measured P(v) of m/z = 42 (CH_2CO^+), assuming the additional velocity imparted to the ketene upon secondary dissociation via C-H bond fission is small (see text). The black trace is the total primary P(E_T) (from Figure 4) shown for comparison. The "ketene portion" is scaled using the results of the branching calculations at model E_T's discussed in Chapter 3

2.3.4 Detection of Methyl Radicals, CH_3

Our study on the product branching in the unimolecular dissociation of vinoxy can never be conclusive without detecting neutral methyl radicals yielded from channel (2). We use 10.5 eV photoionization to probe CH_3, accumulating data at m/z = 15. The recorded image is converted to a net speed distribution, shown in Figure 2.7. The signal at m/z = 15 is marginally detectable and thus the signal-to-noise ratio of the P(v_{net}) is unsatisfactory. The P(v_{net}) spans a wide range of speeds making fitting very ambiguous. According to our previous work, vinoxy radicals prepared in the ground state by photolysis of chloroacetaldehyde dissociate to produce methyl + CO products with negligible secondary recoil translational energy. Thus, a good fit for the fast part of the P(v_{net}) we present here cannot be achieved without imparting an exaggerated amount of secondary recoil translational energy. This leads us to ascribe the fastest part of m/z = 15 to the dissociative ionization of vinoxy radicals.

In order to characterize the dissociative ionization of vinoxy to form methyl cations, we used the model developed by Brynteson and Butler[29] which predicts the angular distribution and secondary recoil translational energy relative to the primary E_T for a barrier-less dissociation channel. To model the CH_3^+ for dissociative ionization of vinoxy, the model predicts a P(v_{net}) for CH_3^+ by vector addition of the velocity of the stable vinoxy radical being photoionized and the velocity imparted to the CH_3^+ during the dissociative ionization. Since Gaussian calculations done on the cationic surface of vinoxy suggest that the exit channel for methyl + CO is a straight dissociation, we expect this model to work well for our system. The gray line in Figure 2.7 shows the predicted P(v_{net}) for dissociative ionization of vinoxy to CH_3^+. For the model, we inputted the portion of the C−Cl bond fission P(E_T) representing stable vinoxy radicals predicted using our branching calculations described in Chapter 3. This predicted P(v_{net}) had been scaled by the amount of dissociation events in the primary P(E_T) that lead to stable vinoxy and the product yield of the dissociative ionization estimated from the relative photoionization cross section of CH_3 to CH_3^+ and vinoxy to CH_3^+ reported by Osborn et al.[26] Since the model predicts too small a width for the secondary recoil translational energy distribution when $\vec{J}$ is near a principle axis, so the ratio between secondary E_T and the primary E_T is sharply peaked, we broadened the predicted P(v_{net}) by convolving it with a Gaussian function to try to account for the real spread in the secondary P(E_T).

To predict the P(v_{net}) representing methyl radicals produced from secondary dissociation of neutral vinoxy, we used the forward convolution procedure described by Alligood et al.[30] We use the portion of the P(E_T) representing vinoxy that then dissociates to methyl + CO from our branching calculations in Chapter 3. Without considering strong forward-backward scattering in the secondary dissociation, the slow part of the P(E_T) could not be well fit either. Assuming forward-backward scattering and a secondary recoil translational distribution represented by a half-normal distribution peaked at 0 kcal/mol with a sigma of 5 kcal/mol, we get the predicted P(v_{net}) for shown in blue line in Figure 2.7 (in the calculation, each primary velocity was scaled by the amount of dissociation events from the primary P(E_T) that lead to methyl products). The Gaussian function was peaked at 0 kcal/mol to reflect the results of our previous study and the width of 5 kcal/mol had to be added in order for the predicted P(v) to fit the data at slow speeds. The black line is the sum of the two traces, which gives an overall satisfactory fit but still cannot describe the observed signal at higher speeds.

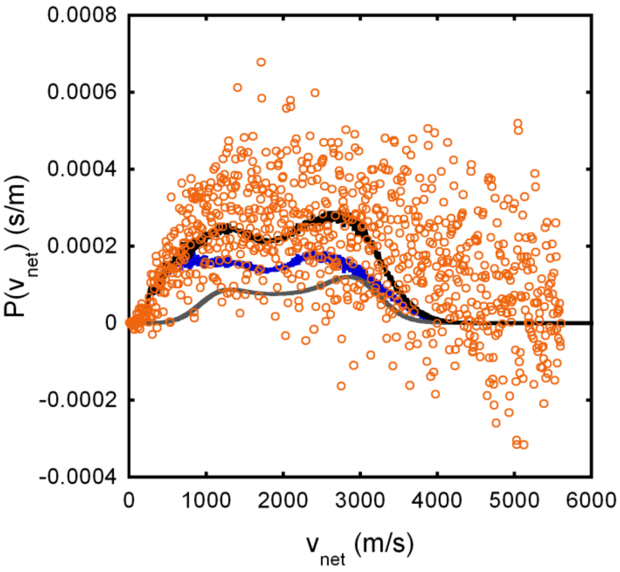

Figure 2.7: Speed distribution for *m/z* = 15 (CH_3^+) fragments derived from the ion image. The gray line is the predicted P(v_{net}) of CH_3 yielded by dissociative photoionization of “stable” vinoxy radical, calculated from the predicted stable portion of the primary C−Cl bond fission P(E_T) using the model described in Brynteson and Butler.[29] The blue line is the predicted P(v_{net}) using the predicted portion of the primary C−Cl bond fission P(E_T) leading to vinoxy that dissociates to CH_3 + CO, while assuming forward-backward scattering with secondary recoil translational energy imparted a half-normal distribution peaked at 0 kcal/mol with a sigma of 5 kcal/mol. The black line is the sum of the two traces and represents the overall fit to the data. The predicted portions of the primary C−Cl P(E_T) are discussed in Chapter 3.

2.4 Discussion

This study focused on characterizing the branching between the unimolecular dissociation channels of the vinoxy radical to H + ketene and methyl + CO products. We used a similar methodology from a previous study done by our group to generate vinoxy radicals, with high internal energies and under collision-free conditions, by photolysis of the precursor chloroacetaldehyde, but using 157 nm light instead of 193 nm light. We then looked for the ketene products and methyl products from the secondary dissociation of the nascent vinoxy to ascertain the branching between the two channels. Although the contamination in the methyl signal did not allow us to experimentally determine the branching ratio, the ketene signal provided key information on how the branching fraction to the H + ketene product channel changes with vibrational energy in the vinoxy radical. The motivation for this study was the large discrepancy between the experimental and predicted branching found in the previous study where the secondary dissociation of vinoxy was dominated by the methyl + CO channel with a negligible amount of ketene produced.

Our results show a marked change in the branching between the two channels from the previous study. Not only do we see a substantial amount of ketene products that can be attributed to the secondary dissociation of the vinoxy radical, but we also find a small amount of methyl as evidenced by the signal at m/z = 15. As opposed to the previous study, which was done with a much lower distribution of energies in the vinoxy radical, the secondary dissociation now favors the production of ketene + H over the production of methyl + CO products. Due to the ambiguity in fitting the signal at m/z = 15, it is difficult to calculate a branching ratio between the two channels for this study from the experimental data.

If we look at the internal energy in the radicals, we find that the vinoxy radicals produced from C−Cl bond fission of chloroacetaldehyde at 157 nm have higher internal energies compared to those produced in the previous study. This might be expected from the larger photon energy at 157 nm as compared to 193 nm. Interestingly, the majority of vinoxy radicals produced in this study have internal energies greater than 50 kcal/mol (and have vibrational energies consistent with being formed in the excited electronic state) while those in the previous study have internal energies lower than 50 kcal/mol. Assuming that the radicals undergo internal conversion to the ground electronic state, RRKM calculations predict that the branching to the H + ketene channel dominates the methyl + CO channel when there is a great deal of vibrational energy in the radical since the transition state for the H + ketene channel is looser than that for the isomerization channel. Therefore, the larger amount of ketene produced from secondary dissociation in this study is consistent with what we would expect from applying statistical transition state theory to the H + ketene channel.

Our analysis of the product branching in the unimolecular dissociation of vinoxy radicals relies on the assumption that C−Cl bond fission in chloroacetaldehyde at 157 nm produced vinoxy radicals that undergo internal conversion to the ground electronic state before they dissociate. The nascent vinoxy radicals are likely formed in the Ã and B̃ excited electronic states, but can of course internally convert to the ground state PES via the avoided crossings and conical intersections calculated by Yarkony and co-workers. The primary C−Cl bond fission P(E_T)s for Cl($^2P_{3/2}$) and Cl($^2P_{1/2}$) are bimodal, with a high kinetic energy feature peaking near E_T = 40 kcal/mol in both that indicates dissociation along a repulsive energy surface. Both P(E_T)s also have a broad and slow feature, which is isotropic. Our energy and angular momentum constraints give onsets, shown in Figure 2.4, that suggest C−Cl photofission events that partition less than

19 kcal/mol to E_T can form nascent vinoxy radicals in the B̃ state while most of the high-kinetic energy component to the P(E_T) peaking near 40 kcal/mol can produce vinoxy in the Ã state but not in the B̃ state.

We have undertaken EOM-CCSD calculations of the excited singlet and triplet states of chloroacetaldehyde; they are consistent with the assignment of the product channels. Our preliminary EOM-CCSD calculations with 6-311++G(3df,2p) basis are shown in Appendix A. The excited singlet state of chloroacetaldehyde with the highest oscillator strength is S_4; it is predissociated by a repulsive diabat at larger C−Cl distances and correlates adiabatically to Cl + vinoxy in the B̃ state. The S_3 state has a very similar vertical excitation energy as the S_4 state (about 7.5 eV) but is strongly repulsive in the Franck-Condon region. It correlates adiabatically to Cl + vinoxy in the Ã state. Thus we infer that dissociation along the S_3 state likely results in the high-kinetic energy component of the C−Cl photofission P(E_T), while dissociation along S_4 results in all or a portion of the low kinetic energy component of our P(E_T) assigned to Cl + vinoxy in the B̃ state. The calculated triplet states of chloroacetaldehyde, shown in the Appendix], also include both repulsive and predissociative excited state accessed in the Franck-Condon region. We note that our model for predicting the angular momentum imparted during C−Cl bond fission assumes that the excited state is repulsive in the Franck-Condon region. Thus, it should accurately predict the angular momentum in the high kinetic energy portion of the bimodal P(E_T) but not the low kinetic energy portion. The branching ratio is only sensitive to the partitioning between rotational and vibrational energy in the high kinetic energy portion of the P(E_T), so our model should correctly predict this partitioning in the region of the P(E_T) that we have used for the barrier height determinations.

Finally, it is interesting to compare the dynamics on the repulsive excited singlet states of chloroacetaldehyde with that on the ^1E, ^3E, and Rydberg excited states of CH_3Cl. The $Cl(^2P_{1/2})/Cl(^2P_{3/2})$ branching ratios and anisotropy parameters for the photodissociation of CH_3Cl has been studied at 193 nm by several groups as reviewed by Suits and co-workers[31] and at both 193 and 157 nm in Doppler measurements by Matsumi et al.[32,33] Although Matsumi et al. interpret their Doppler results at 157 nm as indicative of a bimodal C−Cl recoil kinetic energy distribution, more recent work by Lin et al.[34] detect a unimodal recoil kinetic energy distribution peaking near 85 kcal/mol; the Lin paper did not measure the $Cl(^2P_{1/2})/Cl(^2P_{3/2})$ branching ratio or photofragment anisotropies. The $Cl(^2P_{1/2})/Cl(^2P_{3/2})$ branching ratio for CH_3Cl excited at 157 nm was reported to be 0.65 ± 0.13[33] by Matsumi et al. but should be revised to roughly 0.9 using more recent REMPl line strength factors as discussed by Suits and co-workers. This compares closely with our measured $Cl(^2P_{1/2})/Cl(^2P_{3/2})$ ratio for chloroacetaldehyde of 0.82 ± 0.16. The partial $Cl(^2P_{1/2})/Cl(^2P_{3/2})$ branching ratio is smaller in the low-kinetic component of our C−Cl photofission $P(E_T)$ and near unity in the high kinetic energy portion, so our high kinetic energy distribution evidences a similar Cl spin orbit branching ratio to that observed for CH_3Cl at 157 nm. The Cl photofragement anisotropy is similar for both $Cl(^2P_{1/2})$ and $Cl(^2P_{3/2})$ in our data, weakly parallel (with an average β_2 of 0.23) in the high-kinetic energy portion of the $P(E_T)$ and isotropic in the low-kinetic energy portion. The weakly parallel anisotropy suggests optical excitation via both parallel and perpendicular transitions at 157 nm which each lead, presumably via nonadiabatic transitions en route, to both $Cl(^2P_{1/2})$ and $Cl(^2P_{3/2})$.

We fit the methyl signal from secondary dissociation in this work by assuming that a small amount of kinetic energy is imparted to the methyl fragment upon secondary dissociation of the vinoxy radical. If the secondary dissociation does occur on the ground state PES, then we would expect a similar secondary P(E_T) for this dissociation channel to that used in the study by Miller et al. While Miller et al. fit their methyl data assuming that the velocity imparted to the methyl product when vinoxy dissociated was negligible, a better fit was obtained for our data in this paper by assuming the secondary P(E_T) peaked at 0 kcal/mol but increasing the spread in recoil kinetic energy imparted in the dissociation. We thus use a half normal distribution for the secondary P(E_T) for the dissociation of vinoxy to CH_3 + CO that has a sigma of 5 kcal/mol. This difference may be a result of the much larger amount of energy in the vinoxy radical that can be imparted to the methyl radical.

While we have assigned as much of the signal as we can, there are still possible issues with dissociative ionization of vinoxy. First, there is some discrepancy between the signal at m/z = 15 from dissociative ionization of the vinoxy radical to CH_3^+ in this study and that from the previous study on the photodissociation of chloroacetaldehyde at 193 nm. In the previous study, the contribution of dissociative ionization to the signal at m/z = 15 was determined to be negligible whereas this study attributes a decent portion of the signal to dissociative ionization. While the m/z = 15 appearance energy varies with the internal energy of the radical, G4 calculations on the cationic surface of vinoxy show that the barrier to forming CH_3^+ + CO is 10.4 eV from the zero-point level of ground state vinoxy. This energy is consistent with the appearance energy of CH_3^+ for vinoxy found in a few references (10.3 eV)[26,27] and therefore photoionization at an energy above this appearance energy should give signal from stable vinoxy radicals at m/z = 15. It is therefore surprising that the previous chloroacetaldehyde study was able to fit the signal at m/z = 15 without a contribution from dissociative ionization. Experimental and theoretical work on the cationic surface of vinoxy would be beneficial in characterizing the dynamics on this surface and its contribution to the methyl signal.

Not only can vinoxy undergo dissociative ionization to form CH_3^+ + CO, but it can also form H + CH_2CO^+. According to Lee et al.,[27] the dissociative ionization of vinoxy to H + CH_2CO^+ is significant when the photoionization energy is greater than 12.5 eV. Assuming this energy represents a barrier on the cationic surface to the formation of H + CH_2CO^+, stable vinoxy radicals with vibrational energies up to the isomerization threshold (40.6 kcal/mol) excited to the cationic surface using a photoionization energy of 10.5 eV would not have enough energy to surmount this barrier. In agreement with this analysis, Miller et al. found no evidence of dissociative ionization of stable radicals to $m/z = 42$, despite having a substantial number of radicals with vibrational energy near the isomerization threshold (using a slightly higher photoionization energy of 10.6 eV). We therefore do not expect any signal at $m/z = 42$ from the dissociative ionization of vinoxy to H + CH_2CO^+ using a photoionization energy of 10.5 eV.

2.5 References

(1) Westbrook, C. K.; Dryer, F. L. Chemical Kinetics and Modeling of Combustion Processes. *Symp. Int. Combust. Proc.* **1981**, *18*, 749-767.

(2) Brezinsky, K. The High-Temperature Oxidation of Aromatic Hydrocarbons. *Prog. Energy Combust. Sci*. **1986**, *12*, 1-24.

(3) Balucani, N.; Leonori, F.; Casavecchia, P.; Fu, B.; Bowman, J. M. Crossed Molecular Beams and Quasiclassical Trajectory Surface Hopping Studies of the Multichannel Nonadiabatic O(^{3}P) + Ethylene Reaction at High Collision Energy. *J. Phys. Chem. A.* **2015**, *119*, 12498-12511.

(4) Leonori, F.; Balucani, N; Nevrly, V.; Bergeat, A.; Falcinelli, S.; Vanuzzo, G.; Casavecchia, P. Experimental and Theoretical Studies on the Dynamics of the O(^{3}P) + Propene Reaction: Primary Products, Branching Ratios, and Role of Intersystem Crossing. *J. Phys. Chem. C* **2015**, *119*, 14632-14652.

(5) McKee, K. W.; Blitz, M. A.; Cleary, P. A.; Glowacki, D. R.; Pilling, M. J.; Seakins, P. W., Wang, L. Experimental and Master Equation Study of the Kinetics of OH + C_2H_2: Temperature Dependence of the Limiting High Pressure and Pressure Dependent Rate Coefficients. *J. Phys. Chem. A* **2007**, *111*, 4043-4055.

(6) Bernhard, K. I.; Santiago, A.; He, H.; Asmar, F.; Weiner, B. R. Pressure and Temperature Dependence of the C_2H_3O + NO_2 Reaction. *Chem. Phys. Lett.* **1991**, *178*, 150-156.

(7) Liu, F.; Beames, J. M.; Petit, A. S.; McCoy, A. B.; Lester, M. I. Infrared-Driven Unimolecular Reaction of CH_3CHOO Criegee Intermediates to OH Radical Products. *Science* **2014**, *345*, 1596-1598.

(8) Osborn, D. L.; Choi, H.; Mordaunt, D. H.; Bise, R. T.; Neumark, D. M.; Rohlfing, C. M. Fast Beam Photodissociation Spectroscopy and Dynamics of the Vinoxy Radical. *J. Chem. Phys.* **1997**, *106*, 3049-3066.

(9) Morton, M. L.; Szpunar, D. E.; Butler, L. J. Photodissociating Methyl Vinyl Ether to Calibrate O + Ethylene Product Branching and to Test Propensity Rules for Product Channel Electronic Accessibility. *J. Chem. Phys*. **2001**, *115*, 204-216.

(10) Miller, J. L.; McCunn, L. R.; Krisch, M. J.; Butler, L. J.; Shu, J. Dissociation of the Ground State Vinoxy Radical and Its Photolytic Precursor Chloroacetaldehyde: Electronic Nonadiabaticity and the Suppression of the H + Ketene Channel. *J. Chem. Phys*. **2004**, *121*, 1830-1838.

(11) Matsika, S. ; Yarkony, D. R. Photodissociation of the Vinoxy Radical Through Conical, and Avoided, Intersections. *J. Chem. Phys.* **2002**, *117*, 7198-7206.

(12) Piechowska-Strumik, K.; Lauvergnat, D.; Bacchus-Montabonel, M.-C.; Desouter-Lecomte, M. Quantum Dynamics Around a Non Planar Conical Intersection in Vinoxy Radical Relaxation. *Chem. Phys. Lett.* **2006**,425, 16–21.

(13) Young, R. A.; Yarkony, D. R. A Novel Conical Intersection Topography and Its Consequences: The 1, 2 ^{2}A Conical Intersection Seam of the Vinoxy Radical. *J. Chem. Phys*. **2005**, *123*, 084315.

(14) Bennett, D. I.; Butler, L. J.; Werner, H.-J. Comparing Electronic Structure Predictions for the Ground State Dissociation of Vinoxy Radicals. J. *Chem. Phys*. **2007**, *127*, 094309.

(15) McKown, B. G.; Ceriotti, M.; Womack, C. C.; Kamarchik, E.; Butler, L. J.; Bowman, J. M. Effects of High Angular Momentum on the Unimolecular Dissociation of CD_2CD_2OH: Theory and Comparisons with Experiment. *J. Phys. Chem. A* **2013**, *117*, 10951-10963.

(16) Brynteson, M. D.; Womack, C. C.; Booth, R. S.; Lee, S.–H.; Lin, J. J.; Butler, L. J. Radical Intermediates in the Addition of OH to Propene: Photolytic Precursors and Angular Momentum Effects. *J. Phys. Chem. A* **2014**, *118*, 3211-3229.

(17) Heck, A. J. R.; Chandler, D.W. Imaging Techniques for the Study of Chemical Reaction Dynamics. *Annu. Rev. Phys. Chem*. **1995**, *46*, 335-372.

(18) Eppink, A. T. J. B.; Parker, D. H. Velocity Map Imaging of Ions and Electrons Using Electrostatic Lenses: Application in Photoelectron and Photofragment Ion Imaging of Molecular Oxygen. *Rev. Sci. Instrum*. **1997**, *68*, 3477–3484.

(19) Chang, B.; Hoetzlein, R. C.; Mueller, J. A.; Geiser, J. D.; Houston, P. L. Improved Two-Dimensional Product Imaging: The Real-Time Ion Counting Method. *Rev. Sci. Instrum*. **1998**, *69*, 1665-1670.

(20) Dribinski, V.; Ossadtchi, V. A.; Mandelshtam; Reisler, H. Reconstruction of Abel-Transformable Images: The Gaussian Basis-Set Expansion Abel Transform Method. *Rev. Sci. Instrum*. **2002**, *73*, 2634-2642.

(21) Curtiss, L. A.; Redfern, P. C.; Raghavachari, K.; Pople, J. A. Gaussian-3X (G3X) Theory: Use of Improved Geometries, Zero-Point Energies, and Hartree-Fock Basis Sets. *J. Chem. Phys*. **2001**, *114*, 108-117.

(22) Curtiss, L. A.; Redfern, P. C.; Raghavachari, K. Gaussian-4 Theory. *J. Chem. Phys*. **2007**, *126*, 084108.

(23) Frisch, M. J.; Trucks, G. W.; Schlegel, H. B.; Scuseria, G. E.; Robb, M. A.; Cheeseman, J. R.; Scalmani, G.; Barone, V.; Mennuci, B.; Petersson, G. A.; et al. Gaussian 09, Revision A.02; Gaussian, Inc.: Wallingford, CT, 2009.

(24) Liyanage, R.; Yang Y.; Hashimoto, S.; Gordon, R. J.; Field, R.W. Electronic Control of the Spin-Orbit Branching Ratio in the Photodissociation and Predissociation of HCl. *J. Chem. Phys.* **1995**, *103*, 6811-6814.

(25) Adiabatic ionization energy calculated at the G4//B3LYP/6-311++G(3df,2p) level of theory

(26) Savee, J. D.; Welz, O.; Taatjes, C. A.; Osborn, D. L. New Mechanistic Insights to the O(^{3}P) + Propene Reaction from Multiplexed Photoionization Mass Spectrometry. *Phys. Chem. Chem. Phys.* **2012**, *14*, 10410-10423.

(27) Lee, S-H; Huang, W-J; Chen, W-K Dynamics of the Reaction of Atomic Oxygen with Ethene: Observation of All Carbon-Containing Products by Single-Photon Ionization. *Chem. Phys. Lett.* **2007**, *446*, 276-280.

(28) NIST Chemistry WebBook (http://webbook.nist.gov/chemistry/)

(29) Brynteson, M. D.; Butler, L. J. Predicting the Effect of Angular Momentum on the Dissociation Dynamics of Highly Rotationally Excited Radical Intermediates. *J. Chem. Phys.* **2015**, *142*, 054301.

(30) Alligood, B. W.; Straus, D. B.; Butler, L. J. Analyzing Velocity Map Images to Distinguish the Primary Methyl Photofragments from those Produced upon C−Cl Bond Photofission in Chloroacetone at 193 nm. *J. Chem. Phys.*, **2011**, *135*, 034302.

(31) Townsend, D.; Lee, S. K.; Suits, A. G. DC Slice Imaging of CH_3Cl Photolysis at 193.3 nm. *J. Phys. Chem. A* **2004**, *108,* 8106-8114.

(32) Matsumi, Y.; Das, P. K.; Kawasaki, M. Doppler Spectroscopy of Chlorine Atoms Generated from Photodissociation of Hydrogen Chloride and Methyl Chloride at 157 and 193 nm. *J. Chem. Phys.* **1990**, *92*, 1696-1701.

(33) Matsumi, Y.; Das, P. K.; Kawasaki, M. Erratum: Doppler Spectroscopy of Chlorine Atoms Generated from Photodissociation of Hydrogen Chloride and Methyl Chloride at 157 and 193 nm [J. Chem. Phys. 92, 1696 (1990)]. *J. Chem. Phys.* **1992**, *97*, 5261.

(34) Lin, J. J.; Chen, Y; Lee, Y. Y.; Lee, Y. T.; Yang, X. Photodissociation Dynamics of CH_3Cl at 157.6 nm: Evidence for $CH_2(\tilde{X}^3B_1/\tilde{a}^1A_1)$ + HCl Product Channels. *Chem. Phys. Lett.* **2002**, *361*, 374–382.

CHAPTER 3

INCORPORATING ANGULAR MOMENTUM IN STATISTICAL PREDICTIONS OF PRODUCT BRANCHING: REASSESSING THE BARRIER FOR THE UNIMOLECULAR DISSOCIATION OF VINOXY TO H + KETENE

The model description and data presented in this chapter were previously published in the Journal of Physical Chemistry A. The following content was adapted from with permission form [C. - S. Lam., J. D. Adams, and L. J. Butler, "The Onset of H + Ketene Products from Vinoxy Radicals Prepared by Photodissociation of Chloroacetaldehyde at 157 nm" J. Chem. Phys. A, DOI 10.1021/acs.jpca.6b01256 (2016)], Copyright 2016, American Chemical Society.

3.1 Introduction

When studying the chemical dynamics of highly reactive radical species, the photodissociation of halogenated precursors is commonly used to produce the radical under controlled conditions. These photolytically-produced radicals are imparted with a range of internal energies allowing some of them to surmount energetic barriers on their potential energy surface and undergo dissociation. If the internal energy is greater than several barriers, a competition between those channels ensues. While the dynamics can be investigated experimentally, modelling such behavior is difficult as the dynamics depends on how the total available energy is partitioned between translational, electronic, vibrational, and rotational energy after the photodissociation event. Oftentimes, the energy partitioning is non-statistical and conservation of angular momentum results in the rotational energy in the radical fragment changing as the radical moves along the PES while conserving total energy. This chapter details a model for the dynamics of photolytically-produced radicals that takes into account energy partitioning and conservation of angular momentum. In particular, we will look at modelling the competition between unimolecular dissociation channels of radicals produced from the photodissociation of halogenated precursors.

Over the past few decades, a variety of methods for predicting energy partitioning in both unimolecular and bimolecular reactions have been developed and tested.[1-4] While a statistical prediction for energy partitioning can be applied to a number of systems, it is not well suited to photodissociation dynamics that occur upon excitation to a repulsive excited state. For these systems, the energy partitioning is better characterized by an impulsive model[4-7] which offers a prediction for the partitioning of energy between relative translational energy and rotational energy of the photofragments. These early models give qualitative physical insight, but do not accurately predict the rotational energy imparted to the photofragments. In recent years, our group has developed a rotational model[8,9] that accurately predicts the angular momentum vector imparted to a radical from the photodissociation of a halogenated precursor by assuming the repulsive force acts in the Franck-Condon region and using the measured relative velocity between the photofragments. Since the relative translational energy of the radical + halogen system can be measured using photofragment translational spectroscopy[10,11], this model can be used to predict the rotational energy and subsequently the vibrational energy after applying conservation of energy. The rotational model can be a powerful predictive tool when used in conjunction with photofragment translational spectroscopy.

The key feature of the rotational model is that it uses conservation of angular momentum to not only predict the rotational energy of the radical fragment, but also the rotational energy at any point along its PES. This allows us to take into account the how the rotational energy en route to products affects the vibrational energy available to surmount barriers. The other important features of the model are that it explicitly includes a distribution of impact parameters over the vibrational wave function of the precursor and also includes the vibrational energy distribution in the precursor. Using the rotational model, we can thereby account for many of the important factors in predicting the dynamics of photolytically-produced radicals if the radicals are produced in the ground electronic state.

This chapter details our efforts to develop a branching model that combines the rotational model developed by our group and Rice-Ramsperger-Kassel-Marcus (RRKM) calculations.[12] We predict the product branching in the dissociation of the nascent radical from the distribution of kinetic energy imparted from photodissociation of the halogenated precursor. While RRKM theory is a common method for calculating the rates for unimolecular dissociation processes, its implementation usually assumes that the rotational energy in the species is thermalized. Instead, we calculate RRKM[13] rate constants with the correct sums and densities of vibrational states accounting for the change in rotational energy from the radical's minimum energy geometry to the transition state (TS) for each unimolecular dissociation channel. The model also accounts for the dependence of the rotational energy partitioned to the radical fragment on the relative translational energy imparted to the photofragments during photodissociation of the halogenated precursor. From the primary carbon-halogen bond fission P(E_T), the model then predicts the portions of the P(E_T) that produces radicals that undergo unimolecular dissociation via a transition state en route to each product channel.

In this chapter, we also show the predictions made by our branching model for the unimolecular dissociation of vinoxy radicals formed from the photodissociation of chloroacetaldehyde at 157 nm. Excitation at 157 nm is expected to promote chloroacetaldehyde to an excited state that is directly repulsive in the C−Cl bond and we thus assume that the rotational energy of the vinoxy is well described by the rotational model. We predict the branching between the H + ketene and methyl + CO channels assuming the dissociation of vinoxy occurs along its ground state PES. By taking advantage of momentum conservation in the dissociation to H + ketene, we can then directly compare the predictions of this model to the data taken. This analysis provides an independent measure of the barrier to the H + ketene channel (under the assumption that the dissociation is adiabatic and well-predicted by RRKM theory).

3.2 Development of Model

3.2.1 Rotational Model

When carbon-halogen bond fission imparts high relative kinetic energies to the radical + halogen co-fragments, the radicals are formed with high rotational energies unless the impact parameter is small. To determine the rotational angular momentum of the radical fragments, we use the rotational model developed by our group, summarized here. The rotational model uses angular momentum conservation to predict the angular momentum imparted to the radical moiety upon the cleavage of the C−X bond. Neglecting the angular momentum of the photon and the electronic angular momentum of the products (assumed to be negligible), supersonic expansion of a molecular beam should rotationally cool the precursor thus giving it an initial angular momentum of essentially zero. After the dissociation, the total angular momentum of the fragments must be zero as well.

$$\vec{J}_{\mathrm{tot}} = \vec{J}_{\mathrm{orb}} + \vec{J}_{\mathrm{rot}} = \vec{0} \qquad (1)$$

Here $\vec{J}_{orb}$ represents the orbital angular momentum of the radical + halogen system and $\vec{J}_{rot}$ represents the rotational angular momentum of the radical fragment. Thus, $\vec{J}_{rot}$ is equal in magnitude and opposite in direction to $\vec{J}_{orb}$ which can be calculated classically. Since the impulsive force is along the C−X bond, the rotational angular momentum can be calculated using

$$-\vec{J}_{\mathrm{rot}} = \vec{J}_{\mathrm{orb}} = \vec{r} \times \mu \vec{v}_{\mathrm{rel}} \qquad (2)$$

where $\vec{r}$ is the vector between the center-of-mass of the radical moiety in the precursor and the halogen atom, μ is the reduced mass of the radical + halogen system, and $\vec{v}_{\mathrm{rel}}$ is the relative velocity vector. Assuming the repulsive force within the Franck Condon region of the excited-state potential acts along the C−X bond, the direction of $\vec{v}_{\mathrm{rel}}$ is oriented along the C−X bond and the magnitude of $\vec{v}_{\mathrm{rel}}$ is determined from the measured relative translational energy imparted to the halogen atom and the radical fragment, E_{T}. So, all of the terms can be calculated from the equilibrium geometry of the precursor and the measured relative translational energy. The rotational energy of the radical is then given by

$$E_{\mathrm{rot}} = \frac{1}{2} \vec{J}_{\mathrm{rot}}^{\;T} I^{-1} \vec{J}_{\mathrm{rot}} \qquad (3)$$

where $\vec{J}_{\mathrm{rot}}^{\;T}$ is the transpose of the angular momentum vector and I^{-1} is the inverse of the inertia tensor. Thus we can account for the fact that the rotational energy imparted to the radical from the C−X bond photodissociation depends on the relative translational kinetic energy. This model can then predict the ratio of rotational energy to translational energy ($E_{\mathrm{rot}}/E_{\mathrm{T}}$) of the radical moiety from the geometry of the halogenated precursor.

The geometry of the radical moiety formed from the halogenated precursor is different from the equilibrium geometry of the radical and so the two will have different inertia tensors. Since the rotational angular momentum vector, $\vec{J}_{\mathrm{rot}}$, is constant in both magnitude and direction, the two geometries will have different rotational energies according to Equation (3). The same can be said about any other stationary points along the PES, such as the TS or other minima. By preserving the angular momentum vector from its orientation in the radical moiety and changing the geometry to that of each stationary point, we can account for the different inertia tensor and obtain the $E_{\mathrm{rot}}/E_{\mathrm{T}}$ ratios for any stationary point. This can also be applied to points along a reaction coordinate, thus giving an $E_{\mathrm{rot}}/E_{\mathrm{T}}$ ratio at each point; this determines how the rotational energy changes as the radical changes its geometry from the equilibrium geometry of radical to the geometries at the transition state for a given channel.

For the calculations at the minimum or at any TS, we use geometries directly outputted from geometry optimization calculations. Electronic structure packages generally rotate the coordinate system and report each geometry in a "standard orientation." This difference in the coordinate system between the points makes it incorrect to directly take the vector from its orientation in the radical moiety and superimpose it onto the geometry of interest. To account for this change, we transform the angular momentum vector into the coordinate system used in the standard orientation thus ensuring that the vector has the same magnitude and orientation relative to the moiety. For more detail, see Appendix B.

3.2.2 Branching Model

Using this rotational model, we see that the rotational energy imparted to the radical changes as it reaches a barrier en route to products. The sum of the vibrational, rotational, and potential energy at the barrier must equal the total energy of the radical at equilibrium geometry, so if the rotational energy decreases en route to the TS, there is more energy available to surmount the barrier to the reaction. Thus to calculate the correct density of vibrational states at the equilibrium geometry for an RRKM rate constant and the correct sum of states at the TS, one must account for this change in rotational energy to calculate the unimolecular rate constant.

Figure 3.1 shows a diagram of the energetics involved in a general unimolecular reaction. The total energy in the radical, E^*, consists of rotational energy, E_{rot}, and vibrational energy, E_{vib}, while the total energy at the TS, $E^{\ddagger}$, consists of both rotational and vibrational energy, $E_{\mathrm{rot}}{}^{\ddagger}$and $E_{\mathrm{vib}}{}^{\ddagger}$, as well as translational energy along the reaction coordinate, $E_{\mathrm{t}}{}^{\ddagger}$. The barrier height, E_{o}, is defined as the energy difference between the zero-point corrected minimum energy of the radical and the zero-point corrected energy of the TS (this is the G4 barrier height). Thus, $E^* - E_{\mathrm{o}} = E^{\ddagger}$. If we want to account for the effect that E_{rot} and $E_{\mathrm{rot}}{}^{\ddagger}$ have on this picture, we must subtract them from E^* and $E^{\ddagger}$, respectively, so that we calculate the correct density of vibrational states at the reactant and the correct sum of states in the orthogonal degrees of freedom at the TS. Since most RRKM calculations only allow the input of thermal distributions of rotational energies, we introduce an “effective barrier” to allow us to calculate the density and sum of vibrational states at the right energies, E_{vib} and $E_{\mathrm{vib}}{}^{\ddagger}$. We thus define the “effective” energy in the TS, $E^{\ddagger}{}_{\mathrm{effective}}$, and the “effective barrier height”, $E_{\mathrm{o,effective}} = E_{\mathrm{o}} + E_{\mathrm{rot}}{}^{\ddagger} - E_{\mathrm{rot}}$. If $E_{\mathrm{rot}}{}^{\ddagger}$ is greater than E_{rot}, then $E_{\mathrm{o,effective}}$ is greater than E_{o}; if $E_{\mathrm{rot}}{}^{\ddagger}$is less than E_{rot}, then $E_{\mathrm{o,effective}}$ is less than E_{o}. This correctly adjusts $E_{\mathrm{vib}}{}^{\ddagger}$as needed. A decrease in the rotational energy en route to the TS makes the barrier easier to cross. Therefore, we use the effective barrier height, $\mathrm{E}_{\mathrm{o,effective}}$, and $E_{\mathrm{vib}} = E^*$ as our input to an RRKM calculation to correctly predict the branching fraction to each product channels.

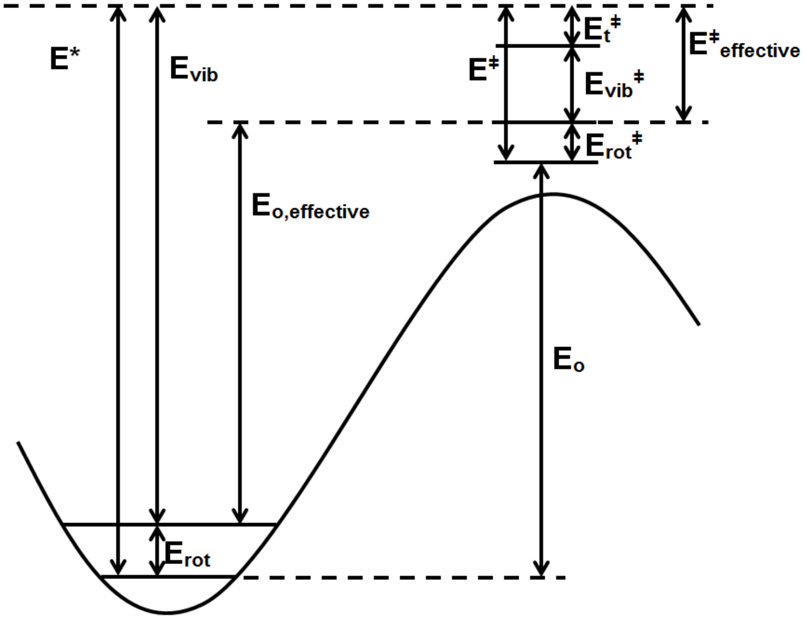

Figure 3.1. Diagram of the energies involved in a general unimolecular reaction. E^* is the total internal energy in the radical which consists of vibrational energy, E_{vib}, and rotational energy, E_{rot}. $E^‡$ is the total internal energy at the critical configuration which consists of vibrational energy, $E_{\mathrm{vib}}^‡$, rotational energy, $E_{\mathrm{rot}}^‡$, and the translational energy along the reaction coordinate, $E_{\mathrm{t}}^‡$. E_{o} is the energy difference between the zero-point energy of the radical and that of the critical configuration, thus representing the barrier height. We are concerned with the "effective" barrier height, $E_{\mathrm{o,effective}}$, which is the energy difference between the zero-point energy of the radical plus E_{rot} and the zero-point energy of the critical configuration plus $E_{\mathrm{rot}}^‡$. Note that if $E_{\mathrm{rot}}^‡$ is greater than E_{rot}, then $E_{\mathrm{o,effective}}$ is greater than E_{o}; if $E_{\mathrm{rot}}^‡$ is less than E_{rot}, then $E_{\mathrm{o,\ effective}}$ is less than E_{o}. The effective energy in the critical configuration, $E^‡_{\mathrm{effective}}$, then consists of $E_{\mathrm{t}}^‡$ and $E_{\mathrm{vib}}^‡$.

The rotational model is used in this scheme to approximate the rotational energy of the radical, E_{rot}, and TS, $E_{\mathrm{rot}}^{\ddagger}$, for the channels of interest. Since the energies we get from the model are then used to calculate E_{vib} and $E_{\mathrm{o,effective}}$, there are two points that need to be made about using the rotational model. The first point is that the rotational energy imparted to the radical upon dissociation depends on the geometry of the precursor. If the precursor has conformers with the halogen atom oriented at different dihedral angles to the molecular plane, the repulsive force will impart an angular momentum vector to the moiety that is different for each conformer. To account for this, we consider each conformer separately and sum their respective contributions in the end. The second point is that the rotational energy imparted to the radical or at any other stationary point depends on the recoil translational energy. For each E_{T} in the measured C−X bond fission P(E_{T}), we calculate a value for E_{rot} from the $E_{\mathrm{rot}}/E_{\mathrm{T}}$ ratio for the radical and calculate a value for $E_{\mathrm{rot}}^{\ddagger}$ from the $E_{\mathrm{rot}}/E_{\mathrm{T}}$ ratio for the TS. Since, these energies are used to calculate the effective barrier height and both depend on E_{T}, the effective barrier height depends on E_{T} as well. For instance, a radical formed from a C−X bond fission event with an E_{T} value of 4 kcal/mol will have a different effective barrier height compared to one formed from C−X bond fission that imparted an E_{T} value of 18 kcal/mol. Therefore, we need to consider the effective barrier heights for each value of E_{T} in the primary P(E_{T}).

The first part of the branching calculations involves calculating the effective barrier heights for the product channels. The $E_{\mathrm{rot}}/E_{\mathrm{T}}$ ratios at each geometry along the intrinsic reaction coordinate (IRC) for a given channel are calculated from the rotational model and multiplied by the values of E_{T} in the measured primary P(E_{T}) to obtain the rotational energy at each geometry. Rotationally corrected IRCs were then constructed by adding the rotational energy to the B3LYP energies from the IRC with $\vec{J}_{\mathrm{rot}} = 0$. An example set of rotationally corrected IRCs for the unimolecular dissociation of vinoxy is shown in Figure 3.2 (for further explanation of the channels shown, see Section 3.3). The effective barrier height is the zero-point-corrected energy difference between the saddle point and minimum energy geometry on the rotationally corrected IRC. While we could simply subtract the energies at those points in the rotationally corrected IRC to get the effective barrier height, these energies do not include zero-point corrections and are calculated at a lower level of theory. However, we can use the G4 barrier heights and then make corrections to those values using the $E_{\mathrm{rot}}/E_{\mathrm{T}}$ ratios at the minimum and transition state instead. We find that

$$E_{\mathrm{o,effective}} = E_o + \left[\left(\frac{E_{\mathrm{rot}}}{E_{\mathrm{T}}}\right)_{\mathrm{at\ TS}} - \left(\frac{E_{\mathrm{rot}}}{E_{\mathrm{T}}}\right)_{\mathrm{at\ min}}\right] E_{\mathrm{T}} \qquad (4)$$

where $E_{\mathrm{o,effective}}$ is the effective barrier height, E_{o} is the G4 barrier height, and $\left(\frac{E_{\mathrm{rot}}}{E_{\mathrm{T}}}\right)_{\mathrm{at\ TS}}$ and $\left(\frac{E_{\mathrm{rot}}}{E_{\mathrm{T}}}\right)_{\mathrm{at\ min}}$ are the $E_{\mathrm{rot}}/E_{\mathrm{T}}$ ratios at the TS and minimum energy points on the IRC, respectively. In some cases, the rotational corrections can actually cause the minimum or saddle point to shift to another geometry along the IRC, usually nearby. We account for this in the effective barrier height (see Appendix B). After this step, we are left with the effective barrier heights for each channel at all E_{T} values in the primary P(E_{T}).

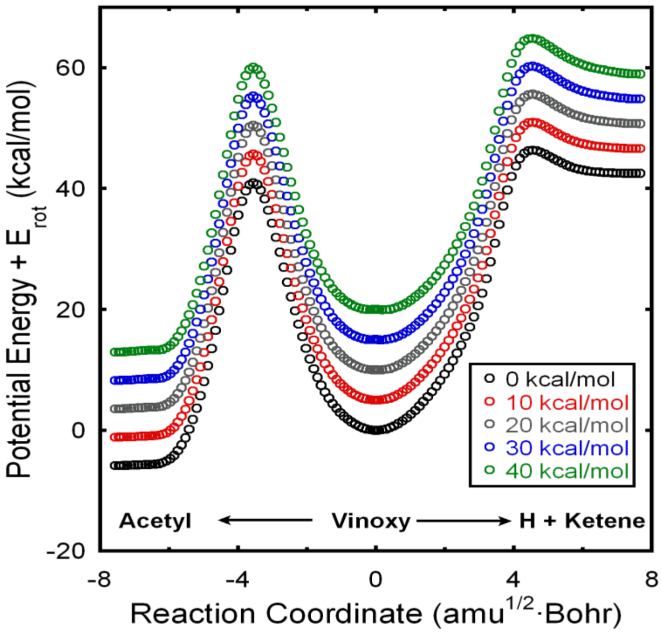

Figure 3.2: Example of the rotationally corrected IRCs for the unimolecular dissociation of the vinoxy radical to H + ketene and isomerization of the vinoxy radical to the acetyl radical produced at various C−Cl photofission relative translational energies. The label at the bottom of the plot indicates which products/intermediate is formed moving in one direction along the reaction coordinate. Energies are not zero-point corrected in this figure and the rotational model used the anti conformer of the chloroacetaldehyde precursor.

The second part of the calculations involves characterizing the vibrational energy of the radicals. Since the effective barrier heights depend on E_T, radical fragments produced from C−X photodissociation with different E_T's have different reaction dynamics. Thus we calculate the vibrational energy of the radicals produced in small E_T ranges within the primary C−X bond fission P(E_T). To calculate E_{vib} for radicals produced from C−X photodissociation, we used the following equation

$$E_{\mathrm{vib}} = h\nu + E_{\mathrm{int}}(\mathrm{precursor}) - D_{\mathrm{o}}(\mathrm{C-X}) - E_{\mathrm{int}}(\mathrm{X}) - \left[1 + \left(\frac{E_{\mathrm{rot}}}{E_{\mathrm{T}}}\right)_{\mathrm{radical}}\right] E_{\mathrm{T}} \tag{5}$$

where $h\nu$ is the photon energy used for photodissociation, E_{int}(precursor) is the internal energy of the halogenated precursor, D_o(C−X) is the carbon-halogen bond dissociation energy, and E_{int}(X) is the internal energy of the halogen. Equation (5) uses conservation of energy and approximates the rotational energy in the radical using E_{rot}/E_T ratio from the rotational model. While it is possible to use average values or the value at the equilibrium geometry for the terms in Equation (5), we consider all possible values of E_{int} (precursor) and E_{rot}/E_T of vinoxy by determining the distributions for each, P(E_{int}(precursor)) and P(E_{rot}/E_T).

Assuming the supersonic expansion of the beam cools the rotational energy of the precursor, E_{int}(precursor) is composed of mostly vibrational energy and so we can approximate P(E_{int}(precursor)) using Maxwell-Boltzmann statistics taking the molecules to be in thermal equilibrium with the nozzle. We first use the Beyer-Swinehart algorithm[14,15] to determine the vibrational degeneracy within a small range about a given E_{vib}. For each E_{vib}, the degeneracy is then weighted by the respective Boltzmann factor to produce P(E_{int}(precursor)). The Beyer-Swinehart algorithm uses the vibrational frequencies of the precursor conformer of interest and an energy grain of 0.1 cm^{-1}. The counts are binned in 0.1 kcal/mol increments centered at each

E_{vib}. The average internal energy calculated from this predicted distribution is in good agreement with the values predicted from statistical mechanics.

As for P($E_{\mathrm{rot}}/E_{\mathrm{T}}$), the nuclear configuration of the precursor changes as it vibrates along any of its normal modes of vibration and so the $E_{\mathrm{rot}}/E_{\mathrm{T}}$ ratio depends on the instantaneous geometry of the precursor along the vibrational mode. Using our rotational model, we can calculate $E_{\mathrm{rot}}/E_{\mathrm{T}}$ imparted at various vibrational displacements from equilibrium along a given normal mode of the precursor. To find the value of P($E_{\mathrm{rot}}/E_{\mathrm{T}}$), we approximate the probability of finding the precursor with that displacement using the square of the harmonic vibrational wave function and then make the appropriate Jacobian corrections. The vibrational mode for the conformer of interest that produces the largest change in $E_{\mathrm{rot}}/E_{\mathrm{T}}$ at the classical turning points is chosen for this analysis and the range of displacements extended beyond the classical turning points for the mode.

Using Equation (5) and by convolving P(E_{int}(precursor)) and P($E_{\mathrm{rot}}/E_{\mathrm{T}}$) together, a vibrational energy distribution, P(E_{vib}), for the radical fragments from C−X photodissociation with a given E_{T} can be constructed. If we can measure the P(E_{T}) for each spin-orbit state (either $J = 3/2$ or $J = 1/2$) of the halogen cofragment separately, we make a P(E_{vib}) for the radicals produced with the halogen cofragment in both spin-orbit states by taking into account the spin-orbit splitting. These P(E_{vib})s are then scaled by the relative probability of producing the radical and the respective spin-orbit state from C−X bond fission with a given range of E_{T} using the weighted P(E_{T})s for each process. The contributions are then added together to produce a total P(E_{vib}) at a given E_{T}. Both P(E_{int}(precursor)) and P($E_{\mathrm{rot}}/E_{\mathrm{T}}$) are normalized before calculating P(E_{vib}) to ensure it would be normalized after the convolution (but prior to scaling). P(E_{vib})

values are binned in E_{vib} increments smaller than the E_{T} increment of the experimentally determined P(E_{T})s.

The final part of the calculations used RRKM calculations to determine the product branching. From the previous parts, we now have a P(E_{vib}) for the radical fragment and an effective barrier height at each E_{T} in the primary P(E_{T}). At a given E_{T} value, we calculate the RRKM rate constant for each channel, k_{n}, using the E_{vib}'s from the P(E_{vib}), the effective barriers for that channel, and the vibrational frequencies for the radical and TSs leading to the products. To get the branching fraction to each channel for radicals with a given E_{vib}, we calculate, $k_{\mathrm{n}}/k_{\mathrm{tot}}$, where $k_{\mathrm{tot}} = \sum_{\mathrm{n}} k_{\mathrm{n}}$. Once we have the branching fraction for every value of E_{vib} in P(E_{vib}) for a given E_{T}, we then get a branching fraction at that E_{T} to each channel by discretely integrating the product of the P(E_{vib}) and $k_{\mathrm{n}}/k_{\mathrm{tot}}$ or over all values of E_{vib}.

$$\text{branching to channel n} = \int_{E_{\mathrm{vib},i}}^{E_{\mathrm{vib},f}} P(E_{\mathrm{vib}}) \left(\frac{k_{\mathrm{n}}}{k_{\mathrm{tot}}}\right) dE_{\mathrm{vib}} \qquad (6)$$

We then determine the portion of the radicals going to this channel by multiplying the branching fraction at each E_{T} by the experimentally determined P(E_{T}) value at the same E_{T}. Doing this for all of the E_{T} values in the P(E_{T}) thus gives us the portion of the primary P(E_{T}) that we predict to give radicals that then dissociate through a given channel.

3.3 Model Predictions for Photodissociation of Chloroacetaldehyde at 157 nm and the Branching of Vinoxy

In Chapter 2, we detailed a velocity map imaging study on the photodissociation of chloroacetaldehyde at 157 nm. The primary goal of this study was to resolve the discrepancy between the experimental and RRKM predictions for the branching between the two major product channels of the vinoxy radical, H + ketene and methyl + CO. While we were unable to measure a branching ratio between these two channels, we were able to make a few qualitative statements about the product branching based on the ketene data taken at *m/z* =42. As a complementary study, this section uses the branching model described above to predict the portion of the C−Cl bond fission P(E_T) producing vinoxy radicals that undergo dissociation to H + ketene and methyl + CO. By taking advantage of momentum conservation in the dissociation to H + ketene, we find that we can directly compare the predictions of this model to the ketene data.

3.3.1 Considerations for the Branching Model

There were a few things we must consider when using the model for this system. First, excitation of chloroacetaldehyde at 157 nm is expected to put the molecule onto a few excited-state surfaces that are repulsive in Franck-Condon region. We therefore expect the branching calculations, specifically assuming $\vec{J}$ imparted from an impulsive force in the Franck-Condon region, to be appropriate for this system. We also assume that the subsequent dynamics occurs on the ground state PES of vinoxy despite the possibly of generating vinoxy in the Ã or B̃ state. Previous experimental work[16] has used the same assumption pointing to an effective internal conversion mechanism from the Ã or B̃ state to the ground state. This internal conversion mechanism has also been supported by theoretical studies of the vinoxy system.[17,18] It is also worth noting that the before dissociating to methyl + CO, the vinoxy radical isomerizes to the acetyl radical; however, the barrier for the isomerization to acetyl is much larger than the subsequent barrier to form the methyl + CO products. We therefore treat the isomerization barrier as a bottleneck for this channel and assume that any vinoxy radicals that form acetyl go on to produce methyl + CO.

Second, the spin-orbit state of the Cl atom cofragment was account for in the branching calculations since we detected the Cl($^2P_{3/2}$) and Cl($^2P_{1/2}$) cofragments separately in the velocity map imaging study. Separate P(E_{vib})s were made for vinoxy radicals produced from C−Cl photodissociation with Cl($^2P_{3/2}$) and with Cl($^2P_{1/2}$) as the cofragment by taking the internal energyof Cl to be either 0 or 2.5 kcal/mol, respectively. These P(E_{vib})s were then scaled by the relative probability of producing vinoxy and the respective spin−orbit state from C−Cl bond fission with that given range of E_T using the weighted P(E_T)s for each process. The contributions were then added together to produce a total P(E_{vib}) at a given $\mathrm{E_T}$ binned in 0.1 kcal/mol increments. The weighted P(E_T)s for photodissociation events leading to Cl($^2P_{3/2}$) and Cl($^2P_{1/2}$) were used to account for the branching ratio as well as the number of radicals produced from photodissociation events with that range of E_T. These distributions were smoothed by averaging the P(E_T) values determined from the data in each E_T range of 2.5 kcal/mol, putting the average value in the weighted center of the range, and then interpolated to a spacing of 0.5 kcal/mol (shown in Appendix B).

Third, the aldehydic H of the vinoxy radical moves out of the C-C-O plane when it leaves to form H + ketene products or moves over to the terminal C atom to form the acetyl radical. Since the vinoxy radical has a planar structure, the H atom can depart or move on either side of the radical leading to two possible TSs (enantiomers) for each product channel that are energetically equivalent. However, the dynamics through the two TSs will be different when we consider the rotational energy as the angular momentum vector has the same orientation in both, but the geometries of the TSs, and thus their inertia tensors, are different. Therefore, the enantiomers of the two TSs (shown in Figure 3.3) were also considered giving four sets of effective barrier heights: two for the isomerization (and thus formation of methyl + CO products), and two for the formation of H + ketene products. When calculating the RRKM rate constants, we summed the rate constants for all channels going to the same products giving us a total rate constant for the isomerization channel and a total rate constant for the H + ketene channel. The branching fractions and portions of the primary C−Cl bond fission P(E_T) we calculated thus represent the product branching to H + ketene and methyl + CO and not the branching through a particular channel or TS.

Finally, we needed to consider the possible conformers of chloroacetaldehyde and their respective contributions to the portions of the P(E_T) producing unstable radicals. Chloroacetaldehyde has three conformers: one syn and two anti, that differ in their respective Cl−C−C−O dihedral angles. While we did run the model with all three conformers, we found that the two anti conformers produced identical contributions when run separately. We are therefore able to describe the dynamics of both using only one of the anti conformer geometries. To account for the conformers of chloroacetaldehyde, the calculations were run for each conformer using the C−Cl bond fission P(E_T)s for photodissociation events leading to Cl($^2P_{3/2}$) and Cl($^2P_{1/2}$) scaled by the relative population of that conformer in the molecular beam. This provided us with the contributions of each conformer to the portions of the C−Cl fission P(E_T) forming vinoxy radicals that dissociate to form H + ketene and methyl + CO. The contributions from each conformer to the portions were then summed together to give the total portions.

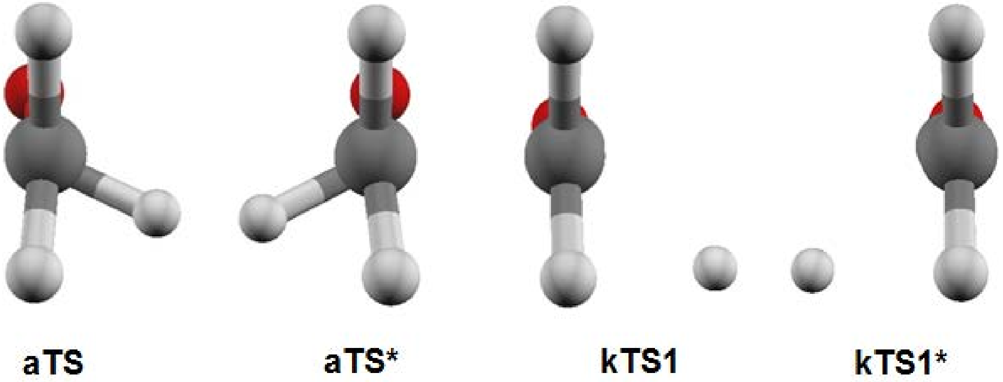

Figure 3.3: Depiction of TSs for the isomerization channel (aTS) and H + ketene channel (kTS1) from the vinoxy radical. The “*” in the name of the transition states denotes that it is the enantiomer of the given transition state. These geometries and their vibrational frequencies were calculated at the B3LYP/6-311++G(3df,2p) level of theory.

3.3.2 Results

Using the rotationally corrected IRCs, we were able to determine the effective barrier heights for all four channels leading from the vinoxy radical to either the acetyl radical (through aTS and aTS*) or H +ketene products (through kTS1 and kTS1*). The effective barrier heights for these channels were calculated over an E_T range of 0 – 70 kcal/mol in 0.5 kcal/mol increments to match the range and increments of the experimentally determined P(E_T)s. We ran these calculations using both conformers of chloroacetaldehyde in the rotational model to give two sets of effective barrier heights, shown in Figure 3.4. At $E_T = 0$ kcal/mol, the effective barrier heights are just the G4 barrier heights for the isomerization channel and the H + ketene channel which are 40.6 kcal/mol and 42.2 kcal/mol, respectively. From there, the barrier heights depend on the change in rotational energy as the vinoxy radical reaches the TSs on the PES.

Looking at Figure 3.4, the notable aspect of both plots is that the calculations using a different conformer produced different results. This is to be expected as the dihedral angle of the Cl atom differs in each and so C−Cl bond fission in each conformer imparts an angular momentum vector to the radical moiety with a different orientation. However, we do see similar trends in the effective barrier heights for the isomerization channel and H + ketene channel. The effective barriers for the TSs leading to H + ketene, kTS1 and kTS1*, tend to decrease as E_T increases and this is the case for both conformers. This implies that vinoxy radicals produced from photodissociation events with larger E_T values have an easier time getting over the barrier compared to the case in which we do not consider rotational energy. The barriers for the isomerization channels, aTS and aTS*, appears to increase when the anti conformer is used in the calculation and decrease when the syn conformer is used in the calculation. However, the differences between the effective barrier heights and the G4 barrier heights tend to be small (less than 1 kcal/mol) suggesting that the rotational corrections do not affect the barriers for this channel to a large extent. The rotational corrections have a bigger effect on the barriers for the H + ketene channel because the difference between the effective and G4 barrier heights tends to be larger. While the effect on either channel may seem small, the branching will depend on which channels dominate over a particular range of E_T values and the sums and densities of vibrational states for those channels over that range.

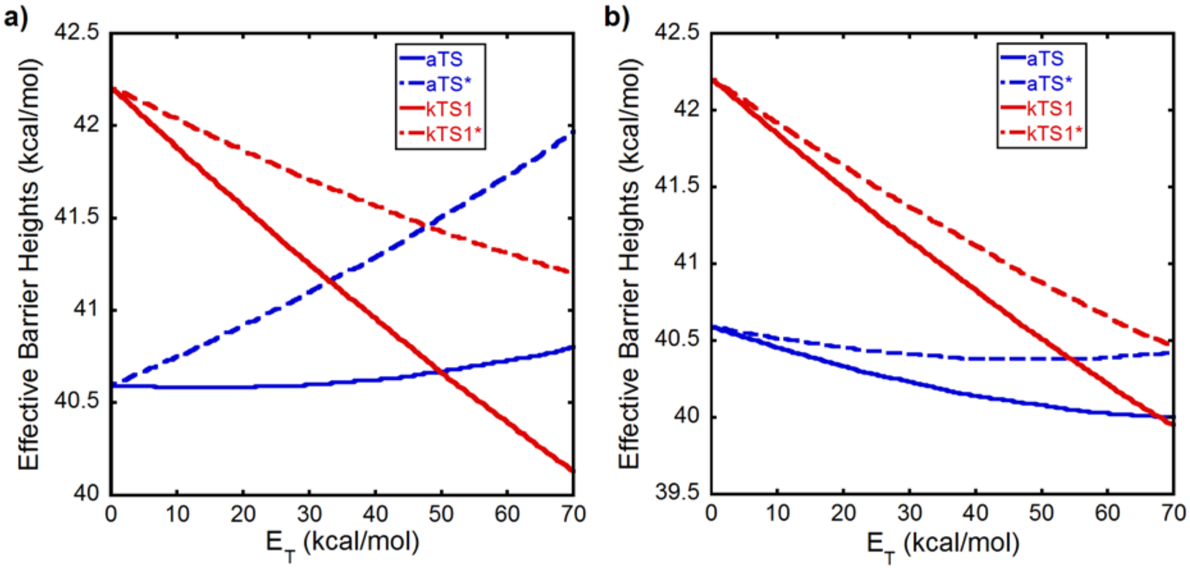

Figure 3.4: Plot of the E_T dependence on the effective barrier height calculated from the rotational model using the anti conformer (a) and the syn conformer (b).

Following the outlined procedure and taking into account our particular considerations for this system, we were able to calculate the branching fractions for each product channel at every E_T in our total C−Cl bond fission P(E_T). Figures 3.5 and 3.6 show the E_T dependence of the branching fractions for the H + ketene and methyl + CO product channels calculated using the anti conformer and syn conformer, respectively. At lower E_T's, we see that the branching fraction for each product channel is relatively constant and the H + ketene product channel clearly dominates. As E_T increases, we see more branching to the methyl + CO product channel; however, the H + ketene product channel still dominates over most, if not all, of the E_T range. It is also interesting to note that at higher E_T's, the branching fraction do not sum to unity because we start producing stable vinoxy radicals. While the branching fractions alone provide useful information, the overall goal of the branching calculations is to calculate the portions of the primary C−Cl bond fission P(E_T) producing vinoxy radicals that dissociate to H + ketene and methyl + CO.

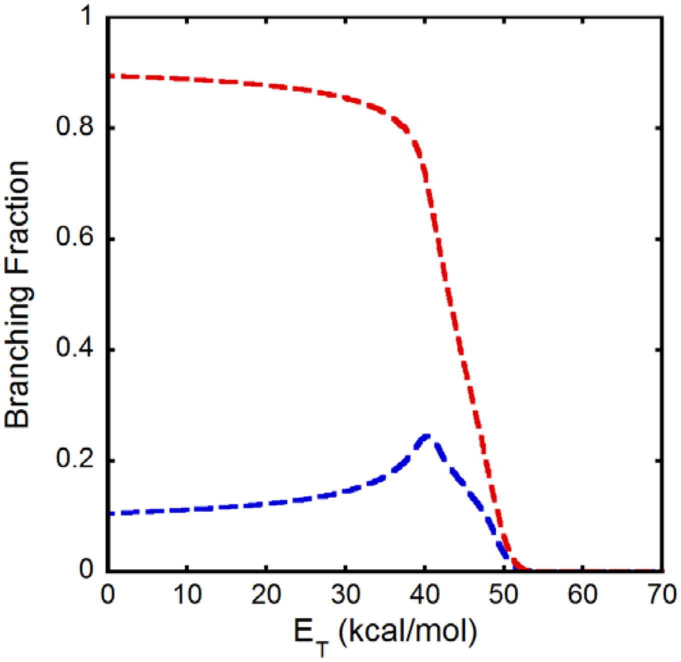

Figure 3.5: E_T dependence of the branching fraction for the H + ketene channel (shown in red) and the methyl + CO channel (shown in blue) from our branching calculations using the G4 barrier heights for both product channels and the anti conformer of chloroacetaldehyde. At higher E_T's, the branching fractions do not sum to unity because some of the vinoxy radicals are stable. The inflection in the branching fraction of the methyl + CO product channel is a result of the differing behavior between the effective barrier heights of aTS and aTS* as E_T increases.

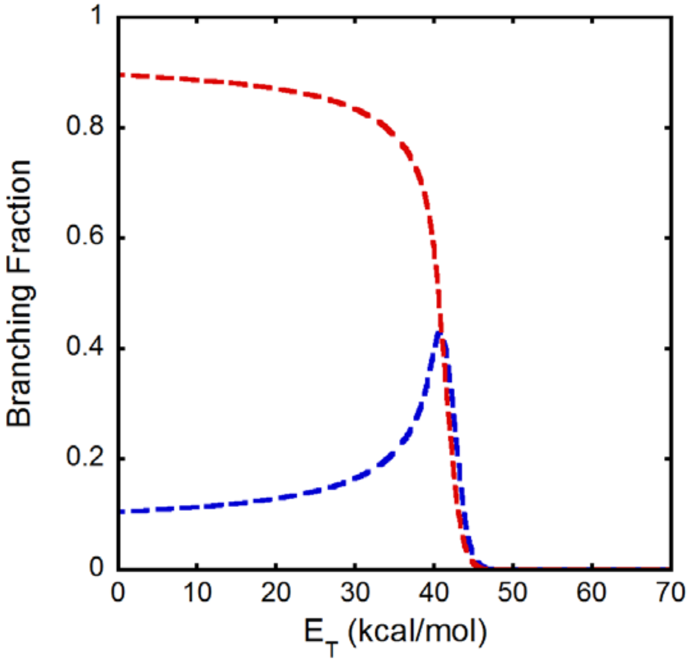

Figure 3.6: E_T dependence of the branching fraction for the H + ketene channel (shown in red) and the methyl + CO channel (shown in blue) from our branching calculations using the G4 barrier heights for both product channels and the syn conformer of chloroacetaldehyde.

The results of the branching calculations using the calculated G4 barrier heights for both channels are shown in Figure 3.7. In the upper frame, the red dashed line shows the portion of the primary C−Cl bond fission P(E_T) leading to vinoxy radicals that produce H + ketene products and the blue dashed line shows that producing methyl + CO products. The primary C−Cl bond fission P(E_T) is shown in black solid line for reference and the portion of the P(E_T) representing vinoxy radicals that are stable to secondary dissociation is shown in dashed gray line (this was obtained by subtracting the portions leading to the two sets of products from the primary P(E_T)). From this figure, it looks as though the production of ketene dominates at lower E_T values (i.e. higher E_{vib} values); the contribution from vinoxy radicals going to methyl + CO products is low at lower E_T values and gradually increases. Stable vinoxy radicals dominate at E_T values greater than 50 kcal/mol.

The recoil kinetic energy imparted in the dissociation of vinoxy to H + ketene is expected to have little effect on the net speed of ketene given the large mass difference between the fragments. This allowed us to approximate the speed distribution of the vinoxy radicals that dissociate to H + ketene from the experimental speed distribution of ketene and thus derive a measured P(E_T) for vinoxy radicals that produce ketene. This experimental result is shown in green line in Figure 3.7. Our branching calculations predict a P(E_T) for vinoxy radicals that produce ketene and so we can compare the measured ketene portion to that predicted from our RRKM calculations using the G4 barrier of 42.2 kcal/mol. We show both the predicted and experimental ketene portions in dashed red line and solid green line, respectively, in the lower frame of Figure 3.7 for comparison. The measured ketene portion was scaled relative to the predicted portion in the range of E_T from 5 to 15 kcal/mol where we expect the branching to remain relatively constant. While the lower E_T values give a decent agreement to the experiment, the calculations predict too much ketene at higher E_T values near 40 kcal/mol, where the vibrational energy in the vinoxy radical is near the calculated threshold for dissociation to H + ketene.

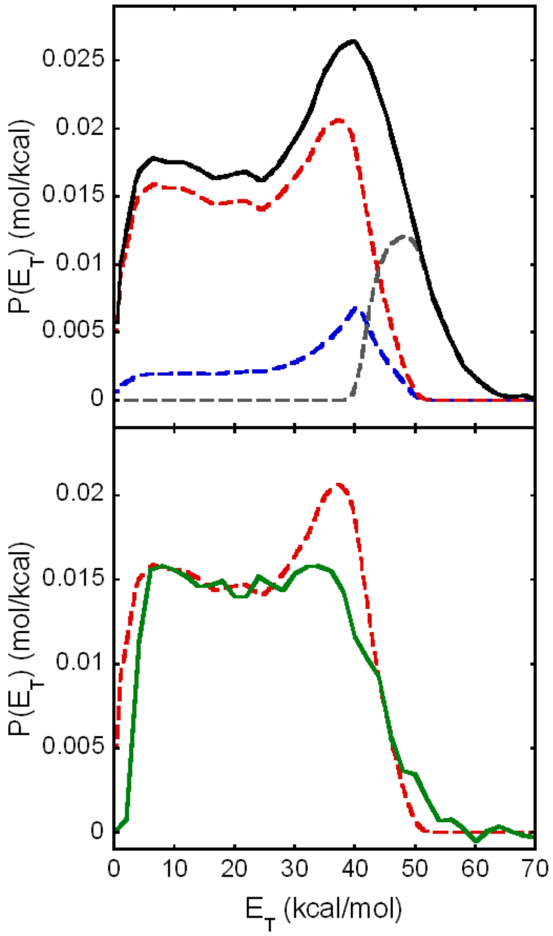

Figure 3.7: Results of the branching calculations using the calculated G4 barrier height (42.2 kcal/mol) for the H loss channel. The upper frame shows the total primary C−Cl bond fission P(E_T) (solid black curve) along with the predicted portions that produce H + ketene products (dashed red curve), methyl + CO products (dashed blue curve), and stable vinoxy radicals that do not dissociate (dashed gray curve). The "stable" portion of the P(E_T) is the distribution of C−Cl photofission events that our model predicts partitions insufficient vibrational energy to the vinoxy radicals to surmount the lowest barrier en route to dissociation. The lower frame shows a comparison of the experimental (solid green curve) and predicted (dashed red curve) portion of the primary P(E_T) that results in H + ketene products. The experiment portion has been scaled to match the predicted portion and is the same curve as that depicted in Figure 2.6. Note how the branching calculations predict more vinoxy radicals producing H + ketene at higher translational energies than the experimental portion shows.

To resolve the disagreement between the measured and predicted portion of the P(E_T) leading to ketene using the calculated G4 barrier heights for both channels, we decided to alter the barrier height used in our calculation to improve the comparison. In our branching calculations, the effective barrier heights for a given channel are determined by correcting the G4 barrier height for the channel based on the rotationally corrected IRCs. However, we could choose to use a barrier height for a channel that is different from the calculated G4 barrier height. Changing the energy of the barrier but the not the TS geometry, we apply the same rotational corrections to this new barrier height to get effective barrier heights. The plots of the effective barrier heights would have the same curvature as those previously calculated using the G4 barrier heights (Figure 3.4), but the curves for the H + ketene channels (in red) would be shifted upward if we used a barrier to the H + ketene channel that was larger than that calculated with the G4 method. We therefore ran our branching calculation changing only the H + ketene barrier height to try to get a ketene portion that better agreed with the experimentally-determined ketene portion.

The best agreement was achieved using a barrier height of 44.6 kcal/mol for the H + ketene channel; the results of the branching calculation using this barrier height are shown in Figure 3.8. The upper frame shows the portions of the primary C−Cl fission P(E_T) that produce vinoxy that dissociates to H + ketene and methyl + CO products along with the portion that is stable to secondary dissociation. There is clearly less production of ketene at higher E_T values than we saw with the calculated G4 barrier height and production of methyl now dominates in the E_T range of 40 to 52 kcal/mol. In the bottom frame, we see that the measured and predicted portions that produce ketene agree more closely, as there is no longer too much ketene predicted at higher E_T values near 40 kcal/mol. These results suggest that the difference in energy between the barrier to H + ketene and the isomerization barrier en route to CH_3 + CO is underestimated in the G4 results; the best fit to our data results from using a H + ketene barrier that is about 4.0 ± 0.5 kcal/mol higher than the isomerization barrier.

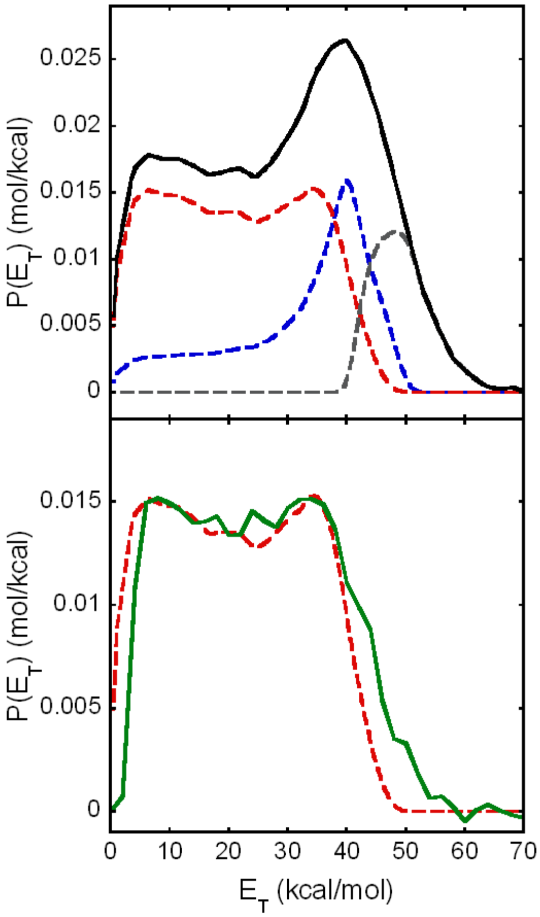

Figure 3.8: Results of the branching calculations using a barrier height of 44.6 kcal/mol for the H loss channel. The upper frame shows the total primary C−Cl bond fission P(E_T) (solid black curve) along with the predicted portions that produce H + ketene products (dashed red curve), methyl + CO products (dashed blue curve), and stable vinoxy radicals that do not dissociate (dashed gray curve). The "stable" portion of the P(E_T) is the distribution of C−Cl photofission events that our model predicts partitions insufficient vibrational energy to surmount the lowest barrier en route to dissociation. The lower frame shows a comparison of the experimental (solid green curve) and predicted (dashed red curve) portion of the primary P(E_T) that results in H + ketene products. The experiment portion has been scaled to match the predicted portion and is the same curve as that depicted in Figure 2.6. The experimental and predicted portions agree much better using this barrier height than the calculated G4 barrier height.

For comparison, we show the E_T dependence of the branching fractions for the H + ketene and methyl + CO product channels from our branching calculations using the new barrier height for the H + ketene channel and each conformer of chloroacetaldehyde in Figures 3.9 (anti conformer) and 3.10 (syn conformer). Note that the branching fractions at lower E_T values are still relatively constant and the H + ketene product channel dominates in this region. However, branching to the methyl + CO product channel becomes more significant at higher E_T values and the methyl + CO product channel dominates at E_T value greater than 35 kcal/mol. This is the E_T range where the branching calculations using the G4 barrier heights predicted more ketene than we observed experimentally. Therefore, the new barrier height corrects for the overestimate in the predictions using the G4 barrier height while preserving the behavior at lower E_T's that was consistent with the data.

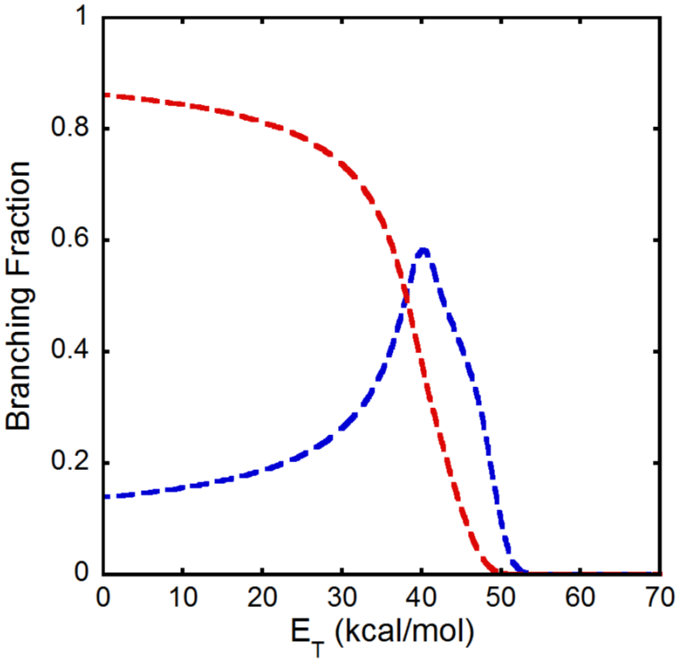

Figure 3.9: E_T dependence of the branching fraction for the H + ketene channel (shown in red) and the methyl + CO channel (shown in blue) from our branching calculations using a barrier height of 44.6 kcal/mol for the H + ketene channel and the anti conformer of chloroacetaldehyde. At higher E_T's the branching fractions do not sum to unity because some of the vinoxy radicals are stable.

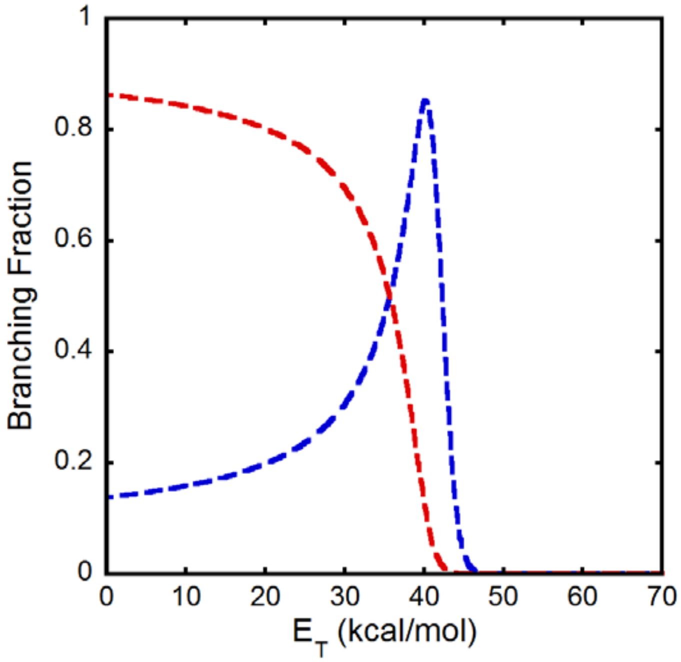

Figure 3.10: E_T dependence of the branching fraction for the H + ketene channel (shown in red) and the methyl + CO channel (shown in blue) from our branching calculations using a barrier height of 44.6 kcal/mol for the H + ketene channel and the syn conformer of chloroacetaldehyde.

3.4 Discussion

To accurately treat the chemical dynamics of radicals produced from the photodissociation of a halogenated precursor, it is important to account for the partitioning of the total energy in the radical into vibration and for the effects of angular momentum conservation as the radical surmounts a barrier on the PES. We therefore developed a model that takes these factors into account and predicts the portions of the primary carbon-halogen bond fission $P(E_T)$ that would produce radicals that dissociate to each of the product channels. This model incorporates RRKM rate constants to determine the branching between channels and uses the rotational model developed by our group to predict the effects of the rotational energy in the nascent radical on the dynamics. Assuming that the photodissociation dynamics occurs on an excited surface of the precursor that is repulsive in the Franck-Condon region and the unimolecular dissociation of the nascent radicals proceeds on the ground electronic state PES, we expect the branching model to accurately describe the system.

To help analyze the data presented in Chapter 2, we applied the branching model to the photodissociation of chloroacetaldehyde at 157 nm. We primarily wanted to see how the rotational energy imparted to the vinoxy radical during photodissociation affected the dynamics of the radical. From the effective barrier heights (Figure 3.4), we find that the effective barrier to the H + ketene channel decreases in photodissociation events that impart a larger amount of recoil translational energy to the system. This implies that the rotational energy of the radical at the TS geometry is less than the rotational energy at the minimum geometry along the rotationally corrected IRC. Considering conservation of angular momentum, the lower rotational energy at the TS geometry is likely due to the opening of the C-C-O bond angle in the vinoxy radical as it nears the TS, which slows down the rotational motion of the radical. For the isomerization barrier, we see varied and minimal effects; the effective barrier heights either increase or decrease from the G4 barrier height, but not by much. Since the C-C-O bond angle is similar in both the vinoxy radical and TS geometries, the varied effects are likely due to where the moving H atom is in relation to the axis of rotation. While the overall difference in the effective barrier heights for both channels from their respective G4 barrier heights is no greater than 2 kcal/mol, this difference is enough to make the H + ketene product channel dominate at nearly all E_T's (Figures 3.5 and 3.6). This is initially surprising given that the barrier en route to the CH_3 + CO channel is the lower one at $J = 0$. Therefore, we see how the rotational energy of a photolytically-produced radical can play a big role in its subsequent dissociation dynamics.

While the results of the branching calculations using the G4 barrier heights for the H + ketene channel and the isomerization channel to the acetyl radical (see Figure 3.7) agree with the data at most E_T values, there is a discrepancy at high E_T values near the threshold for production of H + ketene. In a previous study on the photodissociation of chloroacetaldehyde at 193 nm, Miller et al.[19] observed suppression of the H + ketene channel and attributed this to nonadiabatic recrossing. However, Young and Yarkony[20] found that the conical intersections in proximity to the TSs en route to H + ketene products would not facilitate any nonadiabatic recrossing. Based on these past studies, we have attempted to analyze our data using statistical transition state theory without considering nonadiabatic recrossing. It is possible, then, that the negligible branching to H + ketene observed in the previous study by Miller et al. may simply be the result of a higher barrier for the H + ketene channel than that predicted using the G4 electronic structure method. While our G4 barrier heights are in good agreement with the previous G3//B3LYP calculations, these barriers are not consistent with Miller's data nor with the internal energy dependence of the branching to H + ketene obtained in the current study.

By running the branching calculations with a barrier height of 44.6 kcal/mol for the H + ketene channel as opposed to the G4 barrier height (see Figure 3.8), we were able to obtain a better agreement between the predicted and experimental ketene portions of the P(E_T). This new barrier height is slightly above the barrier height predicted from the high-level *ab initio* calculations (43.0 kcal/mol) done by Bennett et al.[21] While this change in barrier height is relatively small, its effect can be rather large as methyl production only occurs at vibrational energies below and several kcal/mol above the H + ketene barrier height. A higher barrier for the H + ketene channel would therefore allow the methyl + CO channel to dominate the product branching over a larger range of vibrational energies in the radical. In turn, this would increase the branching fraction for methyl + CO. Overall, the results of the branching calculations suggest that the barrier height of the H + ketene channel is higher than predicted by the G4 method. Note that our data is sensitive to the difference in the H + ketene barrier and the isomerization barrier, and the analysis relies on a C−Cl bond energy, so the robust conclusion is that the H + ketene barrier is 4.0 ± 0.5 kcal/mol above the isomerization barrier (44.6 – 40.6) if one assumes that the product branching is statistical. Since the fit between the predicted and experimental ketene portion of the P(E_T)s is good, this interpretation of the data is also consistent with the assumption that the secondary dissociation of vinoxy occurs along the ground electronic state PES despite the fact that the nascent vinoxy radicals are likely produced in the $\tilde{A}$ or $\tilde{B}$ state.

In using statistical transition state theory for our branching model, we also assumed that tunneling does not contribute significantly to the branching between the channels. While the barrier to the H + ketene product channel is too broad for tunneling to be significant, tunneling through the isomerization channel to acetyl en route to CH_3 + CO is possible. However, most of our vibrational energy distribution is above this barrier, so we do not expect tunneling to contribute significantly to the branching to this channel. The very small fraction of radicals formed with vibrational energies just below the isomerization barrier might dissociate via tunneling on the time scale of the short delay between our photodissociation and ionization laser, but the analysis of the onset of the ketene + H product channel would be unaffected.

In the vinoxy study described in Chapter 2, we were unable to calculate an experimental branching ratio for the H + ketene and methyl + CO channels due to ambiguity in fitting the signal at m/z = 15. However, we can use the results of the branching calculations that best fit the signal at m/z = 42 to predict a branching ratio. Since we predicted the portions of the C–Cl bond fission P(E_T) that produce vinoxy radicals which go to either channel, we can simply integrate the area under each partial P(E_T) to find the amount of unstable vinoxy radicals that produce ketene + H and methyl + CO upon secondary dissociation. We therefore calculate a branching of ketene to methyl as ~ 2.1:1. Using the photoionization cross-sections of these species at 10.5 eV, we can also predict the ratio of the photoion signal between the species, $\frac{N_{\text{ketene}^+}}{N_{\text{methyl}^+}}$. The photoionization cross section of ketene to *m/z* = 42 is a factor of 4.3 larger than that of methyl radicals to *m/z* = 15, so we predict a signal ratio of ~9 from the predicted product branching of 2.1:1. This suggests that the ketene signal should be ~ 9 times greater than the methyl signal and would explain the low signal-to-noise for the m/z = 15 data shown in Chapter 2 (Figure 2.7). Since the appearance energy of fragments from ketene and methyl radical are well above the photoionization energy used in this experiment, we do not expect to lose any neutral ketene and methyl products to dissociative ionization.

Much like in our results, the photodissociation of methyl vinyl ether at 193 nm also produced vinoxy radicals mostly in the Ã state.[22] Other similarities between the two studies include the production of vinoxy radicals with high internal energies (as well as a similar range of internal energies in the nascent vinoxy) and larger branching to H + ketene over CH_3 + CO. While we have rationalized the larger branching to H + ketene by citing the higher internal energy in the vinoxy radical, this preferential branching to H + ketene products when vinoxy is formed in its Ã state could instead result from a direct dissociation pathway on the Ã state. A more extensive computational study of the dynamics on the Ã state would be helpful in finding such a pathway and, if it exists, seeing how it competes with relaxation to the ground state.

While Miller et al. did not attribute any of the signal at *m/z* = 42 to ketene from the secondary dissociation of vinoxy, they did see signal from the ketene co-fragment to HCl photoelimination. Minor HCl photoelimination channels have also previously been detected by Lin et al.[23] in the photodissociation of CH_3Cl at 157 nm. We should therefore account for the possibility of HCl photoelimination in the photodissociation at 157 nm and how much that contributes to the ketene signal. It is important to note that contributions to the ketene signal from HCl photodissociation does not change the conclusions reached from our branching calculations using the G4 barrier heights. When scaling the predicted and experimental ketene portions, we looked at the E_T range from 5 – 15 kcal/mol. Since we would only detect stable ketene from HCl photoelimination and these fragments will have higher recoil translational energies, we do not expect any contribution from this primary channel in the scaling range. Therefore, we would still conclude that the G4 barrier heights predict too much ketene if there are contributions from HCl photoelimination in the data. If anything, any contribution from HCl photoelimination would change the determination of the H + ketene barrier height as we could be accounting for more ketene from the secondary dissociation of vinoxy than is actually present. In the present work, the small unfit signal on the fast edge of the ketene portion in Figure 3.8 may be due to ketene from HCl photoelimination, which we consider in Appendix B. In Chapter 4, we take a more in-depth look at the other primary channels in the photodissociation of chloroacetaldehyde at 157 nm, namely, the contribution from HCl photoelimination.

Overall, the branching model provides a unique insight into the effects of rotational energy on the dynamics of photolytically-produced radicals.

3.5 References

(1) Levine, R. D.; Bernstein, R. B. *Acc. Chem. Res.* **1974**, *7*, 393-400.

(2) Band, Y. B.; Freed, K. F. *J. Chem. Phys.* **1975**, *63*, 3382-97.

(3) Mitchell, R. C.; Simons, J. P. *Faraday Discuss. Chem. Soc.* **1967**, *44*, 208-17.

(4) Riley, S. J.; Wilson, K. R. *Faraday Discuss. Chem. Soc.* **1972**, *53*, 132-46.

(5) Busch, G. E.; Wilson, K. R. *J. Chem. Phys.* **1972**, *56*, 3626-38.

(6) Holdy, K. E.; Klotz, L. C.; Wilson, K. R. *J. Chem. Phys.* **1970**, *52*, 4588-99.

(7) North, S. W.; Blank, D. A.; Gezelter, J. D.; Longfellow, C. A.; Lee, Y. T. *J. Chem. Phys.* **1995**, *102*, 4447-60.

(8) McKown, B. G.; Ceriotti, M.; Womack, C. C.; Kamarchik, E.; Butler, L. J.; Bowman, J. M. *J. Phys. Chem. A* **2013**, *117*, 10951-10963.

(9) Brynteson, M. D.; Womack, C. C.; Booth, R. S.; Lee, S.–H.; Lin, J. J.; Butler, L. J. *J. Phys. Chem. A* **2014**, *118*, 3211-3229.

(10) Felder, P. *Chimica* **1994**, *48*, 43-9.

(11) Ashfold, M. N. R; Lambert, I. R.; Mordaunt, D. H.; Morley, G. P.; Western, C. M. *J. Phys. Chem.* **1992**, *96*, 2938-49

(12) Klippenstein, S. J. *Comprehensive Chemical Kinetics.* **2003**, *39*, 55-103.

(13)The RRKM code was obtained from W. L. Hase and D. L. Bunker, *Quantum Chemistry Program Exchange 234*, 1974.

(14) Beyer, T.; Swinehart, D. F. Algorithm 448: Number of Multiply-Restricted Partitions. *Comm. ACM* **1973**, *16*, 379.

(15) Stein, S. E.; Rabinovitch, B. S. *J. Chem. Phys.*, **1973**, *58*, 2438-45.

(16) Osborn, D. L.; Choi, H.; Mordaunt, D. H.; Bise, R. T.; Neumark, D. M.; Rohlfing, C. M. *J. Chem. Phys.* **1997**, *106*, 3049-66.

(17) Matsika, S.; Yarkony, D. R. *J. Chem. Phys.* **2002**, *117*, 7198-206.

(18) Piechowska-Strumik, K.; Lauvergnat, D.; Bacchus-Montabonel, M.-C.; Desouter-Lecomte, M. *Chem. Phys. Lett.* **2006**,425, 16–21.

(19) Miller, J. L.; McCunn, L. R.; Krisch, M. J.; Butler, L. J.; Shu, J. *J. Chem. Phys*. **2004**, *121*, 1830-8.

(20) Young, R. A.; Yarkony, D. R. *J. Chem. Phys*. **2005**, *123*, 084315.

(21) Bennett, D. I.; Butler, L. J.; Werner, H.-J. J. *Chem. Phys*. **2007**, *127*, 094309.

(22) Morton, M. L.; Szpunar, D. E.; Butler, L. J. *J. Chem. Phys*. **2001**, *115*, 204-16.

(23) Lin, J. J.; Chen, Y; Lee, Y. Y.; Lee, Y. T.; Yang, X. *Chem. Phys. Lett.* **2002**, *361*, 374–82.

CHAPTER 4

CHARACTERIZATION OF PRIMARY PRODUCT BRANCHING IN THE PHOTODISSOCIATION OF CHLOROACETALDEHYDE AT 157 nm

4.1 Introduction

In the previous chapters, we detailed our velocity map imaging study on the photodissociation of chloroacetaldehyde at 157 nm,[1] undertaken with the purpose of characterizing the unimolecular dissociation of the vinoxy radical. We detected a significant amount of products from the H + ketene and methyl + CO product channels finding that the H + ketene product channel dominated for the high internal energy radicals produced at 157 nm. This is in contrast to the results of the previous study done by Miller et al.[2] on the photodissociation of chloroacetaldehyde at 193 nm, which produced lower internal energy radicals that primarily dissociated to CH_3 + CO. While we were unable to calculate a branching ratio between the channels due to difficulty in fitting the *m/z* = 15 (CH_3^+) signal, we used our branching calculations to predict a branching ratio for H + ketene/methyl + CO of 2.1:1 (averaged over the ro-vibrational distribution of radicals produced with 157 nm photodissociation of chloroacetaldehyde). The statistical model assumes the dissociation of vinoxy radicals occurs on the ground-state potential energy surface and accounts for the change in rotational excitation of the nascent vinoxy radicals between equilibrium geometry and the transition states for unimolecular dissociation to H + ketene and CH_3 + CO. The model uses the measured relative velocity between the Cl and vinoxy to predict the angular momentum in the vinoxy radical assuming it is imparted at the equilibrium geometry of the precursor from a repulsive force in the Franck-Condon region. Based on the data and electronic structure calculations, C−Cl photofission of chloroacetaldehyde produced vinoxy radicals in both its $\tilde{A}$ and $\tilde{B}$ electronical states. We made no attempt to characterize any other primary photodissociation channels of chloroacetaldehyde at 157 nm.

While the vinoxy radical is of great interest due to its role as an intermediate in combustion reactions, chloroacetaldehydes are of interest in atmospheric chemistry due as they are intermediates in the degradation of chlorinated alkanes and alkenes. In fact, monochloroacetaldehyde has been detected as an intermediate in the oxidative degradation of 1,3-dichloropropene[3] and is a major product in the OH-initiated oxidation of ethyl chloride and 1,2-dichloroethane, which is used in the production of vinyl chloride.[4,5] Photolysis and reaction with OH radicals and Cl atoms are the primary loss channels for chloroacetaldehydes determining the atmospheric lifetime of these species.[5] While the kinetics of the chloroacetaldehydes have been studied in great detail, few studies have been done on their photodecomposition and therefore little is known about the primary photodissociation pathways. Such studies can provide insight into the excited-state dynamics of the chloroacetaldehydes and provide information not only on the species released into the atmosphere by photolysis of the chloroacetaldehydes, but also the relative amounts of the species if the branching between the primary channels can be determined. Therefore, characterizing the photodissociation processes of chloroacetaldehyde provides useful information for atmospheric chemists.

In the previous study on the photodissociation of chloroacetaldehyde at 193 nm, Miller et al. observed two primary channels: C- Cl bond fission and HCl elimination. Photoelimination of hydrogen halides is often observed in the photodissociation of organohalides and this process have been shown to proceed via three-center, four-center, or “roaming-type” mechanisms.[6-11] Miller et al. found HCl photoelimination in chloroacetaldehyde to be a minor channel compared to C−Cl bond fission and calculated the branching ratio between C−Cl photofission and HCl photoelimination to be 27.14:1. While they did not characterize the mechanism for HCl elimination, they assumed it was the result of a four-center process and thus produced ketene as the primary cofragment. In the end, they attributed all of their m/z=42 signal to ketene from HCl photoelimination by momentum-matching the signal with their m/z = 36 data and concluded that secondary dissociation of vinoxy to H + ketene produced from C−Cl bond fission is insignificant. Although they noted that ketene from HCl photoelimination could undergo secondary dissociation, they did not attempt to characterize the portion that does due to poor signal-to-noise in their m/z = 42 data.

Despite HCl photoelimination being a minor channel in the photodissociation of chloroacetaldehyde at 193 nm, it can still contribute to the signal at m/z = 42 and therefore should be considered in the photodissociation at 157 nm. In our previous study, we were able to conclude that HCl photoelimination did not significantly contribute to the m/z = 42 data using our branching calculations (see Section 3.4). From our calculations, we found that the portion of the C−Cl bond fission $P(E_T)$ leading to vinoxy that produces H + ketene fit the shape of the m/z = 42 data well (Figure 3.8) suggesting that the signal could be primarily attributed to secondary dissociation of vinoxy radicals. That being said, we still find there to be a small amount of fast ketene left unfit by the results of the branching calculations which is likely stable ketene from HCl photoelimination. While this provides evidence that HCl photoelimination does occur at 157 nm, it only gives us information about the elimination events with high relative kinetic energies, which would produce ketene fragments with internal energies below any unimolecular dissociation barriers. The work in Chapter 3 gave no about the lower-kinetic energy elimination events or whether ketene attributed to HCl elimination that we saw in the imaging data is consistent with the full HCl photoelimination P(E_T). So, we expect HCl photoelimination to occur in the photodissociation of chloroacetaldehyde at 157 nm. In this chapter, we report data detecting HCl elimination channel and confirming its contribution to the *m/z* = 42 imaging data.

As for other possible primary photodissociation channels of chloroacetaldehyde, an earlier study done by Nelson et al.[12] on the oxidation of chlorocarbon compounds provides evidence for a C−C bond fission channel. Nelson et al. found that chloral (CCl_3CHO) decayed fairly rapidly upon photolysis at 254 nm in air. From their observations, they concluded that the photolysis of chloral in oxygen must produce Cl atoms through a means other than simple C−Cl bond fission of the molecule. Instead, they proposed a reaction scheme in which C−C bond fission of chloral occurs via photolysis and then oxygen reacts with the chlorinated photofragment to produce Cl atoms that then rapidly remove more chloral from the reaction mixture. Overall, the reaction scheme was consistent with the results thus supporting the claim that chloral undergoes C−C bond fission. While chloral has more chromophores than chloroacetaldehyde, the electronic character of the molecules following excitation at 254 nm is similar as evidenced by their UV spectra in the region of 235-345 nm.[5] If the excited state corresponding to this transition in chloral has a pathway leading to C−C bond fission and the character of this state is similar to that of chloroacetaldehyde, then it is possible that chloroacetaldehyde has a similar pathway available to it. Thus, the photodissociation of chloroacetaldehyde at 254 nm likely has a C−C bond fission channel as well.

Further evidence that a C−C bond photofission channel in the photodissociation of chloroacetaldehyde is seen from the photodissociation studies of chloroacetone at 308 nm[13,14] and 193 nm.[15] While chloroacetone has a methyl group in place of the aldehydic H atom in chloroacetaldehyde, a comparison of the UV absorption spectra of chloroacetone[16] and chloroacetaldehyde[6] in the region from 230-340 nm suggests the similar electronic character of the molecules as both spectra have the same feature around 308 nm, assigned to the n(O) → π^*(C=O) transition. While we could not find a reported VUV absorption spectrum for chloroacetone, the VUV absorption spectrum of chloroacetaldehyde has been reported[17] and the electronic assignments for the spectral features involve the Cl and C=O chromophores. Since the two molecules have similar C=O and alpha carbon C−Cl chromophores, we expect similar excited state photodissociation dynamics for these two molecules suggesting a C−C bond fission channel might occur in chloroacetaldehyde as it did in chloroacetone. This chapter detects this product channel and determines its branching fraction.

Waschewsky et al.[13] and Alligood et at.[15] observed both C−Cl and C−C bond fission in their study on the photodissociation of chloroacetone at 308 nm and 193 nm, respectively. In both studies, they only observed C−C bond fission producing CH_2Cl and CH_3CO and detected no significant cleavage of the other C−C bond in the molecule. This is analogous to the C−C bond fission that would occur in chloroacetaldehyde further evincing that the presence of the methyl group does not significantly affect the dynamics of chloroacetone as compared to that of chloroacetaldehyde. The branching ratio between these two primary dissociation channels was also calculated at both photodissociation wavelengths. At 308 nm, the branching ratio between C−Cl bond fission and C−C bond fission was 4.6:1;[14] and at 193 nm, the branching ratio was 11:1.[15] So, it appears that C−C bond fission can effectively compete with C−Cl bond fission in the photodissociation of chloroacetone. Not only would it be interesting to observe C−C bond fission in the photodissociation of chloroacetaldehyde, but it would also be interesting to see if this channel effectively competes with the other primary channels as we see with chloroacetone.

In order to fully characterize the photodissociation of chloroacetaldehyde, we were motivated to use the same methodology as in the previous study by photodissociating chloroacetaldehyde at 157 nm but focus on the primary photodissociation channels. In this chapter, we outline our study on the photodissociation of chloroacetaldehyde at 157 nm done at the National Synchrotron Radiation Research Center (NSRRC) in Hsinchu, Taiwan. The purpose of this study is two-fold: (1) characterize the primary photodissociation processes of chloroacetaldehyde and (2) reinvestigate the unimolecular dissociation channels of vinoxy produced from C−Cl bond fission. We hoped that reinvestigating the dissociation of vinoxy would provide more information about the system (such as the branching between H + ketene and methyl + CO) and allow us to check the consistency of the analysis from our imaging lab study. One of the benefits of performing this study at the NSRRC is the use of tunable VUV photoionization, which allows us to reduce the amount of dissociative ionization by setting the energy just above the photoionization threshold of the fragment we want to detect. Another benefit is that the velocity distribution measured for the methyl is not affected by the dissociative ionization in the TOF data on a scattering apparatus. This is especially helpful for the analysis of the *m/z* = 15 data as it allows us to easily distinguish between the signal from dissociative ionization of vinoxy radicals and that from the neutral vinoxy CH_3 + CO product channel. This chapter thus reports our data all three primary photodissociation channels of chloroacetaldehyde and branching to each of these channels.

4.2 Experimental Details

4.2.1 NSRRC Scattering Apparatus

The data presented in this chapter were taken at the National Synchrotron Radiation Research Center (NSRRC), in Hsinchu, Taiwan, using the U9 Chemical Dynamics Beamline and a crossed laser-molecular beam scattering apparatus. The apparatus has been described in detail elsewhere;[18-20] we provide a brief description here. A 3% molecular beam of chloroacetaldehyde was created by first seeding the vapor pressure of the liquid sample (50% solution in water from Sigma-Aldrich, used without further purification) in neon with a total backing pressure of ~600 Torr. The gaseous mixture was then supersonically expanded into a rotating source chamber through an Even-Lavie pulsed nozzle with a 0.4 mm orifice. The nozzle operated at 100 Hz and was held at a temperature of 60°C. The rotating source was set at an angle of 10° or 20° with respect to the detector axis. The molecular beam intersected the 157 nm unpolarized output of a LPF 200 Lambda Physik Laser Technik laser propagating perpendicularly to the plane created by the molecular beam and the detector axis. The beam was focused to an area of ~24 mm^2 at its intersection with the molecular beam and the pulse energy was maintained around 8 mJ.

Following photodissociation, the resulting fragments recoil with a range of net velocities representing the vector sum of the recoil velocities (from both primary and secondary dissociation) and the velocity of the precursor in the molecular beam. Those fragments with a net velocity vector pointing into the detector travelled 10.05 cm to enter the ionizer region, where they were ionized by tunable VUV synchrotron radiation. The synchrotron output was first passed through a 30 cm gas cell containing ~10 Torr of argon to filter out higher harmonics. The ionized fragments were then accelerated by a series of ions lenses through a quadrupole mass filter and counted by a Daly detector. The data reported herein were taken with a lower mass resolution than in our previous studies at the NSRRC, so evidences, for example, a contribution at m/z = 35 from signal a mass unit higher. These contributions were identified by their velocity distributions. A multichannel scaler recorded the signal count as a function of total time-of-flight (TOF), which is the sum of the flight time of the neutral fragments to the ionizer and the flight time of the ionized fragments to the detector. The neutral flight time is recovered from the total TOF by subtracting the ion flight time calculated using the calibrated ion flight constant of 5.43 μs amu$^{-1/2}$. The data were collected is 1-μs bins and the time-of-flights were corrected to account for the measured 1.1 μs electronic delay between the laser and the triggering of the multichannel scaler. All TOF spectra in this chapter show the neutral flight time.

The TOF spectra were fit to recoil kinetic energy distributions (P(E_T)s) by forward convolution fitting using the CMLAB2 program.[21] The molecular beam velocity was characterized using a photodepletion (hole-burning) technique. By operating the photolysis laser at 50 Hz and the pulsed nozzle at 100 Hz, only half of all molecular beam pulses underwent photodissociation thus allowing for the measurement of the TOF for the molecular beam with and without the laser. These measurements were taken with the rotating source chamber set on-axis with the detector. Subtraction of the “laser on” TOF spectrum from the “laser off” TOF spectrum resulted in the TOF spectrum of the part of the molecular beam being photodissociated. This TOF spectrum was then transformed into a velocity distribution, which typically had a maximum at 800 m/s and a full width at half-maximum of 270 m/s (see Appendix C.1).

4.2.2 Computational Methods

We calculated minima and transition states relevant to the primary dissociation of chloroacetaldehyde and dissociation of subsequent photoproducts with the more recent G4 protocol. Optimized molecular geometries and vibrational frequencies were found using the B3LYP density functional and the 6-311++G(3df,2p) basis set. The geometries converged to a root-mean-square (rms) force below 1×10^{-5} and an rms displacement below 4×10^{-5}, where both values are in atomic units. Wave functions for doublet species were spin-unrestricted, and wave functions for singlet species were spin-restricted. The computation of the zero-point vibrational energies used the B3LYP/6-311++G(3df,2p) vibrational frequencies scaled by 0.9854[22] as the G4 method required.[23] The G4 method is the latest in the series of Gn theories, which are composite methods based on a sequence of single-point energy calculations. To confirm the calculated transition states lead to the desired products, we also ran an intrinsic reaction coordinate (IRC) calculation at the B3LYP/6-311++G(3df,2p) level. The calculations use the GAUSSIAN09 program, version A.02.[24]

4.3 Results

In the following sections, we present the scattering data for the photodissociation of chloroacetaldehyde with forward convolution fits. We begin with an overview of the primary photodissociation channels of chloroacetaldehyde observed in this study and the energetics of those channels. In Section 4.3.2, we present the time-of-flight (TOF) spectra of the primary photodissociation products from C−Cl bond fission and HCl photoelimination, taken at $m/z = 35$ (Cl^+), $m/z = 36$ ($H^{35}Cl^+$), and $m/z = 38$ ($H^{37}Cl^+$). Section 4.3.3 details the TOF spectra for the products from primary C−C bond photofission, taken at $m/z = 29$ (HCO^+) and $m/z = 49$ (CH_2Cl^+). The estimates of the branching ratios between the three primary photodissociation channels are then described in Section 4.3.4. In Section 4.3.5, we present the TOF spectra of the products from the unimolecular dissociation of vibrationally excited vinoxy radicals. Data were taken at $m/z = 15$ (CH_3^+), $m/z = 28$ (CO^+), and $m/z = 42$ (CH_2CO^+). Section 4.3.6 presents evidence of the unimolecular dissociation of ketene resulting from HCl photoelimination which appears in the TOF spectrum of $m/z = 14$ (CH_2^+). In Section 4.3.7, we discuss the likelihood of the unimolecular dissociation of vibrationally excited formyl radicals resulting from C−C bond fission of chloroacetaldehyde. Finally, Section 4.3.8 presents the calculations of the partial photoionization cross section of vinoxy to CH_3^+ at 9.845, 10.5, and 11.44 eV.

4.3.1 Overview of Primary Photodissociation Channels of Chloroacetaldehyde

In the current study, we observed three primary photodissociation channels of chloroacetaldehyde using 157 nm photons (eqs 1-3): C−Cl bond fission producing vinoxy radicals, HCl photoelimination producing ketene, and C−C bond fission producing CH_2Cl and HCO radicals. While the C−Cl bond fission and HCl photoelimination channels have been observed previously in photodissociation studies done at other wavelengths, this study provides the first direct evidence of a C−C bond fission channel. From the TOF data, we determined the translational energy distributions, P(E_T)s, for each primary channel. The scattering data show that the C−Cl bond fission channel has a significantly different P(E_T) from the previous study. We attribute the additional fast signal at high kinetic energies to multiphoton dissociation; however, we use the C−Cl bond fission P(E_T) derived in this study to analyze the other scattering data.

$$CH_2ClCHO + h\nu \rightarrow CH_2CHO + Cl \qquad \Delta H_{0K} = 73.4 \text{ kcal/mol} \qquad (1)$$

$$\rightarrow H_2C{=}C{=}O + HCl \qquad \Delta H_{0K} = 7.43 \text{ kcal/mol} \qquad (2)$$

$$\rightarrow CH_2Cl + HCO \qquad \Delta H_{0K} = 77.2 \text{ kcal/mol} \qquad (3)$$

Since the primary processes impart a range of translational energies, the products from the primary photodissociation channels are formed with a range of internal energies. Comparing the internal energy of the products to the barriers along their ground state potential energy surface (PES) shows that some of the products from the photodissociation may have enough internal energy to undergo dissociation themselves. Therefore, the internal energy distribution of the products is useful in the discussion of this secondary dissociation. From conservation of energy, the internal energy, $E_{\text{int}}(\text{A})$ of a product, A, formed from the photodissociation of a precursor A−B is given by the equation:

$$h\nu + E_{\mathrm{int}}(\mathrm{A-B}) = \Delta H_{0\mathrm{K}} + E_{\mathrm{T}} + E_{\mathrm{int}}(\mathrm{A}) + E_{\mathrm{int}}(\mathrm{B}) \tag{4}$$

where $h\nu$ is the energy of the photon, E_{int}(A-B) is the internal energy of the precursor, E_{T} is the recoil translational energy imparted to the fragments, and E_{int}(B) is the internal energy of the cofragment to R. Supersonic expansion of the molecular beam cools the rotational energy of the precursor, so E_{int}(A-B) is the thermal vibrational energy at the nozzle temperature of 60°C, which is1.45 kcal/mol. The values of $\Delta H_{0\mathrm{K}}$ for the primary photodissociation channels are given in Equations (1)-(3) and were calculated at the G4//B3LYP/6-311++G(3df,2p) level of theory. E_{int}(B) is discussed in the relevant sections below where B represents either Cl, HCl, or CH_2Cl.

4.3.2 Primary Photodissociation Channels: C−Cl Bond Fission and HCl Photoelimination

Due to the resolution of the quadrupole, we detected *m/z* + 1 ion signal in the TOF spectra taken at *m/z* for the primary photodissociation products of C−Cl bond fission and HCl photoelimination. We therefore analyzed all of the data at the mass-to-charge ratios for these channels collectively and present the analysis of both channels together in this section. Like in the velocity map imaging study, we observed signal at *m/z* = 35 (Cl^+) corresponding to C−Cl bond fission. The presence of the HCl photoelimination channel was confirmed by detecting signal at both *m/z* = 36 ($H^{35}Cl^+$) and *m/z* = 38 ($H^{37}Cl^+$). Since the data taken at *m/z* = 38 ($H^{37}Cl^+$) cannot not have any bleed in from *m/z* + 1 ion signal (as there is no product that gives signal at *m/z* = 39), we determined the P(E_{T}) for all HCl photoelimination events from the TOF spectrum taken at this mass-to-charge ratio. Figure 4.1 shows the TOF spectrum collected at *m/z* = 38 ($H^{37}Cl^+$) with a source angle of 10° and ionization energy of 15 eV. The experimental data are shown in red open circles and are fit using a forward-convolution method. The fit corresponding to primary HCl photoelimination is depicted in solid blue line and was derived from the P(E_{T}) depicted in solid blue line in Figure 4.2. The P(E_{T}) peaks at 8 kcal/mol and has a tail that extends to 60 kcal/mol. Interestingly, this P(E_T) peaks near the same recoil kinetic energy as that measured for HCl photoelimination by Miller et al. in the photodissociation of chloroacetaldehyde at 193 nm; however, they do not see as many photodissociation events with higher translational energies. Since the photon energy is higher in our study, we have more energy in the system that can be converted into translation. The other contribution to the TOF spectra in Figure 4.1 shown in solid purple line is from the dissociation of molecular clusters in the beam, which is characterized by an identical and slow velocity distribution seen at several *m/z* values.

We then determined the P(E_T) for all C−Cl bond fission events from fitting the TOF spectrum taken at *m/z* = 35 (Cl^+). Figure 4.3 shows the TOF spectrum collected at *m/z* = 35 (Cl^+) with a source angle of 20° and ionization energy of 13.68 eV. The experimental data are shown in open red circles. The fit shown in solid blue line corresponds to bleed in from the *m/z* = 36 ($H^{35}Cl^+$) data and was made using the P(E_T) for HCl photoelimination shown in Figure 4.2. The fit corresponding to C−Cl bond fission is shown in solid green line and was derived from the P(E_T) in Figure 4.4. For comparison, the C−Cl bond fission P(E_T) derived from the velocity map imaging study is also shown in Figure 4.4 in dashed black line. While the two P(E_T)s have similar shapes, it appears that there are more dissociation events with higher kinetic energies observed in this study. The high kinetic energy feature in the P(E_T) derived in this study peaks at about 42 kcal/mol, which is consistent with the resolution of the two apparatuses (~2 kcal/mol). The larger fast signal may result from multiphoton dissociation events or, possibly, photodissociation of the monomer hydrate and dimer hydrate of chloroacetaldehyde. We did not observe any stable vinoxy radicals at *m/z* = 43 (vinoxy radicals are known to give negligible signal at parent ion upon photoionization[25]), but signal from dissociative ionization of stable vinoxy radicals formed in high-kinetic energy C−Cl bond photofission events are observed in the TOF spectra taken at $m/z = 15$ (CH_3^+) and $m/z = 29$ (HCO^+) (Figures 4.15 and 4.9, respectively). We also note that the fitting is consistent among all of the $m/z = 35$ (Cl^+) data, shown in Figure 4.5, taken at a different source angle and at different ionization energies. In the calculation of the branching ratios between the primary channels (Section 4.3.3).and the subsequent analysis of the unimolecular dissociation of vinoxy (Section 4.3.4 and Section 4.3.8), we use the C−Cl bond fission P(E_T) derived in this study. We show alternative fits for the $m/z = 35$ and $m/z = 36$ using the C−Cl bond fission P(E_T) derived in the velocity map imaging study in Appendix C.2.

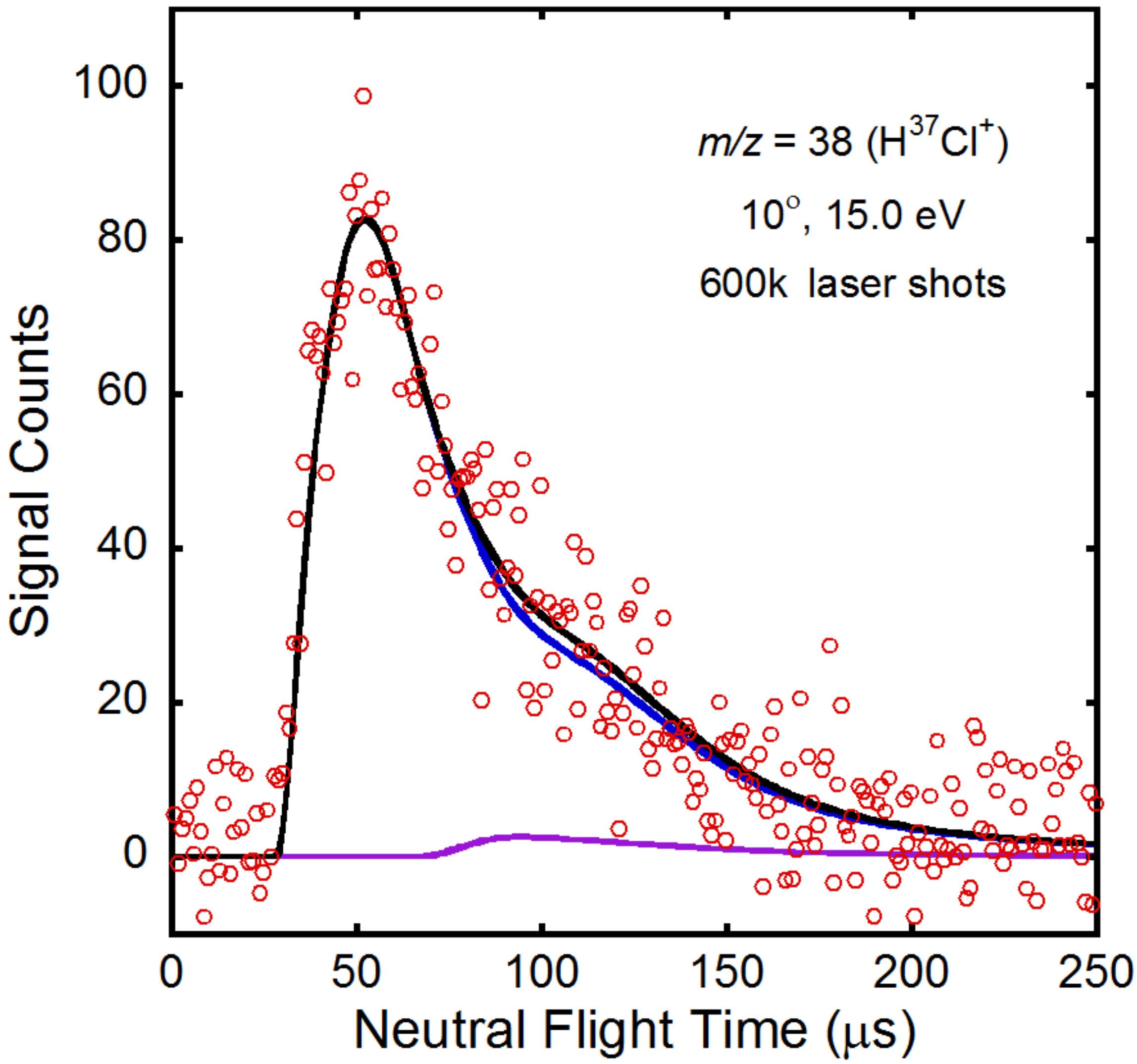

Figure 4.1: TOF spectrum taken at m/z = 38 ($H^{37}Cl^{+}$) with a source angle of 10° and an ionization energy of 15.0 eV. Data are shown in red circles. Primary HCl photoelimination is fit by the solid blue line using the P(E_T) shown in Figure 4.2. The contribution attributed to photodissociation of clusters in the molecular beam is shown in solid purple line.

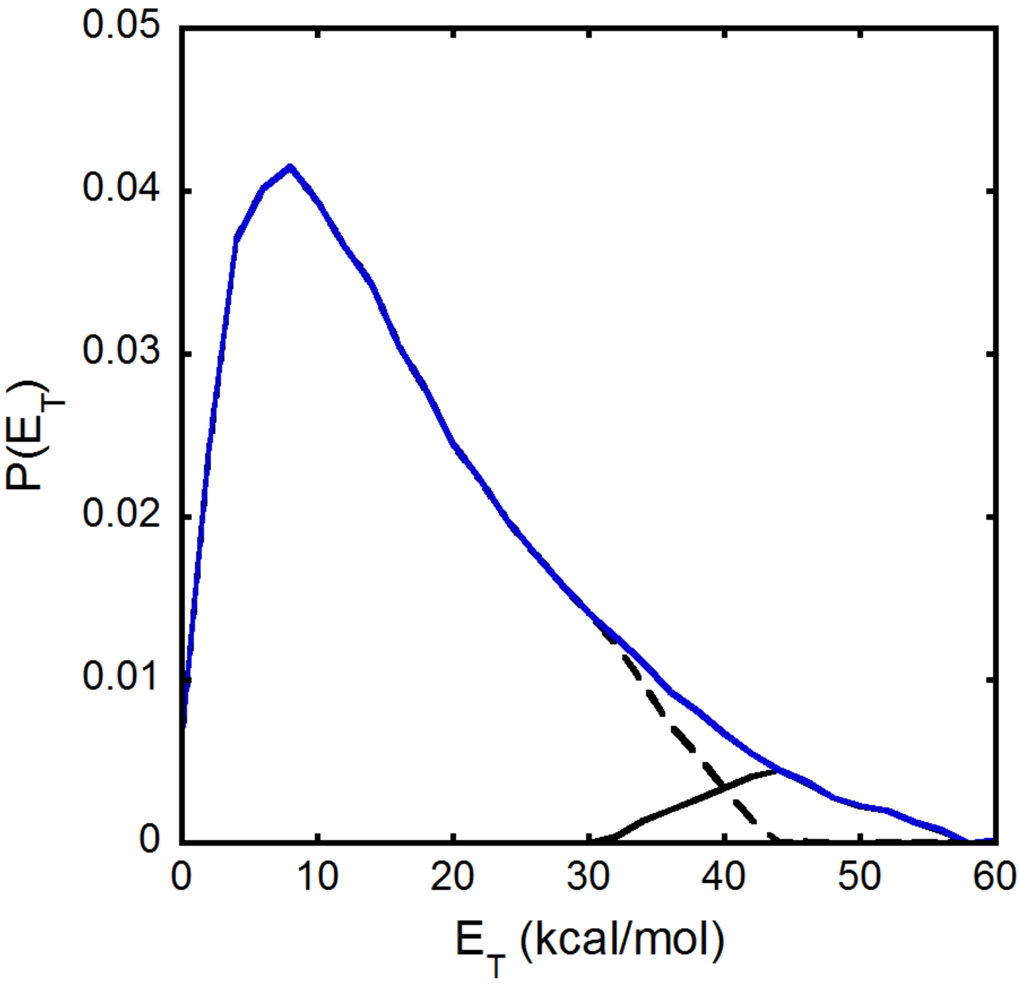

Figure 4.2: Photofragment recoil kinetic energy distribution for HCl photoelimination in chloroacetaldehyde at 157 nm. The total P(*E*$_T$) (solid blue line), peaking at 8 kcal/mol, is derived by forward convolution fitting of the signal at *m/z* = 38 ($H^{37}Cl^+$) shown in Figure 4.1. The portion of the P(*E*$_T$) producing stable ketene, which does not have enough internal energy to undergo secondary dissociation, is shown in solid black line and is derived from the signal at *m/z* = 42 (CH_2CO^+) unfit by secondary dissociation of vinoxy. The remaining portion of the P(*E*$_T$), shown in dashed black line, represents the unstable ketene that undergo subsequent unimolecular dissociation.

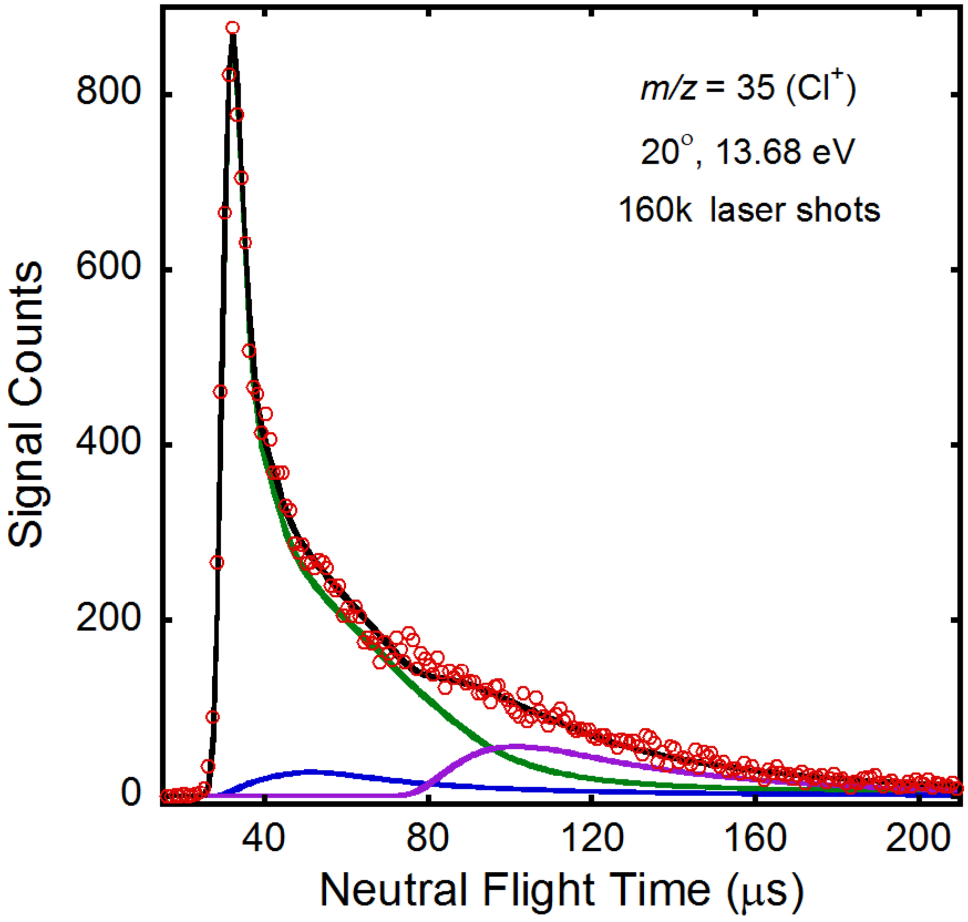

Figure 4.3: TOF spectrum taken at *m/z* = 35 (Cl^+) with a source angle of 20° and an ionization energy of 13.68 eV. Data are shown in red circles. Primary C−Cl bond fission is fit by the solid green line using the P(E_T) shown in Figure 4.4. The contribution from bleed in of *m/z* = 36 ($H^{35}Cl^+$) is shown in solid blue line and is fit using the primary HCl photoelimination P(E_T) shown in Figure 4.2. The fit shown as the solid purple line represents the contribution attributed to photodissociation of clusters in the molecular beam.

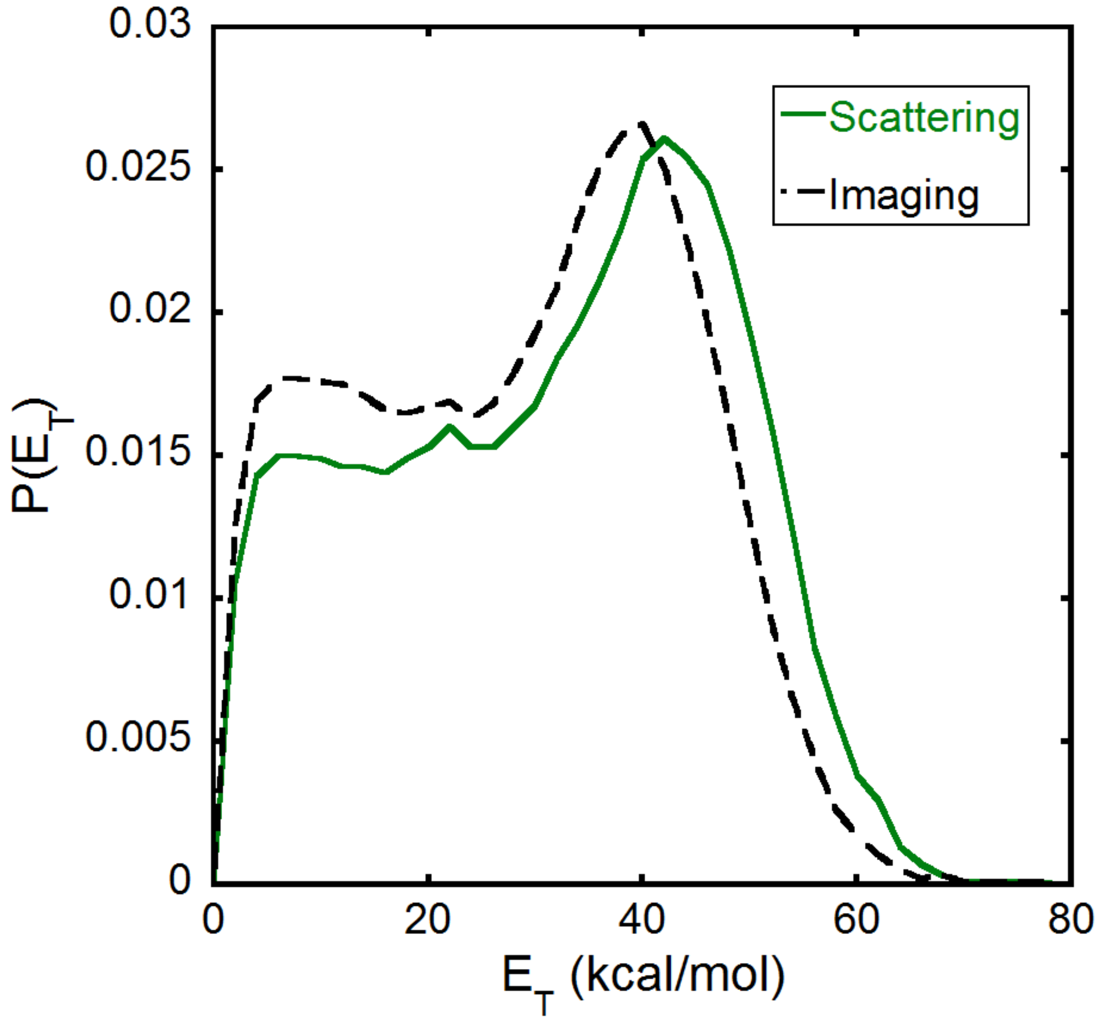

Figure 4.4: Photofragment recoil kinetic energy distribution for C−Cl bond fission in chloroacetaldehyde at 157 nm. The P(E_T) shown in solid green line is derived by forward convolution fitting of the signal at m/z = 35 (Cl^+) shown in Figure 4.3. For comparison, the C−Cl bond fission P(E_T) derived from the velocity map imaging study is shown in dashed black line.

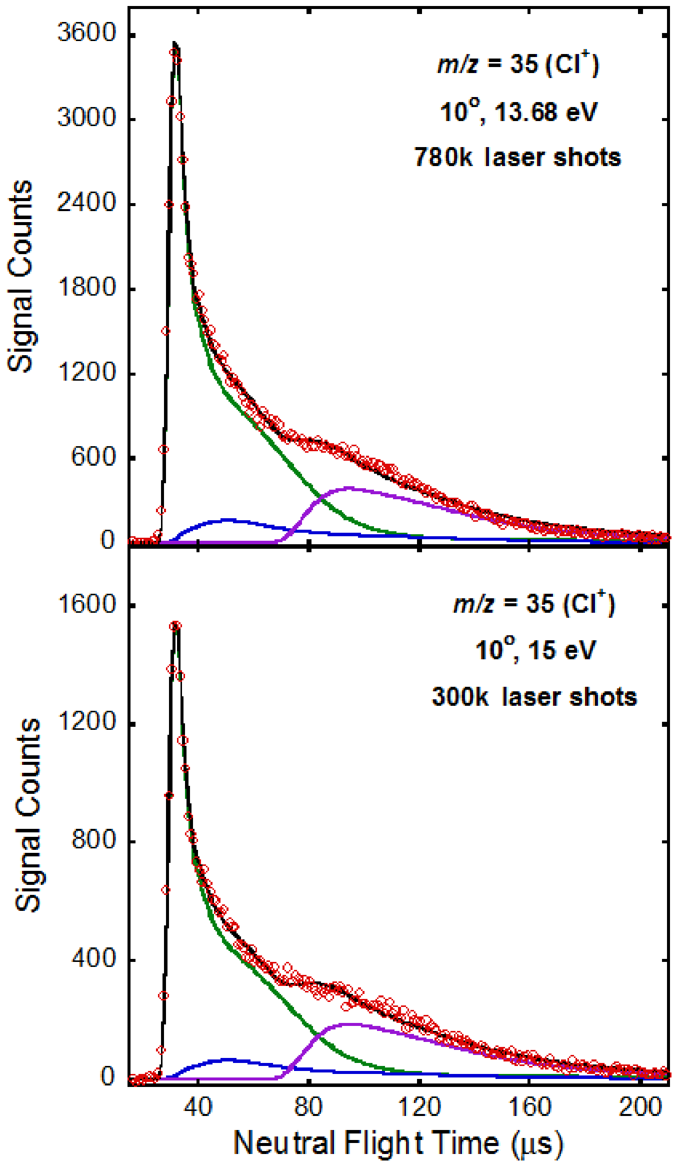

Figure 4.5: TOF spectrum taken at m/z = 35 (Cl^+) with a source angle of 10° and two different ionization energies. The upper frame shows the data taken at an ionization energy of 13.68 eV and the lower frame shows the data taken at an ionization energy of 15.0 eV. Data are shown in red circles. Primary C−Cl bond fission is fit by the solid green line using the P(E_T) shown in Figure 4.4. The contribution from bleed in of m/z = 36 ($H^{35}Cl^+$) is shown in solid blue line and is fit using the primary HCl photoelimination P(E_T) shown in Figure 4.2. The fit shown as the solid purple line represents the contribution attributed to photodissociation of clusters in the molecular beam.

Although we accounted for the bleed in from *m/z* = 36 ($H^{35}Cl^+$) into the TOF spectrum of *m/z* = 35 (Cl^+) using the HCl photoelimination P(E_T) derived from the TOF spectrum of *m/z* = 38 ($H^{37}Cl^+$), we note that there are a few inconsistencies between the *m/z* = 36 and *m/z* = 38 data. Figure 4.6 shows the TOF spectra collected at *m/z* = 36 ($H^{35}Cl^+$) with a source angle of 10° and ionization energies of 15 eV (top frame) and 13.68 eV (bottom frame). In both spectra, we show the fits derived from the HCl photoelimination P(E_T), shown in Figure 4.2, in solid blue line. Not only does there appear to be extra fast signal that cannot be accounted for using the P(E_T), but it also appears as though the fast signal does not show the same dependence on ionization energy as the signal attributed to HCl photoelimination. While we expect bleed in from *m/z* = 37 (Cl^+), the signal from that process is too fast and cannot account for the entire fast signal in the *m/z* = 36 TOF spectra. It is possible that $H^{35}Cl$ elimination has a slightly different P(E_T) than does $H^{37}Cl$ elimination, but the signal at *m/z* = 38 for the latter is uncomplicated by the low quadrupole resolution so we present a P(E_T) derived from the *m/z* = 38 TOF spectrum. While it would be more accurate to incorporate all of the signal from the *m/z* = 36 data to the bleed in observed in the *m/z* = 35 TOF spectrum, we note that doing so does not significantly alter the fits. Therefore, we use the P(E_T) depicted in Figure 4.4 and note that we may be overestimating the amount of C−Cl bond fission events.

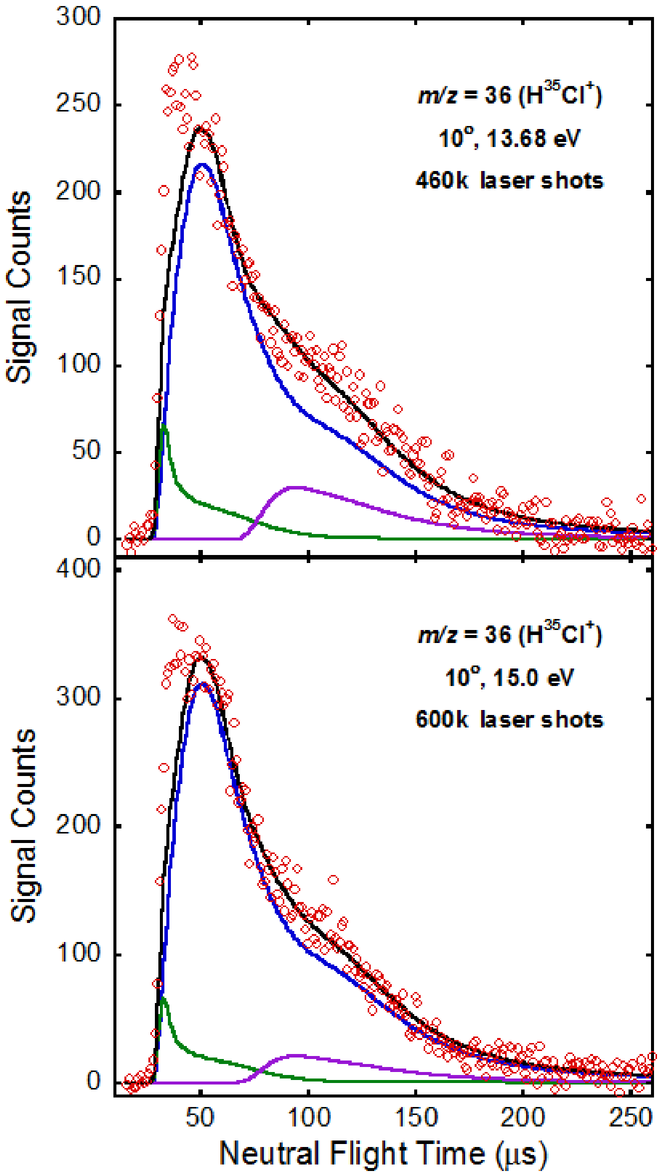

Figure 4.6: TOF spectrum taken at *m/z* = 36 ($H^{35}Cl^+$) with a source angle of 10° and two different ionization energies. The upper frame shows the data taken at an ionization energy of 13.68 eV and the lower frame shows the data taken at an ionization energy of 15.0 eV. Data are shown in red circles. Primary HCl photoelimination is fit by the solid blue line using the P(E_T) shown in Figure 4.2. The contribution from bleed in of *m/z* = 37 (Cl^+) is shown in solid green line and is fit using the primary C−Cl bond fission P(E_T) shown in Figure 4.4. The contribution attributed to photodissociation of clusters in the molecular beam is shown in solid purple line. It is interesting to note that the primary HCl photoelimination P(E_T) derived from the TOF spectrum taken at *m/z* = 38 ($H^{37}Cl^+$) does not fit all of the data taken at *m/z* = 36 ($H^{35}Cl^+$).

4.3.3 Primary Photodissociation Channels: C−C Bond Fission

Evidence for C−C bond fission is given in the TOF spectra at *m/z* = 49 (CH_2Cl^+) shown in Figure 4.7. The experimental data are shown in red circles. Since we expected a portion of the formyl radical to be formed with enough vibrational energy to undergo subsequent unimolecular dissociation due to its low barrier to dissociation (see Section 4.3.8), we determined the $P(E_T)$ for all C−C bond fission events from the TOF spectrum taken at *m/z* = 49 (CH_2Cl^+). The fit corresponding to C−C bond fission is depicted in solid orange line in Figure 4.7 and was derived from the $P(E_T)$ shown in Figure 4.8. The $P(E_T)$ peaks at 8 kcal/mol and has a tail that extends to about 45 kcal/mol. The other contribution to the TOF spectrum at *m/z* = 49 (CH_2Cl^+) is dissociation of clusters in the molecular beam. It was not possible to fit the TOF data with a single $P(E_T)$ and we also expect to see signal at this mass from clusters based on the energetics of producing CH_2Cl^+ ions from chloroacetaldehyde monomers. Uncertainty in the amount of signal from cluster only affects the C−C bond fission $P(E_T)$ in the range from 0 – 4 kcal/mol and we therefore expect it to incorporate minimal error into our subsequent branching ratio calculations.

Figure 4.9 shows the TOF spectrum collected at *m/z* = 29 (HCO^+) with a source angle of 20° and ionization energy of 11.53 eV. The fit corresponding to momentum-matched cofragments of CH_2Cl is shown in solid orange line; it peaks as expected at 50 μs. However, the integrated signal under the orange fits in the *m/z* = 29 TOF spectra show much less signal at HCO^+ than expected based on the relative photoionization cross sections.[26,27] We therefore suspect that the formyl radical undergoes unimolecular dissociation, which is reasonable considering that the barrier to forming H + CO is only 16.5 kcal/mol. The sharp and narrow peak at fast times is characteristic of dissociative ionization of stable vinoxy radicals and fit it in solid green line using the stable portion of the C−Cl bond fission $P(E_T)$ calculated from our branching calculations (see Section 4.3.4). We also included a contribution from dissociation of molecular clusters. However, there is still unfit signal at intermediate times between the cluster and C−C bond fission contributions. We were unable to identify the source of this signal. While we could possibly attribute the signal to unimolecular dissociation of the biradical cofragment (HCCHO) from a three-center HCl photoelimination process, our calculations of the ground-state PES for this biradical suggest is unlikely to be competitive (Appendix C.3).

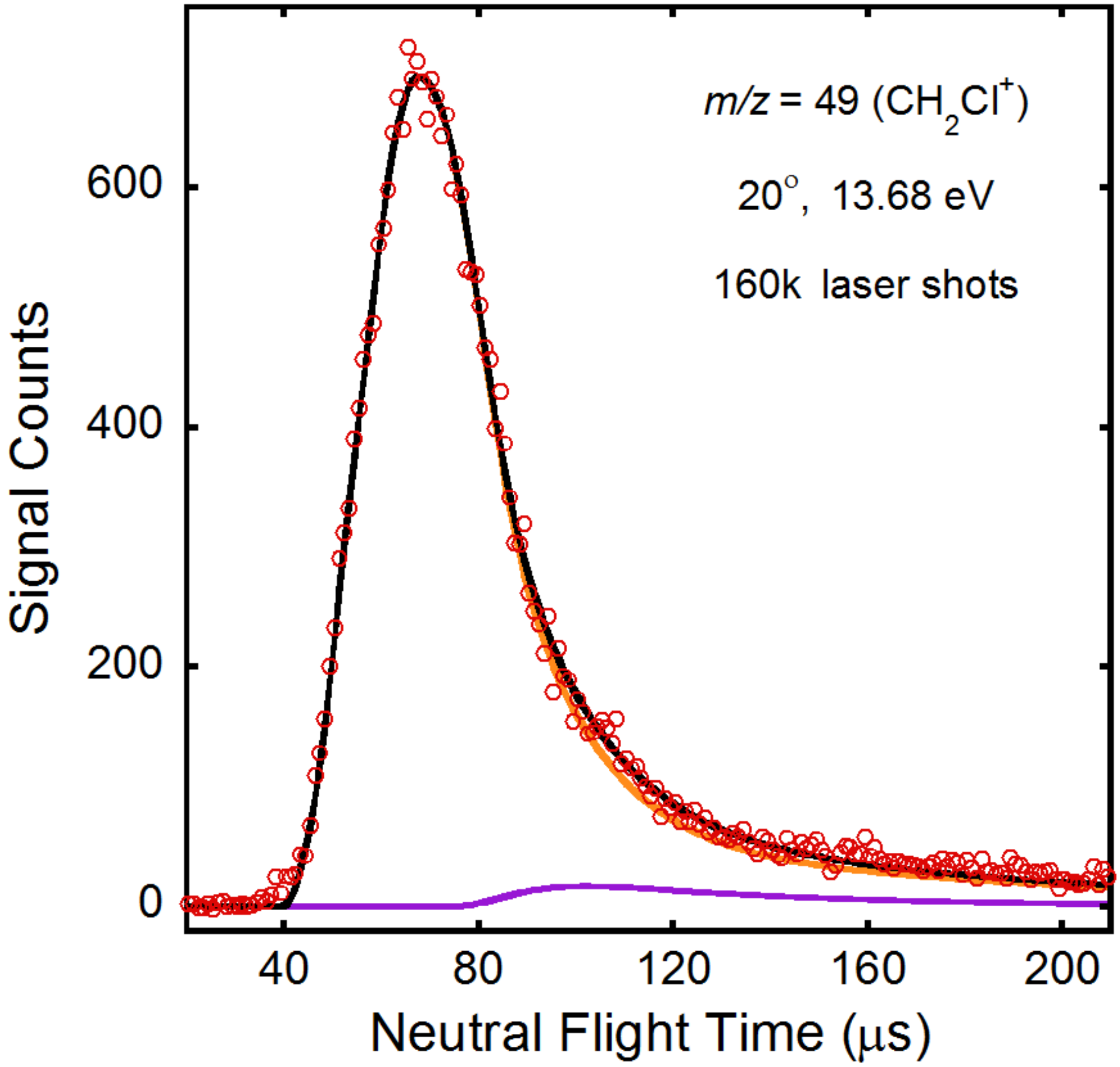

Figure 4.7: TOF spectrum taken at $m/z = 49$ (CH_2Cl^+) with a source angle of 20° and an ionization energy of 13.68 eV. Data are shown in red circles. Primary C−C bond fission is fit by the solid orange line using the P(E_T) shown in Figure 4.8. The contribution attributed to photodissociation of clusters in the molecular beam is shown in solid purple line.

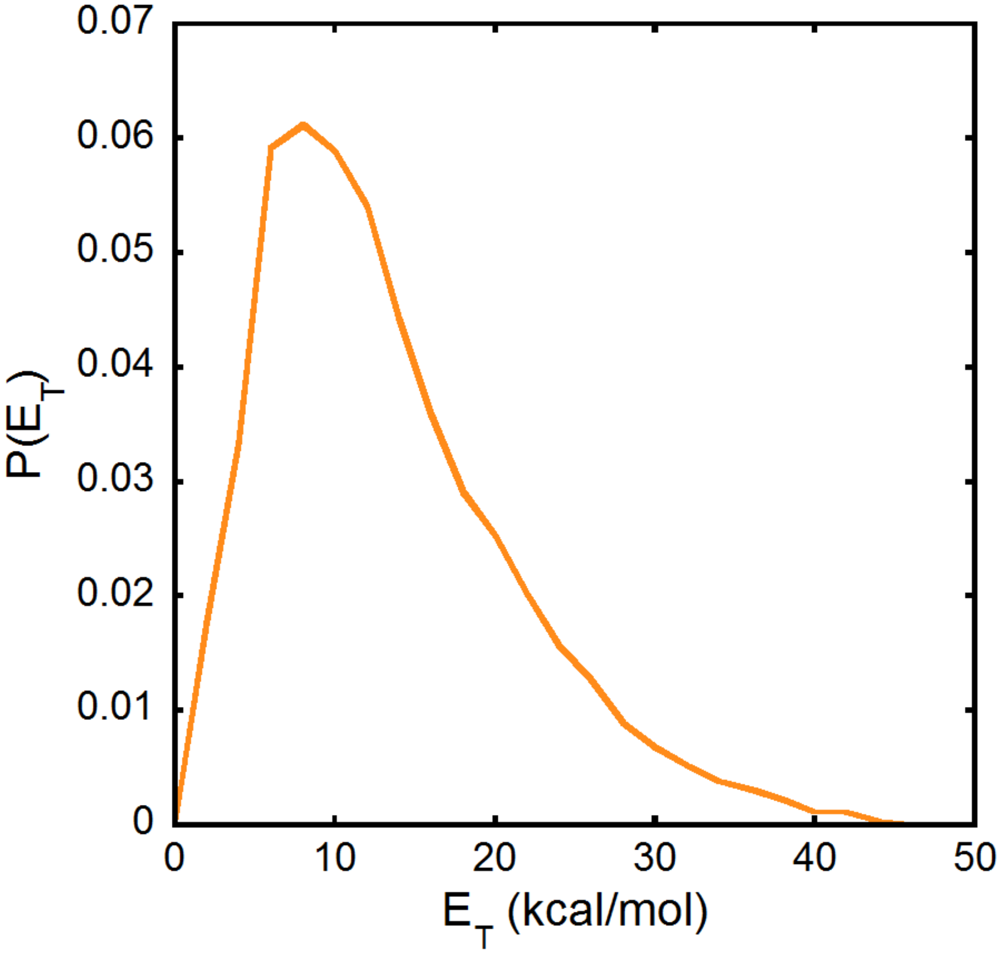

Figure 4.8: Photofragment recoil kinetic energy distribution for C−C bond fission in chloroacetaldehyde at 157 nm. The P(E_T), peaking at 8 kcal/mol, is derived by forward convolution fitting of the signal at *m/z* = 49 (CH_2Cl^+) shown in Figure 4.7.

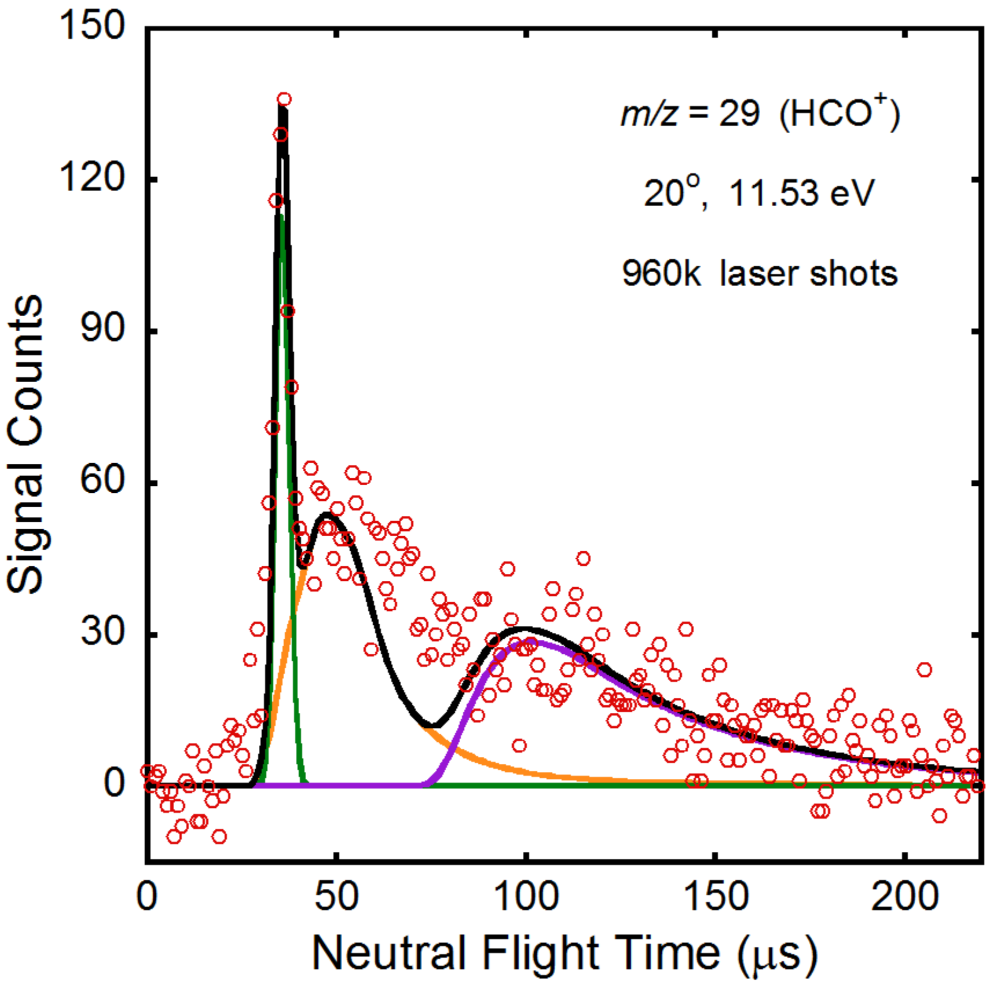

Figure 4.9: TOF spectrum taken at *m/z* = 29 (HCO^+) with a source angle of 20° and an ionization energy of 11.53 eV. Data are shown in red circles. The contribution from the momentum-matched cofragments to C−C bond fission is fit by the solid orange line using the P(E_T) shown in Figure 4.8. Dissociative ionization of stable vinoxy to HCO^+ is shown as the solid green line and is fit using the portion of the C−Cl bond fission P(E_T) producing stable vinoxy radicals (shown in dashed gray line in Figure 4.10). The fit shown in solid purple line is the contribution attributed to photodissociation of clusters in the molecular beam. Since not all of the signal is accounted for by the fits, there is likely another source of *m/z* = 29.

4.3.4 Branching Ratios for Primary Photodissociation Channels

To fully characterize the relative branching between the three primary photodissociation channels of chloroacetaldehyde, we calculated the branching ratio between the C−Cl bond photofission channel and both the HCl photoelimination and C−C bond photofission channels. For the branching ratio between the C−Cl bond fission channel and HCl photoelimination channel, we used the signal acquired at *m/z* = 35 (Cl^+) and *m/z* = 36 ($H^{35}Cl^+$) with a source angle of 10° and ionization energy of 13.68 eV. For the branching ratio between the C−Cl bond fission channel and C−C bond fission channel, we used the signal acquired at *m/z* = 35 (Cl^+) and *m/z* = 49 (CH_2Cl^+) with a source angle of 20° and ionization energy of 13.68 eV. (We used the spectra at a 20° source angle because *m/z* = 49 (CH_2Cl^+) showed a large beam-dependent signal at slower neutral flight times.) We first integrated the signal under the corresponding fits at each mass and calculated the ratio of these signals. The ratio of signals is given below as obs($^{35}Cl^+/H^{35}Cl^+$) and obs($^{35}Cl^+/CH_2Cl^+$), respectively. We then corrected these ratios for the expected signal based on kinematic corrections and Jacobian factors, TS($H^{35}Cl/^{35}Cl$) and TS($CH_2Cl/^{35}Cl$), as well as for the photoionization cross sections of the fragments (averaged over the bandwidth of the synchrotron radiation), σ_{X/X^+}. We used the photoionization cross section of Cl reported by Ruscic and Berkowitz[28] correcting for the lower cross section in the continuum beyond the ^1S_o threshold recommended by Berkowitz[29] based on subsequent studies. For HCl, we used the photoionization cross section reported by Frohlich and Glass-Maujean.[30] Since there are no reported photoionization cross sections for CH_2Cl, we used the relative cross section, $\sigma_{CH_2Cl/CH_2Cl^+}/\sigma_{Cl/Cl^+}$, calculated from a photodissociation study on dichloromethane done on the same instrument (in preparation for publication[26]). We obtain

$$\frac{\Phi_{\text{C-Cl}}}{\Phi_{\text{HCl}}} = \text{obs}\left(\frac{{}^{35}\text{Cl}^{+}}{\text{H}^{35}\text{Cl}^{+}}\right) \times \text{TS}\left(\frac{\text{H}^{35}\text{Cl}}{{}^{35}\text{Cl}}\right) \times \left(\frac{\sigma_{\text{HCl/HCl}^{+}}}{\sigma_{\text{Cl/Cl}^{+}}}\right) = \left(\frac{75328}{13813}\right) \times \left(\frac{143732}{62697}\right) \times \left(\frac{16\ \text{Mb}}{22.8\ \text{Mb}}\right) = 8.8, \quad (4)$$

and

$$\frac{\Phi_{\text{C-Cl}}}{\Phi_{\text{C-C}}} = \text{obs}\left(\frac{{}^{35}\text{Cl}^{+}}{\text{CH}_2\text{Cl}^{+}}\right) \times \text{TS}\left(\frac{\text{CH}_2\text{Cl}}{{}^{35}\text{Cl}}\right) \times \left(\frac{\sigma_{\text{CH}_2\text{Cl/CH}_2\text{Cl}^{+}}}{\sigma_{\text{Cl/Cl}^{+}}}\right) = \left(\frac{19001}{30371}\right) \times \left(\frac{34137}{10780}\right) \times (1.37) = 2.7. \quad (5)$$

The combination of these two ratios yields total primary photodissociation branching fractions for C−Cl:HCl:C−C of 0.67:0.08:0.25. Interestingly, C−C bond fission effectively competes with C−Cl bond fission in the primary photodissociation of chloroacetaldehyde at 157 nm. While HCl photoelimination is a minor channel, the relative amount of those dissociation events compared to C−Cl bond fission is calculated to be larger in this study as compared to the previous study at 193 nm done by Miller et al. As previously noted, we may be overestimating the amount of C−Cl bond fission events because we are unsure of the contribution from multiphoton dissociation events and, possibly, dissociation of the monomer hydrate and dimer hydrate of chloroacetaldehyde. Therefore, we expect the branching ratios calculated in Equations (4) and (5) to be maximum values such that there may be more HCl photoelimination and C−C bond fission events relative to C−Cl bond fission. For comparison, we present the same calculations using the C−Cl bond fission P(E_T) determined in the velocity map imaging study in Appendix C.4.

4.3.5 Unimolecular Dissociation of Vibrationally Excited Vinoxy Radicals Resulting From Primary C−Cl Bond Fission

Vinoxy radicals produced from primary C−Cl bond photofission of chloroacetaldehyde can undergo two subsequent unimolecular dissociation pathways: C-H bond fission yielding H +

ketene and isomerization to acetyl followed by C−C bond fission yielding CH_3 + CO. The pathways are shown below:

$$CH_2CHO \rightarrow H_2C{=}C{=}O \text{ (ketene)} + H \tag{6}$$

$$\rightarrow CH_3CO \text{ (acetyl radical)} \rightarrow CH_3 + CO \tag{7}$$

We observed signal at all of the mass-to-charge ratios corresponding to the products from the secondary dissociation of vinoxy. While there are certain consistencies between the data from this study and the data from our velocity map imaging study, we note that the data in this study required addition analysis. We were able to distinguish the separate contributions to the signal at $m/z = 42$ (CH_2CO^+); however, characterizing the contributions to the signal at $m/z = 15$ (CH_3^+) proved to be difficult except for the contribution from dissociative ionization of vinoxy to CH_3^+.

Using our branching calculations, we first determined the portions of the primary C−Cl bond fission P(E_T), shown in Figure 4.4, that produces vinoxy that we expect to dissociate to H + ketene or CH_3 + CO products respectively. To summarize, the branching calculations assume that the unimolecular dissociation of vinoxy occurs on the ground state PES and that the excitation of the photolytic precursor is to an excited-state PES of chloroacetaldehyde that is repulsive along the C−Cl bond in the Franck-Condon region. The inputs for the branching calculations include the geometry of chloroacetaldehyde and vinoxy, the experimentally determined C−Cl bond fission P(E_T), the vibrational normal modes of vinoxy at its minimum geometry and at each transition state, the nozzle temperature, and the barrier heights for the H + ketene and isomerization channels. Since the barrier to CH_3 + CO from the acetyl radical is much lower than the barrier to isomerization (see Figure 2.1), we use the isomerization barrier height in the calculations and assume all radicals that undergo isomerization subsequently dissociate to CH_3 + CO. To account for the different conformers for chloroacetaldehyde, we scale the C−Cl bond fission P(E_T) by the relative population of each conformer in the molecular beam at the nozzle temperature, run the branching calculations for each conformer separately, and then sum their contributions. Because the scattering instrument uses single photon photoionization rather than REMPI, we were unable to detect the separate spin-orbit states of the Cl atoms from primary C−Cl bond fission and therefore we do not distinguish between the separate states in our branching calculations (see Chapter 3). In the velocity map imaging study, we found a barrier height of 44.6 kcal/mol for the H + ketene channel to be more consistent with the data than the G4 barrier height (42.2 kcal/mol).We therefore used this new barrier height in the analysis of the data in this study for consistency and provide the fits using the G4 barrier height in Appendix C.5. Note however that the data the data can be well fit with either barrier height. The results of the branching calculations are shown in Figure 4.10 along with the total C−Cl bond fission P(E_T) from Figure 4.2 shown in solid green line. The dashed red line shows the portion of the C−Cl bond fission P(E_T) producing vinoxy which dissociates to H + ketene and the dashed blue line shows the portion producing vinoxy which dissociates to CH_3 + CO (here we assume that all the Cl atom signal fit in green in the TOF spectra are produced from the single photon photodissociation of chloroacetaldehyde, although there may be a contribution from multiphoton dissociation at the earliest arrival times in the TOF spectrum). We used these portions to fit the respective contributions from the unimolecular dissociation of vinoxy to the TOF spectra taken at the mass-to-charge ratio of the products. We also show the portion predicted to produce stable vinoxy radicals in dashed gray line, which we used to fit the contributions from dissociation ionization or multiphoton dissociation of vinoxy.

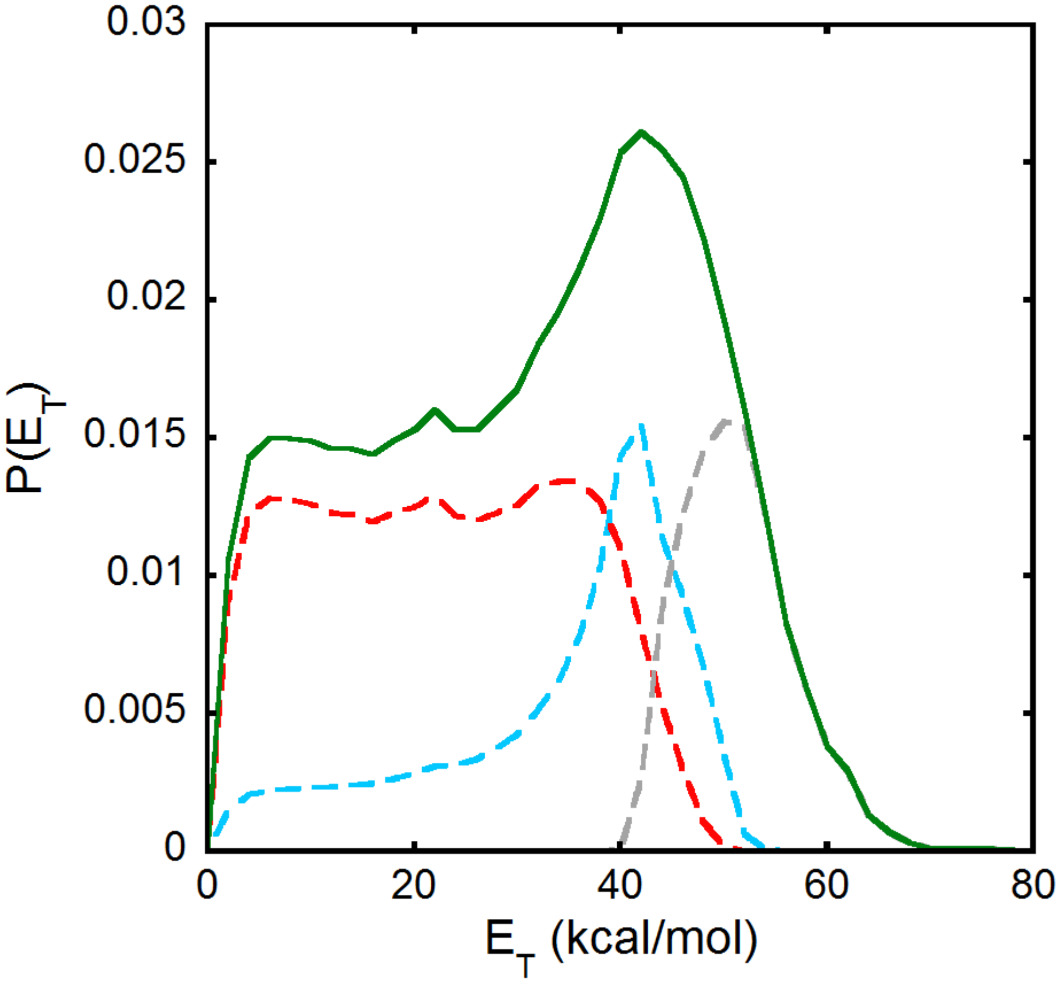

Figure 4.10: Results of the branching calculations using a barrier height of 44.6 kcal/mol for the H loss channel. The total primary C−Cl bond fission P(E_T) derived from the scattering data is shown in solid green line along with the predicted portions that produce H + ketene products (dashed red curve), methyl + CO products (dashed blue curve), and stable vinoxy radicals that do not dissociate (dashed gray curve). The "stable" portion of the P(E_T) is the distribution of C−Cl photofission events that our model predicts partitions insufficient vibrational energy to surmount the lowest barrier en route to dissociation.

Figure 4.11 shows the TOF spectrum collected at $m/z = 42$ (CH_2CO^+) with a source angle of 10° and ionization energy of 10.5 eV. The fit corresponding to the secondary dissociation of vinoxy is shown in dashed green line and were derived using the predicted portion of the primary C−Cl bond fission P(E_T) producing vinoxy that dissociates to H + ketene (dashed red line in Figure 4.10). While we assumed in the previous study that the ketene fragments receive negligible recoil from the secondary dissociation since ketene is much heavier than the H atom cofragment, this assumption is not appropriate for ketene from the slower moving vinoxy radicals. In this case, the secondary recoil imparted to the fragments is significant compared to the velocity imparted in the primary dissociation. The dashed green fit in Figure 4.11 to ketene from the unimolecular dissociation of vinoxy radicals was thus calculated from the vector sum of the velocities of vinoxy predicted to dissociate to H + ketene and the recoil velocity between H and ketene calculated assuming an isotropic angular distribution and the secondary recoil translational energy distribution, P(E_T,2°), shown in Figure 4.12. This gives an excellent fit to ketene product with neutral flight times slower than the peak at 38 μs. The P(E_T,2°) has a roughly Gaussian shape and peaks at 3 kcal/mol, which is lower than the exit barrier for the H + ketene channel. To check for consistency, we refit the velocity map imaging data taken at $m/z = 42$ in the Discussion using the same angular distribution and P(E_T,2°). Finally, the fit corresponding to stable ketene from HCl elimination of chloroacetaldehyde is shown in solid blue line and was derived from the P(E_T) in solid black line shown in Figure 4.2. This P(E_T) thus corresponds to the portion of the HCl photoelimination events that produces stable ketene products. Interestingly, this P(E_T) has a similar shape and peaks close to the same E_T as that predicted from the velocity map imaging data (Appendix C.5). By subtracting this portion from the total P(E_T), we get the predicted unstable portion shown in dashed black line in Figure 4.2.

It is worth noting that the neutral ketene products should be detected in this study without bias as the photoionization energy used to collect the $m/z = 42$ (CH_2CO^+) TOF spectrum is above the photoionization threshold for ketene (9.62 eV[31]) yet below the first appearance energy yielding daughter ions (11.75 eV[31]). We also do not expect any contribution from dissociative ionization of vinoxy to CH_2CO^+. According to Lee et al.,[32] the dissociative ionization of CH_2CHO to CH_2CO^+ + H becomes significant at a photoionization energy greater than 12.5 eV. However, the vinoxy radicals produced in the study by Lee et al. had an average internal energy of 13 kcal/mol. Based on the predicted stable portion of the primary C−Cl bond fission $P(E_T)$, we calculate that the average internal energy of the stable vinoxy radicals is 58.9 kcal/mol. Assuming that the rotational energy imparted to the vinoxy is well described by our rotational model,[33,34] we calculate that the stable vinoxy radicals produced have an average vibrational energy of 33.5 kcal/mol. These radicals could be detected at $m/z = 42$ (CH_2CO^+) with a photoionization energy of 11.6 eV (assuming the internal energy in the vinoxy products from the study by Lee et al. is primarily in vibrations), which is much larger than the photoionization energy used to collect the TOF spectrum. While the maximum amount of vibrational energy in the stable vinoxy radicals can be 40.6 kcal/mol, the extra vibrational energy would still not lower the appearance energy threshold enough to detect CH_2CO^+ from the dissociative ionization at a photoionization energy of 10.5 eV. Therefore, it is not possible to observe dissociative ionization of vinoxy to CH_2CO^+.

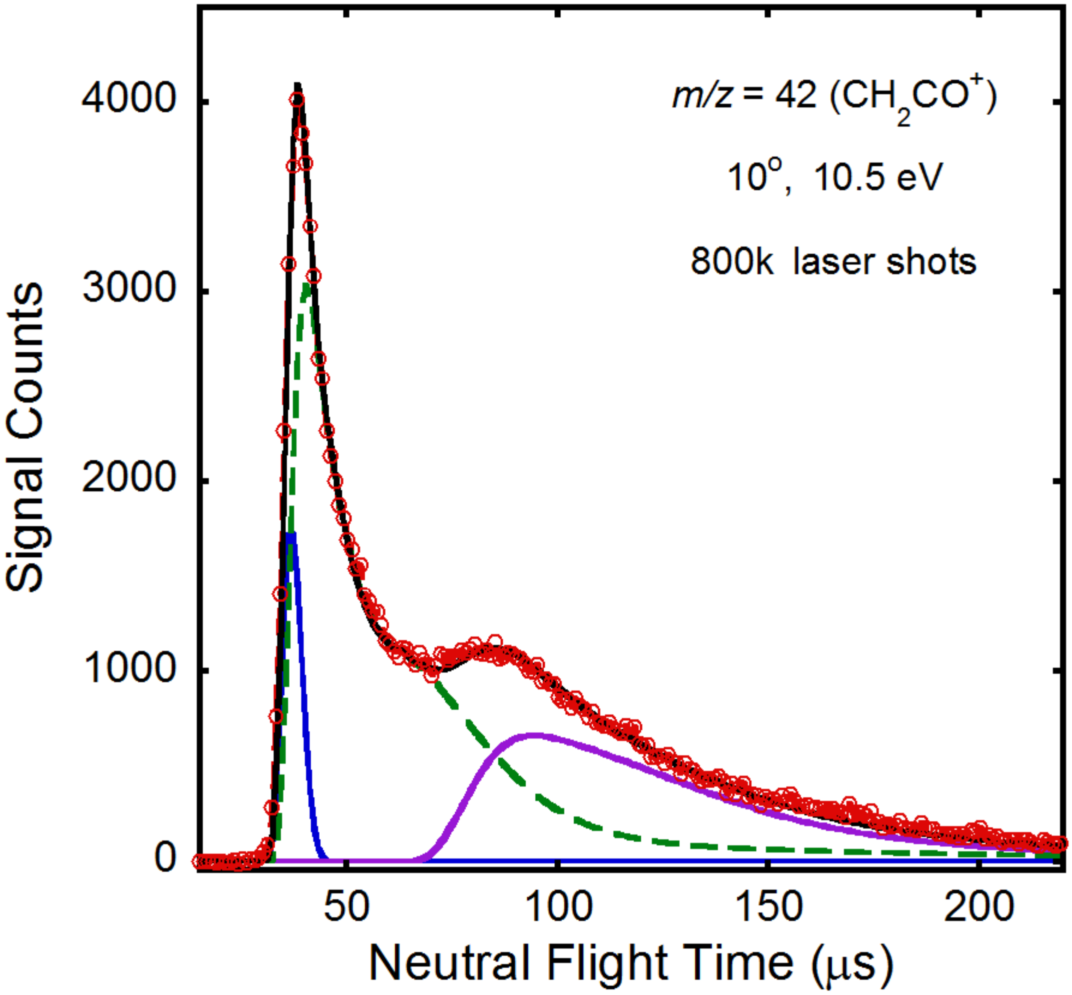

Figure 4.11: TOF spectrum taken at *m/z* = 42 (CH_2CO^+) with a source angle of 10° and an ionization energy of 10.5 eV. Data are shown in red circles. The dashed green fit shows the contribution from the dissociation of vibrationally hot vinoxy to H + CH_2CO and is calculated from the recoil translational energy of the vinoxy fragment (shown in dashed red line in Figure 4.10) and from the P(E_T,2°) in Figure 4.12 using an isotropic angular distribution. The contribution from stable ketene produced by HCl photoelimination is shown in solid blue and is derived from the high-kinetic energy portion of the P(E_T) in Figure 4.2 shown in solid black line. The fit shown in solid purple line is the contribution from clusters in the molecular beam.

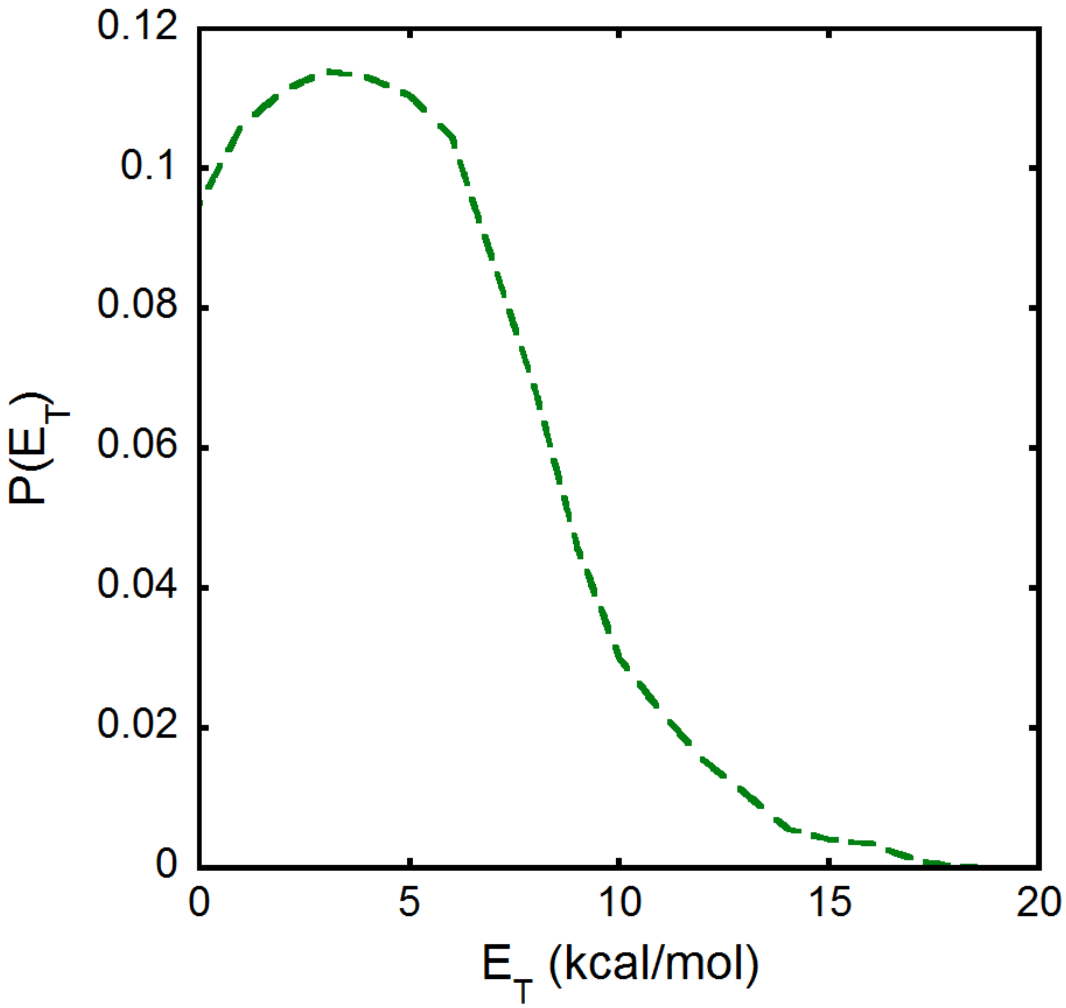

Figure 4.12: Product recoil kinetic energy distribution for the unimolecular dissociation of the vionxy radical to H + ketene. The P(E_T,2°) is derived using an isotropic angular distribution by forward convolution fitting of the signal under the dashed green fit in the *m/z* = 42 (CH_2CO^+) TOF spectrum in Figure 4.11.

Figure 4.13 depicts the TOF spectra taken at *m/z* = 15 (CH_3^+) with a source angle of 10° and at ionization energies of 10.5 eV (top frame) and 11.44 eV (bottom frame). The first interesting feature of the data is the sharp peak at ~34 μs, which clearly stands out from the rest of the signal and scales with the ionization energy to a different extent than the rest of the signal. This peak results from the dissociative ionization of stable vinoxy radicals to CH_3^+ in the ionizer and thus has the same neutral flight time as the parent fragment. In our prior velocity map imaging study, the velocity distribution of CH_3^+ from dissociation ionization of stable vinoxy was difficult to identify because that instrument detects the net velocity of the ion, not the velocity of the neutral fragment. The fit for this contribution is shown in solid green line and was derived from the portion of the C−Cl bond fission P(E_T) producing stable vinoxy radicals (shown in dashed gray line in Figure 4.10). The stable portion predicted by our branching calculations appears to be consistent with the data.

The other interesting feature in this TOF spectra is the fast signal around 22 μs fit in solid olive line , which is consistent with the fast signal observed in the data taken at *m/z* = 15 in the velocity map imaging study. This signal is too fast to be from dissociative ionization of any other fragment and cannot be fit by a secondary dissociation of any fragment produced from the single photon photodissociation of chloroacetaldehyde. We therefore attribute this signal to multiphoton dissociation, more specifically, the dissociation of stable vinoxy induced by absorption of another photon. The fit corresponding to this contribution is shown in solid olive-colored line. Since only the stable vinoxy radicals have the necessary lifetime to absorb a second 157 nm photon, we used the portion of the primary C−Cl bond fission P(E_T) producing stable vinoxy radicals for the fit along with the P(E_T,2°) shown in Figure 4.14. This adequately fits the fast edge of the signal and overlaps the contribution from secondary dissociation of vinoxy to CH_3 + CO as shown in Figure 4.13.

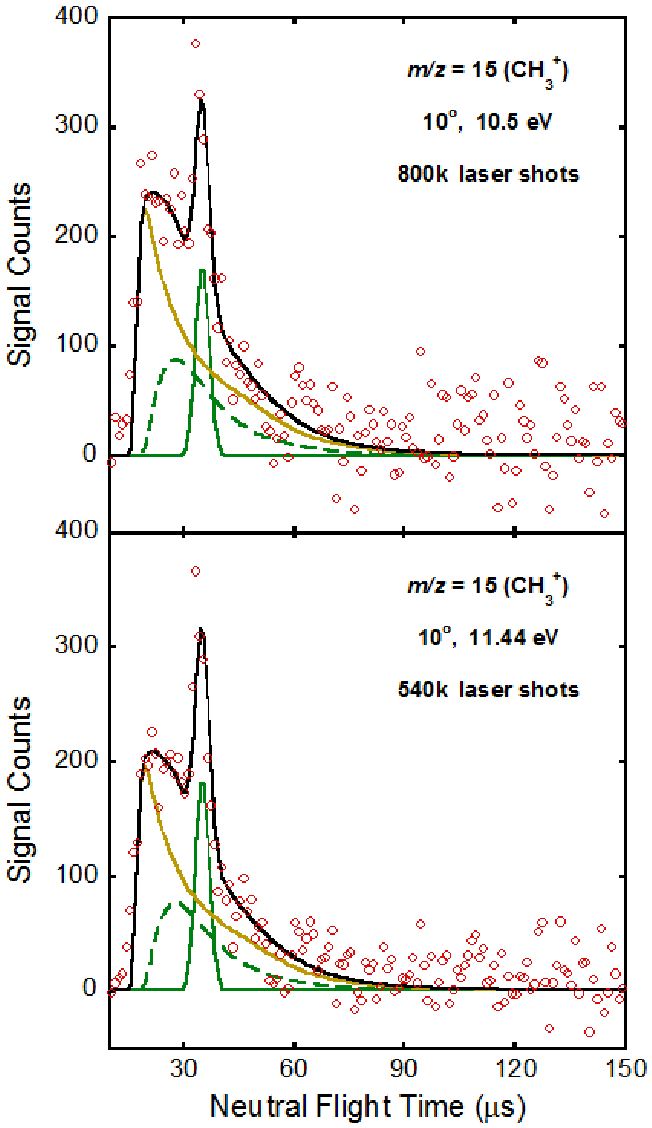

Figure 4.13: TOF spectrum taken at $m/z = 15$ (CH_3^+) with a source angle of 10° and two different ionization energies. The upper frame shows the data taken at an ionization energy of 10.5 eV and the lower frame shows the data taken at an ionization energy of 11.44 eV. Data are shown in red circles. The dashed green fit shows the contribution from the dissociation of vibrationally hot vinoxy to CH_3 + CO and is calculated using the P(E_T) shown in dashed blue line in Figure 4.10 and accounting for the recoil of CH_3 from CO using the P(E_T,2°) in Figure 4.15 and an isotropic angular distribution. Dissociative ionization of stable vinoxy radicals to CH_3^+ is shown in solid green line and was fit using the dashed gray line in Figure 4.10. The olive-colored fit shows the contribution from the dissociation of vinoxy induced by absorption of another 157 nm photon and is calculated from the P(E_T,2°) in Figure 4.14.

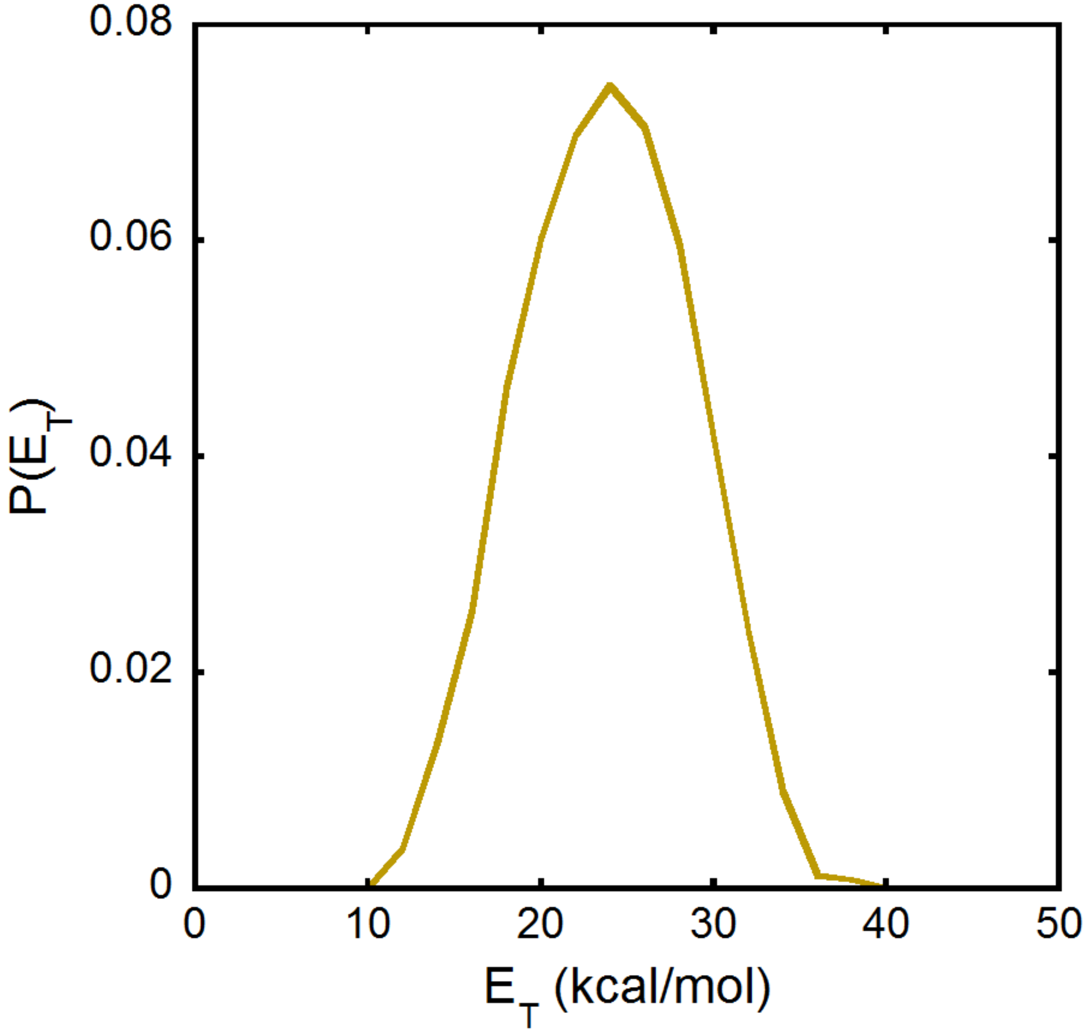

Figure 4.14: Product recoil kinetic energy distribution for the dissociation of vinoxy to CH_3 + CO following the absorption of another 157 nm photon. The P(E_T,2°) is derived using an isotropic angular distribution by forward convolution fitting of the signal under solid olive-colored fit in the m/z = 15 (CH_3^+) TOF spectra in Figure 4.13.

The fit for the contribution from secondary dissociation of vinoxy is shown in dashed green line; it was derived from the portion of the primary C−Cl bond fission P(E_T) producing vinoxy that dissociates to CH_3 + CO (shown in dashed blue line in Figure 4.10) and accounting for the recoil of CH_3 from CO using the P(E_T,2°) shown in in Figure 4.15 and an isotropic angular distribution. This P(E_T,2°) peaks at 16 kcal/mol, which is significantly different from the previous velocity map imaging study and P(E_T,2°) from the study by Miller et al. It is possible to use a half-normal distribution peaked at 0 kcal/mol to fit the data, but this fit can only account for the signal at neutral flight times slower than the peak at 34 μs. Therefore, the dissociation must impart a significant amount of recoil to the methyl fragment. While a symmetric forward/backward-scattered angular distribution was used in the velocity map imaging study, we were able to get a much better fit using an isotropic distribution. The anisotropic angular distribution could not recreate the shape of the peak and required contributing too much of the signal to multiphoton dissociation. Even though we are capable of getting a good total fit to the data, we have no way of confirming how much signal comes from multiphoton dissociation versus secondary dissociation of vinoxy. Due to the arbitrary scaling of the contributions in the TOF spectrum of m/z = 15 (CH_3^+), we were unable to calculate branching ratios between unstable vinoxy and the CH_3 + CO channel or between the H + ketene and CH_3+ CO channels.

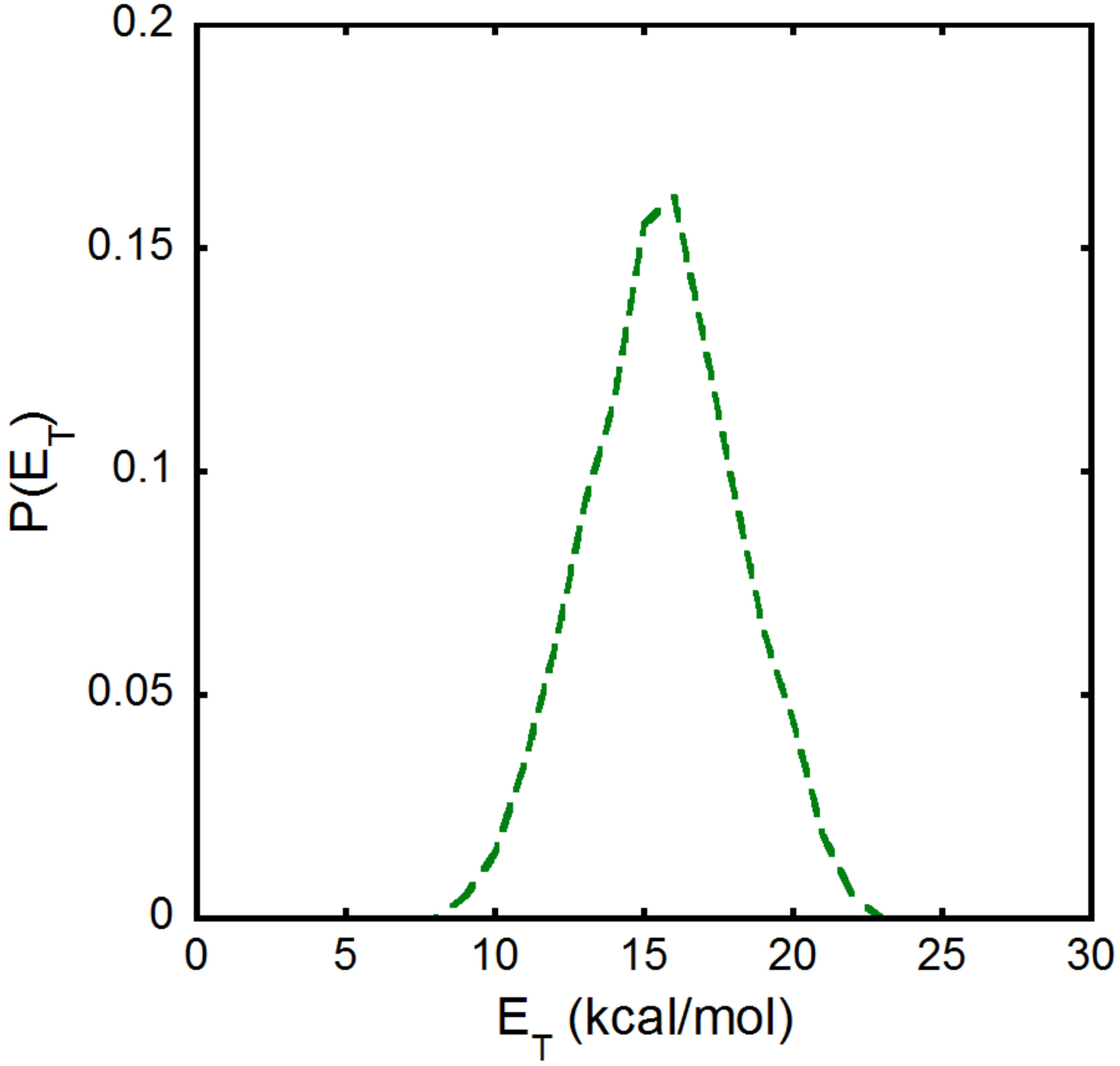

Figure 4.15: Product recoil kinetic energy distribution for the unimolecular dissociation of the vionxy radical to CH_3 + CO. The P(E_T,2°) is derived using an isotropic angular distribution by forward convolution fitting of the signal under the dashed green fit in the *m/z* = 15 (CH_3^+) TOF spectra in Figure 4.13.

Finally, Figure 4.16 shows the TOF spectrum taken at *m/z* = 28 (CO^+) with a source angle of 10° and ionization energy of 15 eV. The fits corresponding to momentum matched cofragments from secondary dissociation of vinoxy to CH_3 + CO and multiphoton dissociation of vinoxy are shown in dashed green line and solid olive-colored line, respectively. Both fits are consistent with the data. It is worth noting that the olive fit corresponding to multiphoton dissociation of vinoxy appears to be momentum-matched to the fast shoulder in the *m/z* = 28 (CO^+) data. This implies that the fast signal in the *m/z* = 15 (CH_3^+) data is consistent with a process that produces CH_3 + CO when stable vinoxy radials absorb a photon. We discuss the other fits in the TOF spectrum taken at *m/z* = 28 (CO^+) in the following sections.

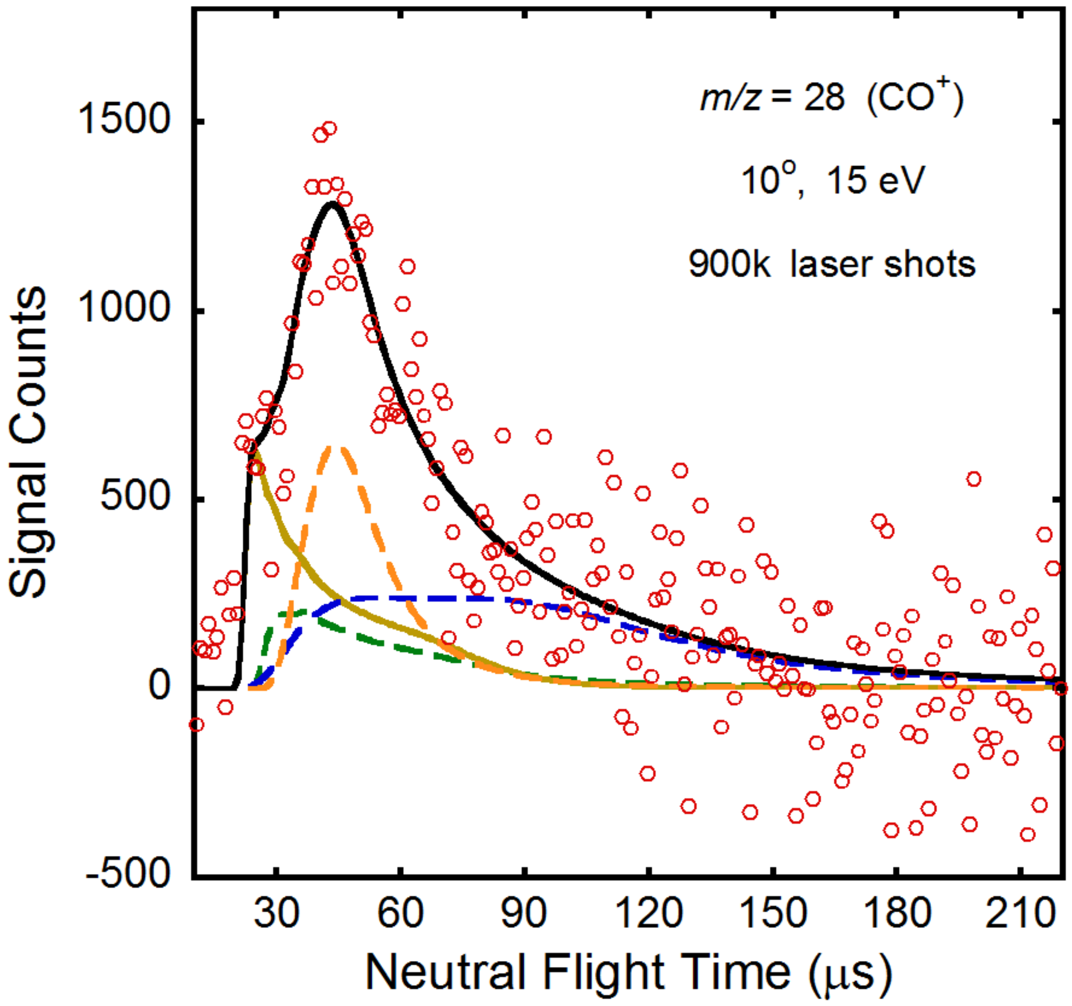

Figure 4.16: TOF spectrum taken at m/z = 28 (CO^+) with a source angle of 10° and an ionization energy of 15.0 eV. Data are shown in red circles. The dashed green fit shows the contribution from the dissociation of vibrationally hot vinoxy from C−Cl bond fission to CH_3 + CO and is calculated from the P(E_T,2°) in Figure 4.15. The olive-colored fit shows the contribution from the dissociation of vinoxy induced by absorption of another 157 nm photon and is calculated from the P(E_T,2°) in Figure 4.14. The dashed blue line shows the fit representing the dissociation of vibrational hot ketene from HCl photoelimination to CH_2 + CO and is calculated from the P(E_T,2°) in Figure 4.18. Unimolecular dissociation of HCO products from C−C bond fission is fit by the dashed orange line and is calculated using the P(E_T,2°) in Figure 4.20.

4.3.6 Unimolecular Dissociation of Vibrationally Excited Ketene Resulting From Primary HCl Photoelimination

In the TOF spectrum taken at *m/z* = 42, we observed only a small contribution from stable ketene produced from HCl photoelimination. This implies that a considerable portion of the ketene produced from primary HCl photoelimination is unstable and thus has enough vibrational energy to undergo unimolecular dissociation. Ketene has two possible dissociation channels: C-H bond fission yielding H + HCCO (eq 8) and C−C bond fission yielding CH_2 + CO (eq 9).[35]

$$CH_2CO \rightarrow HCCO + H \qquad D_o = 105.2\ \text{kcal/mol} \qquad (8)$$

$$\rightarrow CH_2 + CO \qquad D_0 = 86.1\ \text{kcal/mol} \qquad (9)$$

Since the dissociation energy of the C−C bond fission is much lower than that of the C-H bond fission, we would expect to see a substantial amount of CH_2 + CO products. We observed signal at *m/z* = 14 (CH_2^+) corresponding to dissociation of ketene and at *m/z* =28 (CO^+) from the momentum-matched cofragments.

Figure 4.17 shows the TOF spectrum taken at *m/z* = 14 (CH_2^+) with a source angle of 10° and an ionization energy of 11.53 eV. The TOF spectrum is composed of two features: a slow shoulder at 100 μs and a fast peak at 21 μs. There appears to be no appreciable bleed in from *m/z* =15 (CH_3^+) since we do not observe the sharp peak from the *m/z* =15 TOF spectrum due to dissociative ionization. Even if there is a bit of bleed in, the fast signal in the m/z = 15 data is too slow to account for all of the fast signal in the *m/z* = 14 data. We thus attributed the fast peak in TOF spectrum taken at *m/z* = 14 (CH_2^+) to dissociation of CH_2Cl following absorption of another157 nm photon and the slow shoulder to secondary dissociation of ketene. The fit corresponding to secondary dissociation of ketene to CH_2 + CO is shown in Figure 4.17 in dashed blue line and was derived from the unstable portion of the HCl photoelimination P(E_T) (shown in dashed black line in Figure 4.2). For the secondary dissociation, we used the P(E_T,2°) shown in Figure 4.18 and a symmetric 1/sinθ angular distribution calculated at 15° increments with the $\cos\theta = -1$ and 1 points adjusted to the value of 2.256 before normalization. The dissociation of ketene to CH_2 + CO is barrier-less along the ground-state singlet PES and we therefore expect the P(E_T,2°) corresponding to this process to resemble an exponential decay. The P(E_T,2°) also extends out to 60 kcal/mol, which is well within the expected maximum translational energy for this multiphoton process by energy conservation. It is also worth noting that producing CH_2^+ from chloroacetaldehyde clusters and dissociative ionization of methyl fragments are not energetically allowed at the ionization used for data collection. The appearance energy of CH_2^+ from CH_3 (15.09 eV[29]) is also well above the photoionization energy used to take the m/z = 14 TOF spectrum.

The fit corresponding to CH_2Cl dissociating after absorbing another 157 nm is shown in solid olive-colored line in Figure 4.18. Similar to the multiphoton process discussed in the previous section, only the stable CH_2Cl fragments from primary C−C bond fission will have enough time to absorb another photon. Since the barrier for C−Cl bond fission of CH_2Cl is large (93.7 kcal/mol[36]) and we expect the total internal energy available to the CH_2Cl + HCO fragments from C−C bond fission to be partitioned roughly evenly between the two, we expected all of the CH_2Cl fragments to be stable. We therefore used the complete C−C bond fission P(E_T) for the forward-convolution fitting and the P(E_T,2°) shown in Figure 4.19. This P(E_T,2°) peaks at 20 kcal/mol and spans a range from 0 – 100 kcal/mol, which is consistent with the absorption of another 157 nm photon (182 kcal/mol). We were able to obtain a good overall fit to the shape of the fast peak using an isotropic angular distribution for the multiphoton process. While we do not show this contribution from the cofragments to CH_2 to the TOF spectrum taken *m/z* = 35 (Cl^+), it is an underlying contribution much like the bleed in from *m/z* = 36 ($H^{35}Cl^+$) and likely does not contribute much signal.

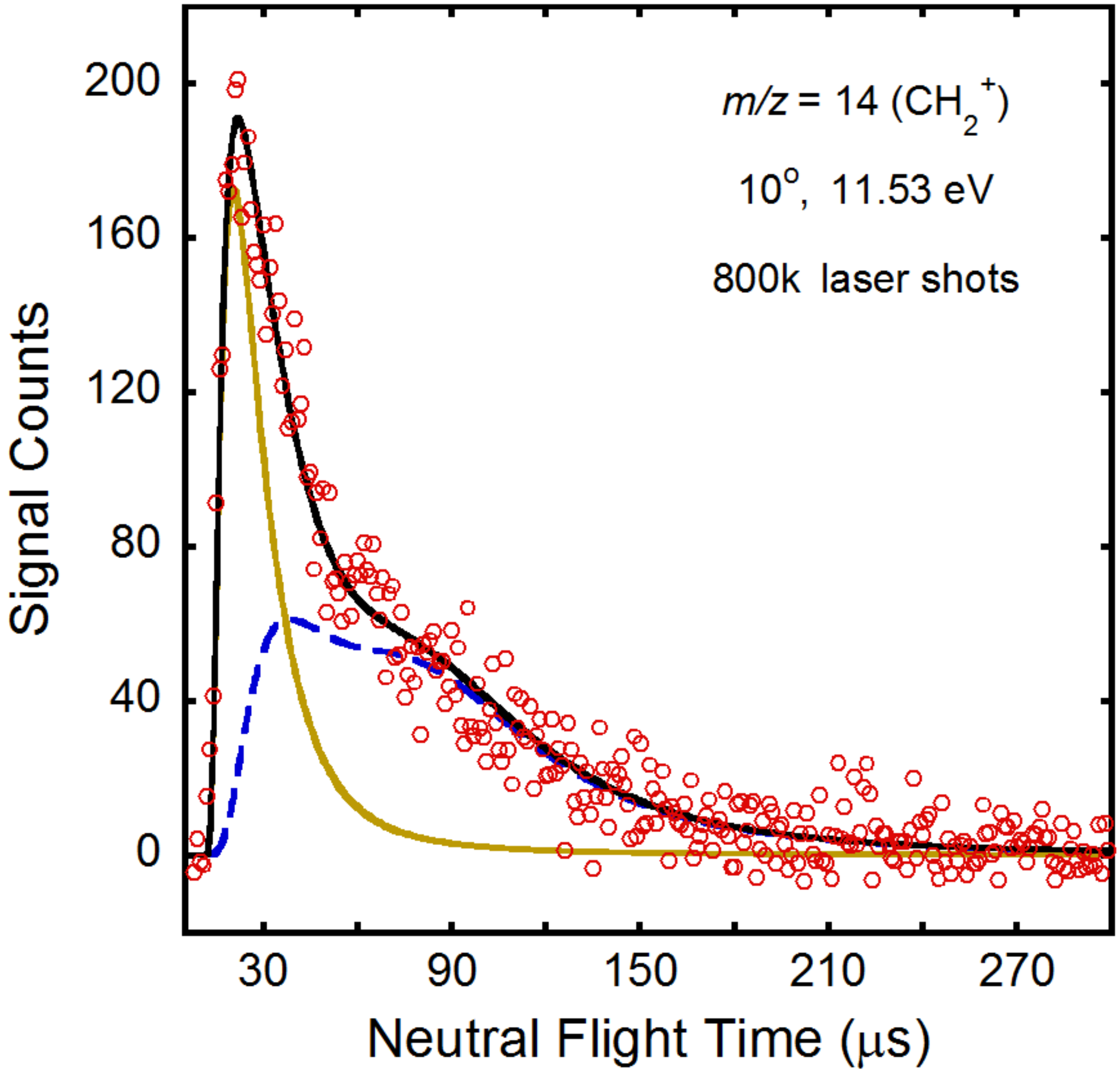

Figure 4.17: TOF spectrum taken at m/z = 14 (CH_2CO^+) with a source angle of 10° and an ionization energy of 11.53 eV. Data are shown in red circles. The dashed blue fit shows the contribution from the dissociation of vibrationally hot ketene from HCl photoelimination to CH_2 + CO and is calculated from the P(E_T,2°) in Figure 4.18 and the angular distribution noted in the text. The olive-colored fit shows the contribution from the dissociation of CH_2Cl induced by absorption of another 157 nm photon and is calculated from the P(E_T,2°) in Figure 4.19.

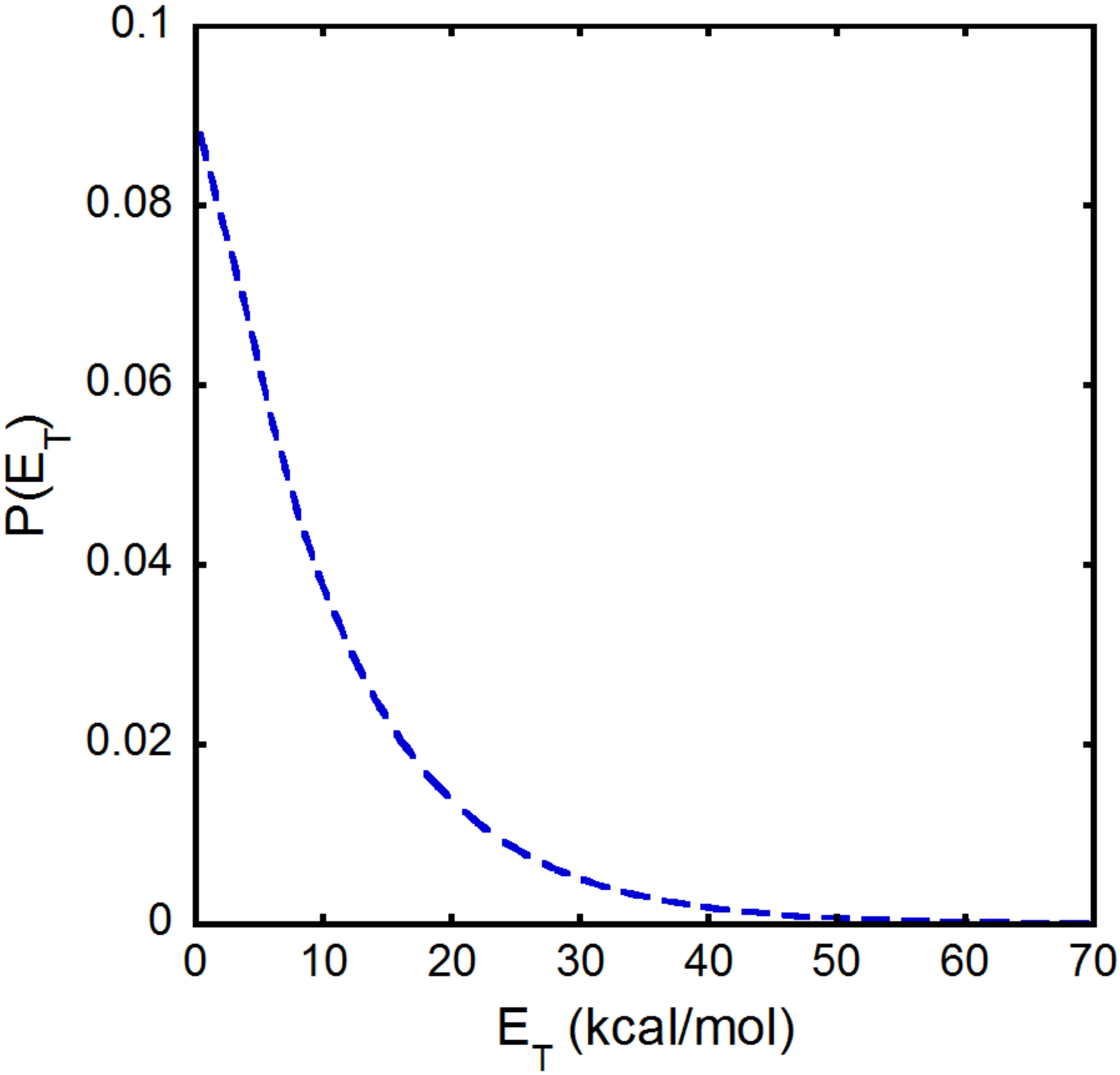

Figure 4.18: Product recoil kinetic energy distribution for the unimolecular dissociation of the ketene products from HCl photoelimination to CH_2 + CO. The P(E_T,2°) is derived using the angular distribution noted in the text by forward convolution fitting of the signal under the dashed blue fit to the slow shoulder in the $m/z = 14$ (CH_2^+) TOF spectrum in Figure 4.17.

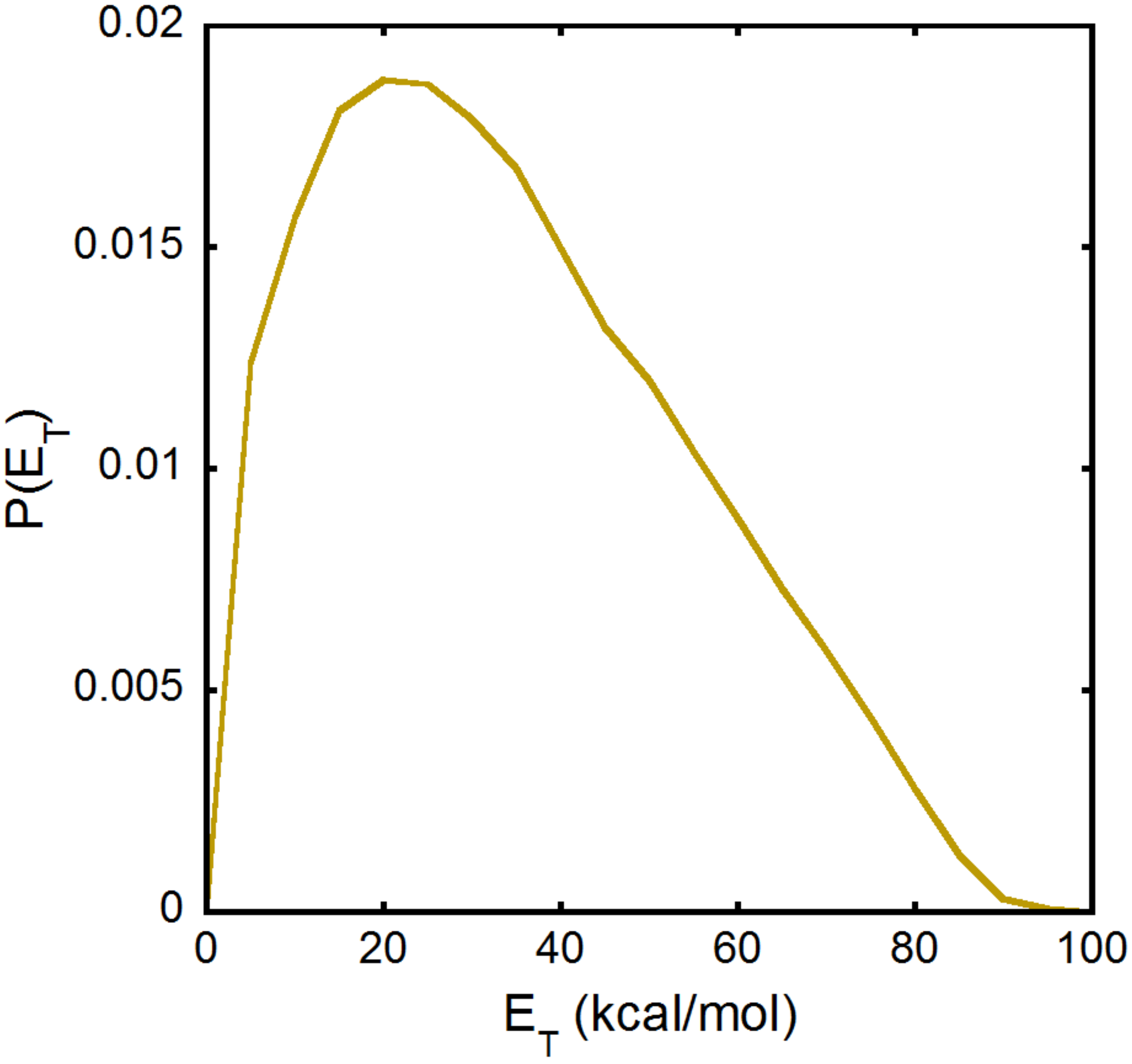

Figure 4.19: Product recoil kinetic energy distribution for the dissociation of the CH_2Cl to CH_2 + Cl induced by absorption of another 157 nm photon. The P(E_T,2°) is derived using an isotropic angular distribution by forward convolution fitting of the signal under the solid olive-colored fit to the fast peak in the $m/z = 14$ (CH_2^+) TOF spectrum in Figure 4.17.

4.3.7 Unimolecular Dissociation of Vibrationally Excited Formyl Radicals Resulting From Primary C−C Bond Fission

In Section 4.3.3, we noted that the signal in the TOF spectrum taken at *m/z* =29 (HCO^+) is momentum-matched to CH_2Cl fragments in the TOF spectrum taken at *m/z* =49 (CH_2Cl^+). However, we observe less signal in the *m/z* = 29 (HCO^+) data than we expected assuming that C−C bond fission yields one HCO fragment and one CH_2Cl fragment. While we do not expect nascent CH_2Cl fragment to undergo subsequent unimolecular dissociation since the barrier is too high, HCO has a small barrier along its ground state PES to H + CO products with a height of 17 kcal/mol.[37] From the C−C bond fission P(E_T), we calculate the range of internal energy in the CH_2Cl + HCO system to be 66.4-106.4 kcal/mol. Even if the partitioning of the total internal energy between the CH_2Cl and HCO fragments from C−C bond fission favors the CH_2Cl fragment (as much 80% of the available energy), there is enough energy left over for some portion of the HCO to undergo subsequent unimolecular dissociation. We therefore propose that the large peak in the TOF spectrum taken at *m/z* = 28 (CO^+) is from secondary dissociation of HCO products from primary C−C bond fission. The fit corresponding to this contribution is shown in Figure 4.16 in dashed orange line. Since we are unsure of which portion of the C−C bond fission P(E_T) produces unstable HCO fragments, we used the complete primary P(E_T) for the forward-convolution fitting. We also used the P(E_T,2°) shown in Figure 4.20 and an isotropic angular distribution. The P(E_T,2°) peaks around 1 kcal/mol, which is consistent with the exit barrier of the dissociation channel (~3 kcal/mol). It is worth noting that while an isotropic angular distribution was used to fit the contribution, the choice of angular distribution is arbitrary and we get a good fit with a symmetric forward-backward-scattered angular distribution as well, albeit with a different P(E_T,2°).

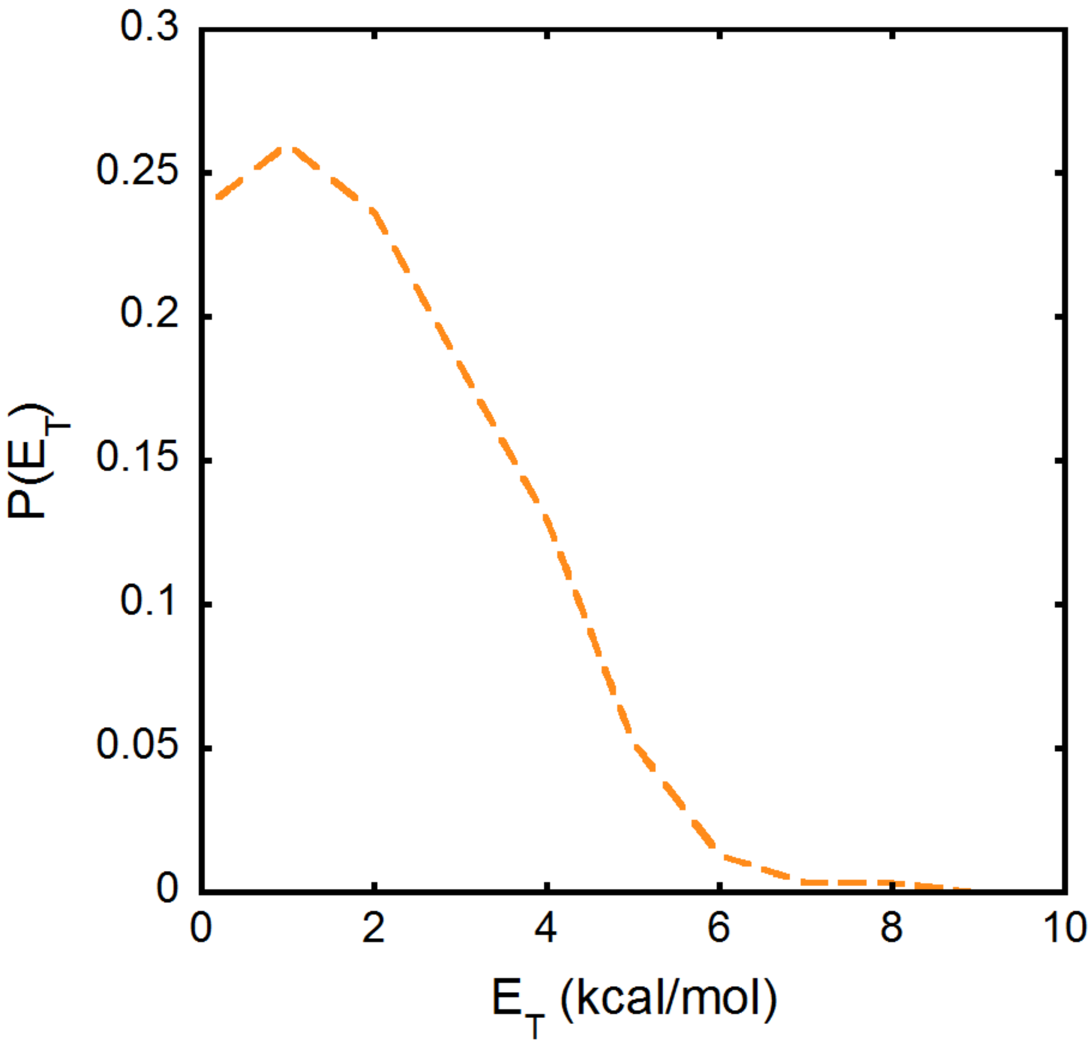

Figure 4.20: Product recoil kinetic energy distribution for the unimolecular dissociation of the HCO radicals from C−C bond fission to H + CO. The P(E_T,2°) is derived using an isotropic angular distribution by forward convolution fitting of the signal under the dashed orange fit to the peak at 42 μs in the m/z = 28 (CO^+) TOF spectrum in Figure 4.10.

4.3.8 Partial Photoionization Cross Section for Vinoxy to CH_3^+ + CO

While we did not observe any signal at *m/z* = 43 (CH_2CHO^+) from stable vinoxy, we did detect stable vinoxy radical at *m/z* = 15 (CH_3^+) and *m/z* = 29 (HCO^+) due to dissociative ionization of vinoxy to CH_3^+ and HCO^+, respectively. Since the quantum yield of vinoxy and Cl fragments from C−Cl bond fission is 1:1 and the photoionization cross section of Cl is known, we can estimate the partial photoionization cross section for vinoxy appearing at CH_3^+, $\sigma_{\mathrm{CH_2CHO/CH_3^+}}$ using the equation

$$\frac{\Phi_{\mathrm{CH_2CHO}}}{\Phi_{\mathrm{Cl}}} = \frac{1}{1} = \mathrm{obs}\left(\frac{^{35}\mathrm{Cl}^+}{\mathrm{CH_3}^+}\right) \times f_{^{35}\mathrm{Cl}}{}^{-1} \times \mathrm{TS}\left(\frac{\mathrm{CH_2CHO}}{^{35}\mathrm{Cl}}\right) \times \left(\frac{q_{\mathrm{X}}}{q_{13.67\ \mathrm{eV}}}\right) \times \left(\frac{\sigma_{\mathrm{CH_2CHO/CH_3^+}}}{\sigma_{\mathrm{Cl/Cl^+}}\ @13.67\ \mathrm{eV}}\right) \tag{10}$$

$$\frac{1}{1} = \left(\frac{0.016845}{0.00100}\right) \times \left(\frac{1}{0.7578}\right) \times \left(\frac{16248}{12565}\right) \times \left(\frac{10.8\ \mu\mathrm{A}}{26.1\ \mu\mathrm{A}}\right) \times \left(\frac{\sigma_{\mathrm{CH_2CHO/CH_3^+}}@\ 10.5\ \mathrm{eV}}{22.8\ \mathrm{Mb}}\right) \tag{11}$$

$$\frac{1}{1} = \left(\frac{0.016845}{0.001585}\right) \times \left(\frac{1}{0.7578}\right) \times \left(\frac{16248}{12565}\right) \times \left(\frac{14.7\ \mu\mathrm{A}}{26.1\ \mu\mathrm{A}}\right) \times \left(\frac{\sigma_{\mathrm{CH_2CHO/CH_3^+}}@\ 11.44\ \mathrm{eV}}{22.8\ \mathrm{Mb}}\right) \tag{12}$$

where $\mathrm{obs}\left(\frac{^{35}\mathrm{Cl}^+}{\mathrm{CH_3}^+}\right)$ is the observed signal from stable vinoxy in the *m/z* = 15 (CH_3^+) and *m/z* = 35 (Cl^+) data corrected for the number of laser shots, $f_{^{35}\mathrm{Cl}}$ is the isotopic abundance of ^{35}Cl, $TS\left(\frac{\mathrm{CH_2CHO}}{^{35}\mathrm{Cl}}\right)$ is the correction for kinematic factors, q_{X} is the photocurrent at the photoionization energy used to collect the TOF spectrum (this provides a representation of the photon flux), and $\sigma_{\mathrm{Cl/Cl^+}}$ is the photoionization cross section of Cl at 13.67 eV averaged over the synchrotron bandwidth. For these calculations, we used the portion of the C−Cl bond fission P(E_T) producing stable vinoxy predicted from our branching calculations (shown in dashed gray line in Figure 4.4). Since we have TOF data for CH_3 at ionization energies of 10.5 eV and 11.44 eV, we estimated the partial cross section at both ionization energies. We found the partial photoionization cross section of vinoxy appearing at CH_3^+ to be 1.9 Mb and 2.2 Mb at ionization energies of 10.5 eV and 11.44 eV, respectively. Note that when accumulating the signal at m/z = 15 at 11.44 eV, we alternated scans with m/z = 35 to average out any drifts in beam intensity or laser power; however, the signal at 10.5 eV were not taken with this precaution, so the partial cross section at this photoionization energy should be regarded as preliminary.

G4 calculations on the cationic surface of vinoxy show that the barrier to forming CH_3^+ + CO is 10.4 eV relative to the zero-point level of the vinoxy radical (see Appendix C.6), which is consistent with the appearance energy of CH_3^+ for vinoxy found in a few references (10.3 eV).[32,38] Therefore, these results agree with the observation of dissociative ionization of vinoxy to CH_3^+ at photoionization energies of 10.5 eV and 11.44 eV as well as the increase in the cross section at higher photoionization energies. Our cross sections are also consistent with the maximum cross section value of 5.2 Mb determined from the data of Osborn et al. in their study on the $O(^3P)$ + propene reaction.[38] However, we note that the appearance energy depends on the internal energy of the vinoxy fragments and thus we may expect to see dissociative ionization at lower photoionization energies. The average vibrational energy of the stable vinoxy radicals from C−Cl bond fission in this study is 33.5 kcal/mol. Based on this vibrational energy, we could in principle detect CH_3^+ from dissociative ionization of vinoxy at a minimum photoionization energy of 9.4 eV. The *m/z* = 15 TOF data at a photoionization energy of 9.845 eV did not evidence signal from dissociative ionization of vinoxy radicals.

It is worth noting that the error in these estimates is primarily dependent on the amount of signal in the TOF spectrum taken at *m/z* = 35 (Cl^+) that we attribute to primary C−Cl bond fission and the photoionization cross section of Cl. We have already discussed the possibility of the fast signal in the TOF data taken at $m/z = 35$ (Cl^+) being from a multiphoton process or dissociation of monomer or dimer hydrates of the precursor. If this is the case, then we are overestimating the Cl signal from C−Cl bond fission and therefore our estimates of $\sigma_{\mathrm{CH_2CHO/CH_3^+}}$ are minimum possible values. While the assignment of the fast signal in the TOF data taken at $m/z = 35$ (Cl^+) would alter the C−Cl bond fission P(E_T) and therefore the portion resulting in stable vinoxy, we get a comparable fit to the peaks from dissociative ionization in the TOF spectra taken at $m/z = 15$ (CH_3^+) using the stable portion of the C−Cl bond fission P(E_T) derived in the velocity map imaging study (see Appendix C.7).

4.4 Discussion

This study details the characterization of the primary photodissociation channels of chloroacetaldehyde at 157 nm and the reassessment of the subsequent dissociation dynamics of the vinoxy radicals produced by C−Cl bond fission. We first demonstrated that chloroacetaldehyde undergoes three primary dissociation channels: C−Cl bond fission, HCl photoelimination, and C−C bond fission. While C−Cl bond fission and HCl photoelimination have been observed in prior photodissociation studies of chloroacetaldehyde,[1,2] this study provides the first direct evidence of the C−C bond fission channel. Using the scattering data, we then estimated the branching ratios between the primary channels; we determined C−Cl bond fission and C−C bond fission to be major channels and HCl photoelimination to be a minor channel. We then investigated the unimolecular dissociation of vinoxy radicals from C−Cl bond fission to characterize the dynamics observed in the previous velocity map imaging study. While the analysis of the $m/z = 42$ (CH_2CO^+) data is consistent between the two studies, the analysis of the $m/z = 15$ (CH_3^+) data is markedly different. We also presented evidence of the subsequent dissociation of the products from the other two primary channels: ketene from HCl photoelimination dissociating CH_2 + CO and HCO from C−C bond photofission dissociating to H + CO.

As in the velocity map imaging study, the translation energy distribution for the C−Cl photofission channel (Figure 4.3) shows two main features: a low-kinetic-energy “shoulder”and a high-kinetic energy peak at 42 kcal/mol. These features suggest that we still observe nascent vinoxy radicals formed in the electronically excited Ã and B̃ states. In the previous study, we concluded that the high-kinetic energy component likely corresponds to vinoxy produced in the Ã state following excitation to the S_3 state of chloroacetaldehyde and the low-kinetic energy component likely corresponds to vinoxy produced in the B̃ state following excitation to the S_4 state of chloroacetaldehyde. Nevertheless, we do not expect the electronic state of the nascent vinoxy to affect the dynamics of the radical as previous studies[39-42] suggest that vinoxy undergoes internal conversion to the ground electronic state and dissociates along the ground state PES. We also note that there is additional signal on the high-kinetic energy side of the C−Cl bond fission P(E_T) that we did not observe in the velocity map imaging study. This may be due to a small amount of multiphoton dissociation events or, possibly, photodissociation of the monomer and dimer hydrates in the molecular beam.

The C−C bond fission channel is of particular interest because it has not been directly observed before in the photodissociation of chloroacetaldehyde and it effectively competes with the C−Cl bond fission channel. The translational energy distribution for this channel peaks at 8 kcal/mol, which suggests a small exit barrier to the dissociation. Compared to the other photodissociation pathways of chloroacetaldehyde at 157 nm, the C−C bond fission P(E_T) has the smallest range of recoil translational energies (0 – 40 kcal/mol). These features are similar to the C−C bond fission channel observed in the photodissociation of chloroacetone at 193 nm; however, the C−C bond fission P(E_T) derived in that study peaks at a lower E_T (~6 kcal/mol) and only ranges from 0 -14 kcal/mol. In contrast to the chloroacetone study at 193 nm, we also report a smaller branching ratio between C−Cl bond fission and C−C bond fission. Since chloroacetaldehyde and chloroacetone have the same chromophore and same structure (with the exception of a methyl group in place of the aldehydic H atom), we expect the photodissociation dynamics of the two molecules to be quite similar to one another. Assuming the branching between C−Cl bond fission and C−C bond fission in chloroacetaldehyde at 193 nm is similar to that of chloroacetone, we see more branching to C−C bond fission at the higher photon energy of 157 nm.

Since the singlet excited states of chloroacetaldehyde in the vicinity of the excitation energy (S_2, S_3, and S_4) are all repulsive along the C−Cl bond in the Franck-Condon region, we would expect C−Cl bond fission to be the dominant channel. Therefore, there must be internal conversion between the states such that the molecule eventually finds itself on a state on which C−C bond fission can occur. In fact, Lucazeau and Sandorfy[17] suggested that there is a high chance of crossing between PESs to explain the diffuse character of the VUV absorption spectrum for chloroacetaldehyde. Based on TD-DFT calculations, there may be a possible route to C−C bond fission along the T_1 state which rises to a barrier and then falls as the C−C bond is stretched. This result is consistent with the theoretical trajectories done by Shen et al.[43] in their study on the observed selectivity of the C−C bond fission channel in the photodissociation of chloroacetone at 308 nm. While they found that the effectiveness of the non-adiabatic $S_1 \rightarrow S_0$ transition in the vicinity of the barriers to each C−C bond fission channel explained the selectivity, they were not certain that the C−C bond fission ultimately occurred on the ground-state singlet surface based on the experimentally determined P(E_T) for the process. At an excitation of 308 nm, the only energetically accessible state to chloroacetone is the T_1 state and the same is true of chloroacetaldehyde. Therefore, it is possible that the C−C bond fission occurs on this state following intersystem crossing from the S_1 state. For this state to be responsible for the observed C−C bond fission in the photodissociation at 157 nm, there must be an effective internal conversion process to the T_1 state. At this time, it is unclear what this process could be and would require a more in-depth study of the excited-state dynamics of chloroacetaldehyde.

The HCl photoelimination P(E_T) previously derived by Miller et al. in their photodissociation study at 193 nm[2] peaked around 8 kcal/mol and ranged from 0 – 40 kcal/mol. Similarly, the P(E_T) derived in this study (Figure 4.2) peaks at 8 kcal/mol; however, it ranges from 0 – 60 kcal/mol instead. This is consistent with the larger photon energy used in this study as there is more available energy that can be partitioned into translation. While Miller et al. were unable to characterize the portion of ketene cofragments from HCl photoelimination that undergo unimolecular dissociation, we were able to show that the portion of the HCl photoelimination P(E_T) that corresponds to events producing stable ketene is quite small. This demonstrates that there are HCl fragments produced with significant vibrational energy following the dissociation. While we could not characterize the internal energy of the HCl fragments directly, the stable portion of the HCl photoelimination P(E_T) shown in Figure 4.2 suggests that when $E_T = 44$ kcal/mol the ketene fragments have less than 84 kcal/mol of internal energy (the barrier to dissociation of ketene to CH_2 + CO). The momentum-matched HCl would have greater than 47.6 kcal/mol, which corresponds to roughly 6 quanta in vibration (assuming rotational energy is negligible). When the HCl photoelimination partitions less than 44 kcal/mol to relative kinetic energy, some of the ketene dissociates to CH_2 + CO leaving the HCl with less than 6 quanta in vibration. While this amount of excitation is reasonable for the HCl products from HCl photoelimination, we cannot make any definite conclusions about how the internal energy is partitioned between vibration and rotation. A complementary study on the characterization of the vibrational and rotational energy distributions of HCl products would therefore be beneficial and would provide information about the internal energy available to the ketene cofragments.

While we have assumed that the HCl photoelimination proceeds via a four-center mechanism thus producing ketene as a cofragment, a three-center mechanism is also possible which would produce the HCCHO biradical cofragment. Similar systems have shown evidence of both mechanism types; however, we cannot confirm if we observe the three-center mechanism. Based on electronic structure calculations (Appendix C.2), the lowest barrier on the ground state PES of the HCCHO radical is isomerization to ketene where it can further undergo dissociation to CH_2 + CO like the ketene products do. This makes it difficult to confirm the presence of the HCCHO radical and evidence of the three-center mechanism. Prior studies have found that the vibrational and rotational energy distributions of the HCl product produced from the two mechanism types are generally different. Therefore, another benefit to further characterizing the internal energy distribution of the HCl products from photodissociation of chloroacetaldehyde would be to confirm the presence of two distinct mechanisms for HCl photoelimination.

Another interesting aspect about the scattering data for HCl photoelimination is the notable difference between the TOF spectra taken at $m/z = 36$ ($H^{35}Cl^+$) and at $m/z = 38$ ($H^{37}Cl^+$). The TOF spectra taken at $m/z = 36$ ($H^{35}Cl^+$) show faster signal that is dependent on the ionization energy used to collect the data. This signal is not observed in the TOF spectrum taken at $m/z = 38$ ($H^{37}Cl^+$). If the extra fast signal observed at $m/z = 36$ ($H^{35}Cl^+$) is from bleed in of the $m/z = 37$

(Cl^+) signal, then we would not expect to see the same signal in the *m/z* = 38 ($H^{37}Cl^+$) since there is no bleed in to that data from higher masses. Based on the resolution of the quadrupole, the maximum amount of bleed in from the *m/z* + 1 signal into the *m/z* signal is 10% and the amount of signal observed at *m/z* = 37 (Cl^+) is not enough to account for all of the fast signal in Figure 4.6. One possibility is that HCl photoelimination occurs via two distinct mechanisms which experience different isotope effects from Cl. As for the dependence on the ionization energy, HCl produced in different vibrational energy states may be more efficiently ionized at one ionization energy over the other.

Another goal of this study was to reassess the unimolecular dissociation pathways of the vinoxy radical from the velocity map imaging study. While we found the barrier height of 44.6 kcal/mol for the H + ketene to be the consistent with the data, we did not fit the data in this study by assuming that the secondary recoil imparted to the ketene fragment is negligible. We were able to get a good fit to the data using the P(E_T,2°) shown in Figure 4.12 and an isotropic angular distribution. This angular distribution is consistent with the corresponding channel ($CH_3COCH_2 \rightarrow CH_3 + CH_2CO$) in the photodissociation study on chloroacetone at 193 nm.[15] However, if we allow the angular distribution for vinoxy to H + ketene to be anisotropic, good fits to the data can be achieved using either the 44.6 kcal/mol barrier or the G4 barrier (see fits in Appendix C.8). For consistency, Figure 4.21 shows the speed distribution for the *m/z* = 42 fragments from the velocity map imaging study fit with the P(E_T,2°) in Figure 4.12 and an isotropic angular distribution. Apart from the small unfit signal at large net speeds, which is likely from stable ketene produced by HCl photoelimination, the fit agrees with the data reasonably well. Thus although we used a barrier of 44.6 kcal/mol for the H + ketene product channel of vinoxy, we can also obtain good fits to the data using the lower G4 barrier. Those fits require attributing more of the high-kinetic energy ketene to the unimolecular dissociation of vinoxy to H + ketene and less to stable ketene from HCl photoelimination.

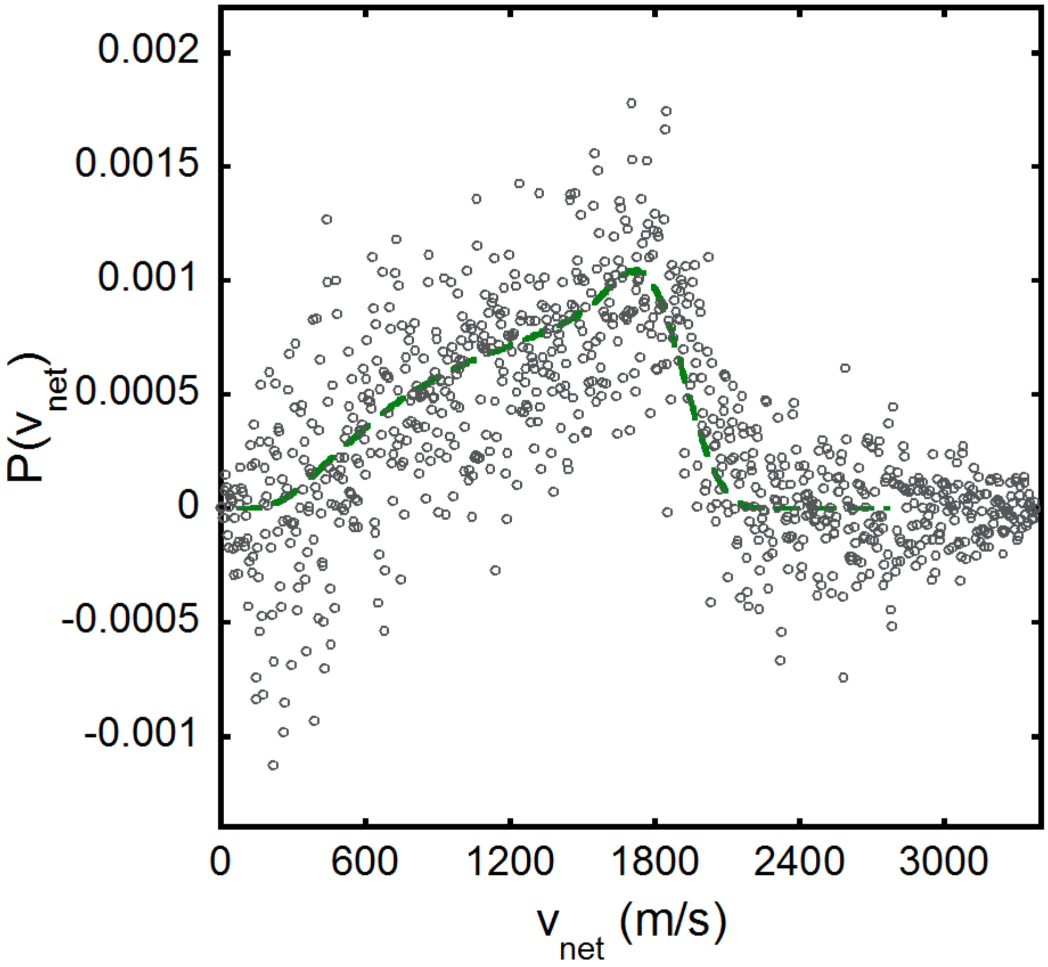

Figure 4.21: Speed distribution for *m/z* = 42 (CH_2CO^+) fragments (open gray circles) derived in the velocity map imaging study shown with the fit (dashed green line) derived from the secondary P(E_T) in Figure 4.12 and an isotropic angular distribution, which were found to give the best fit to the data taken in this study at the same mass-to-charge ratio. For the primary process, we used the portion of primary C−Cl bond fission predicted to yield vinoxy that dissociates to H + ketene derived in the velocity map imaging lab study (Figure 3.8). The fit agrees reasonable well with the data.

The largest discrepancy between the results from the velocity map imaging study and this study comes from the m/z = 15 (CH_3^+) data. The best fit to the TOF spectra taken at m/z = 15 (CH_3^+) in this study not only utilizes a different P(E_T,2°) from the velocity map imaging study, but also a different angular distribution. Part of this issue is likely due to the poor signal-to-noise in the velocity map imaging data, which made fitting difficult. The P(E_T,2°) peaks at 16 kcal/mol, which is a significant amount of recoil kinetic energy compared to the zero recoil kinetic energy suggested by Miller et al.[2] However, we did find that the fast signal observed in the velocity map imaging study also appears in the data from this study and so this signal must be real. In the end, we attributed this signal to dissociation of vinoxy radicals following the absorption of another 157 nm photon. The fast signal is also momentum matched to the fast shoulder in the TOF spectrum taken at m/z = 28 (CO^+), which suggests that CO is its cofragment and the signal comes from the neutral products. According to EOM-CCSD calculations, vinoxy has excited states close to the excitation energy with decent oscillator strength so it is possible for stable vinoxy radicals to absorb another photon. Without further calculations on the excited state PES, we cannot say anything about how reasonable the P(E_T,2°) and angular distribution we derived for this multiphoton process are. Since the contributions from both processes overlap and we cannot be sure how much we process contributes to the observed signal, we are unable to calculate a branching ratio between the secondary dissociation channels.

4.5 References

(1) Lam, C.-S., Adams, J. D.; Butler, L. J. The Onset of H + Ketene Products from Vinoxy Radicals Prepared by Photodissociation of Chloroacetaldehyde at 157 nm. *J. Chem. Phys.* **2016**, 120, 2521-2536.

(2) Miller, J. L.; McCunn, L. R.; Krisch, M. J.; Butler, L. J.; Shu, J. Dissociation of the Ground State Vinoxy Radical and Its Photolytic Precursor Chloroacetaldehyde: Electronic Nonadiabaticity and the Suppression of the H + Ketene Channel. *J. Chem. Phys*. **2004**, *121*, 1830-1838.

(3) Tuazon, E. C., Atkinson, R.; Winer, A. M.; Pitts, J. N. A Study of the Atmospheric Reactions of 1,3-Dichloropropene and Other Selected Organochlorine Compounds. *Arch. Environ. Contam. Toxicol.* **1984**, *13*, 691-700.

(4) Calvert, J. G. Derwent, R. G., Orlando, J. J.; Tyndall, G. S.; Wallington, T. J. *Mechanisms of Atmospheric Oxidation of the Alkanes*. Oxford University Press: New York, 2008.

(5) Starcke, J.; Zabel, F.; Elsen, L.; Nelsen, W.; Barnes, I.; Becker, K. H. *Physico-Chemical Behaviour of Atmospheric Pollutants*; Kluwer Academic Publishers: Dordrecht, 1990.

(6) Lin, J. J.; Chen, Y.; Lee, Y. Y.; Lee, Y. T.; Yang, X. Photodissociation Dynamics of CH_3Cl at 157.6 nm: Evidence for $CH_2(\tilde{X}^3B_1/\tilde{a}^1A_1)$ + HCl Product Channels. *Chem. Phys. Lett.* **2002**, *361*, 374-382.

(7) Lin, S.-R.; Lin, S.-C.; Lee, Y.-C.; Chou, Y.-C.; Chen, I.-C.; Lee, Y.-P. Three-Center versus Four-Center HCl-elimination in Photolysis of Vinyl Chloride at 193 nm: Bimodal Rotational Distribution of HCl (v7) Detected with Time-Resolved Fourier-Transform Spectroscopy. *J. Chem. Phys.* **2001**, *114*, 160-168.

(8) Saha, A.; Kawade, M. SenGupta, S. Upadhyaya, H. P.; Kumar, A; Naik, P. D. Photodissociation Dynamics of Benzyol Chloride at 235 nm: Resonance-Enhanced Multiphoton Detection of Cl and HCl. **2014**, *118*, 1185-1195.

(9) Lee, P.-W.; Scrape, P. G.; Butler, L. J.; Lee, Y.-P. Two HCl-Elimination Channels and Two CO-Formation Channels Detected with Time-Resolved Infrared Emission upon Photolysis of Acryloyl Chloride [$CH_2CHC(O)Cl$] at 193 nm. *J. Phys. Chem. A* **2015**, *119*, 7293-7304.

(10) Brynteson, M. D.; Womack, C. C.; Booth, R. S.; Lee, S.-H.; Lin, J. J. Butler, L. J.; Radical Intermediates in the Addition of OH to Propene: Photolytic Precursors and Angular Momentum Effects. *J. Phys. Chem. A* **2014**, *118*, 3211-3229.

(11) Booth, R. S.; Brynteson, M. D.; Lee, S.-H.; Lin, J. J.; Butler, L. J. Further Studies into the Photodissociation Pathways of 2-Bromo-2-nitroproane and the Dissociation Channels of the 2-Nitro-2-propyl Radical Intermediate.

(12) Nelson, L.; Shanahan, I; Sidebottom, H. W.; Treacy, J.; Nielsen, O. J. Kinetics and Mechanism for Oxidation for 1,1,1-Trichloroethane. *Int. J. Chem. Kinet.* **1990**, *22*, 577-590.

(13) Waschewsky, G. C. G.; Kash, P. W.; Myers, T. L.; Kitchen, D. C.; Butler, L. J. What Woodward and Hoffman Didn’t Tell Us: The Failure of the Born-Oppenheimer Approximation in Competing Reaction Pathways. *J. Chem. Soc. Faraday Trans.* **1994**, *90*, 1581-1598.

(14) Kitchen, D. C.; Myers, T. L.; Butler, L. J. Determination of Absolute Product Branching Ratios in Mass Spectrometric Experiments: Detecting Acetyl Radicals at CH_2CO^+. *J. Phys. Chem.* **1996**, *100*, 5200-5204.

(15) Alligood, B. W.; Fitzpatrick, B. L.; Szpunar, D. E.; Butler, L. J. Chloroacetone Photodissociation at 193 nm and the Subsequent Dynamics of the $CH_3C(O)CH_2$ Radical - An Intermediate Formed in the OH + Allene Reaction En Route to CH_3 + Ketene. *J. Chem. Phys.* **2011**, *134*, 054301.

(16) Burkholder, J. B.; Gilles, M. K.; Gierczak, T.; Ravishankara, A. R. The Atmospheric Degradation of 1-Bromopropane ($CH_3CH_2CH_2Br$): The Photochemistry of Bromoacetone. *Geophys. Res. Lett.* **2002**, *29*, 1822-1825.

(17) Lucazeau, G.; Sandorfy, C. On the Far-Ultraviolet Spectra of Some Simple Aldehydes. *J. Mol. Spectrosc.* **1970**, *35*, 214-231.

(18) Ratliff, B. J.; Alligood, B. W.; Butler, L. J.; Lee, S.-H.; Lin, J. J. Product Branching from the CH_2CH_2OH Radical Intermediate of the OH + Ethene Reaction. *J. Phys. Chem. A* **2011**, *115*, 9097-9110.

(19) Lin, J. J.; Chen, Y.; Lee, Y. Y.; Lee, Y. T.; Yang, X. Photodissociation Dynamics of CH_3Cl at 157.6 nm: Evidence for CH_2 (X^3B_1/a^1A_1) + HCl Product Channels. *J. Chem. Phys. Lett.* **2002**, *361*, 374-382.

(20) Lee, Y. T.; McDonald, J. D.; LeBreton, P. R., Herschbach, D. R. *Rev. Sci. Instrum.* **1969**, *40*, 1402-8.

(21) CMLAB2, version 6/93, modified by J. D. Myers. This is an interactive version built on the original cmlab2 program: Zhao, X. Ph.D. Dissertation, University of California, 1988.

(22) Curtiss, L. A.; Redfern, P. C.; Raghavachari, K.; Pople, J. A. Gaussian-3X (G3X) Theory: Use of Improved Geometries, Zero-Point Energies, and Hartree-Fock Basis Sets. *J. Chem. Phys*. **2001**, *114*, 108-117.

(23) Curtiss, L. A.; Redfern, P. C.; Raghavachari, K. Gaussian-4 Theory. *J. Chem. Phys*. **2007**, *126*, 084108.

(24) Frisch, M. J.; Trucks, G. W.; Schlegel, H. B.; Scuseria, G. E.; Robb, M. A.; Cheeseman, J. R.; Scalmani, G.; Barone, V.; Mennuci, B.; Petersson, G. A.; et al. Gaussian 09, Revision A.02; Gaussian, Inc.: Wallingford, CT, 2009.

(25) Scrape, P. G.; Roberts, T. D.; Lee, S.-H.; Butler, L. J. Dissociation Pathways of the CH_2CH_2ONO Radical: NO_2 + Ethene, NO + Oxirane, and a Non-Intrinsic Reaction Coordinate HNO + Vinoxy Pathway. *J. Phys. Chem. A* **2016**, *120*, 4973-4987.

(26) Scrape, P. G.; Adams, J. D.; Xu, R.; Li. S; Butler, L. J. Manuscript in preparation.

(27) FitzPatrick, B. L.; Alligood, B. W.; Butler, L. J.; Lee, S.-H.; Lin, J. J. Primary Photodissociation Pathways of Epichlorohydrin and Analysis of the C−C Bond Fission Channels From an $O(^3P)$+Allyl Radical Intermediate. *J. Chem. Phys.*, **2010**, *113*, 094306.

(28) Ruscic, R.; Berkowitz, J. Photoionization of Atomic Chlorine. *Phys. Rev. Lett.* **1983**, *50*, 675-678.

(29) Berkowitz, J. *Atomic and Molecular Photoabsorption: Absolute Total Cross Sections*; Academic: San Diego, California, 2002.

(30) Frohlich, H.; Glass-Maujean, M. Photoabsorption, Photodissociation, and Photoionization Cross Sections of HCl. *Phys. Rev. A* **1990**, *42*, 1396-1404.

(31) NIST Chemistry WebBook (http://webbook.nist.gov/chemistry/)

(32) Lee, S-H; Huang, W-J; Chen, W-K Dynamics of the Reaction of Atomic Oxygen with Ethene: Observation of All Carbon-Containing Products by Single-Photon Ionization. *Chem. Phys. Lett.* **2007**, *446*, 276-280.

(33) McKown, B. G.; Ceriotti, M.; Womack, C. C.; Kamarchik, E.; Butler, L. J.; Bowman, J. M. Effects of High Angular Momentum on the Unimolecular Dissociation of CD_2CD_2OH: Theory and Comparisons with Experiment. *J. Phys. Chem. A* **2013**, *117*, 10951-10963.

(34) Brynteson, M. D.; Womack, C. C.; Booth, R. S.; Lee, S.–H.; Lin, J. J.; Butler, L. J. Radical Intermediates in the Addition of OH to Propene: Photolytic Precursors and Angular Momentum Effects. *J. Phys. Chem. A* **2014**, *118*, 3211-3229.

(35) Cole, J. P; Gaint-Kurti, G. G. A Statistical, *Ab Initio*, Quantum Mechanical Study of the Photolysis and Final State Distributions of Singlet Ketene. *J. Chem. Phys.* **2003**, *119*, 6003-6016.

(36) Calculated at the G4//B3LYP/6-311++G(3df,2p)

(37) Werner, H.-J.; Bauer, C.; Rosmus, P.; Keller, H.-M.; Stumpf, M.; Schinke, R. The Unimolecular Dissociation of HCO: Oscillations of Pure CO Stretching Resonance Widths. *J. Chem. Phys.* **1995,** *102*, 3593-3611.

(38) Savee, J. D.; Welz, O.; Taatjes, C. A.; Osborn, D. L. New Mechanistic Insights to the O(^{3}P) + Propene Reaction from Multiplexed Photoionization Mass Spectrometry. *Phys. Chem. Chem. Phys.* **2012**, *14*, 10410-10423.

(39) Osborn, D. L.; Choi, H.; Mordaunt, D. H.; Bise, R. T.; Neumark, D. M.; Rohlfing, C. M. Fast Beam Photodissociation Spectroscopy and Dynamics of the Vinoxy Radical. *J. Chem. Phys.* **1997**, *106*, 3049-3066.

(40) Matsika, S.; Yarkony, D. R. Photodissociation of the Vinoxy Radical Through Conical, and Avoided, Intersections. *J. Chem. Phys.* **2002**, *117*, 7198-7206.

(41) Piechowska-Strumik, K.; Lauvergnat, D.; Bacchus-Montabonel, M.-C.; Desouter-Lecomte, M. Quantum Dynamics Around a Non Planar Conical Intersection in Vinoxy Radical Relaxation. *Chem. Phys. Lett.* **2006**,425, 16–21.

(42) Young, R. A.; Yarkony, D. R. A Novel Conical Intersection Topography and Its Consequences: The 1, 2 ^{2}A Conical Intersection Seam of the Vinoxy Radical. *J. Chem. Phys.* **2005**, *123*, 084315.

(43) Shen, L.; Liu, L.; Cao, J.; Fang, W.-H. Insights into Mechanistic Photodissociation of Chloroacetone from a Combination of Electronic Structure Calculation and Molecular Dynamics Simulation. *J. Chem. Phys.* **2011**, *135*, 194305.

CHAPTER 5

CONCLUSIONS

Bimolecular reactions of radical species are common in combustion and atmospheric chemistry; however, such processes are often complex and proceed through radical intermediates that are difficult to probe experimentally. In an effort to improve our understanding of these reactions, we generate the radical intermediate of interest with a range of internal energy via the photodissociation of a halogenated precursor.[1] This dissertation outlines studies on the unimolecular dissociation channels of the vinoxy radical, which is a common intermediate in combustion and other atmospheric processes.[2-8] In our experimental studies, we produced the vinoxy with internal energies that span two unimolecular dissociation barriers of vinoxy via photodissociation of chloroacetaldehyde at 157 nm and probed the recoiling fragments using velocity map imaging and scattering techniques. By invoking conservation of energy and angular momentum, we derive from the measured distribution of translational energy in the halogen cofragment the distribution of rotational and vibrational energy in the nascent vinoxy radicals. The motivation for these studies came from the prior results of Miller et al.[9] who observed a suppression of the H + ketene channel when vinoxy is formed in its ground state following photodissociation of chloroacetaldehyde at 193 nm. By performing the experiment with a higher photon energy in our studies, we produced vinoxy radical with larger internal energies than in the previous study thereby increasing the chances of surmounting the barrier to H + ketene on its ground state potential energy surface (PES).

In our experimental studies, we detected ketene and methyl products from the unimolecular dissociation of vinoxy radicals. While we observed that the production of ketene is favored over the production of methyl, we were unable to calculate the branching ratio between these products channels. These results show a marked change in the observed branching from the study by Miller et al. From the distribution of translational energy, we also concluded that photodissociation of chloroacetaldehyde at 157 nm produces vinoxy primarily in its excited electronic states, namely the Ã and B̃ states. Previous studies[9-12] have suggested excited-state vinoxy readily undergoes internal conversion to the ground state, so we use statistical theories on the ground state potential energy surface to the dissociation dynamics of vinoxy.

In our scattering experiments, we further characterized the primary photodissociation pathways of chloroacetaldehyde and observed secondary dissociation of vibrationally excited products formed from the primary channels. Upon excitation at 157 nm, chloroacetaldehyde underwent C−Cl bond fission, HCl photoelimination, and C−C bond fission. The most interesting channel is C-C bond fission which has not been directly observed before and sufficiently competes with C−Cl bond fission based on our measured branching ratio. Since the singlet excited states of chloroacetaldehyde are repulsive along the C−Cl bond in the Franck-Condon region, the presence of the C−C bond fission channel suggests possible intersystem crossing to the T_1 state of chloroacetaldehyde. This result warrants further study of the dynamics on the excited-state PESs of chloroacetaldehyde.

To help analyze the experimental data, we introduced a method to explicitly account for the rotational energy (imparted to the vinoxy radicals produced photolytically[13,14]) in the RRKM calculations, both at equilibrium geometry and at the relevant transition states for the product branching. Using this model, we characterized the change in branching fraction to the H +ketene product channel of vinoxy radicals as the vibrational energy in the radical increases near the threshold to producing H + ketene. We found that the predicted portion of the P(E_T) for C−Cl photofission in the precursor that produces vinoxy radicals that dissociate to H + ketene products best fits the experimental portion if we use a barrier height for the H + ketene channel that is 4.0 ± 0.5 kcal/mol higher than the isomerization barrier en route to CH_3 + CO products. This is a larger energy difference than that predicted by G4 calculations; it offers a benchmark for higher-level electronic structure determinations of these barriers. Our analysis assumes that statistical transition state theory adequately predicts the product branching. This methodology can be extended to statistical predictions for the unimolecular dissociation of radicals produced photolytically from other halogenated precursors in experiments where the rotational distribution of the radicals is not relaxed to a thermal distribution.

5.1 References

(1) Mueller, J. A.; Miller, J. L.; Butler, L. J.; Qi, F.; Sorkhabi, O.; Suits, A. G. *J. Phys. Chem*. **2000**, *104*, 11261-4

(2) Balucani, N.; Leonori, F.; Casavecchia, P.; Fu, B.; Bowman, J. M. *J. Phys. Chem. A.* **2015**, *119*, 12498-12511.

(3) Leonori, F.; Balucani, N; Nevrly, V.; Bergeat, A.; Falcinelli, S.; Vanuzzo, G.; Casavecchia, P. *J. Phys. Chem. C* **2015**, *119*, 14632-52.

(4) McKee, K. W.; Blitz, M. A.; Cleary, P. A.; Glowacki, D. R.; Pilling, M. J.; Seakins, P. W., Wang, L. *J. Phys. Chem. A* **2007**, *111*, 4043-55.

(5) Westbrook, C. K.; Dryer, F. L. *Symp. Int. Combust. Proc.* **1981**, *18*, 749-67.

(6) Brezinsky, K. *Prog. Energy Combust. Sci*. **1986**, *12*, 1-24.

(7) Bernhard, K. I.; Santiago, A.; He, H.; Asmar, F.; Weiner, B. R. *Chem. Phys. Lett.* **1991**, *178*, 150-6.

(8) Liu, F.; Beames, J. M.; Petit, A. S.; McCoy, A. B.; Lester, M. I. *Science* **2014**, *345*, 1596-98.

(9) Osborn, D. L.; Choi, H.; Mordaunt, D. H.; Bise, R. T.; Neumark, D. M.; Rohlfing, C. *J. Chem. Phys.* **1997**, *106*, 3049-66.

(10) Matsika, S. ; Yarkony, D. R. Photodissociation of the Vinoxy Radical Through Conical, and Avoided, Intersections. *J. Chem. Phys.* **2002**, *117*, 7198-7206.

(11) Piechowska-Strumik, K.; Lauvergnat, D.; Bacchus-Montabonel, M.-C.; Desouter-Lecomte, M. Quantum Dynamics Around a Non Planar Conical Intersection in Vinoxy Radical Relaxation. *Chem. Phys. Lett.* **2006**,425, 16–21.

(12) Young, R. A.; Yarkony, D. R. A Novel Conical Intersection Topography and Its Consequences: The 1, 2 ^{2}A Conical Intersection Seam of the Vinoxy Radical. *J. Chem. Phys*. **2005**, *123*, 084315.

(13) McKown, B. G.; Ceriotti, M.; Womack, C. C.; Kamarchik, E.; Butler, L. J.; Bowman, J. M. Effects of High Angular Momentum on the Unimolecular Dissociation of CD_2CD_2OH: Theory and Comparisons with Experiment. *J. Phys. Chem. A* **2013**, *117*, 10951-10963.

(14) Brynteson, M. D.; Womack, C. C.; Booth, R. S.; Lee, S.–H.; Lin, J. J.; Butler, L. J. Radical Intermediates in the Addition of OH to Propene: Photolytic Precursors and Angular Momentum Effects. *J. Phys. Chem. A* **2014**, *118*, 3211-3229.

APPENDIX A

SUPPLEMENTAL INFORMATION FOR CHAPTER 2

A.1 Geometries of the Conformers of Chloroacetaldehyde

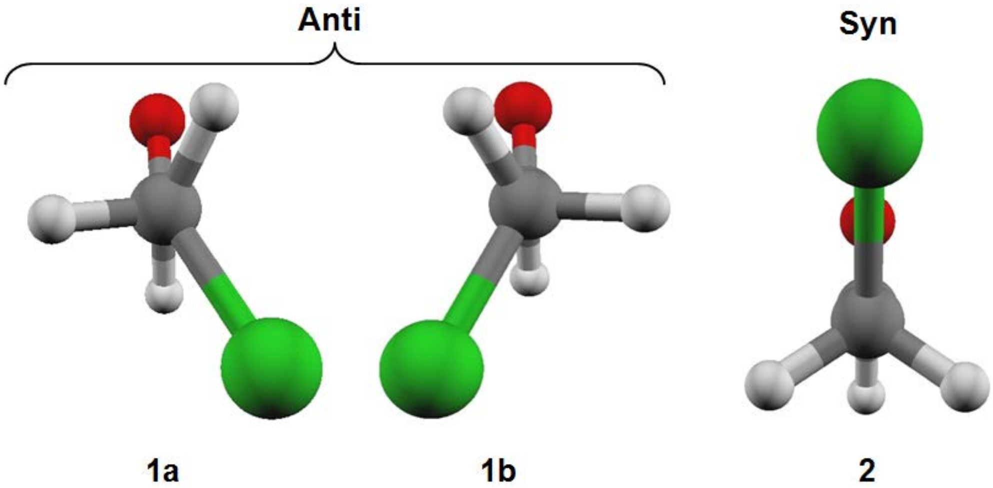

Figure A.1: Geometries of the conformers of chloroacetaldehyde. The lower labels are used when it is necessary to denote a specific conformer.

Table A.1: Cartesian Coordinates (Å) for Conformer Geometries Calculated at B3LYP/6-311++G(3df,2p) level

1a;

C	-1.196270	-0.306673	0.220802
O	-2.299665	-0.071618	-0.185696
H	-0.942720	-1.262367	0.717052
C	-0.062965	0.692929	0.110119
H	-0.021112	1.291401	1.020339
H	-0.213692	1.342945	-0.746343
Cl	1.517936	-0.139332	-0.057184

1b;

C	1.196271	-0.306683	0.220786
O	2.299673	-0.071609	-0.185687
H	0.942723	-1.262397	0.717001
C	0.062970	0.692918	0.110119
H	0.021121	1.291378	1.020347
H	0.213694	1.342948	-0.746334
Cl	-1.517942	-0.139327	-0.057182

2;

C	1.394561	0.386988	0.000000
O	1.681330	-0.773687	0.000000
H	2.175794	1.177551	0.000000
C	0.000000	0.968627	0.000000
H	-0.111105	1.604722	0.879851
H	-0.111105	1.604722	-0.879851
Cl	-1.303913	-0.237744	0.000000

A.2 EOM-CCSD Calculations of Excited States of Chloroacetaldehyde Along the C−Cl Coordinate

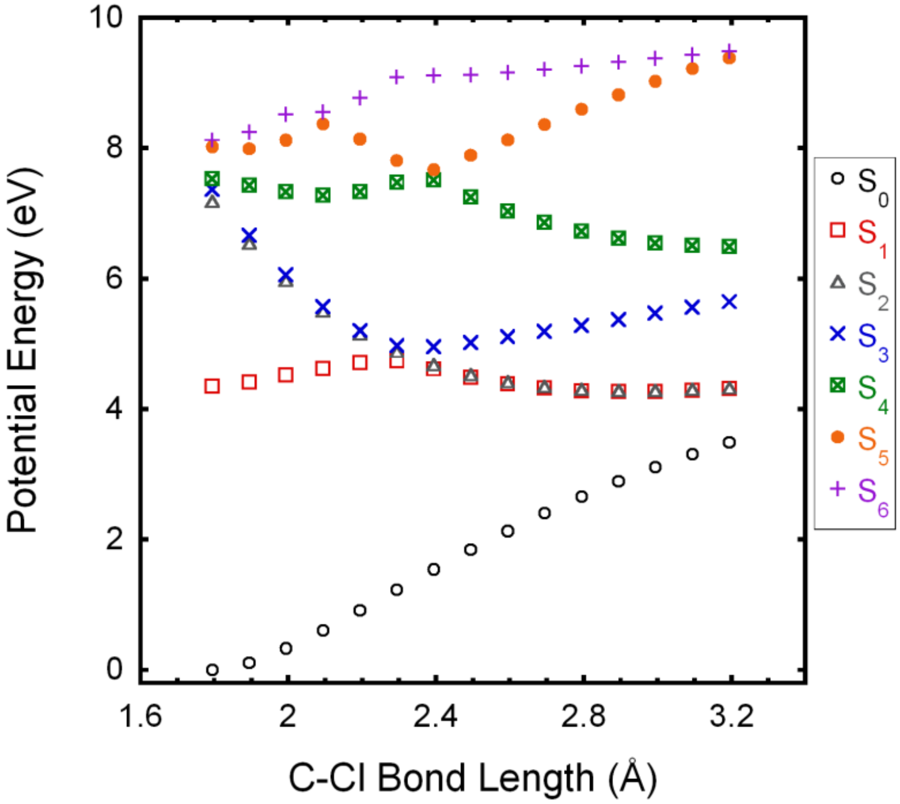

Figure A.2: Singlet excited states of chloroacetaldehyde along the C−Cl bond coordinate calculated at the EOM-CCSD/6-311++G(3df,2p) level of theory. Geometries are optimized geometries on the ground state (S_0) at each C−Cl internuclear distance.

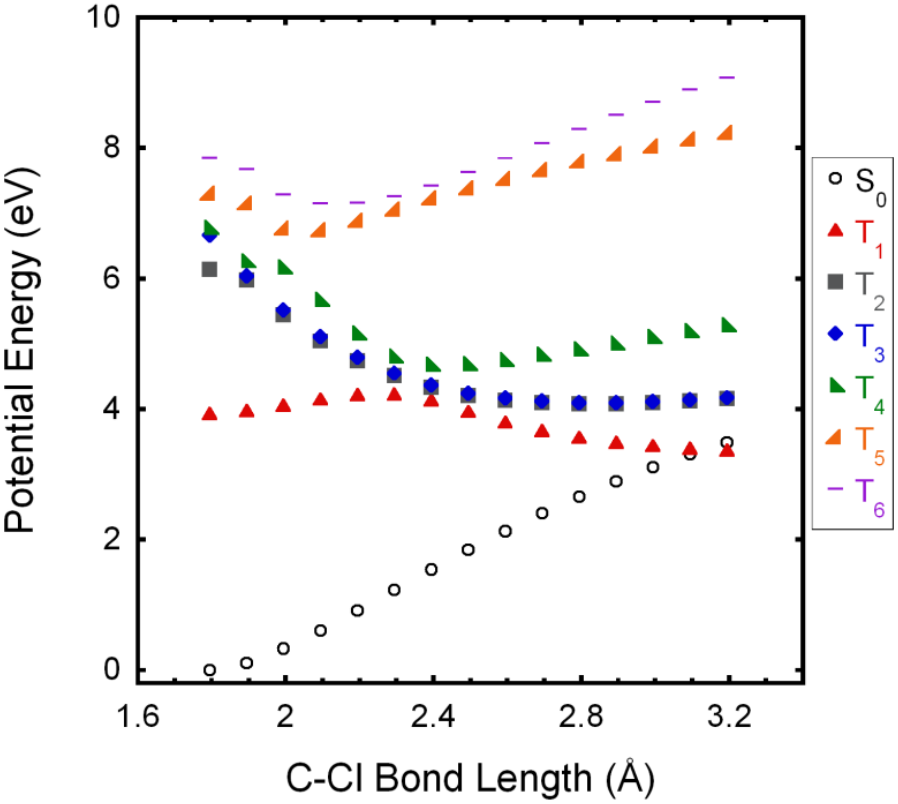

Figure A.3: Triplet excited states of chloroacetaldehyde along the C−Cl bond coordinate calculated at the EOM-CCSD/6-311++G(3df,2p) level of theory. Geometries are the optimized geometries on the ground state (S_0) at each C−Cl internuclear distance.

We also performed the EOM-CCSD calculations with the smaller aug-cc-pVDZ basis set. While the points were slightly lower in energy, the overall shapes of the surfaces were still the same. Note that the EOM-CCSD method does not accurately treat the geometries at large C−Cl bond lengths, so we have used these preliminary calculations only to inform us of the shape of the potential energy surfaces in the Franck-Condon region and at intermediate C−Cl bond distances.

A.3 Rough Division of the C−Cl Bond Fission P(E_T) to Assess the Cl($^2P_{1/2}$)/Cl($^2P_{3/2}$) Branching Ratio in the Fast Component and the Portion of the Slow Component that Can Produce $\tilde{B}$ State Vinoxy

Here we present a rough division of the C−Cl bond fission P(E_T) into a slow portion for which the $\tilde{B}$ state of vinoxy is energetically allowed (energies less than E_T = 20 kcal/mol), a fast portion peaking near 40 kcal/mol, and an intermediate portion. This division is somewhat arbitrary, so we show two options and the corresponding Cl($^2P_{1/2}$)/Cl($^2P_{3/2}$) branching ratios for each. The first option attempts to capture the full features of the fast portion without making these portions similar for the Cl($^2P_{1/2}$) and Cl($^2P_{3/2}$) P(E_T)s. The second option constrains the fast portion to be similar in shape for both the Cl($^2P_{1/2}$) and Cl($^2P_{3/2}$) P(E_T)s.

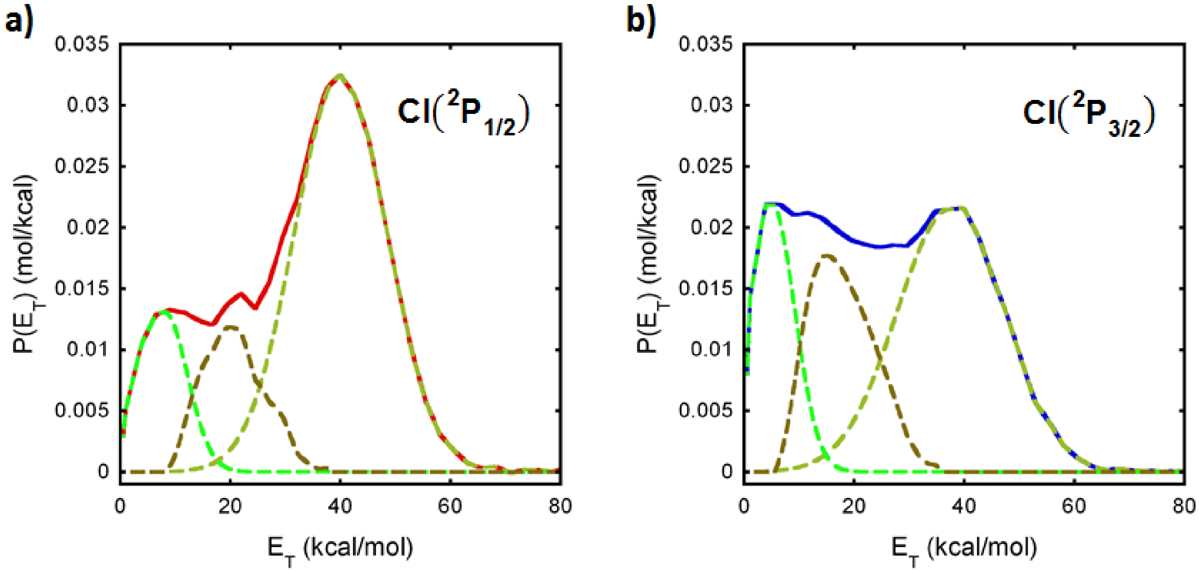

Figure A.4: First option for dividing the C−Cl bond fission P(E_T) into a slow portion that can produce B̃ state vinoxy, a fast portion that peaks near 40 kcal/mol, and an intermediate portion. Panel (a) shows the components of the C−Cl bond fission P(E_T) for Cl($^2P_{1/2}$) in dashed line in varying shades of green and the total P(E_T) for this spin-orbit state shown in solid red line. Panel (b) shows the components of the C−Cl bond fission P(E_T) for Cl($^2P_{3/2}$) in dashed line with the same coloring scheme and the total P(E_T) for this spin-orbit state in solid blue line.

Table A.2: Ratios of the Signal Intensity between the P(E_T)s for each Spin-Orbit State and Cl($^2P_{1/2}$)/Cl($^2P_{3/2}$) Branching Ratios for Each Component of the C−Cl Bond Fission P(E_T) following the First Option for the Division

Portion of P(E_T)	**S[Cl($^2P_{1/2}$)]/S[Cl($^2P_{3/2}$)]**	**Cl($^2P_{1/2}$)/Cl($^2P_{3/2}$) Branching Ratio**
Fast	1.30	1.10
Slow	0.73	0.62
Intermediate	0.62	0.53

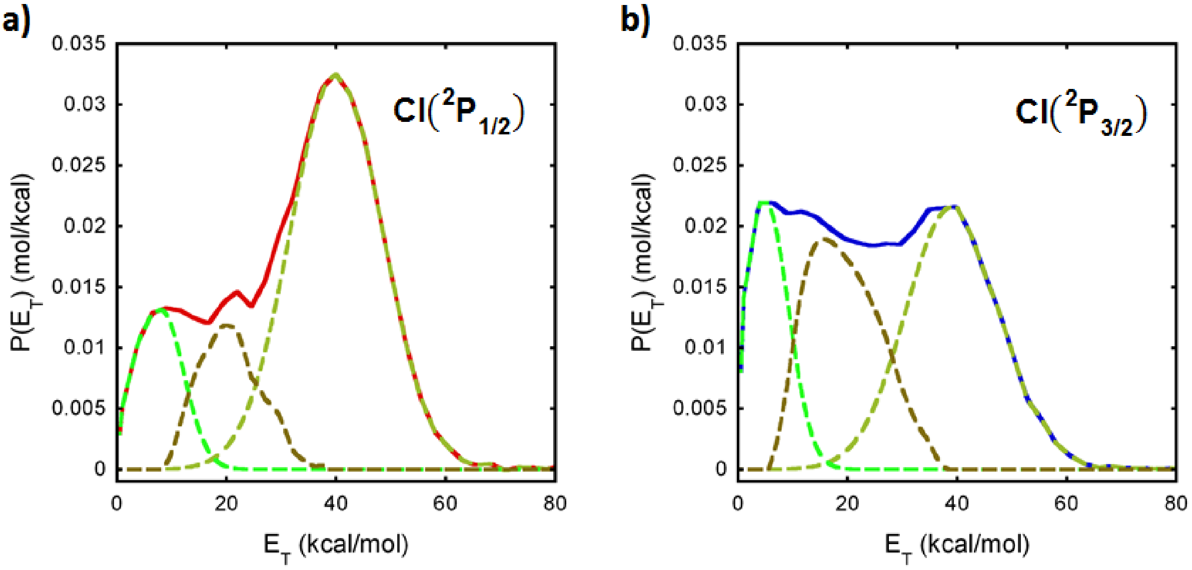

Figure A.5: Second option for dividing the C−Cl bond fission P(E_T) into a slow portion that can produce B̃ state vinoxy, a fast portion that peaks near 40 kcal/mol, and an intermediate portion. Panel (a) shows the components of the C−Cl bond fission P(E_T) for Cl(^{2}P$_{1/2}$) in dashed line in varying shades of green and the total P(E_T) for this spin-orbit state shown in solid red line. Panel (b) shows the components of the C−Cl bond fission P(E_T) for Cl(^{2}P$_{3/2}$) in dashed line with the same coloring scheme and the total P(E_T) for this spin-orbit state in solid blue line.

Table A.3: Ratios of the Signal Intensity between the P(E_T)s for each Spin-Orbit State and Cl(^{2}P$_{1/2}$)/Cl(^{2}P$_{3/2}$) Branching Ratios for Each Component of the C−Cl Bond Fission P(E_T) following the Second Option for the Division

Portion of P(E_T)	**S[Cl(^{2}P$_{1/2}$)]/S[Cl(^{2}P$_{3/2}$)]**	**Cl(^{2}P$_{1/2}$)/Cl(^{2}P$_{3/2}$) Branching Ratio**
Fast	1.49	1.27
Slow	0.72	0.62
Intermediate	0.50	0.42

A.4 Speed Dependence of the Anisotropy Parameter β₂(v) for Cl($^2P_{1/2}$) and Cl($^2P_{3/2}$)

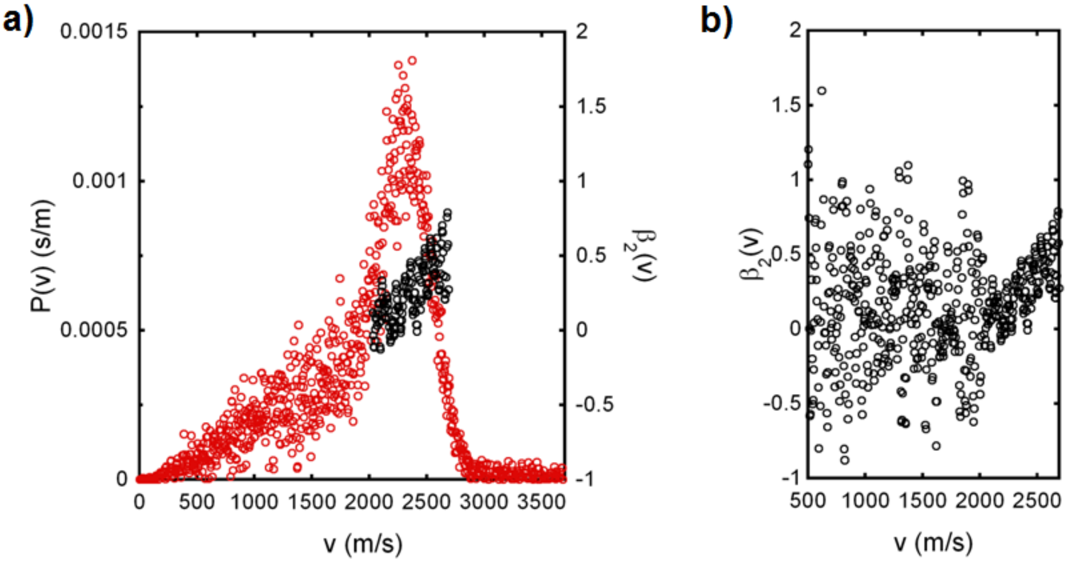

Figure A.6: Speed dependence of the anisotropy parameter $\beta_2(v)$ for Cl($^2P_{1/2}$). Panel (a) shows the anisotropy values (black circles) overlaid on the high kinetic energy portion of the Cl($^2P_{1/2}$) speed distribution (red circles). Panel (b) shows how the anisotropy varies from near isotropic in the slow portion of the speed distribution to weakly parallel in the high kinetic energy portion.

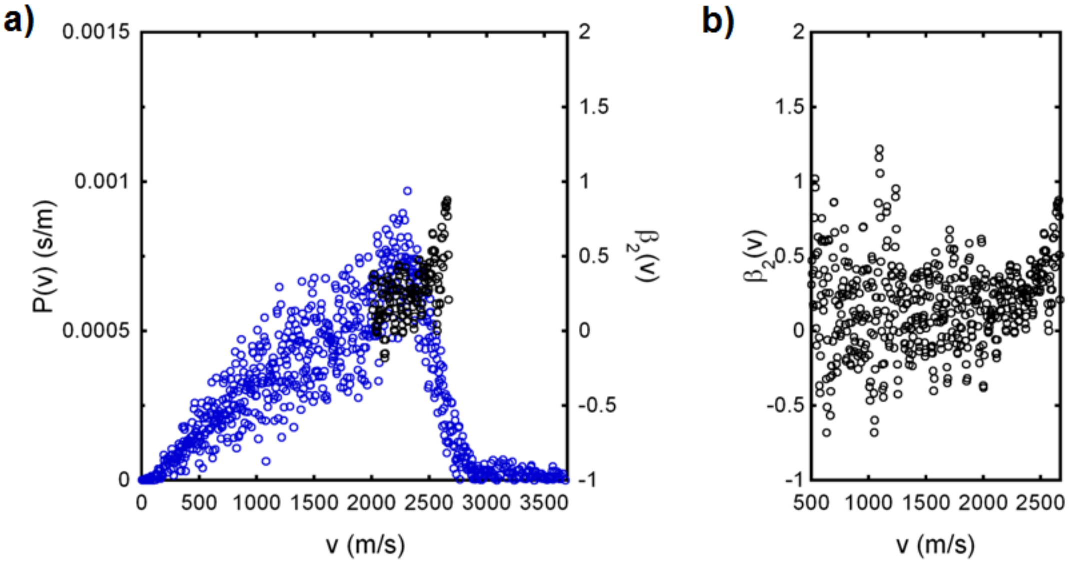

Figure A.7: Speed dependence of the anisotropy parameter $\beta_2(v)$ for Cl($^2P_{3/2}$). Panel (a) shows the anisotropy values (black circles) overlaid on the high kinetic energy portion of the Cl($^2P_{3/2}$) speed distribution (red circles). Panel (b) shows how the anisotropy varies from near isotropic in the slow portion of the speed distribution to weakly parallel in the high kinetic energy portion.

A.5 Gaussian Convolution of the Predicted P(v_{net}) for the Methyl Signal from the Dissociative Ionization of Vinoxy to CH_3^+ + CO

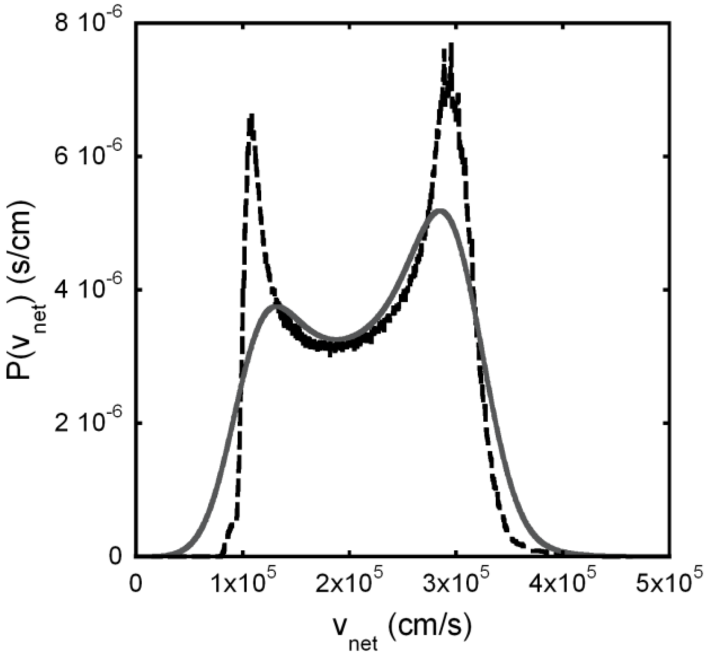

Figure A.8: Gaussian convolution of the predicted P(v_{net}) for CH_3^+ from dissociative ionization of vinoxy. The dashed black line is the predicted P(v_{net}) of CH_3^+ yielded by dissociative photoionization of stable vinoxy radical, calculated from the $P(E_T)$ in gray from Figure 10 using the model described in Brynteson and Butler. The solid gray line is the predicted P(v_{net}) convolved with a Gaussian function with a sigma of 25000 cm/s. We used this convolved P(v_{net}) in fitting the methyl signal shown in Figure 2.7.

APPENDIX B

SUPPLEMENTAL INFORMATION FOR CHAPTER 3

B.1 Correction to the Effective Barrier Height Caused by the Shift of the Minimum or Saddle Point to a Nearby Geometry Along the IRC

The effective barrier height we use for our branching calculations represents the energy difference between the minimum and the saddle point on the rotationally corrected IRC, which we get by adding rotational energy to our calculated IRC (which has $J_{\text{rot}} = 0$). These rotational corrections can actually cause the minimum and/or saddle point to shift to a different geometry along the IRC, usually nearby. In this case, we need to use the $E_{\text{rot}}/E_{\text{T}}$ ratios at the new minimum geometry and/or new saddle point geometry. However, this is not the only correction we have to make. The new minimum and new saddle point geometries also have different potential energies and so we have to redefine the energetics (Figure C.1).

We calculate these terms using the B3LYP energies from the IRC calculation. So, the full expression for calculating the effective barrier heights is given by

$$E_{\text{o, effective}} = E_0 + \left[\left(\frac{E_{\text{rot}}}{E_{\text{T}}}\right)_{\text{at TS}} - \left(\frac{E_{\text{rot}}}{E_{\text{T}}}\right)_{\text{at min}}\right] E_{\text{T}} - |\Delta E_{\text{at TS}}| - |\Delta E_{\text{at min}}|$$

The effective barrier is used in the RRKM calculations.

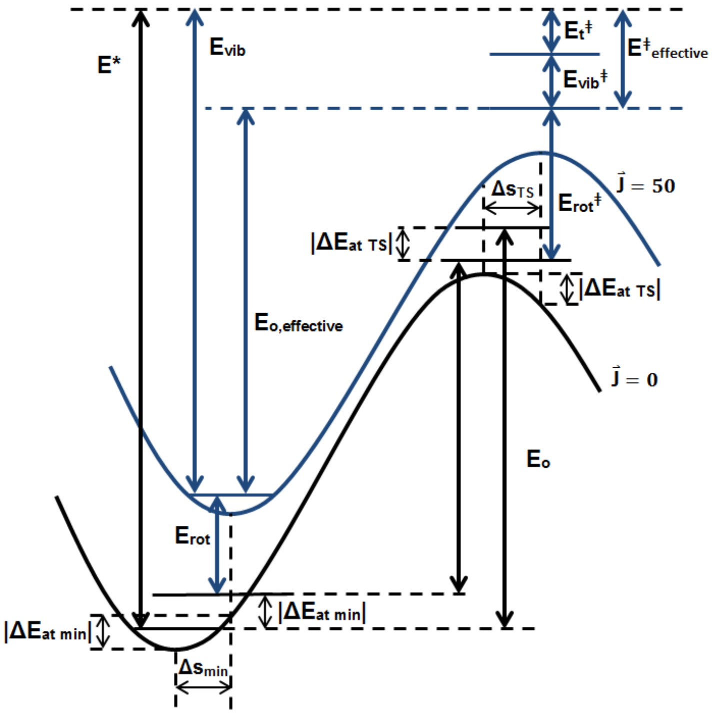

Figure B.1: Diagram of the energetics involved in a unimolecular reaction in which the minimum and saddle point geometries of the rotationally corrected IRC differ from that of the IRC with $\vec{J}_{\text{rot}} = 0$ by Δs_{min} and Δs_{TS}. E^* is the total internal energy in the radical which consists of vibrational energy, E_{vib}, and rotational energy, E_{rot}. $E^‡$ is the total internal energy at the critical configuration which consists of vibrational energy, $E_{\text{vib}}^‡$, rotational energy, $E_{\text{rot}}^‡$, and the translational energy along the reaction coordinate, $E_{\text{t}}^‡$. E_{o} is the energy difference between the zero-point energy of the radical and that of the critical configuration, thus representing the barrier height. Note how the potential energies of the new minimum and saddle point geometries differ from that of the IRC with $\vec{J}_{\text{rot}} = 0$ by $|\Delta E_{\text{at min}}|$ and $|\Delta E_{\text{at TS}}|$, respectively. The effective barrier height, $E_{\text{o, effective}}$, is now the energy difference between the energy of the new minimum geometry ($E_{\text{rot}} + |\Delta E_{\text{at min}}|$) and the energy of the new saddle point ($E_{\text{o}} + E_{\text{rot}}^‡ - |\Delta E_{\text{at TS}}|$).

B.2 Description of the Permutation Vectors Used in the Rotational Model

The rotational model developed by our group transforms the geometry of the radical moiety into any stationary point geometry while preserving the magnitude and direction of the angular momentum vector. In order to accomplish the desired transformation, the model calls for a “permutation vector,” which maps the atoms in the moiety configuration to their corresponding position in the stationary point configuration. The permutation vector basically tells the program how the atoms in the moiety are arranged in the stationary point. In most cases, determining how the atoms in the stationary point are related to the atoms in the moiety is trivial. This is especially true for atoms that make up the backbone structure of a molecule, like the C atoms and O atom in the chloroacetaldehyde moiety which have similar positions in all of the stationary points. Assigning the H atom in the aldehyde group is also trivial as it is easy to tell where it is in the stationary points. However, assigning the positions of terminal H atoms is often tricky as there are a few possibilities and they can have a big effect on the rotational energy in the stationary point (Figure C.3).

In choosing the permutation vector, we assumed that the correct permutation would minimize the displacement of the terminal H atoms in the moiety to get to the vinoxy radical. From there, the permutation vector leading to the transition states are dictated by the assignment of the H atoms in the vinoxy radical. The figures below show all of the permutations for the terminal H atoms that we used for each of the conformers of chloroacetaldehyde.

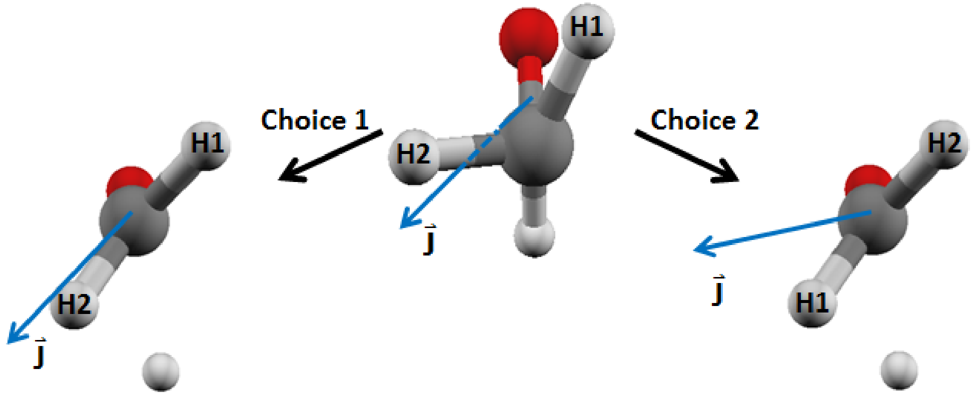

Figure B.2: Depiction of the effects of the permutation vector on the rotational energy in the stationary point. The radical moiety of the anti conformer of chloroacetaldehyde is shown in the center looking along the C-C bond with the O atom is attached to the back carbon. There are two distinct possible choices for the permutation vector leading to the kTS1 transition state in which the H atoms in the moiety (attached to the front carbon and denoted "H1" and "H2") are going to different position in the kTS1 structure. Note how changing where the H atoms go in kTS1 changes the relative position of the angular momentum vector, $\vec{J}$, compared to geometry of the molecule. We say "relative to the geometry of the molecule" because $\vec{J}$ should not change its direction nor magnitude and so only the geometry of molecule with respect to $\vec{J}$ should change. This will result in different E_{rot}/E_T ratios and thus different rotational energies.

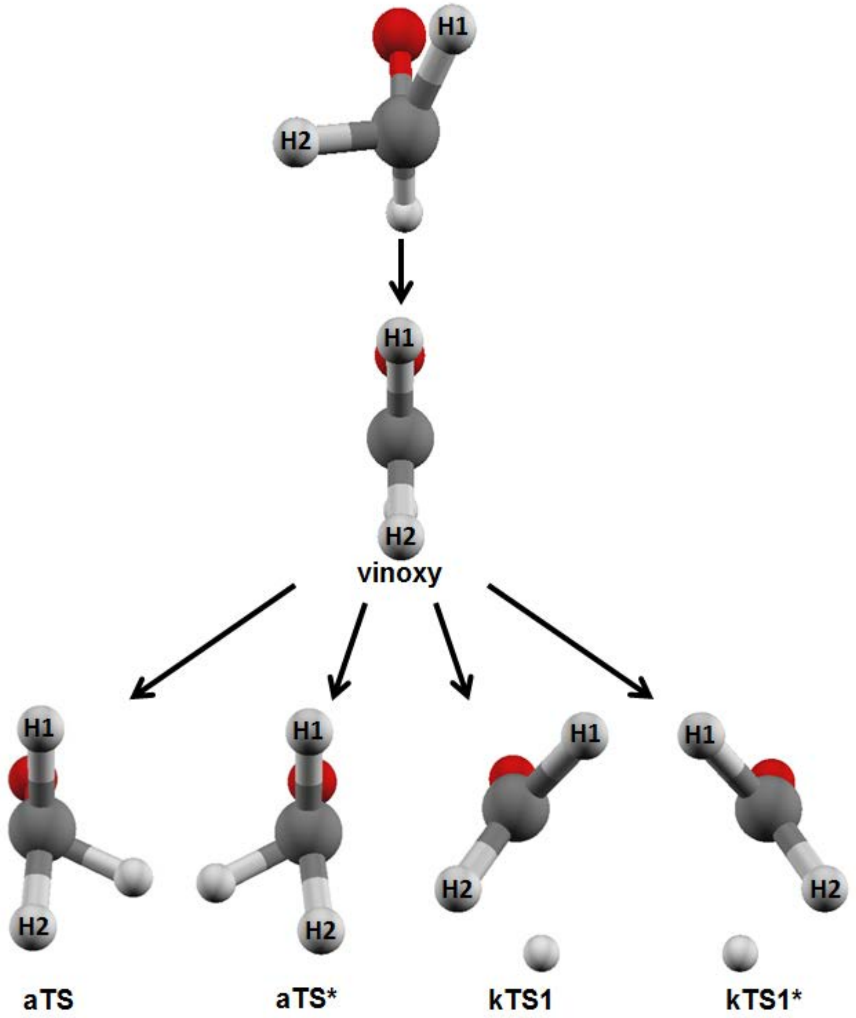

Figure B.3: Permutations of the terminal H atoms used to get from the moiety of the **1a** conformer of chloroacetaldehyde to the vinoxy radial and then to the given transition states. All of the geometries are shown looking down the C-C bond with the O atom on the back carbon. "H1" and "H2" were used to denote where the terminal H atoms in the moiety are going in the given stationary points. The "*" in the name of the transition states denotes that it is the enantiomer of the given transition state as can be seen in the figure.

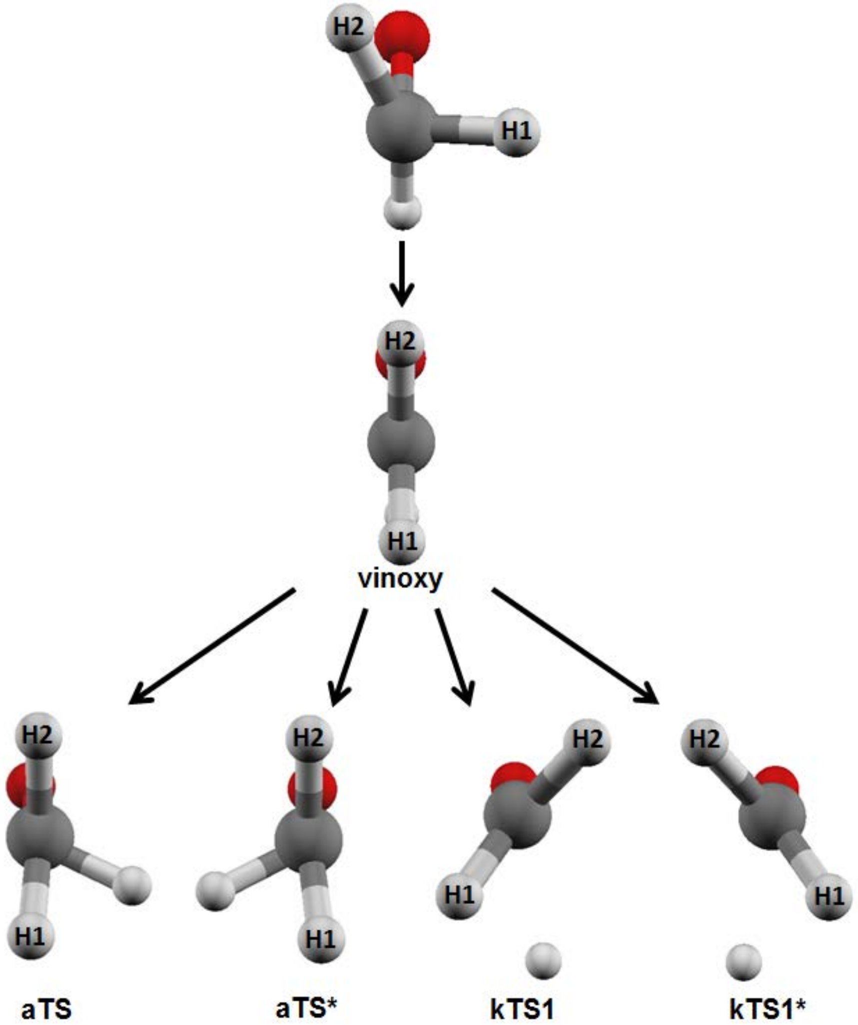

Figure B.4: Permutations of the terminal H atoms used to get from the moiety of the **1b** conformer of chloroacetaldehyde to the vinoxy radical and then to the given transition states. All of the geometries are shown looking down the C-C bond with the O atom on the back carbon. “H1” and “H2” were used to denote where the terminal H atoms in the moiety are going in the given stationary points. The “*” in the name of the transition states denotes that it is the enantiomer of the given transition state as can be seen in the figure.

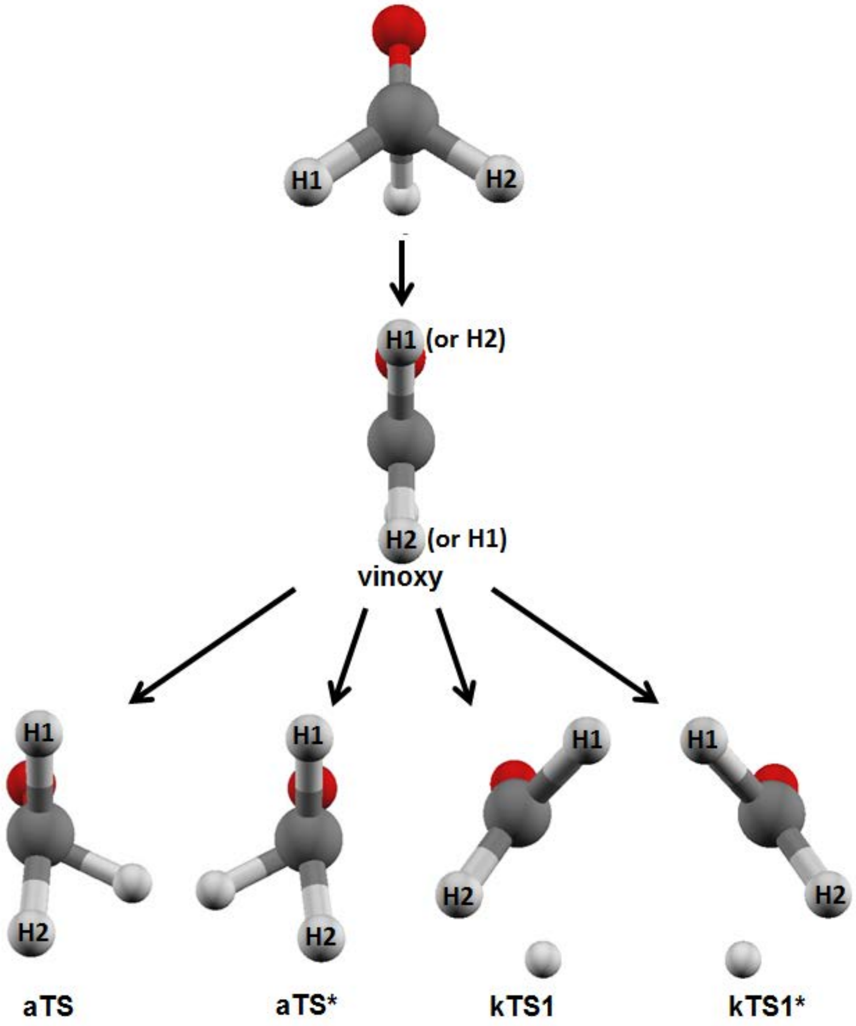

Figure B.5: Permutations of the terminal H atoms used to get from the moiety of the **2** conformer of chloroacetaldehyde to the vinoxy radical and then to the given transition states. All of the geometries are shown looking down the C-C bond with the O atom on the back carbon. "H1" and "H2" were used to denote where the terminal H atoms in the moiety are going in the given stationary points. The "*" in the name of the transition states denotes that it is the enantiomer of the given transition state as can be seen in the figure. Note how due to the symmetry of this particular conformer the assignment of the terminal H atoms in the vinoxy radical can be done either way. Both assignments give the same rotational energies (i.e. E_{rot}/E_T), but the angular momentum vector has a different direction with respect to the geometry of the vinoxy radical.

B.3 Smoothed and Interpolated P(E_T) for Cl($^2P_{3/2}$) and Cl($^2P_{1/2}$) Used in the Branching Calculations

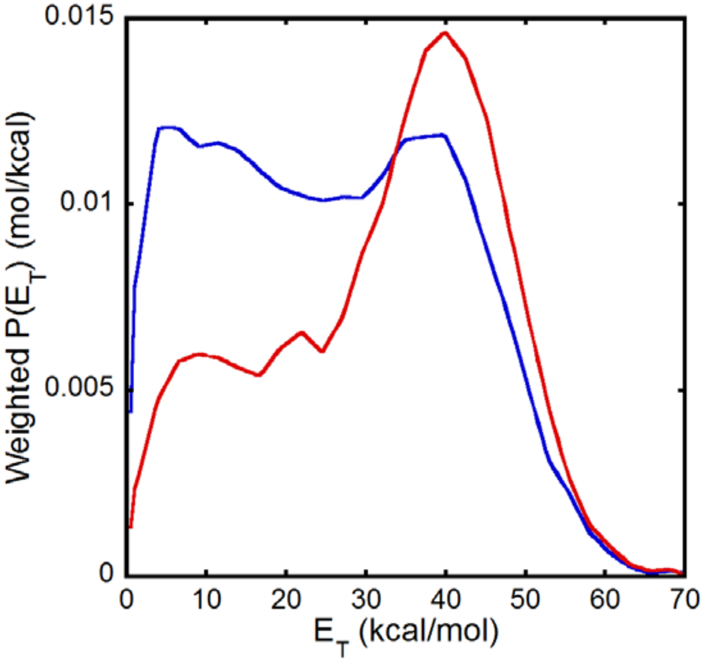

Figure B.6: Weighted relative translational energy distributions for photodissociation events producing vinoxy + Cl($^2P_{3/2}$) (blue) and vinoxy + Cl($^2P_{1/2}$) (red) that have been smoothed and interpolated from their respective experimentally determined P(E_T)s. These P(E_T)s were used in the branching calculations further scaled by the relative population of the conformer of interest in the molecular beam.

B.4 Estimate of the P(E_T) for a Minor HCl Photoelimination Channel Derived from the Difference between the Predicted and Experimental P(v_{net}) for Ketene

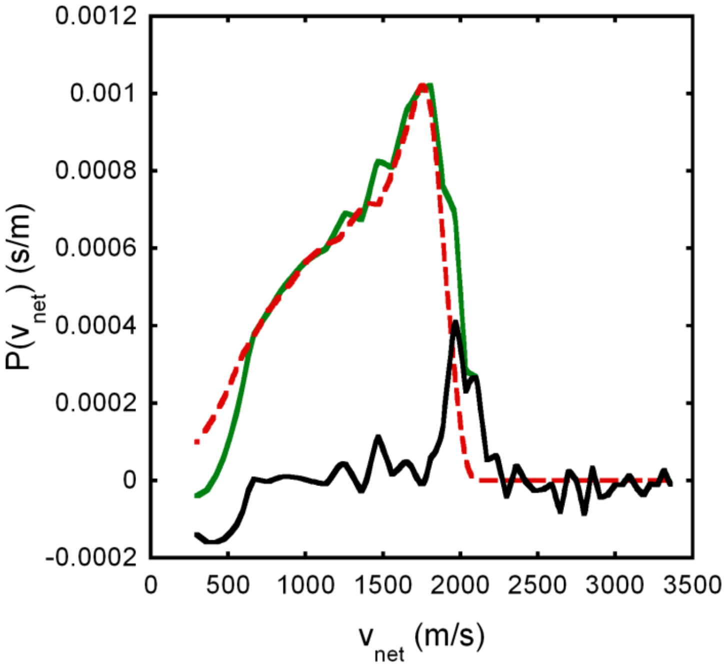

Figure B.7: Experimental (solid green) and predicted (dashed red) speed distributions for ketene. The experimental speed distribution shown here came from the data in Figure 5, which was smoothed and interpolated. The predicted speed distribution was derived by converting the predicted portion of the C−Cl bond fission P(E_T) that produces vinoxy radicals that dissociate to H + ketene from the branching calculations into a speed distribution with the appropriate Jacobian factors and assuming additional recoil velocity imparted to the ketene upon secondary dissociation is negligible. The black curve is the predicted speed distribution for the ketene that is unaccounted for, calculated from the difference between the green and red curves. It may be produced from primary HCl elimination of chloroacetaldehyde.

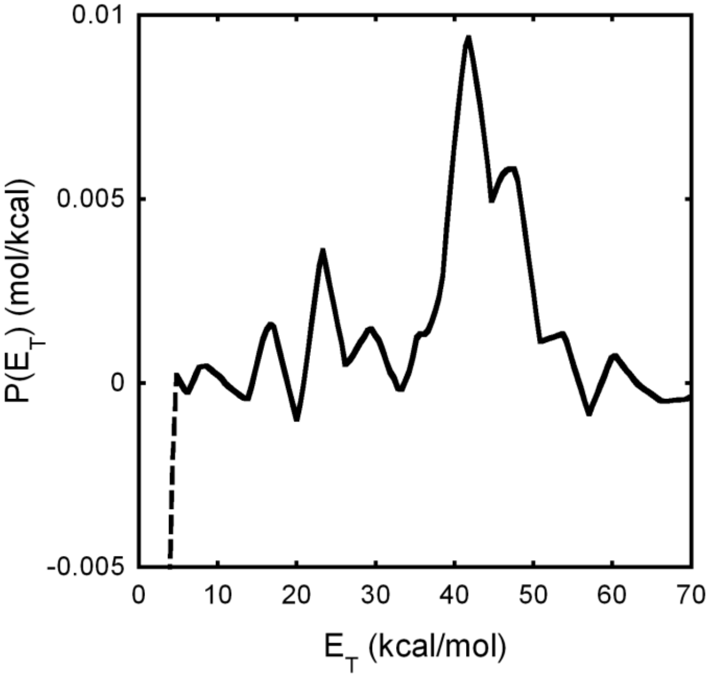

Figure B.8: Predicted relative translational energy distribution, P(E_T), for a possible primary HCl photoelimination channel from chloroacetaldehyde producing stable ketene cofragments. The P(E_T) shown is derived from the dashed black curve in Figure B.7 by applying conservation of momentum, with m_1 = 42 (ketene) and $m_2 = m_{HCl}$, and Jacobian corrections. The dashed black portion of the P(E_T) represents where the values drop below zero due to possible decreased sensitivity close to the center of the phosphor screen.

APPENDIX C

SUPPLEMENTAL INFORMATION FOR CHAPTER 4

C.1 Molecular Beam Speed Distribution

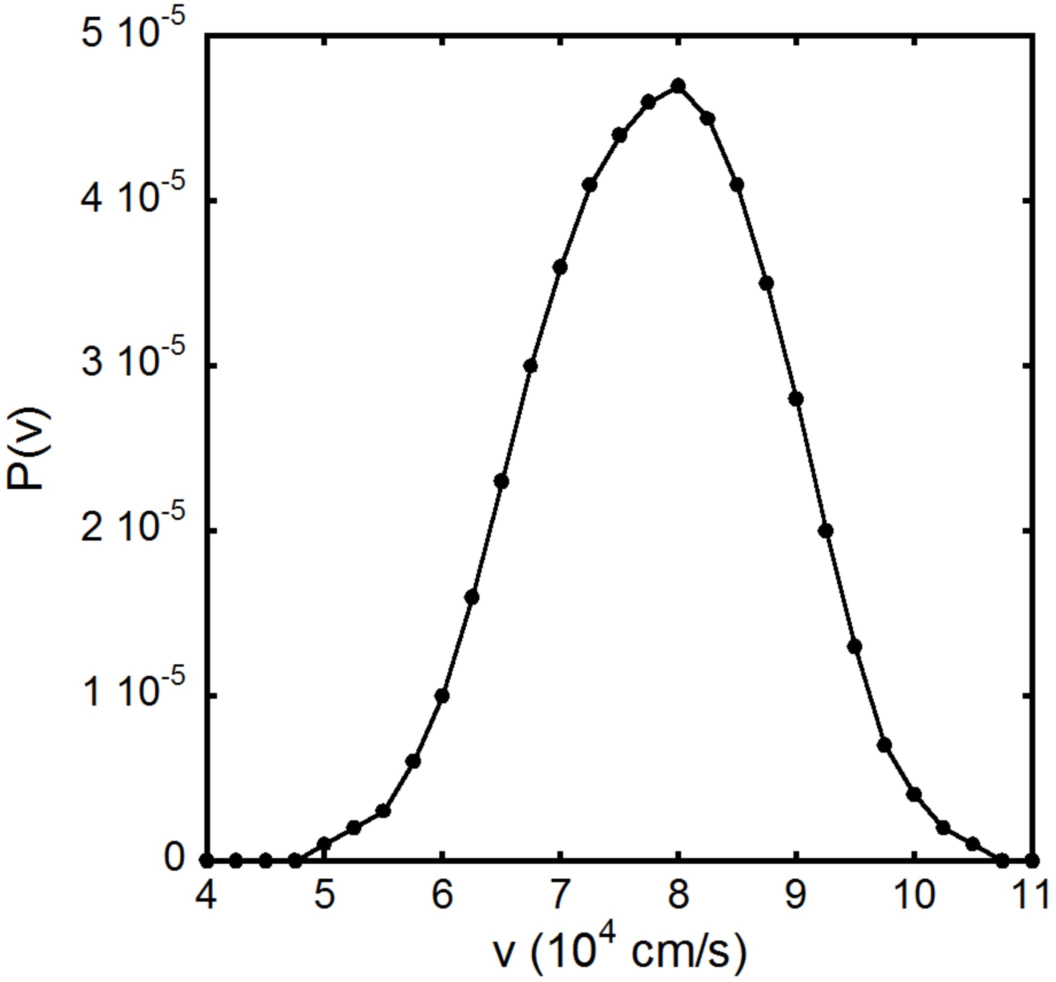

Figure C.1: Molecular beam speed distribution used to fit the time-of-flight data. This distribution was derived from the measured number density distribution obtained in a hole burning experiment.

C.2 Alternative Fits to the *m/z* = 35 and *m/z* = 36 TOF Spectra Using the C−Cl Bond Fission P(E_T) Derived in the Velocity Map Imaging Study

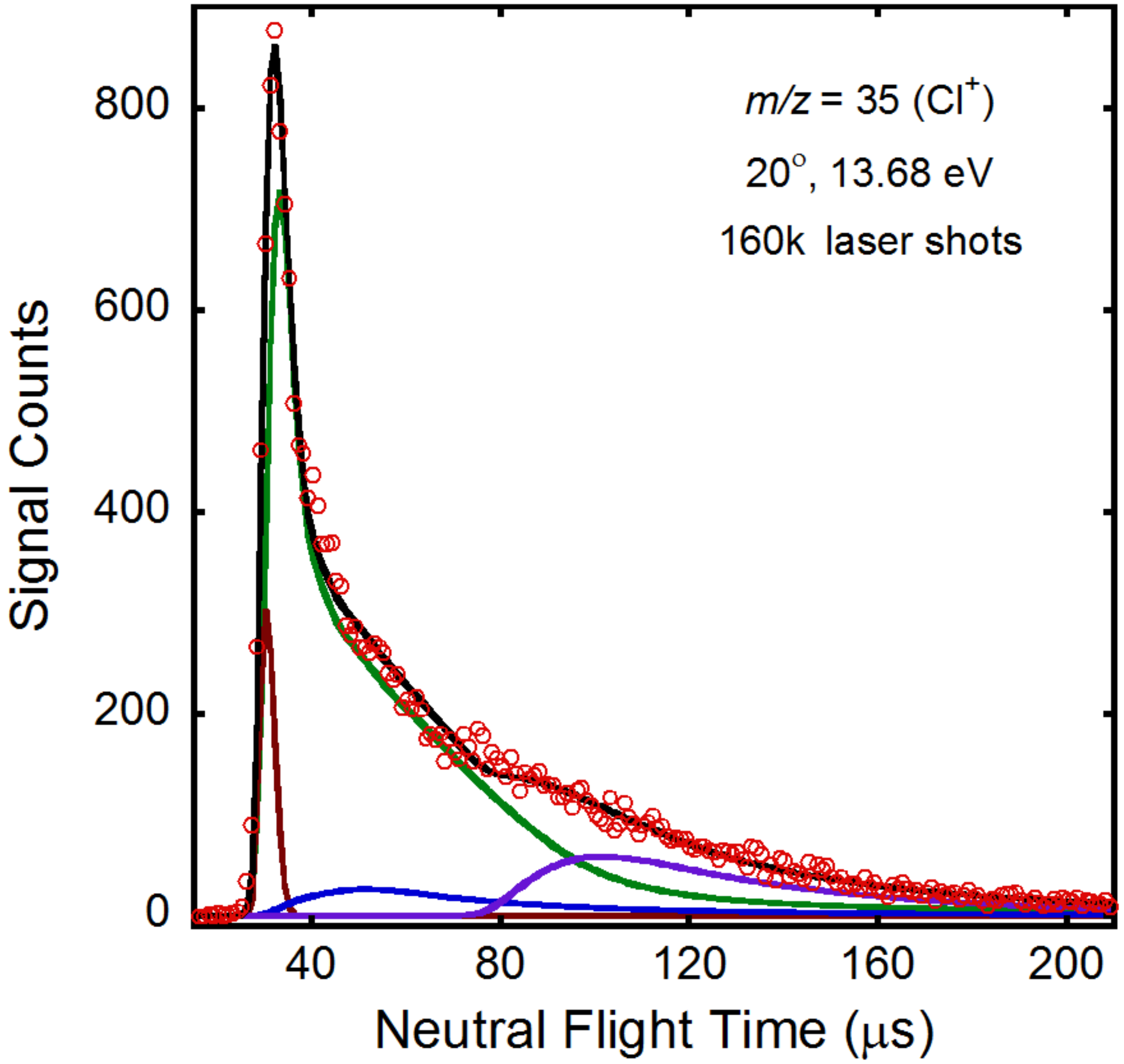

Figure C.2: TOF spectrum taken at *m/z* = 35 (Cl^+) with a source angle of 20° and an ionization energy of 13.68 eV. Data are shown in red circles. Primary C−Cl bond fission is fit by the solid green line using the C−Cl bond fission P(E_T) derived in the velocity map imaging study (see Figure 2.4). The contribution from bleed in of *m/z* = 36 (Cl^+) is shown in solid blue line and is fit using the primary HCl photoelimination P(E_T) shown in Figure 4.2. The fit shown as the solid purple line represents the contribution attributed to photodissociation of clusters in the molecular beam. The fast signal is fit as Cl loss from the dimer hydrate of chloroacetaldehyde. This fit, shown in solid maroon line, is derived the P(E_T) shown in Figure D.3.

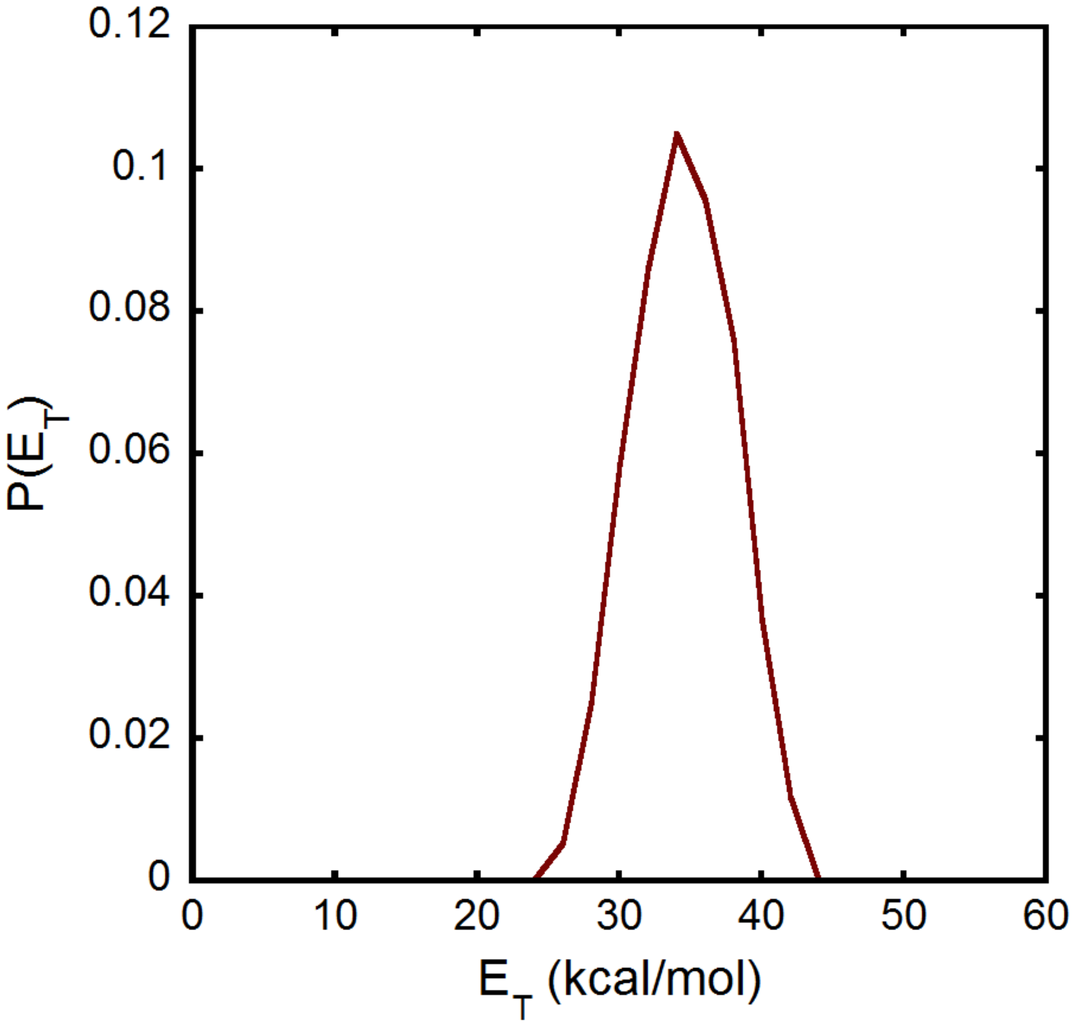

Figure C.3: Photofragment recoil kinetic energy distribution for C−Cl bond fission assuming the fastest signal results from photodissociating the dimer hydrate of chloroacetaldehyde at 157 nm. The P(E_T), peaking at 34 kcal/mol, is derived by forward convolution fitting of the fastest signal in the TOF spectrum taken at m/z = 35 (Cl^+) shown in Figure C.2.

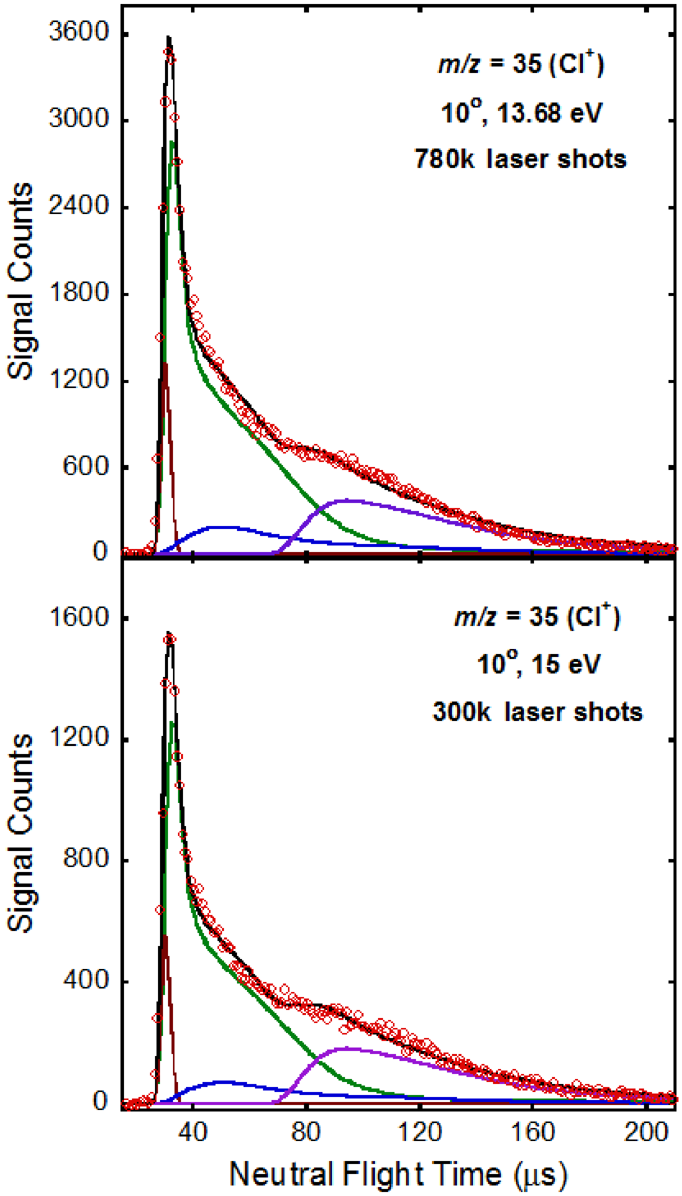

Figure C.4: TOF spectrum taken at *m/z* = 35 (Cl^+) with a source angle of 10° and two different ionization energies. The upper frame shows the data taken at an ionization energy of 13.68 eV and the lower frame shows the data taken at an ionization energy of 15.0 eV. Data are shown in red circles. Primary C−Cl bond fission is fit by the solid green line using the C−Cl bond fission P(E_T) derived in the velocity map imaging study (see Figure 2.4). The contribution from bleed in of *m/z* = 36 ($H^{35}Cl^+$) is shown in solid blue line and is fit using the primary HCl photoelimination P(E_T) shown in Figure 4.2. The fit shown as the solid maroon line corresponds to Cl loss from the dimer hydrate of chloroacetaldehyde and is derived the P(E_T) shown in Figure C.3. The fit shown as the solid purple line represents the contribution attributed to photodissociation of clusters in the molecular beam.

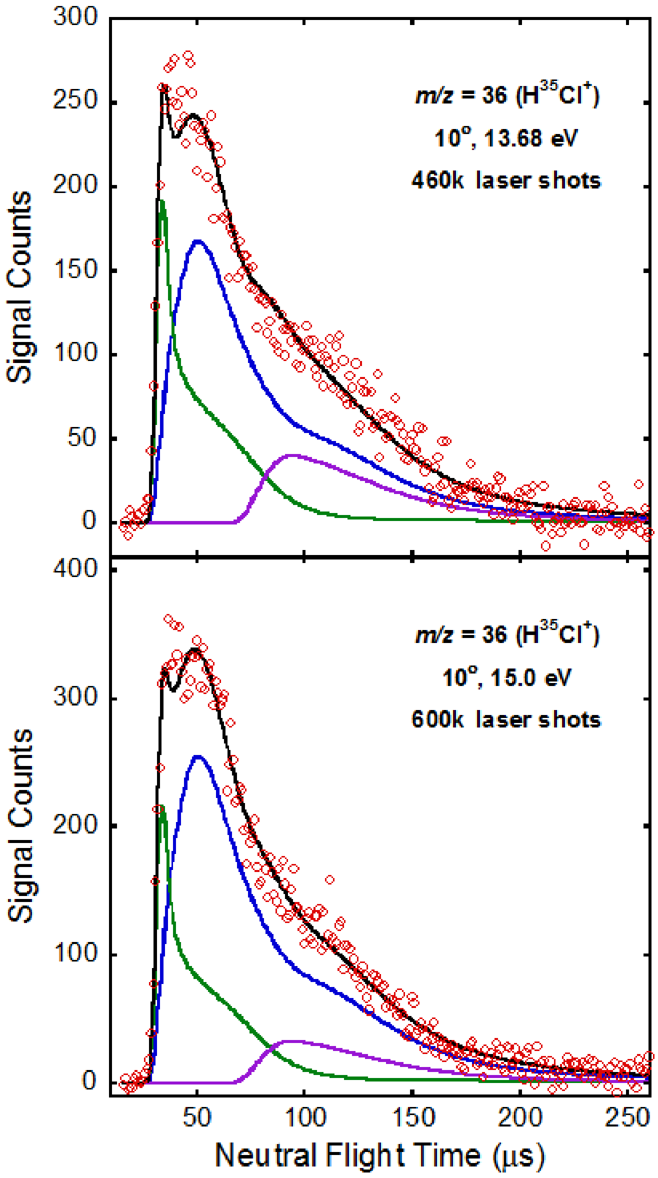

Figure C.5: TOF spectrum taken at m/z = 36 ($H^{35}Cl^+$) with a source angle of 10° and two different ionization energies. The upper frame shows the data taken at an ionization energy of 13.68 eV and the lower frame shows the data taken at an ionization energy of 15.0 eV. Data are shown in red circles. Primary HCl photoelimination is fit by the solid blue line using the P(E_T) shown in Figure 4.2. The contribution from bleed in of m/z = 37 (Cl^+) is shown in solid green line and is fit using the primary C−Cl bond fission P(E_T) derived in the velocity map imaging study (see Figure 2.4). The contribution attributed to photodissociation of clusters in the molecular beam is shown in solid purple line. While we get a better fit to the fast signal in both of these TOF spectra, the contribution of bleed in from m/z = 37 (Cl^+) is much larger than expected based on the signal observed in the m/z = 37 (Cl^+) TOF data.

C.3 Potential Energy Surface of the HCCHO Radical

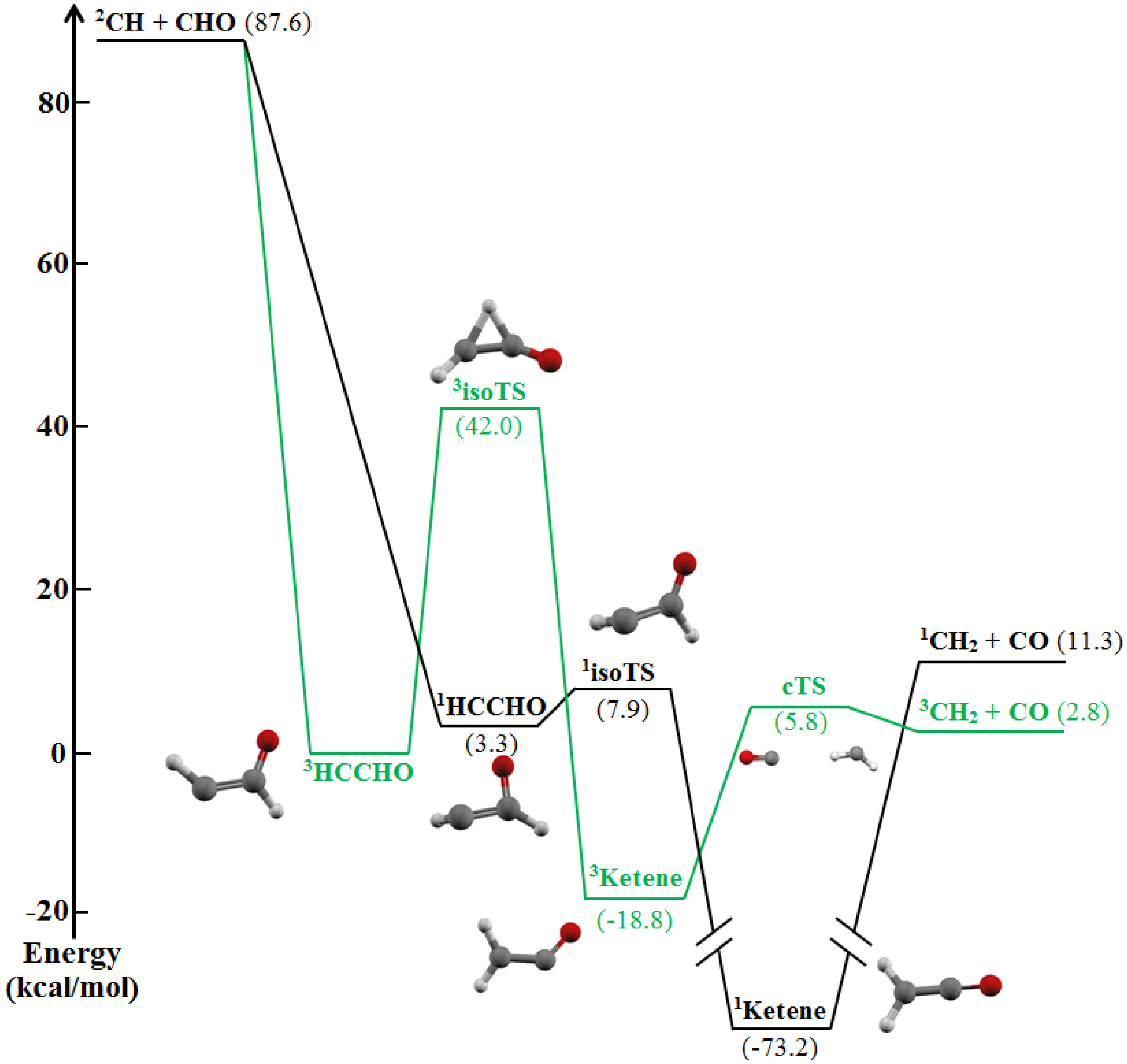

Figure C.6: Selected minima and transition states on the singlet (black) and triplet (green) potential energy surfaces of HCCHO radical. The energies of the stationary points relative to the zero-point level of ground state triplet HCCHO are given in parentheses. They are calculated at the G4//B3LYP/6-311G++(3df,2p) level of theory and include harmonic zero-point energy corrections.

C.4 Calculation of Branching Ratios Between Primary Photodissociation Channels Using the C−Cl Bond Fission P(E_T) From the Velocity Map Imaging Study

Here we recalculate the branching ratios between the primary photodissociation channels using the C−Cl bond fission P(E_T) from the velocity map imaging study shown in Figure 2.4. The purpose of these calculations is to gauge the possible error introduced in the characterization of the primary product branching by attributing the fast signal in the *m/z* = 35 (Cl^+) TOF spectra to C−Cl bond fission. While we use the same *m/z* = 35 (Cl^+) TOF data to calculate these branching ratios, we are not accounting the same signal to C−Cl bond fission (see Figure C.3 and C.4). Since we specifically want to see the effect from different fitting methods to the *m/z* = 35 (Cl^+) data, we did not alter the fits to the *m/z* = 36 ($H^{35}Cl^+$) and *m/z* = 49 (CH_2Cl^+) TOF data used in these calculations. We obtain

$$\frac{\Phi_{\text{C-Cl}}}{\Phi_{\text{HCl}}} = \text{obs}\left(\frac{^{35}\text{Cl}^+}{\text{H}^{35}\text{Cl}^+}\right) \times \text{TS}\left(\frac{\text{H}^{35}\text{Cl}}{^{35}\text{Cl}}\right) \times \left(\frac{\sigma_{\text{HCl/HCl}^+}}{\sigma_{\text{Cl/Cl}^+}}\right) = \left(\frac{69011}{13813}\right) \times \left(\frac{139876}{66299}\right) \times \left(\frac{16\ \text{Mb}}{22.8\ \text{Mb}}\right) = 7.4,$$

and

$$\frac{\Phi_{\text{C-Cl}}}{\Phi_{\text{C-C}}} = \text{obs}\left(\frac{^{35}\text{Cl}^+}{\text{CH}_2\text{Cl}^+}\right) \times \text{TS}\left(\frac{\text{CH}_2\text{Cl}}{^{35}\text{Cl}}\right) \times \left(\frac{\sigma_{\text{CH}_2\text{Cl/CH}_2\text{Cl}^+}}{\sigma_{\text{Cl/Cl}^+}}\right) = \left(\frac{17805}{30371}\right) \times \left(\frac{33445}{11488}\right) \times (1.37) = 2.3.$$

The combination of these two ratios yields total primary photodissociation branching fractions for C−Cl:HCl:C−C of 0.64:0.086:0.28. Overall, attributing the additional fast signal in the *m/z* =35 (Cl^+) data to C−Cl bond fission introduces an uncertainty of about 18% to the individual branching ratios. However, the total primary photodissociation branching ratio does not change significantly.

C.5 Results of Our Branching Calculations Using the G4 Barrier Height for the H + Ketene Channel and Subsequent Fits to the *m/z* = 42 TOF Data

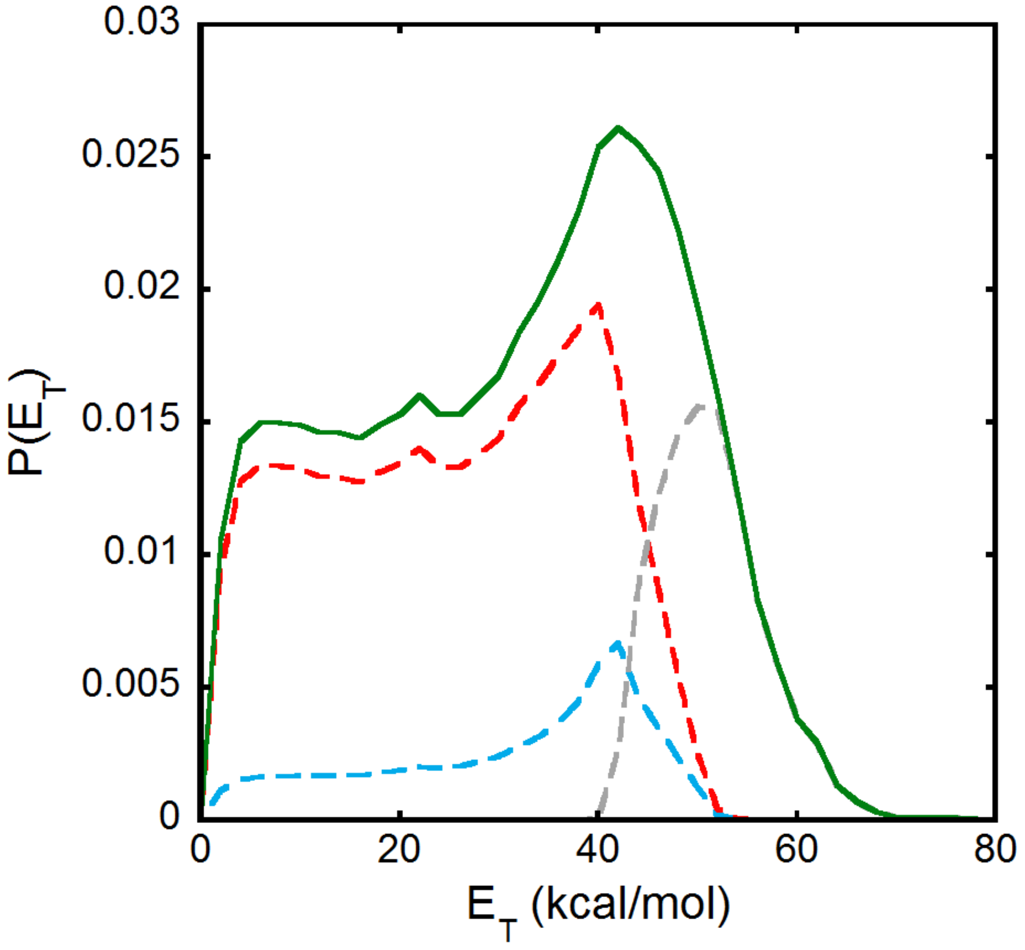

Figure C.7: Results of the branching calculations using the G4 barrier height (42.2 kcal/mol) for the H loss channel. The total primary C−Cl bond fission P(E_T) derived from the scattering data is shown in solid green line along with the predicted portions that produce H + ketene products (dashed red curve), methyl + CO products (dashed blue curve), and stable vinoxy radicals that do not dissociate (dashed gray curve). The "stable" portion of the P(E_T) is the distribution of C−Cl photofission events that our model predicts partitions insufficient vibrational energy to surmount the lowest barrier en route to dissociation.

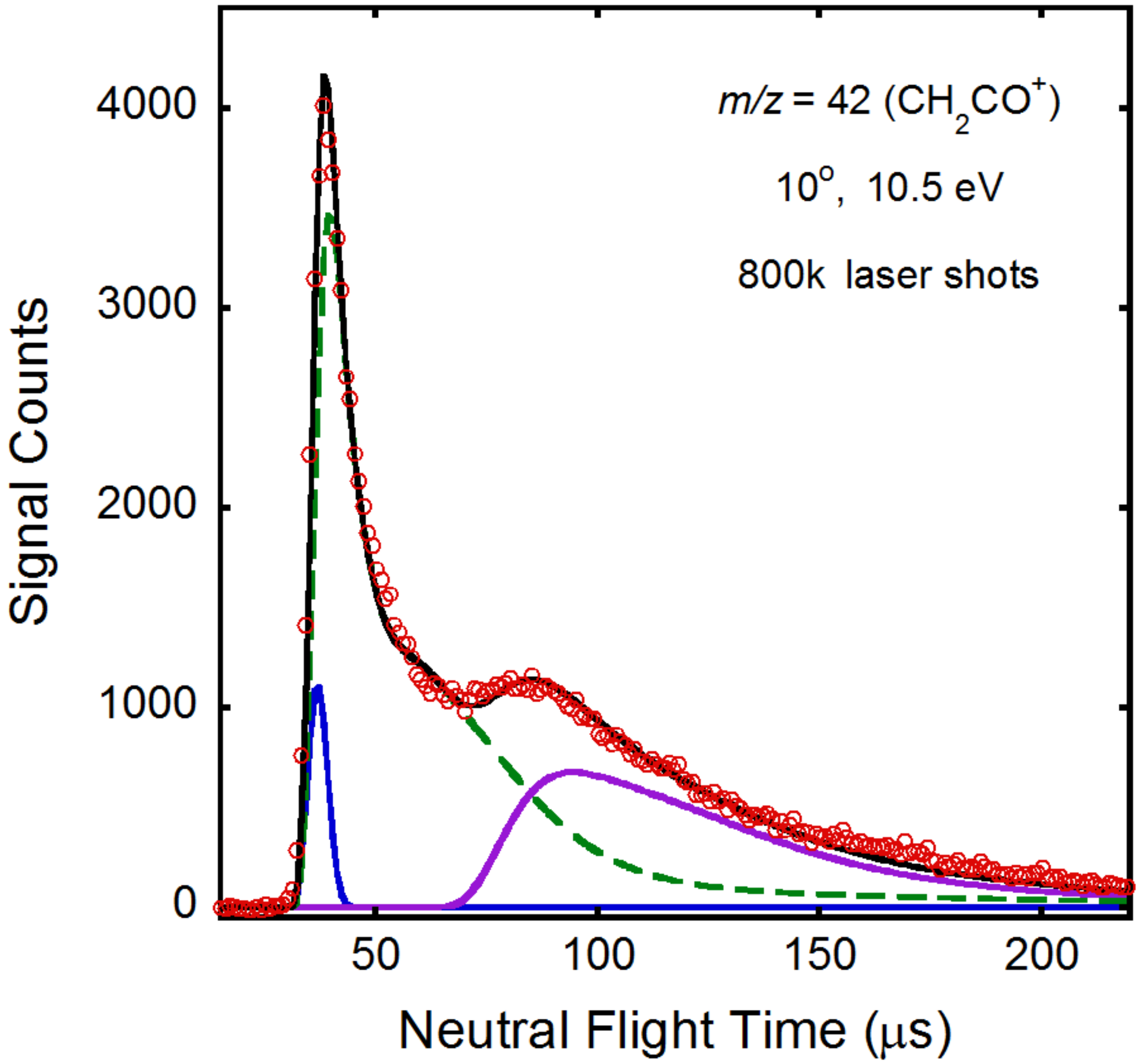

Figure C.8: Alternative fit to the TOF spectrum taken at *m/z* = 42 (CH_2CO^+) using the results from our branching calculations using the G4 barrier height for the H loss channel. TOF spectrum taken at *m/z* = 42 (CH_2CO^+) with a source angle of 10° and an ionization energy of 10.5 eV. The contribution from the dissociation of vibrationally hot vinoxy to H + CH_2CO and is calculated from the recoil translational energy of the vinoxy fragments predicted to dissociate to H + ketene (shown in dashed red line in Figure C.7) and from the P(E_T,2°) in Figure C.10 using an isotropic angular distribution. The contribution from stable ketene produced by HCl photoelimination is shown in solid blue and is derived from the P(E_T) in Figure 4.2 shown in solid black line. The fit shown in solid purple line is the contribution from clusters in the molecular beam.

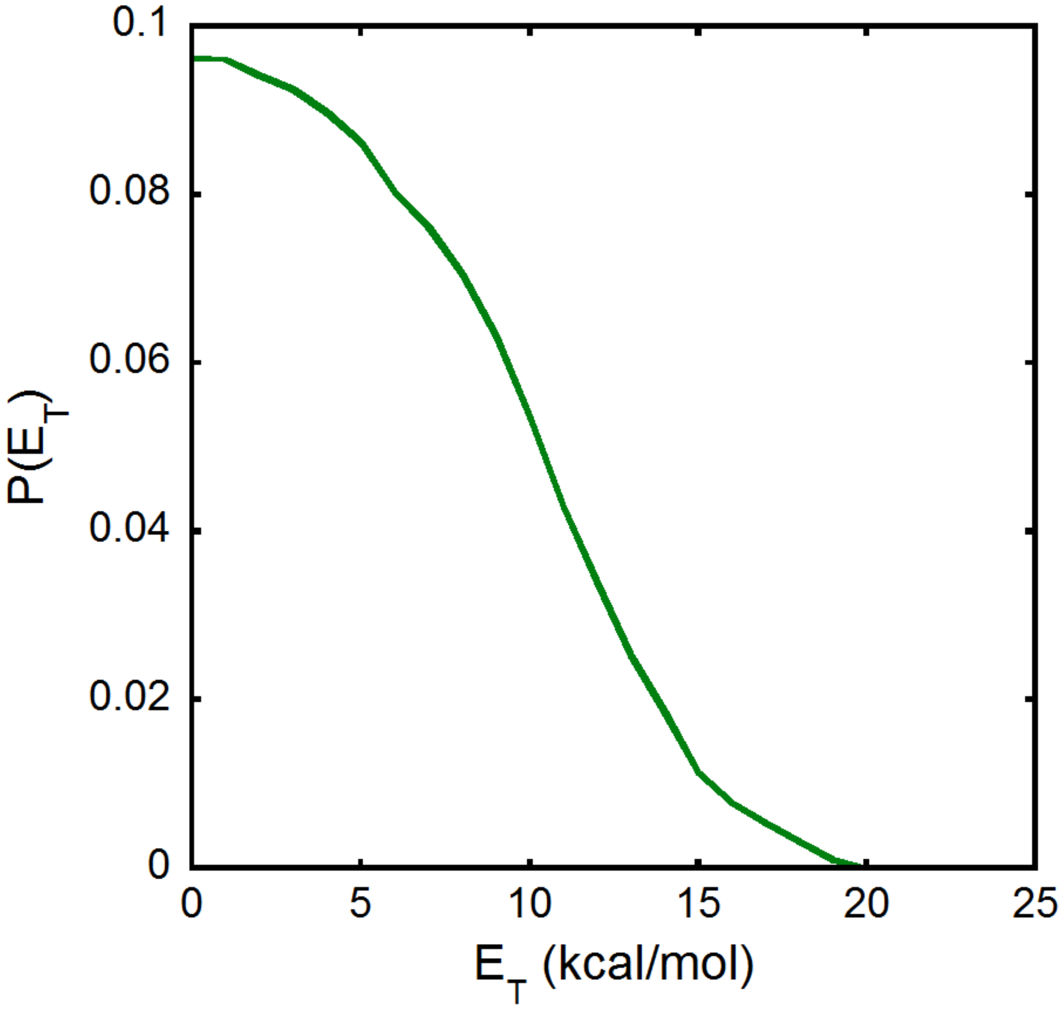

Figure C.9: Product recoil kinetic energy distribution for the unimolecular dissociation of the vinoxy radical to H + ketene. The P(E_T,2°) is derived using an isotropic angular distribution by forward convolution fitting of the signal under the dashed green fit in the m/z = 42 (CH_2CO^+) TOF spectrum in Figure C.8.

C.6 Cationic Potential Energy Surface for Vinoxy

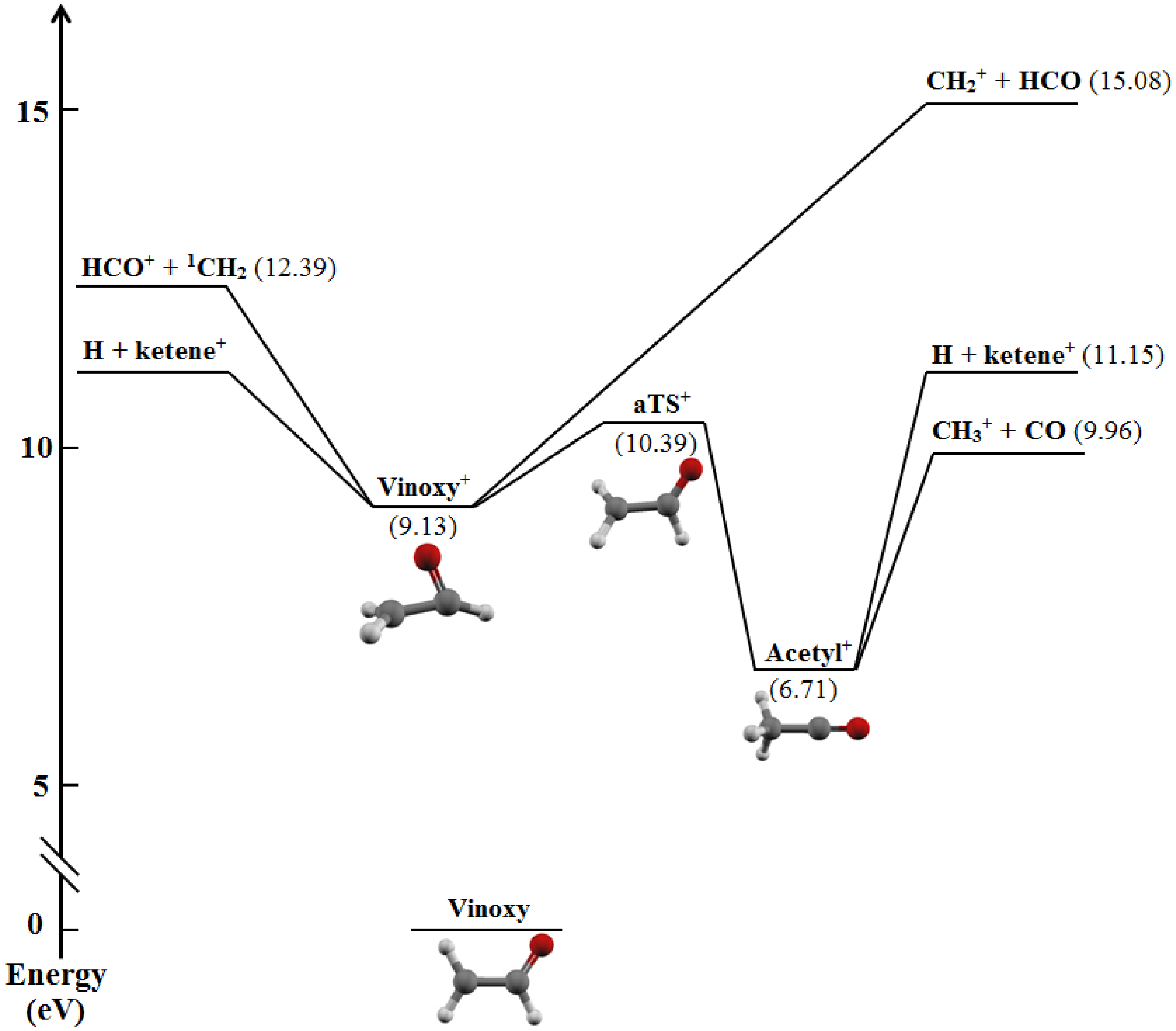

Figure C.10: Selected minima and transition states on the cationic potential energy surface of vinoxy radical. The energies of the stationary points relative to the zero-point level of ground state vinoxy are given in parentheses. They are calculated at the G4//B3LYP/6-311G++(3df,2p) level of theory and include harmonic zero-point energy corrections.

C.7 Comparison of the Contributions to the *m/z* = 15 TOF Data From Dissociative Ionization of Stable Vinoxy Radicals to CH_3^+ Using the Stable Portion of C−Cl Bond Fission P(E_T) From Both Studies

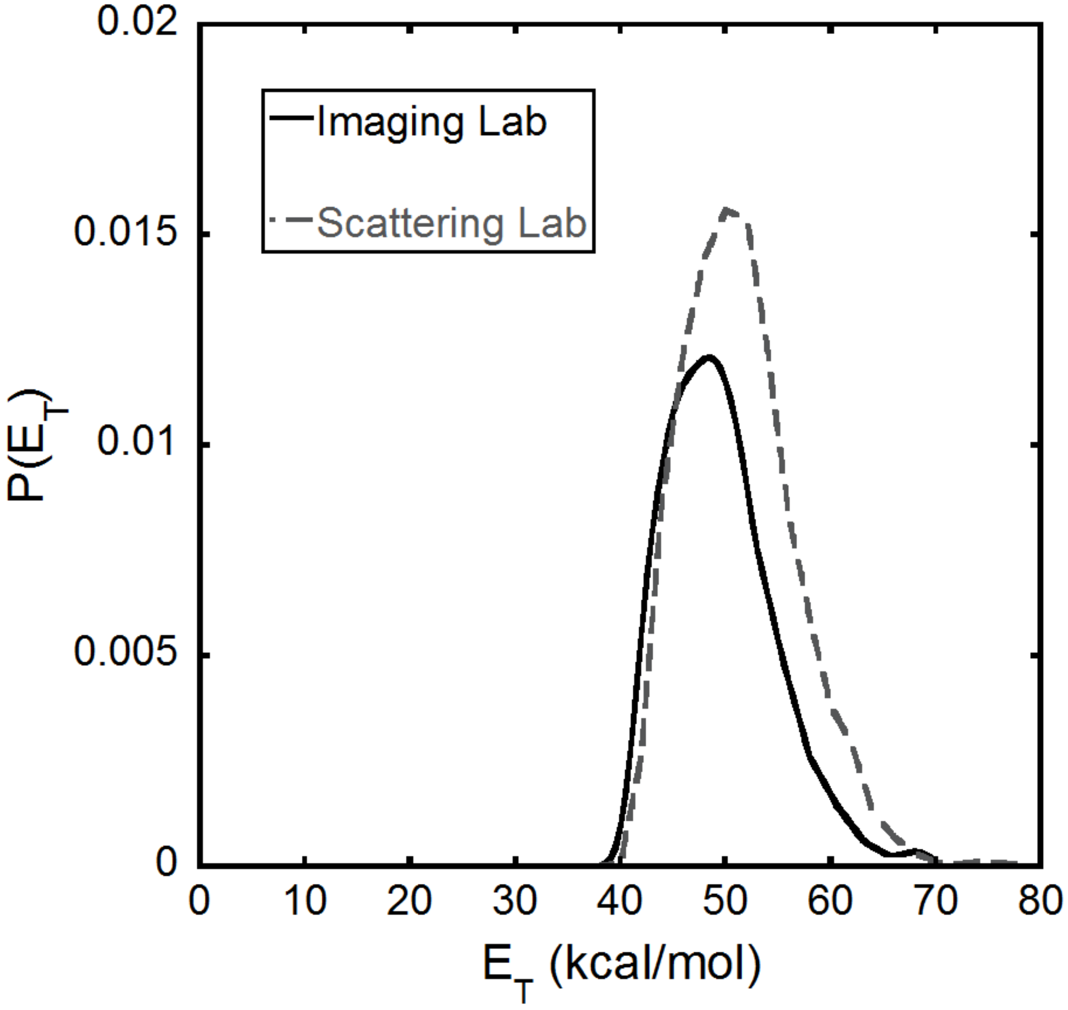

Figure C.11: Comparison of the portion of the C−Cl bond fission P(E_T) producing stable vinoxy predicted by our branching calculations in the both the scattering lab study (dashed gray line) and velocity map imaging study (solid black line) using a barrier height of 44.6 kcal/mol for dissociation of vinoxy to H + ketene.

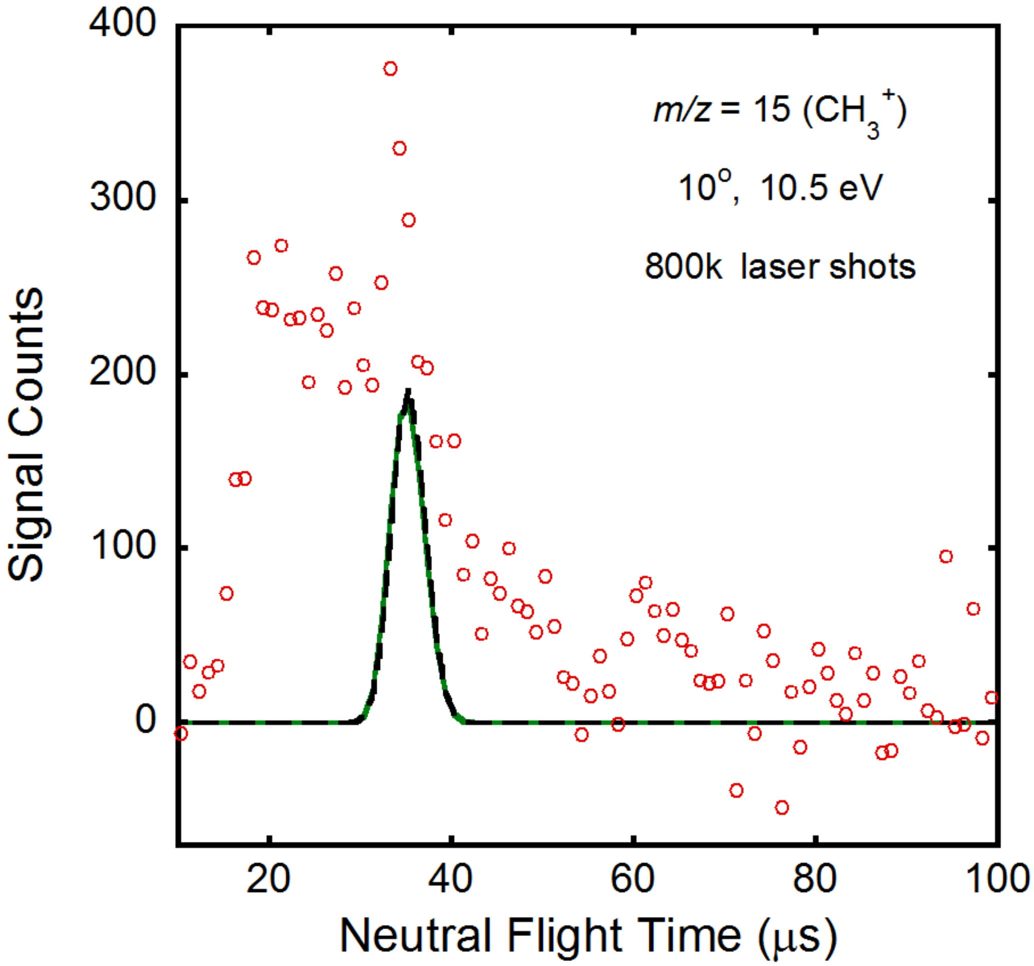

Figure C.12: Comparison of the contributions from dissociative ionization from stable vinoxy to CH_3^+ derived from the stable portion of the C−Cl bond fission P(E_T) determined in this study (solid green line) and the velocity map imaging study (dashed black line). The difference between these contributions is tiny and suggests that assigning the fast signal in the m/z = 35 (Cl^+) TOF data as C−Cl bond fission does not significantly affect the fitting of the m/z = 15 (CH_3^+) TOF data. This is especially reassuring for our calculations of the partial photoionization cross sections of vinoxy appearing at CH_3^+.

C.8 Alternative Fits to the *m/z* = 42 TOF Data Using an Anisotropic Angular Distribution

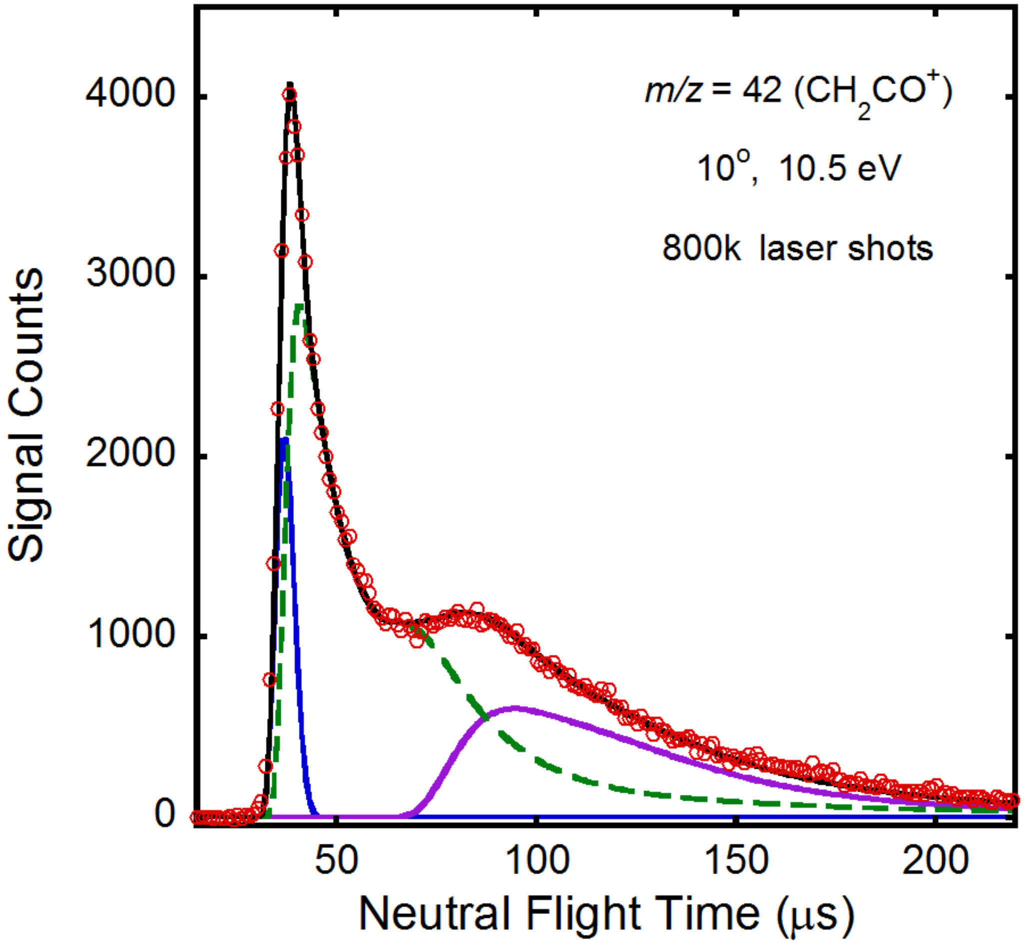

Figure C.13: Alternative fit to the TOF spectrum taken at *m/z* = 42 (CH_2CO^+) using a barrier height of 44.6 kcal/mol for our branching calculations and a different angular distribution for the secondary dissociation of vinoxy. The contribution from the dissociation of vibrationally hot vinoxy to H + CH_2CO and is calculated from the recoil translational energy of the vinoxy fragment predicted to dissociate to H + ketene (shown in dashed red line in Figure 4.10) and from the P(E_T,2°) in Figure C.14 using a symmetric 1/sinθ angular distribution calculated at 15° increments with the cosθ = −1 and 1 points adjusted to the value of 2.256 before normalization. The contribution from stable ketene produced by HCl photoelimination is shown in solid blue and is derived from the high-kinetic energy portion of the P(E_T) in Figure 4.2 shown in solid black line. The fit shown in solid purple line is the contribution from clusters in the molecular beam.

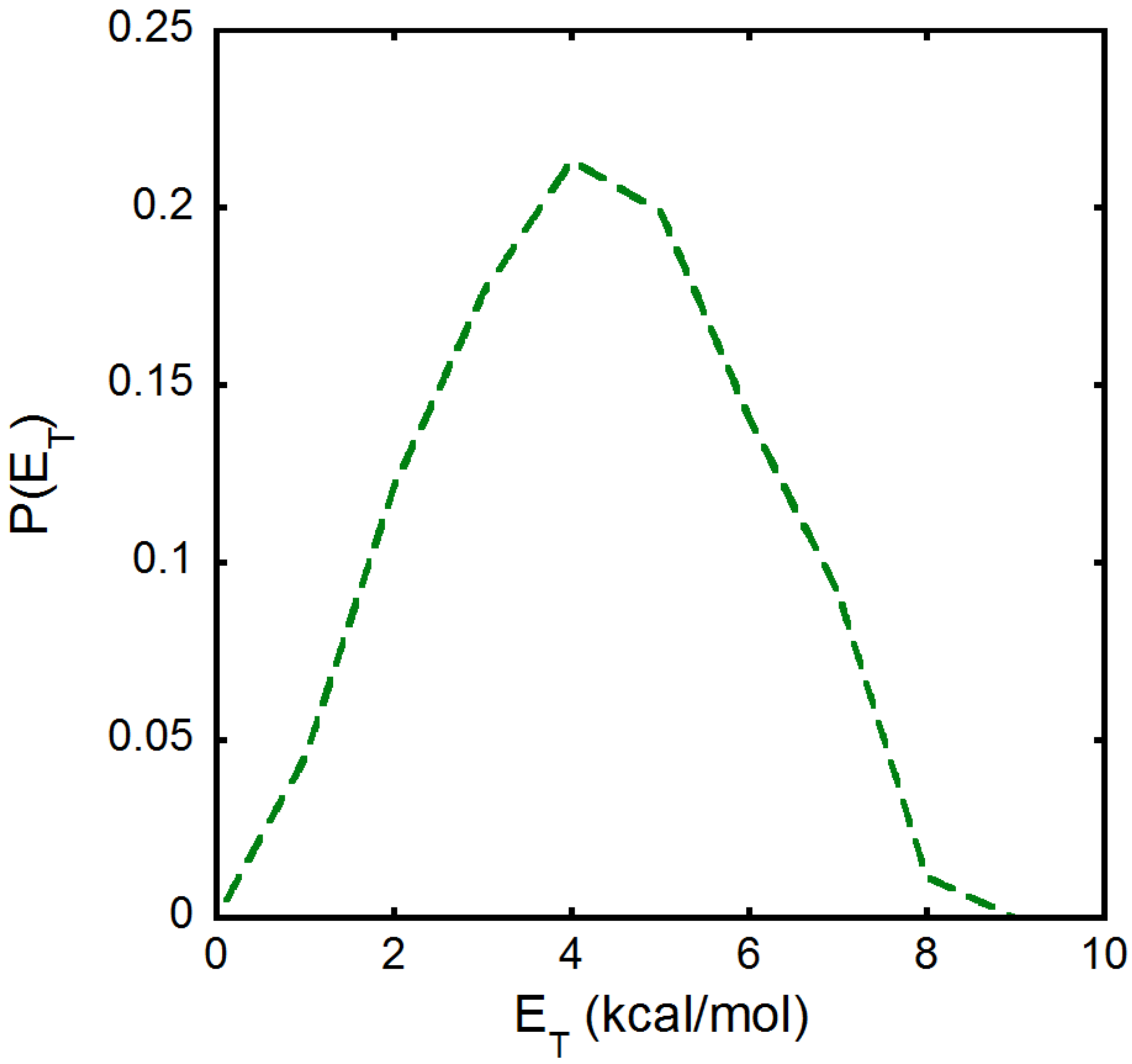

Figure C.14: Product recoil kinetic energy distribution for the unimolecular dissociation of the vinoxy radical to H + ketene using a barrier height of 44.6 kcal/mol for this channel and an anisotropic angular distribution. The P(E_T,2°) is derived from the signal under the dashed green fit in the *m/z* = 42 (CH_2CO^+) TOF spectrum shown in Figure C.14.

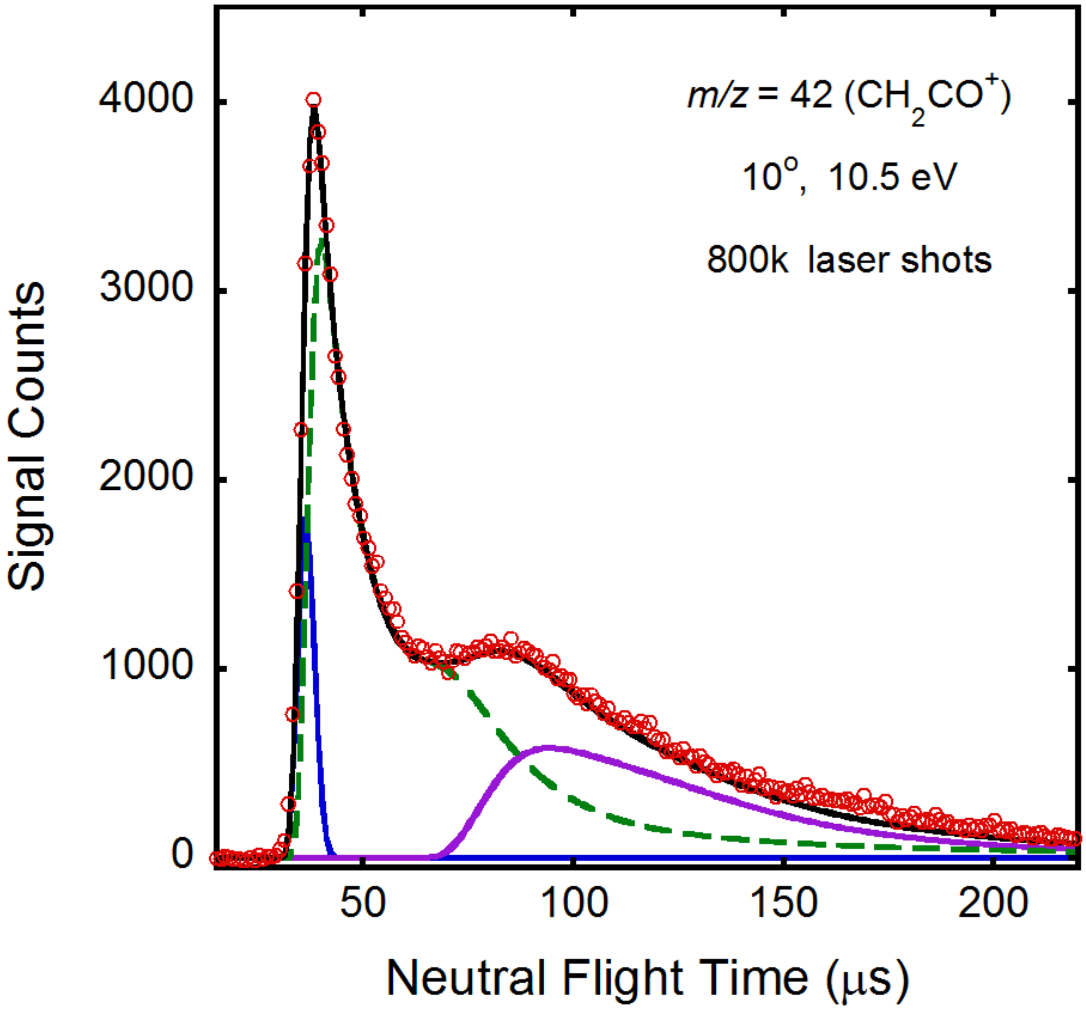

Figure C.15: Alternative fit to the TOF spectrum taken at *m/z* = 42 (CH_2CO^+) using the G4 barrier height for our branching calculations and a different angular distribution for the secondary dissociation of vinoxy. The contribution from the dissociation of vibrationally hot vinoxy to H + CH_2CO and is calculated from the recoil translational energy of the vinoxy fragment predicted to dissociate to H + ketene (shown in dashed red line in Figure C.7) and from the P(E_T,2°) in Figure C.16 using a symmetric 1/sinθ angular distribution calculated at 15° increments with the cosθ = −1 and 1 points adjusted to the value of 2.256 before normalization. The contribution from stable ketene produced by HCl photoelimination is shown in solid blue and is derived from the high-kinetic energy portion of the P(E_T) in Figure 4.2 shown in solid black line. The fit shown in solid purple line is the contribution from clusters in the molecular beam.

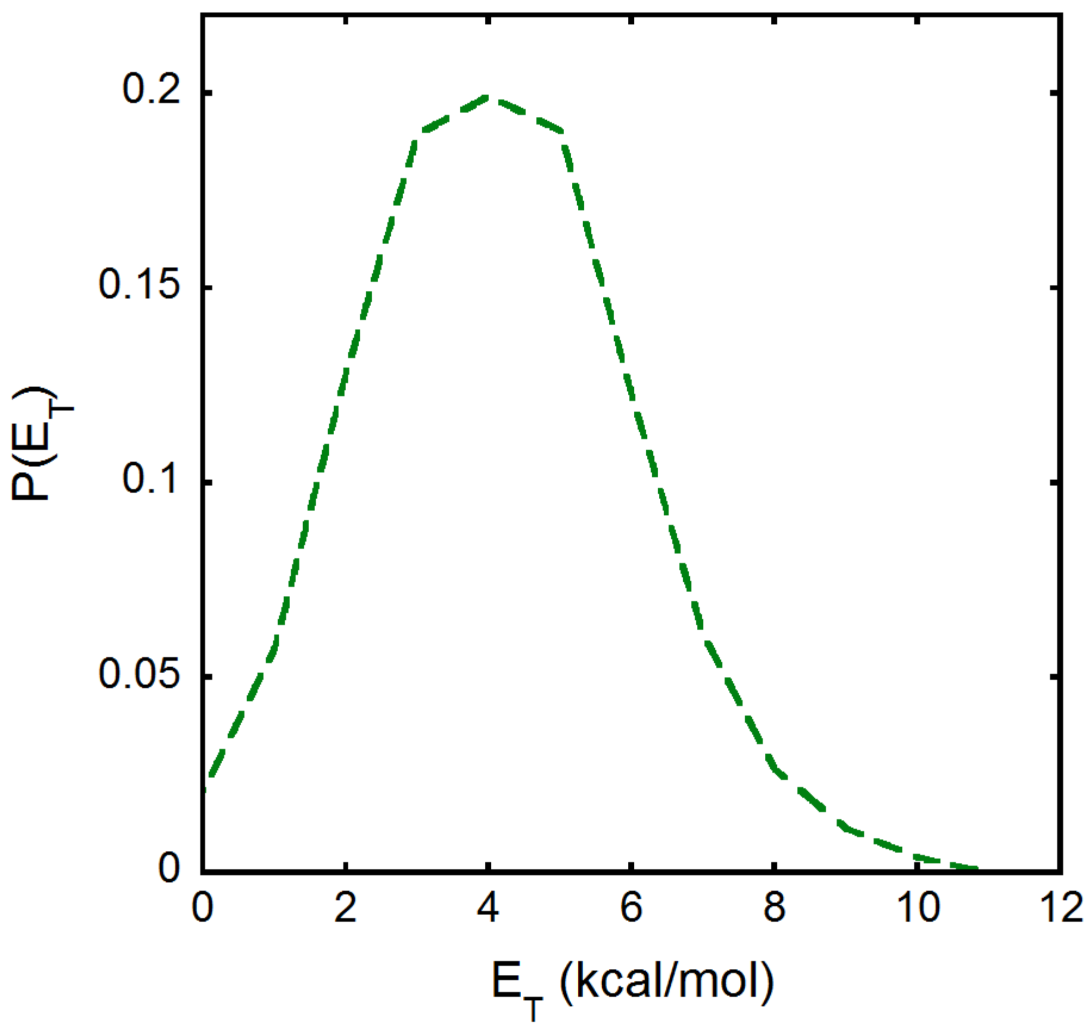

Figure C.16: Product recoil kinetic energy distribution for the unimolecular dissociation of the vinoxy radical to H + ketene using the G4 barrier height for this channel and an anisotropic angular distribution. The P(E_T,2°) is derived from the signal under the dashed green fit in the *m/z* = 42 (CH_2CO^+) TOF spectrum shown in Figure C.15.